Czech Technical University in Prague
Faculty of Electrical Engineering

Doctoral Thesis

August 2014

Jan Šafář

Czech Technical University in Prague

Faculty of Electrical Engineering

Department of Radio Engineering

ANALYSIS, MODELLING AND MITIGATION OF CROSS-RATE INTERFERENCE IN ENHANCED LORAN

Doctoral Thesis

Jan Šafář

Prague, August 2014

Ph.D. Programme: Electrical Engineering and Information Technology

Branch of study: Radioelectronics

Supervisor: Prof. Ing. František Vejražka, CSc.

Supervisor-Specialist: Doc. Dr. Ing. Pavel Kovář

Jan Šafář: *Analysis, Modelling and Mitigation of Cross-Rate Interference in Enhanced Loran,* Thesis submitted in candidature for the degree of Doctor of Philosophy, © August 2014

ABSTRACT

This thesis addresses questions that arise when considering the introduction of new eLoran stations into an existing network. Specifically, the following questions:

1. What is the effect on accuracy performance within a coverage region when a new eLoran station is installed, given the increase in Cross-Rate Interference (CRI) and a modern eLoran receiver's ability to cope with such interference through blanking or cancelling of interfering pulses?

2. What is the best method for selecting a Group Repetition Interval (GRI) for a new station installation given modern eLoran technology, including receiver signal processing techniques?

In answer to the first research question, it was found that the effects of CRI are dependent on a great number of signal parameters and on the choice of receiver signal processing algorithms. It was shown that uncompensated CRI can introduce substantial measurement errors, including a position-dependent bias in the pseudorange measurements. It was further found that state-of-the-art receiver signal processing can significantly mitigate the effects of CRI, however, a combination of several CRI mitigation techniques is required to achieve optimum results, and the residual impact on the measurement error generally cannot be considered negligible.

In answer to the second research question, it was concluded that the basic principles of GRI selection that applied to Loran-C apply equally to eLoran and can be used, when introducing a new eLoran station, to determine a set of candidate GRIs. The differences in performance between the different candidate GRIs are subtle when receiver CRI mitigation is applied and no general rule can be given for the selection of the best GRI. It was proposed that the best GRI for a particular station's configuration is found through coverage and performance modelling, taking into account CRI and modern receiver signal processing algorithms.

Prior to this research it was not possible to accurately quantify the effects of CRI on the coverage and performance of eLoran systems, and GRI selection procedures were only available for the precursor of eLoran, Loran-C. In this work, analytical models of the pseudorange and positioning error due to CRI have been developed, validated and integrated into a coverage prediction tool. As part of this work, an eLoran signal simulator has been developed to enable the candidate to verify the analytical models through receiver performance testing in a controlled radio environment. A review of existing GRI selection methods has also been carried out and a new procedure has been proposed, implementing several important eLoran updates. The tools developed have been used to assess the impact of CRI within the North-West European region and suggest optimal GRIs for two new stations in Ireland. The results should prove to be of great value to the General Lighthouse Authorities of the United Kingdom and Ireland, as they look to implement eLoran in their service area.

ACKNOWLEDGMENTS

I would like to express my gratitude to Professor František Vejražka for his advice and support throughout this work, and to Assistant Professor Pavel Kovář and Dr Petr Kačmařík for numerous discussions that contributed to the progress of this research.

This work would not have been possible without the support of the General Lighthouse Authorities of the United Kingdom and Ireland (GLA). I would like to thank all members of the GLA Research & Radionavigation Directorate, in particular Dr Paul Williams and Dr Alan Grant, for their assistance, advice and the confidence they have shown in me.

CONTENTS

ACRONYMS

ADC	Analogue to Digital Converter
AGARD	Advisory Group for Aeronautical Research and Development
ASF	Additional Secondary Factor
AWGN	Additive White Gaussian Noise
BLUE	Best Linear Unbiased Estimator
CDF	Cumulative Distribution Function
CRI	Cross-Rate Interference
CRLB	Cramer-Rao Lower Bound
CWI	Continuous Wave Interference
DAC	Digital-to-Analogue Converter
DFD	Deterministic Frequency Domain
DOD	Department of Defence
DPE	Direct Position Estimation
DRMS	Distance Root-Mean-Square
DSP	Digital Signal Processing
ECD	Envelope-to-Cycle Difference
ED	Emission Delay
EMRP	Effective Monopole Radiated Power
ESD	Energy Spectral Density
ESPB	eLoran Signal Processing Blockset
FAA	Federal Aviation Administration
FOC	Final Operational Capability
FOM	Figure of Merit
GCD	Greatest Common Divisor
GLA	General Lighthouse Authorities of the United Kingdom and Ireland
GNSS	Global Navigation Satellite Systems
GPS	Global Positioning System
GRI	Group Repetition Interval
HCPR	Half-Cycle Peak Ratio
HDOP	Horizontal Dilution of Precision

HEA	Harbour Entrance and Approach
IALA	International Association of Marine Aids to Navigation and Lighthouse Authorities
IAT	Independent Assessment Team
ICAO	International Civil Aviation Organisation
IFL	International Frequency List
ILA	International Loran Association
IMO	International Maritime Organisation
IOC	Initial Operational Capability
IPS	Ionospheric Prediction Service of the Australian Department of Industry
ITU	International Telecommunication Union
LDC	Loran Data Channel
LF	Low Frequency
LORAN	LOng-RAnge Navigation
LORAPP	Loran Accuracy Performance Panel
LORIPP	Loran Integrity Performance Panel
LPAs	Local Phase Adjustments
LS	Least Squares
LTI	Linear Time Invariant
MPS	Minimum Performance Standards
ML	Maximum Likelihood
MVU	Minimum Variance Unbiased
NELS	North-West European Loran System
NMEA	National Marine Electronics Association
NPA	Non-Precision instrument Approaches
OCXO	Oven Controlled Crystal Oscillator
PCF	Phase Code Function
PCI	Phase-Code Interval
PDF	Probability Density Function
PNT	Position, Navigation and Timing
PPM	Pulse Position Modulation
PPS	Pulse Per Second
PF	Primary Factor
PSD	Power Spectral Density

PVT	Position, Velocity and Time
RF	Radio Frequency
RMS	Root-Mean-Squared
RSS	Root-Sum-Square
RTCA	Radio Technical Commission for Aeronautics
RTCM	Radio Technical Commission for Maritime Services
SAM	System Area Monitor
SDR	Software Defined Radio
SF	Secondary Factor
SFD	Stochastic Frequency Domain
SIR	Signal-to-Interference Ratio
SINAD	Signal-to-Noise-and-Distortion Ratio
SNR	Signal-to-Noise Ratio
SQNR	Signal-to-Quantisation-Noise Ratio
SSP	Standard Sampling Point
SZC	Standard Zero Crossing
TCXO	Temperature-Compensated Crystal Oscillator
TD	Time Difference
TDMA	Time Division Multiple Access
TH	Trinity House
THV	Trinity House Vessel
TOA	Time of Arrival
TOC	Times of Coincidence
TOE	Time of Emission
TOT	Time of Transmission
TU	Technical University
USCG	United States Coast Guard
UTC	Coordinated Universal Time
VTL	Vector Tracking Loop
WAAS	Wide Area Augmentation System
WGN	White Gaussian Noise
WLS	Weighted Least Squares
WSS	Wide-Sense Stationary

Part I

BACKGROUND INFORMATION

1 INTRODUCTION

Over the past couple of decades, the U.S. Global Positioning System (GPS) has become an integral part of our society. Be it on land, at sea or in the air, GPS is an important and often the primary source of Position, Navigation and Timing (PNT) information. Although its qualities make it, in many aspects, superior over other PNT solutions, there are also some serious shortcomings and vulnerabilities common to all Global Navigation Satellite Systems (GNSS) – present, as well as future. These are largely a consequence of the extremely low GNSS signal strength levels at the surface of the Earth and have been documented many times before [1, 2, 3]. The associated safety, environmental and economic risks of relying on a single satellite navigation system have been assessed in report [4], prepared for the U.S. Department of Transportation (the 'Volpe report'). The report concludes that for critical applications, there will always be a need for a redundant system, providing back-up capabilities to GNSS. The solution, suggested by the Volpe report, is a Low Frequency (LF) terrestrial system nowadays called enhanced Loran (or eLoran for short).

So, what is eLoran? In the words of the International Loran Association's eLoran Definition Document [5],

- eLoran is an internationally standardised PNT service for use by many modes of transport and in other applications. It is the latest in the longstanding and proven series of low-frequency, LOng-RAnge Navigation (LORAN) systems.
- eLoran meets the accuracy, availability, integrity, and continuity performance requirements for aviation Non-Precision instrument Approaches (NPA), maritime Harbour Entrance and Approach (HEA) manoeuvres, land-mobile vehicle navigation, and location-based services, and is a precise source of time and frequency for applications such as telecommunications.
- eLoran is an independent, dissimilar, complement to GNSS. It allows GNSS users to retain the safety, security, and economic benefits of GNSS, even when their satellite services are disrupted.

The history of Loran systems can be traced back to the 1940's. Loran was an American development of the British GEE radionavigation system used during the Second World War. Loran systems were used extensively by the U.S. Navy and the Royal Navy. The Royal Air Force also used Loran on raids beyond the range of GEE. Since the Second World War, many long-range radionavigation systems have been in service, for example Loran-A (1950 kHz), Loran-C and its Russian counterpart Chayka (90 kHz – 110 kHz), Decca Navigator (70 kHz – 130 kHz) or Omega (10 kHz – 14 kHz). Loran-C and Chayka are the only low-frequency systems with regional coverage that survived the competition from GNSS and remain operational to date.

Loran's potential to serve as a GNSS complement and back-up in all of the applications mentioned has been confirmed in a report issued by the U.S. Federal Aviation Administration (FAA) in 2004 [6]. This report

presents the results of an extensive evaluation programme conducted by a team of government agency, industry, and academic representatives. The evaluation has been supported by Congressionally mandated funding, which has also enabled modernisation of the U.S. Loran system. The term *eLoran* has been coined in that report. Further, in 2006, the U.S. Department of Transportation and Department of Homeland Security sponsored a task at the Institute for Defense Analyses to form an Independent Assessment Team (IAT) to review the need for eLoran. The IAT, headed by Prof. Bradford Parkinson (widely regarded as the 'Father of GPS'), unanimously recommended that the U.S. Government complete the eLoran upgrade and commit to eLoran as the national backup to GPS for 20 years. Despite the IAT recommendations and other positive official statements on eLoran announced over the last few years [7, 8], in 2009, President Obama signed a law allowing the termination of Loran-C once appropriate certifications were obtained stating that the Loran-C infrastructure was not needed to meet any federal navigation requirement. The U.S. Loran-C system began shutting down in 2010.

eLoran research in the U.S. has not stopped, however, and in 2012, the U.S. Coast Guard Research & Development Center announced it had entered into a Cooperative Research and Development Agreement (CRADA) with UrsaNav, Inc., to evaluate the benefits of an LF wide-area timing system that can operate during periods of GPS unavailability. The project saw some of the U.S. Loran-C towers come on air once again [9]. Over the past couple of years support for eLoran has been building and, in 2013, the Resilient Navigation and Timing Foundation was launched [10] with the goal of convincing the U.S. government to rededicate the old Loran-C sites to eLoran. In February 2014, the topic was reopened during a hearing on navigation aids at the U.S. House of Representatives Transportation Committee, and measures were taken to prevent dismantling remaining Loran-C facilities that could be needed for eLoran [11]. eLoran has come back on the agenda in the U.S.

In Europe, there are currently nine active Loran transmitters operated jointly by Denmark, France, Germany, Norway and the UK. European Loran service providers have created the European eLoran Forum to support the successful introduction, operation, and provision of eLoran services in Europe as part of a European Radionavigation Plan (ERNP). The General Lighthouse Authorities of the United Kingdom and Ireland (GLA), who lead the way in eLoran research and development in Europe, awarded a 15-year contract for the provision of an eLoran radionavigation service to improve the safety of mariners in the UK and Irish waters, and are currently preparing for the roll-out of eLoran Initial Operational Capability (IOC) in seven major ports in the UK [12].

Exciting developments are also happening in Asia. South Korea announced plans to implement a nation-wide eLoran system by 2018. The main motivation are GPS jamming attacks from North Korea that have continued to increase in frequency and duration over the past few years. In 2012, 1016 airplanes and 254 ships in South Korea were reported to have experienced GPS disruptions due to the North Korean jamming [13].

Additionally, Russia, Saudi Arabia, Japan, and China, all of which operate Loran (or Chayka) systems, continue to monitor the ongoing developments.

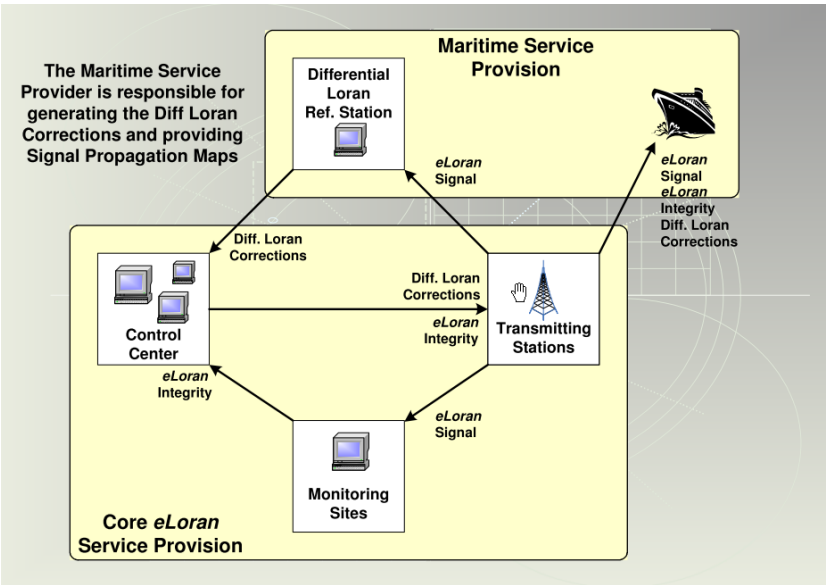

Figure 1: Maritime eLoran service provision (reproduced from [5]).

1.1 ELORAN PRIMER

This section gives a brief overview of the eLoran system and the concepts that underpin its operation. For further details the reader is referred to documents [5] and [6].

1.1.1 *eLoran Service Provision*

According to the eLoran Definition Document [5], eLoran will be divided into *Core Service Provision* components and *Application Service Provision* components. Core service provision includes eLoran transmitters and their associated monitoring and control infrastructure. Application service provision includes that infrastructure required to support the application requirements of specific transport modes, and the time and frequency community (for example, differential Loran reference stations or early sky wave monitors). This is illustrated in Figure 1, which gives an example of an eLoran service provision for the maritime sector. This thesis is focused on the core service provision aspects of eLoran.

1.1.2 *System Performance Requirements*

eLoran meets international performance standards that allow it to serve as a backup to GNSS in a great number of applications across multiple sectors. The performance of positioning systems is commonly specified using the four key metrics of accuracy, availability, continuity and integrity:

- *Accuracy* is the degree of conformance between the estimated position of a platform and its true position. Mathematically rigorous definitions of the most commonly used accuracy measures are given in Chapter 7. In this study, positioning accuracy will be considered in terms of the horizontal position error not exceeded with a probability of 95%.

- *Availability* is a measure of the ability of the system to provide the required function and performance at the initiation of the intended operation. It is normally specified as the percentage of time that the system is available for use.
- *Continuity* is a measure of the capability of the system to perform its function without non-scheduled interruptions during the intended operation. It is specified by the probability that the system will remain available for the duration of a phase of operation, assuming that it was available at the beginning of that phase of operation.
- *Integrity* is the ability of a system to provide timely warnings to users when the system should not be used for navigation. It is usually specified by the probability of an undetected failure occurring per hour of operation.

eLoran can also be used as a precise source of time and frequency. The key performance metrics used in the timing application sector are defined below.

- *Frequency accuracy* is the maximum long-term deviation in frequency from a recognised and maintained source.
- *Timing accuracy* is the absolute offset in time from a recognised and maintained time source.

The performance requirements for the different application sectors are set by relevant international bodies such as the International Maritime Organisation (IMO), International Civil Aviation Organisation (ICAO) and International Telecommunication Union (ITU). eLoran has been designed to meet the demanding accuracy requirements for maritime HEA operations, availability, integrity and continuity requirements for aviation NPA and ITU requirements in Recommendation G.811 for primary reference clocks. The required performance standards are summarised in Table 1.

The eLoran Definition Document [5] sets a position accuracy requirement of $(8 - 20)$ m. In this work, the system will be considered to meet the requirement if it provides positional information with a horizontal position error not greater than 10 m with a probability of 95% (see IMO Resolution A.1046(27)).

1.1.3 *System Architecture and Operation*

eLoran is largely based on the principles of its precursor, Loran-C. It improves upon Loran-C by numerous enhancements in transmitted signal, equipment and operating procedures. These allow eLoran to provide improved performance and additional services when compared to Loran-C, giving it the potential to serve as a backup to GNSS in a variety of applications. This section briefly describes the key components of the modernised system, highlighting the most important updates introduced.

Transmitting Stations

eLoran uses networks of land-based, geographically widely spaced transmitting stations, operating in the Low-Frequency (LF) band. The

METRIC	REQUIREMENT
Positioning Accuracy	$(8-20)$ m
Availability	0.999
Continuity	0.999 over 150 s
Integrity	$1 \cdot 10^{-7}$ per hour
Frequency Accuracy	$1 \cdot 10^{-11}$
Timing Accuracy	50 ns

Table 1: eLoran system performance requirements [5, 6]; eLoran meets the accuracy requirements for maritime HEA operations, availability, integrity and continuity requirements for aviation NPA and ITU requirements in Recommendation G.811 for primary reference clocks.

stations broadcast short groups of accurately timed, phase-coherent, high-power[1] pulses. Users can determine their position by measuring the time of arrival of the pulse groups from at least three stations.

Key eLoran transmitter updates include improved time and frequency control systems to provide higher pulse-to-pulse timing stability and facilitate accurate synchronisation of all stations to Coordinated Universal Time (UTC), and the use of state-of-the-art solid-state technology which provides improved reliability, longevity and reduced running costs.

eLoran Signal

eLoran was designed with backward compatibility in mind and the eLoran signal format is therefore based on the original U.S. Coast Guard Specification of the Transmitted Loran-C Signal [14]. Same as Loran-C, eLoran uses a Time Division Multiple Access (TDMA) scheme to share the allocated LF radio channel among all transmitting stations. eLoran stations are arranged in groups, historically referred to as *chains*. Each chain contains a *master station* and typically two to five *secondary stations*. The stations periodically transmit groups of eight[2]carefully shaped pulses. The timing of the transmissions is established such that nowhere within the geographical coverage area of a chain will any group of pulses from individual stations of the same chain overlap.

Each eLoran station operates with a specified Group Repetition Interval (GRI). The GRI is the time interval between successive pulse groups of the same station. All stations in a chain have the same GRI. The GRI expressed in tens of microseconds is the *identifier* for that chain and is sometimes also referred to as the chain *rate*. Stations are identified within a user's receiver by the GRI and the offset, or Emission Delay (ED), of each station within the GRI (measured relative to the transmission time of the master station). GRIs may range from 40000 μs to 99990 μs, in increments of 10 μs.

Figure 2 shows typical eLoran pulse transmissions within a chain. The carrier phase of some of the pulses is inverted according to special

1 The peak effective monopole radiated power is typically of the order of hundreds of kW.
2 Loran-C master stations broadcast nine pulses in a group. The ninth pulse was added for identification and integrity purposes [14] but is no longer required in eLoran due to receiver automation and the introduction of the Loran Data Channel.

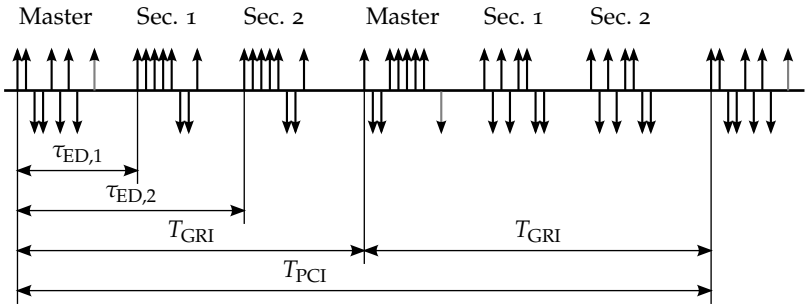

Figure 2: Schematic diagram of eLoran transmissions.

codes which enable automatic synchronisation of the receiver to the signals and help suppress some forms of interference. The phase coding is also illustrated in the diagram of Figure 2 by the orientation of the arrows. Two different phase codes are currently in use; one for the master and one for all secondary stations. The phase code values repeat after a time interval of two GRIs, also referred to as the Phase-Code Interval (PCI).

One of the key differences between eLoran and Loran-C lies in the method of signal synchronisation. In both Loran-C and eLoran, the timing of all master stations is related to a common epoch. This epoch is 0 hr, 0 min, 0 s, 1st January 1958 (UTC), when all master transmissions are assumed to have started. Synchronisation of secondary stations, however, can be accomplished using two different timing control methods.

Most Loran-C chains employ the System Area Monitor (SAM) control, where the ED of each secondary station is continually adjusted so that a specified controlling standard time difference between the master and the respective secondary signal is observed at a SAM station located in the coverage area of the chain. To a certain extent, this compensates for the time fluctuations of the signal propagation speed and improves positioning performance in the vicinity of the SAM.

In eLoran, the Time of Transmission (TOT) control is used. With this method, the transmission time of each secondary signal is set so that the ED is maintained constant at all times. In this way, all eLoran transmissions are tightly synchronised to UTC. This facilitates the use of *all-in-view receivers*, which provide improved performance and coverage through the simultaneous use of signals from multiple chains. The synchronisation of eLoran transmissions to UTC is achieved by methods independent of GNSS.

Another major difference between eLoran and Loran-C is the introduction of a standardised *data channel*. The data is typically modulated onto the navigation pulses, although other methods have also been trialed, as described later in the text. The data channel conveys information such as the station's identity and an almanac of eLoran transmitting and differential monitor sites; the data further includes real-time differential Loran corrections, integrity warnings and UTC messages that allow the eLoran system to meet the performance requirements of the maritime transportation, aviation and timing sectors.

Monitor and Reference Stations

Monitor and reference stations, located in the eLoran coverage area, serve two purposes. First is to provide real-time information to the control centre(s) regarding the quality of signals in space so that users can be notified of any anomalies. Secondly, some of the stations are used as reference stations to generate real-time *differential Loran corrections* which are then broadcast to users via the Loran data channel. Users that are within the usable range of a reference station can use the station's data to compensate for temporal changes in eLoran signals' time of arrival caused by changing propagation conditions and other factors and thereby achieve the full eLoran accuracy. The reference stations are typically deployed in harbour and other critical areas where 10 m level accuracy is required.

It should be noted that, unlike differential GNSS stations, an eLoran reference station does not need a radio transmitter itself. The data generated by the reference station is sent over a secure communications link to one or more eLoran transmitters, where it is modulated onto the LF eLoran signal. Users receive both the navigation and the data signal using the same eLoran receiver.

Control Centre(s)

In contrast to Loran-C, eLoran transmitting stations as well as the monitor\reference stations operate unmanned. The stations are monitored remotely by personnel at control centre(s) that rapidly respond to any failures in order to maintain the published levels of availability and continuity.

Users' Equipment

Much of the improvement achieved in eLoran is due to updated receiver equipment. As mentioned above, eLoran uses all-in-view receivers that operate by *(pseudo)ranging* rather than in the traditional hyperbolic mode, very much like GNSS receivers do. The use of all-in-view receivers, capable of simultaneously processing signals from multiple eLoran chains, results in better positioning accuracy and integrity performance and improved coverage.

In determining the position, eLoran receivers make use of signal *carrier phase measurements*, similarly as Loran-C receivers did. Due to advances in receiver signal processing, the phase measurement error can now be reduced by an order of magnitude or so when compared to Loran-C. This contributes to the (already very good) repeatability of Loran measurements.

To eliminate measurement biases due to propagation related effects, eLoran receivers carry digital maps of propagation corrections produced and published by competent authorities. The accuracy can further be enhanced through the use of differential corrections, as described above.

1.2 CROSS-RATE INTERFERENCE IN LORAN SYSTEMS

In any given eLoran coverage area there are likely to be several chains of eLoran stations, each operating on a different GRI. As each eLoran station broadcasts at the same carrier frequency and uses practically

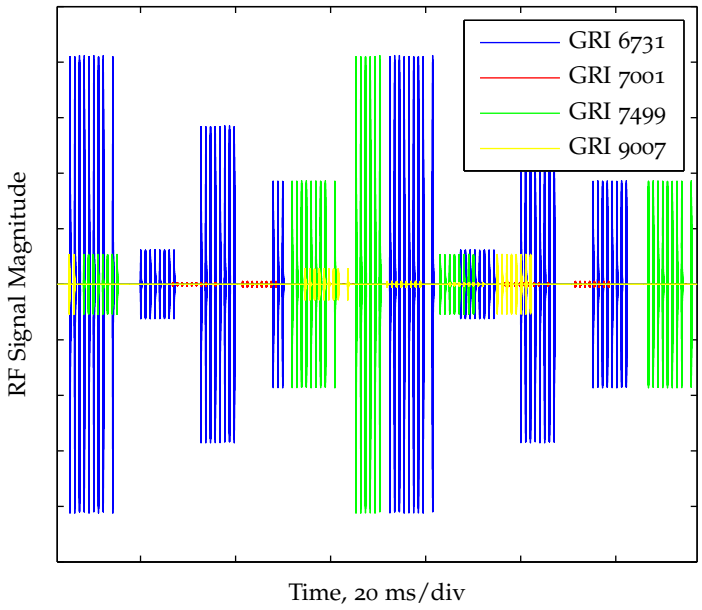

Figure 3: Cross-Rating Loran signals as would be received in Harwich, UK.

the same waveforms, the signals of an eLoran chain are often disturbed by those of other chains (see Figure 3). This is referred to as Cross-Rate Interference (CRI) and, if left uncompensated, is a major source of measurement error in Loran systems. The issue was recognised relatively early in the development of Loran systems and this section provides a brief literature review on this topic.

As early as in the 1970's, proposals for high accuracy limited coverage by Loran-C type stations (for example harbour coverage) has brought out a need for discussion of the methods of minimising CRI between adjacent chains. Initial work focused on mitigating the effects of CRI by the judicious choice of phase codes and GRIs. Roland [15] investigated cross-correlation properties of Loran-C phase codes and proposed new codes accompanied by specific GRI values, which could be used in new Loran-C 'mini-chains' to suppress CRI through averaging.

Feldman [16] presented a frequency domain method for optimum GRI selection. Observing that pairs of GRIs will result in some spectral lines being close in frequency, he developed a method that searched for GRIs whose close spectral lines were near nulls present in the spectrum as a result of the phase codes[3]. Feldman emphasised in his paper that both GRI selection and phase code structure are necessary considerations for the CRI minimisation and recommended changing the current Loran-C phase codes for ones that produce deeper nulls in the spectrum and can therefore achieve a greater CRI suppression.

Gressang [17] presented a successful solution to a serious CRI problem encountered in the operation of a mini-chain within the service area of a standard Loran-C chain. A significant reduction in CRI was achieved in a field trial through the use of balanced phase codes[4] and a specially designed GRI. The results of the test validate the methods

3 The spectral properties of Loran signals are discussed in detail in Chapter 2.
4 I.e. phase codes with an equal number of positive and negative code values.

described by Roland and Feldman [15, 16]. Serious problems caused by unmitigated CRI were also reported by Engelbrecht and Schick [18, 19].

Van Etten [20] suggested an approach whereby CRI is suppressed through the use of a unique family of GRIs and the standard phase codes together with a different strobe phase code pattern in the receiver, leaving out some of the pulses to achieve a balanced pattern.

Frank [21, 22] presented a review of previous work on so called polyphase complementary codes, described generating methods for polyphase sequences and their relation to the theory of Loran phase coding.

More recently, possible changes to the Loran phase codes were also investigated by Swaszek [23]. Swaszek suggested codes with better CRI rejection properties when compared to the standard Loran codes (at the cost of sacrificing some of the sky wave rejection capability) and he also examined the possibility of constructing sets of mutually orthogonal phase codes so as to be able to implement a CDMA system.

In the 1990's when the European Loran-C chains were planned, a time-domain CRI analysis method was developed by a team at the Technical University Delft [24] to support the GRI selection process for the new chains. The method consists of a set of mathematical rules that allow the identification of potentially harmful combinations of GRIs but it does not allow quantification of the CRI-induced errors. The method was later extended [25] to also include the evaluation of data loss in Eurofix[5] data communication.

Despite CRI being possibly the strongest source of interference to Loran, very little work has been done on modelling its effects on the system's performance - presumably due to the complex nature of the interference. A semi-analytical time-domain approach to evaluating the effects of CRI on the acquisition and track modes of a Loran-C receiver was presented by Zeltser and El-Arini [26]. The method can be used to plot the carrier phase tracking error versus time and the predictions of the method were validated by comparison against the performance of several commercially available Loran-C receivers. However, the method is computationally intensive and would not be suitable for use in coverage prediction or GRI selection.

Modern eLoran receivers can mitigate the effects of CRI through the use of signal processing techniques such as 'CRI blanking' and 'CRI cancelling'. Some information about these algorithms can be found in references [27, 28, 29, 30]. However, no analytical performance models are available for these techniques.

Johnson et al. [31] investigated the potential performance improvements to be gained by single-rating all stations in the U.S. Loran system, re-configuring the chains and assuming also that CRI is mitigated by blanking. Although it does not give any analytical expressions for the residual error due to CRI, this paper provides a useful starting point for this research.

Eurofix data link performance under CRI conditions was investigated experimentally in numerous papers [32, 33, 34, 35] and by simulation in references [36, 37]. However, to the author's knowledge, no analytical models quantifying the impact of CRI on Eurofix have been published.

5 Eurofix is an implementation of the Loran data channel used in Europe.

1.3 RESEARCH QUESTIONS

As can be seen from the literature review in the previous section, the issue of CRI has gained a great deal of attention in the past. The problem may become particularly relevant in Europe, as the GLA look to extend eLoran across their entire service area as part of the system's Final Operational Capability (FOC). Previous research provides some guidelines on how to minimise CRI within Loran-C chains, however these now need to be reviewed and updated to eLoran standards. Further, in spite of the attention that CRI has received, no comprehensive analytical models of the effects on Loran (or eLoran) performance have been published. On the topic of CRI, Pelgrum states in his PhD thesis [30]:

> 'It is difficult to give an exact mathematical analysis on the effect of cross rate on receiver performance, because it is a function of many propagation and timing variables.'.

A similar statement regarding CRI was made by Beckman who studied the effects of Continuous Wave Interference (CWI) on Loran-C [38]. This work aims to provide such an analysis.

More specifically, the aim of this research is to analyse the following with respect to eLoran core service provision:

1. What is the effect on accuracy performance within a coverage region when a new eLoran station is installed, given the increase in Cross-Rate Interference and a modern eLoran receiver's ability to cope with such interference through blanking or cancelling of interfering pulses?

2. What is the best method for selecting a Group Repetition Interval for a new station installation given modern eLoran technology, including receiver signal processing techniques?

1.4 THESIS OUTLINE

This thesis is divided into two parts, with the first one (Chapter 1 to Chapter 4) providing necessary background information on eLoran, which then serves as a foundation for the research work presented in the remainder of the thesis.

The current chapter has so far explained the motivation for this work, provided some background information on the eLoran system, and defined the goals of this research. To begin investigating the problem in hand a good understanding of the structure of the eLoran signal is required. Chapter 2 therefore takes a closer look at the eLoran signal waveform, it defines a model of the transmitted signal to be used throughout this thesis, and it derives expressions for several important signal characteristics which will be used in eLoran receiver performance analyses presented later in the thesis.

Chapter 3 expands on these results by exploring the characteristics of the eLoran radio channel and including in the signal model the key channel impairments. The resulting model provides an essential tool for the design of eLoran signal processing algorithms and their performance evaluation, which is the subject of Chapter 5 and Chapter 6.

Chapter 4 gives background information on eLoran receiver equipment and signal processing in order to provide the reader with context

for interpreting subsequent chapters. Based on the findings of the preceding chapters, Chapter 5 develops a receiver signal processing model to enable the assessment of the measurement error under noise and CRI conditions. An optimal receiver structure is proposed based on the principles of Maximum Likelihood estimation, which is then used in Chapter 6 and Chapter 7 to determine bounds on the pseudorange and position estimation error, respectively. The analytical error models derived in this work are validated in Chapter 8 against computer simulations and results of receiver test bench and field experiments. This chapter also details the design of an eLoran signal simulator used in the receiver testing, which was developed as part of this project.

Chapter 9 brings together the models and findings of previous chapters to assess the impact of CRI on the coverage and accuracy performance of eLoran. The chapter therefore provides a tool to answer to the first research question above.

Chapter 10 addresses the issue of CRI in eLoran from a signal design perspective. Specifically, the chapter focuses on mitigating the effects of CRI through the careful selection of the signal GRIs. It reviews GRI selection techniques used in establishing Loran-C chains and proposes a new GRI selection procedure that takes into account all relevant eLoran updates. This part of the thesis therefore provides the answer to the second research question. The following chapter then demonstrates the use of the procedure through a case study involving the addition of two new eLoran stations to the North-West European system.

Finally, Chapter 12 concludes the thesis, summarises the contributions this research makes to the field of radionavigation, and presents suggestions for future work. The aims and contributions of each chapter are also summarised in Table 2 along with the relevant publications by the author. A detailed list of contributions is provided in the following section.

1.5 CONTRIBUTION TO KNOWLEDGE

The candidate claims to have made the following contributions to knowledge:

- Presented a theoretical framework for the analysis of the eLoran navigation signal.
- Developed a signal processing model for an eLoran navigation receiver implementing state-of-the-art CRI mitigation algorithms.
- Derived analytical models of the pseudorange measurement error in an eLoran receiver due to the following factors: Additive White Gaussian Noise (AWGN); uncompensated CRI from single or multiple interferers including the effects of sky wave borne CRI; signal loss due to CRI blanking; residual error after CRI cancelling.
- Analysed the pseudorange measurement error under CRI conditions and demonstrated the impact of non-coprime GRIs and sub-periodic CRI on the pseudorange error statistics.
- Established a relation between sub-periodic CRI and Farey sequences and designed a mathematically rigorous procedure for identifying pairs of GRIs that give rise to this kind of interference.

CHAPTER	AIMS	KEY CONTRIBUTIONS	AUTHOR'S PUBLICATIONS
1 Introduction	Define research objectives		
2 eLoran Signal	Define model of transmitted signal	Framework for analysis of eLoran signals	
3 Channel Characteristics	Develop model of received signal		
4 Receiver Overview	Background information on eLoran receiver operation		
5 Receiver Signal Processing Model	Develop signal processing model to allow evaluation of effects of CRI	Model of eLoran navigation signal processing	[39]
6 Pseudorange Error Model	Study effects of noise and CRI on pseudorange measurements	Pseudorange error models including effects of CRI and modern signal processing	[39]
7 Positioning Accuracy	Develop formalism for modelling eLoran accuracy	Framework for eLoran accuracy modelling	[40]
8 Validation	Validate the pseudorange error and accuracy performance models	Numerical simulation framework; Design and implementation of signal simulator; Simulator and field tests; Calibrated receiver performance model	[41]
9 Coverage and Performance Model	Assess the impact of CRI on eLoran coverage and accuracy performance	Quantification of CRI effects throughout a coverage area; Improved radio noise model	[39, 42, 43, 40]
10 GRI Selection	Develop GRI selection procedure for eLoran	eLoran updates to GRI selection	[44]
11 Case Study: New Stations in Ireland	Demonstrate use of tools developed	Coverage plots incl. stations in Ireland; GRIs	

Table 2: Thesis outline.

- Demonstrated analytically that the pseudorange measurement error due to uncompensated CRI does not average out with increasing integration time (a consequence of the current signal phase codes being unbalanced).
- Calculated the autocorrelation function and Power Spectral Density (PSD) of an amplitude-jittered eLoran signal to enable the analysis of residual measurement error after CRI cancelling.
- Presented a theoretical framework for eLoran accuracy modelling allowing the accurate estimation of the R95 position error from the covariance matrix of the position fix coordinates for elliptical distributions of the position fixes.
- Conducted numerical experiments to verify the analytical pseudorange and position error models derived in this work.
- Designed and implemented a hardware eLoran signal simulator and conducted tests with a state-of-the-art commercially available eLoran receiver to validate the analytical performance models derived in this thesis. This work was presented to the Radio Technical Commission for Maritime Services (RTCM) Special Committee 127 on eLoran systems and there are plans to use the simulator in the development of the Minimum Performance Standards (MPS) for marine eLoran receivers.
- Validated the analytical models and results obtained using the signal simulator through a field experiment involving the use of real off-air signals.
- Integrated the new performance models into a coverage prediction tool originally developed by the GLA.
- Reviewed the atmospheric noise and sky wave propagation models used in the GLA coverage prediction tool and modified the models so that the effects of daytime vs. night-time radio conditions, and the probability distribution and non-stationary nature of atmospheric noise is appropriately taken into account.
- Generated sample plots of the blanking loss distribution for selected stations in North-West Europe.
- Generated daytime, night-time and average accuracy coverage plots for the North-West European system that accurately represent the effects of CRI. To the best of the author's knowledge this is the first time such plots could be created.
- Generated an average accuracy plot for the North-West European system, assuming the receiver is equipped with synchronised atomic clock.
- Reviewed existing GRI selection methods for Loran-C and proposed a new GRI selection procedure for eLoran.
- Generated plots showing time left in an existing GRI after the addition of a new station into the existing chain.
- Identified candidate GRIs for two new eLoran stations in Ireland.

– Generated accuracy coverage plots for the North-West European system after the intended extension with two Irish stations and discussed the effects of different GRI configurations.

During this work, the candidate has presented aspects of this study at numerous international conferences [44, 40, 45, 46, 41, 42] and actively participated in the meetings of the European eLoran Forum and the RTCM Special Committee 127 on eLoran systems. He was awarded the Best Student Paper Award for his presentations at the 2008 and 2009 Conventions of the International Loran Association and his work was also positively received within RTCM, where he is currently leading work on receiver testing.

2 ELORAN SIGNAL

The aim of this chapter is to develop a model of the transmitted eLoran signal, and to clarify related terminology and notation. Time-domain, frequency-domain and equivalent baseband representations of the eLoran navigation signal are presented, and selected signal characteristics are derived. The results obtained in this chapter will be used later in this thesis in developing a receiver signal processing model, and in assessing the performance of eLoran receivers through mathematical analysis, simulation and testing using synthetic eLoran signals.

2.1 ELORAN SIGNAL WAVEFORMS

There are three fundamental requirements that dictate the eLoran signal structure. The signals should:

1. Enable accurate signal Time of Arrival (TOA) measurements for use in PNT applications;
2. Enable the simultaneous use of the allocated LF radio channel by multiple transmitting stations;
3. Provide a data transmission capability.

Additionally, eLoran signals were required to be backward compatible with Loran-C standards, so that the transition to eLoran would not preclude the continued use of legacy Loran-C receivers. This requirement, however, seems to be of lesser importance today, given the decline in Loran-C user base.

The eLoran system is currently undergoing a process of standardisation. The International Loran Association had published a high-level definition document [5], however, at the time of writing, no official signal specification was available. The most pertinent document to date with regard to eLoran signal structure is the LORIPP/LORAPP[1] 'Draft Specification of the eLoran System, Rev. 3.0' [47]. The document builds upon the original U.S. Coast Guard Specification of the Transmitted Loran-C Signal [14], tightens the tolerances on signal timing and shape, and introduces a data transmission technique suitable for the dissemination of differential corrections and integrity messages. It also draws on information contained in 'Loran's Capability to Mitigate the Impact of a GPS Outage on GPS Position, Navigation, and Time Applications', prepared for the U.S. Federal Aviation Administration [6].

The signal definition used in this current work is based on the LORIPP/LORAPP Specification [47]. However, since the main focus of this work is on the system's PNT function (requirements 1 and 2 above), the definition used here does not take into account the effects of possible data modulation[2]. This seems a justifiable simplification as any data modulation used in eLoran has to be designed in such a way that the PNT function is not significantly impaired.

1 The Loran Integrity Performance Panel (LORIPP) and Loran Accuracy Performance Panel (LORAPP) were formed as part of the U.S. Loran-C Evaluation Program.

2 Note that the impact of data modulation on the signal characteristics could be modelled using tools developed later in Chapter 7.

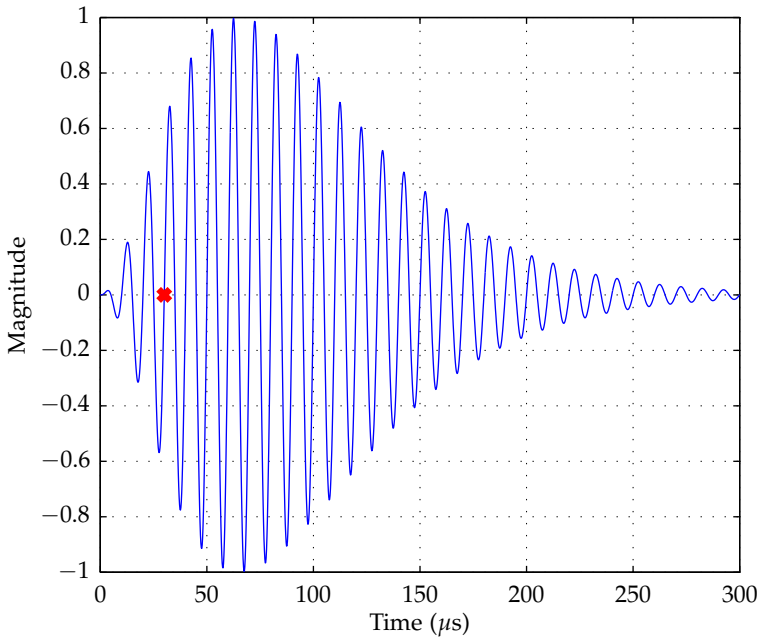

Figure 4: Standard eLoran pulse - transmitting antenna current, $\tilde{i}(t)$; red cross denotes the SZC.

2.1.1 *Transmitter Waveforms*

eLoran is a single frequency, time-shared system. Each eLoran station transmits pulsed signals which have standard leading-edge characteristics. The leading edge of the standard eLoran pulse waveform, against which the actual transmitting antenna current waveform is compared, is defined in [47]. The pulse trailing edge is controlled in order to maintain spectrum requirements, but the shape of this portion of the pulse is not strictly defined. For the purpose of this work, the shape of the standard eLoran pulse envelope, $e(t)$, can be described by the following expression

$$e(t) = \begin{cases} \left(\frac{t}{t_p}\right)^2 \exp\left(2 - 2\frac{t}{t_p}\right) & 0 \leq t \leq t_e \\ 0 & \text{otherwise} \end{cases}, \tag{2.1}$$

where t is time in seconds, t_p is the time at which the pulse reaches its peak amplitude ($t_p = 65\,\mu s$), and t_e, the pulse length, is assumed to be $300\,\mu s$ in this work.

A Radio Frequency (RF) eLoran pulse is obtained by modulating the envelope onto the eLoran carrier. The transmitting antenna current waveform can then be described as[3]

$$\tilde{i}(t) = e(t - \xi)\sin(2\pi f_c t), \tag{2.2}$$

where ξ is referred to as the Envelope-to-Cycle Difference (ECD), and $f_c = 100\,\text{kHz}$ is the eLoran carrier frequency (see Figure 4). Transmitters may be set up to radiate a small positive ECD (typically $0.5\,\mu s$). This is

3 Throughout this work, tilde denotes RF signals (as opposed to their baseband equivalents).

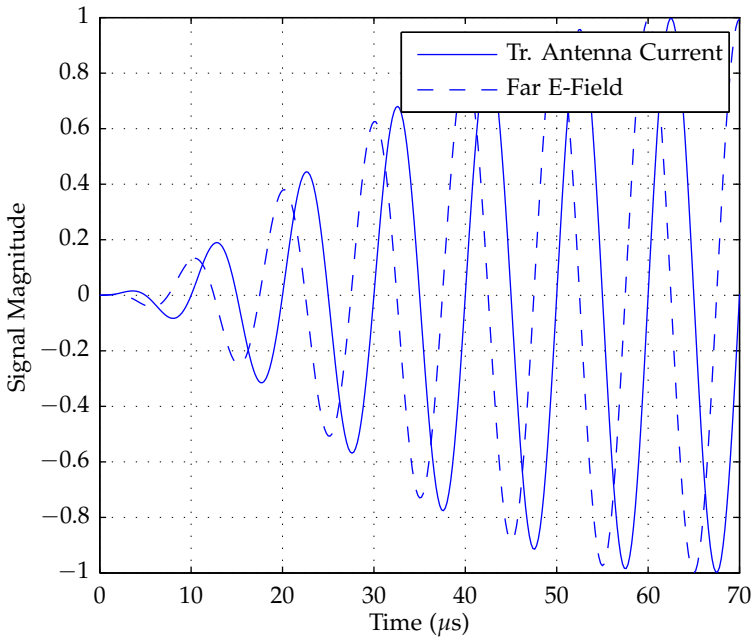

Figure 5: Leading edge of an eLoran pulse - transmitting antenna current and far E-field waveforms for a positively phase-coded pulse.

done in order to compensate for the pulse shape distortion introduced during propagation (see Chapter 3). For simplicity, it will be assumed throughout that $\xi = 0$. This will not impact the results presented in this work, as a change in ECD has practically no effect on the energy and carrier phase of the pulse and hence does not significantly affect the CRI-induced errors studied here. Also note that, for clarity, Equation 2.2 omits phase codes, which will be treated separately.

Specification [47] designates the sixth zero crossing of the transmitting antenna current 30 μs into the pulse as the Standard Zero Crossing (SZC). The SZC is used as a timing reference for measurement of eLoran signal specifications at the transmitter. The pulse timing as well as the carrier phase of the actual eLoran signal are locked to a Caesium clock. The use of *phase-coherent pulses* allows eLoran receivers to employ carrier-phase positioning and thus improve the system's accuracy.

2.1.2 *Far-Field Waveforms*

The principal transformation which occurs between the transmitting antenna current (Equation 2.2) and far E-field is a 90° carrier phase shift (see [47] and Figure 5). In addition, some propagation delay will occur. The eLoran pulse as sensed outside the near far-field by an E-field antenna can thus be approximated[4] by

$$\tilde{a}(t) = e(t-\tau)\cos\left[2\pi f_c (t-\tau)\right], \tag{2.3}$$

4 Note that this work will not consider the effects of signal dispersion during propagation (see discussion on ECDs above).

Group	Master, $C_{M,m}$							
A	1	1	-1	-1	1	-1	1	-1
B	1	-1	-1	1	1	1	1	1
	Secondary, $C_{S,m}$							
A	1	1	1	1	1	-1	-1	1
B	1	-1	1	-1	1	1	-1	-1

Table 3: eLoran Phase Codes [47].

where t now denotes the receiver time and τ will be referred to as the *time offset*[5] of the received pulse. This can be rewritten as

$$\tilde{a}(t) = e(t-\tau)\cos(2\pi f_c t + \theta), \tag{2.4}$$

where $\theta = \text{mod}(-2\pi f_c \tau, 2\pi)$ will be referred to as the *carrier phase offset* (or simply the carrier phase) of the pulse. As can be seen from the above equations, the time offset manifests itself as a carrier phase change. This relationship enables eLoran receivers to obtain precise signal timing information by measuring the carrier phase of the received pulses.

Note that it is assumed here that τ and θ are constant over time. In general, both the time and carrier phase offset may vary with time as a result of the receiver's motion and local oscillator imperfections. These effects will be discussed further in Chapter 3.

2.1.3 *Pulse Groups and Phase Codes*

As mentioned earlier in Chapter 1, eLoran pulses are sent in groups of eight. By transmitting multiple pulses within a GRI, the average signal power can be increased while retaining the advantages of a pulsed, time-shared system.

For reasons that will become clear later (see Section 5.2.2), the pulses are also phase-coded. This is implemented by altering the carrier phase of some of the pulses by 180° (i.e. inverting the polarity of the signal) according to specially designed codes. There are two different phase codes in use (master, secondary; see Table 3). A transmission sequence, also called PCI, encompasses two successive pulse groups (these are usually referred to as *Group A* and *Group B*); thereafter, the sequence repeats (see also Figure 2 in Chapter 1).

As will become clear shortly, the phase coding operation can conveniently be expressed by means of a Phase Code Function (PCF) defined as

$$b(t; \mathcal{C}, T_{\text{GRI}}) = \sum_{m=0}^{7} C_m \delta(t - mT_p) + C_{m+8}\delta(t - mT_p - T_{GRI}).$$

5 The term 'Time of Arrival' (ToA) is also often used in the Loran literature, although this is usually referenced to the time of a specific zero crossing within the pulse. Since this work is primarily concerned with the use eLoran for positioning and navigation, the choice of the reference point for the timing measurements is not important, as any common bias in the timing measurements will cancel out in the position solution.

Here, $\mathcal{C} = \{C_m\}_{m=0}^{15}$ is the assumed phase-code as per [47], $\delta(\cdot)$ is the Dirac delta, T_p is the time interval between two successive pulses in a group ($T_\mathrm{p} = 1\,\mathrm{ms}$), and T_GRI is the GRI of the signal expressed in seconds.

2.1.4 *The eLoran Pulse Train*

By introducing another auxiliary function defined as[6]

$$d(t; T_\mathrm{GRI}) = \sum_{n=-\infty}^{\infty} \delta(t - n \cdot 2T_{GRI}),$$

the complete eLoran signal can conveniently be written using the convolution[7] notation:

$$\begin{aligned}\tilde{s}(t; \tau, \theta, \mathcal{C}, T_\mathrm{GRI}) &= \tilde{a}(t; \tau, \theta) \star b(t; \mathcal{C}, T_\mathrm{GRI}) \star d(t; T_\mathrm{GRI}) \\ &= \sum_{n=-\infty}^{\infty} \sum_{m=0}^{7} \left[C_m \tilde{a}\left(t - mT_\mathrm{p} - 2nT_\mathrm{GRI}; \tau, \theta\right)\right. \\ &\quad \left. + C_{m+8} \tilde{a}\left(t - mT_\mathrm{p} - (2n+1)\,T_\mathrm{GRI}; \tau, \theta\right)\right].\end{aligned} \tag{2.5}$$

Expressing the complete signal waveform as a convolution of several simpler functions significantly simplifies the spectral analysis of Section 2.2.1.

When referring to eLoran pulse trains expressed in the form of Equation 2.5, the following terminology will be used:

- *Time offset of the eLoran signal* refers to the value of τ in $\tilde{s}(\cdot)$; it is assumed that $\tau \in \langle 0, 2T_\mathrm{GRI})$. It is also common within the Loran community to use the term TOA in relation to the received signal timing. Since there isn't a universally accepted definition of TOA in eLoran, the candidate prefers to use the term 'time offset' as defined above when specifying the timing of the signals.
- *Carrier phase of the eLoran signal* refers to the value of θ in $\tilde{s}(\cdot)$.
- *Start of PCI*: PCIs will be assumed to start at time instants defined by $t_n = 2nT_\mathrm{GRI}$, $n \in \mathbb{Z}$.
- *Start of pulse:* The first eight pulses in GRI A of n-th PCI begin at time instants defined by

  $$t_{m,n}^{(\mathrm{A})} = \tau + mT_p + 2nT_{GRI},$$

  where $m = 0, 1, \ldots, 7$, respectively; pulses in GRI B start at

  $$t_{m,n}^{(\mathrm{B})} = \tau + mT_p + (2n+1)\,T_{GRI}.$$

- *Signal amplitude*: The waveform $\tilde{s}(\cdot)$ is normalised so that the pulses have unit amplitude at the peak.

6 Note that, due to the phase codes, the idealised eLoran signal is periodic in $2T_\mathrm{GRI}$ rather than T_GRI.

7 For definition of the convolution integral see Appendix A.

2.2 EQUIVALENT SIGNAL REPRESENTATIONS

Section 2.1 defined the eLoran signal in the time domain. While the time domain description is well suited for signal synthesis (see Sections 8.1 and 8.2), it is not always suitable for signal analysis. A number of problems addressed in this work require the use of some equivalent signal representation. This section introduces two equivalent representations used throughout this thesis - the *complex envelope*, which allows a better insight into receiver signal processing, and the *frequency spectrum*, which will be particularly useful when analysing the issue of CRI.

2.2.1 *Frequency Spectrum*

Recalling Equation 2.5, the frequency spectrum of the RF eLoran signal can be expressed simply as[8]

$$S_{\tilde{s}}(f) = S_{\tilde{a}}(f) \cdot S_b(f) \cdot S_d(f), \tag{2.6}$$

where $S_{\tilde{a}}(f)$, $S_b(f)$ and $S_d(f)$ are the Fourier transforms of signals $\tilde{a}(t;\tau,\theta)$, $b(t;\mathcal{C},T_{\mathrm{GRI}})$ and $d(t;T_{\mathrm{GRI}})$ defined above (for brevity, the dependence of the spectra on τ, θ, $\mathcal{C}$ and T_{GRI} will not be explicitly denoted).

The first term on the right-hand side of Equation 2.6 can be written as follows:

$$\begin{aligned} S_{\tilde{a}}(f) &= \mathcal{F}\{e(t-\tau)\cos(2\pi f_c t+\theta)\} \\ &= \mathcal{F}\left\{e(t-\tau)\frac{1}{2}\left(\mathrm{e}^{\mathrm{j}2\pi f_c t+\mathrm{j}\theta}+\mathrm{e}^{-\mathrm{j}2\pi f_c t-\mathrm{j}\theta}\right)\right\} \\ &= \frac{1}{2}\left[S_e(f-f_c)\mathrm{e}^{-\mathrm{j}2\pi(f-f_c)\tau+\mathrm{j}\theta}+S_e(f+f_c)\mathrm{e}^{-\mathrm{j}2\pi(f+f_c)\tau-\mathrm{j}\theta}\right]. \end{aligned}$$

The spectrum of the pulse envelope, $S_e(f)$, can be calculated using the definition integral of the Fourier transform

$$S_e(f) = \int_{-\infty}^{\infty} e(t)\,\mathrm{e}^{-j2\pi ft}\,\mathrm{d}t = \int_0^{t_\mathrm{e}} \left(\frac{t}{t_p}\right)^2 \mathrm{e}^{2-2\frac{t}{t_p}-j2\pi ft}\,\mathrm{d}t.$$

This integral can be solved by parts; for $t_\mathrm{e} \to \infty$, the integral evaluates as

$$S_e(f) = \left(\frac{\mathrm{e}}{t_\mathrm{p}}\right)^2 \frac{2}{\left(\mathrm{j}2\pi f+\frac{2}{t_\mathrm{p}}\right)^3}. \tag{2.7}$$

The expression for a finite t_e is more complicated and the evaluation is left to the interested reader . For illustration, Figure 6 shows a graph of the Energy Spectral Density (ESD) of the eLoran pulse envelope, $D_e(f) = |S_e(f)|^2$, for $t_\mathrm{e} = 300\,\mu s$ (the pulse length assumed throughout this work). The energy of the pulse, E_e, calculated in the time-domain is equal to the area under the spectral density

$$E_e = \int_{-\infty}^{\infty} |e(t)|^2\,\mathrm{d}t = \int_{-\infty}^{\infty} D_e(f)\,\mathrm{d}f,$$

8 Throughout this document, the frequency spectrum (Fourier transform) of signal $s(t)$ is denoted $S_s(f) = \mathcal{F}\{s(t)\}$ (for definition of the Fourier integral see Appendix A); j denotes the imaginary unit.

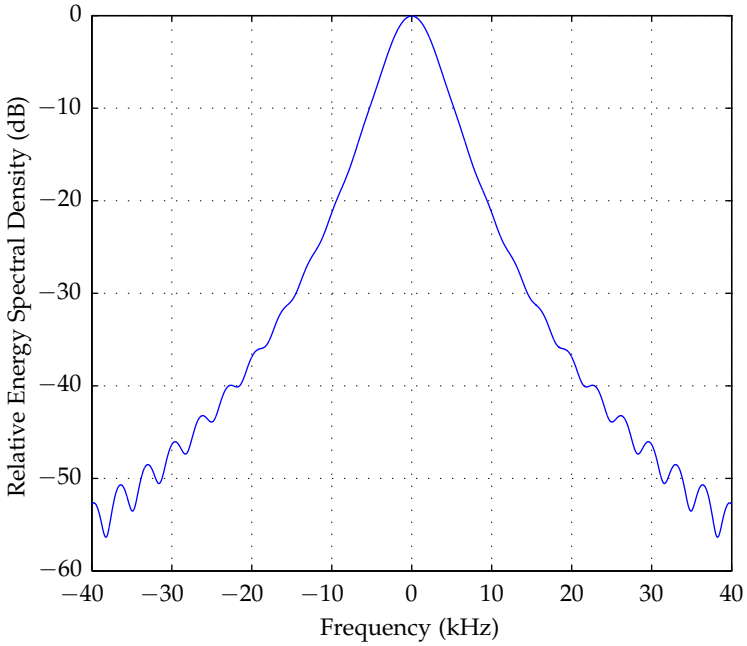

Figure 6: Relative energy spectral density of the eLoran pulse envelope, $D_{e,dB}(f) = 10\log\left(D_e(f)/D_e(0)\right)$ for $t_e = 300\,\mu s$.

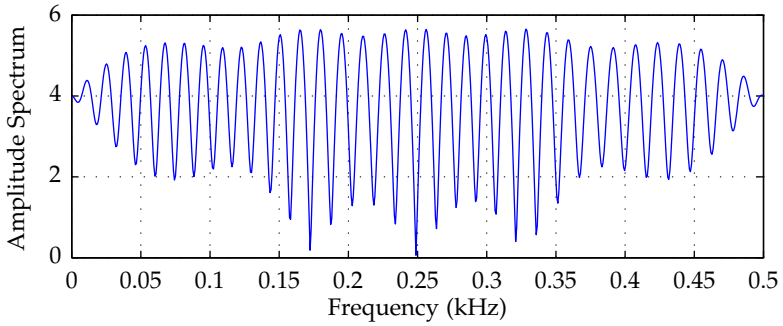

Figure 7: Close-up of the amplitude spectrum of the phase code function, $|S_b(f)|$; master phase code, GRI 6731.

and the shape of the pulse is such that 99% of the pulse energy is contained within a 20 kHz band.

The second term in Equation 2.6 can easily be evaluated using some of the basic properties of the Fourier transform

$$\begin{aligned} S_b(f) &= \mathcal{F}\left\{b\left(t;\mathcal{C},T_{\text{GRI}}\right)\right\} \\ &= \sum_{m=0}^{7} C_m e^{-j2\pi f m T_p} + C_{m+8} e^{-j2\pi f\left(mT_p+T_{\text{GRI}}\right)}. \end{aligned} \tag{2.8}$$

The spectrum resulting from this calculation is a periodic, but rather complex, function of frequency, dependent on the GRI and the phase code used. Figure 7 shows a close-up of the amplitude spectrum of a sample PCF.

It can be shown that the third term in Equation 2.6 equals to

$$\begin{aligned} S_d(f) &= \mathcal{F}\{d(t; T_{\text{GRI}})\} \\ &= \frac{1}{2T_{\text{GRI}}} \sum_{p=-\infty}^{\infty} \delta\left(f - \frac{p}{2T_{\text{GRI}}}\right). \end{aligned}$$

Inserting the above results into Equation 2.6 finally yields the spectrum of the complete eLoran signal:

$$\begin{aligned} S_{\tilde{s}}(f) = \Big[& S_e(f - f_c) \mathrm{e}^{-\mathrm{j}2\pi(f-f_c)\tau + \mathrm{j}\theta} + \\ & S_e(f + f_c) \mathrm{e}^{-\mathrm{j}2\pi(f+f_c)\tau - \mathrm{j}\theta} \Big] \cdot S_b(f) \cdot \\ & \frac{1}{4T_{\text{GRI}}} \sum_{p=-\infty}^{\infty} \delta\left(f - \frac{p}{2T_{\text{GRI}}}\right). \end{aligned} \tag{2.9}$$

As can be seen from Equation 2.9, the spectrum is formed by discrete spectral lines, $1/(2T_{\text{GRI}})$ Hz apart, weighted by the periodic spectrum of the PCF and the spectrum of a single pulse, frequency shifted to $\pm f_c$, and appropriately phase shifted.

The eLoran signal spectrum can also be expressed using the Fourier series coefficients (recall that the signal is periodic in $2T_{\text{GRI}}$). This is mainly convenient for use in numerical calculations (the Fourier series approach eliminates the Dirac deltas, which are difficult to handle in numerical computations). The coefficients can be found by using Theorem A.1 in Appendix A. From Theorem A.1 and Equation 2.9 it is immediately seen that the Fourier series coefficients of the eLoran signal are given by

$$\begin{aligned} c_{\tilde{s}}[p] = \Big[& S_e\left(\frac{p}{2T_{\text{GRI}}} - f_c\right) \mathrm{e}^{-\mathrm{j}2\pi\left(\frac{p}{2T_{\text{GRI}}} - f_c\right)\tau + \mathrm{j}\theta} + \\ & S_e\left(\frac{p}{2T_{\text{GRI}}} + f_c\right) \mathrm{e}^{-\mathrm{j}2\pi\left(\frac{p}{2T_{\text{GRI}}} + f_c\right)\tau - \mathrm{j}\theta} \Big] \cdot \frac{S_b\left(\frac{p}{2T_{\text{GRI}}}\right)}{4T_{\text{GRI}}}, \; p \in \mathbb{Z}. \end{aligned}$$

The *power spectrum* of the signal is then calculated as

$$\left\{ |c_{\tilde{s}}[p]|^2 \right\}_{p=-\infty}^{\infty}.$$

Figure 8 shows a plot of the relative power spectrum of the eLoran signal (only components at positive frequencies are shown), and Figure 9 is a close-up showing the fine structure of the individual spectral lines. The power of the eLoran signal, $P_{\tilde{s}}$, calculated in the time-domain is equal to the sum of the power spectrum coefficients

$$P_{\tilde{s}} = \frac{1}{T_0} \int_{T_0} |\tilde{s}(t)|^2 \, \mathrm{d}t = \sum_{p=-\infty}^{\infty} |c_{\tilde{s}}[p]|^2,$$

with 99% of the signal power being contained within the $(90 - 110)$ kHz band.

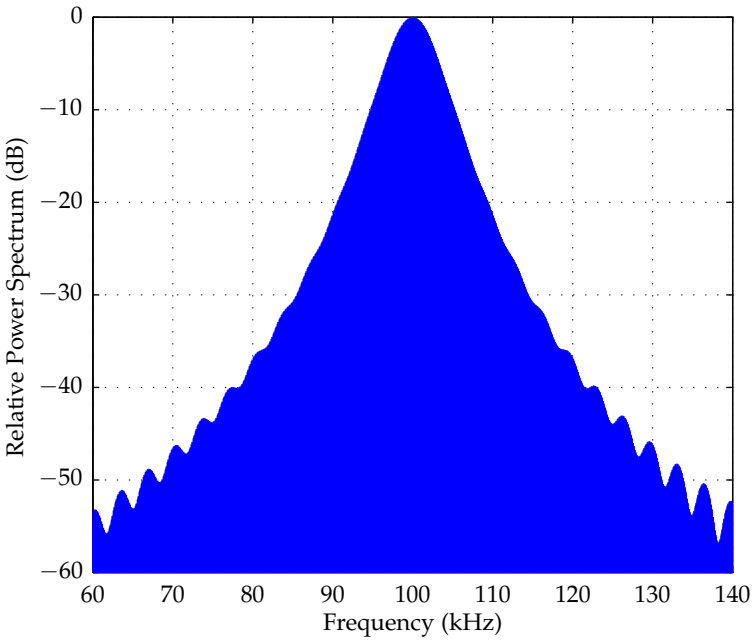

Figure 8: Relative power spectrum of the RF eLoran signal, $\{20\log(|c_{\tilde{s}}[p]|/|c_{\tilde{s},ref}|)\}_{p=-\infty}^{\infty}$; master phase code, GRI 6731.

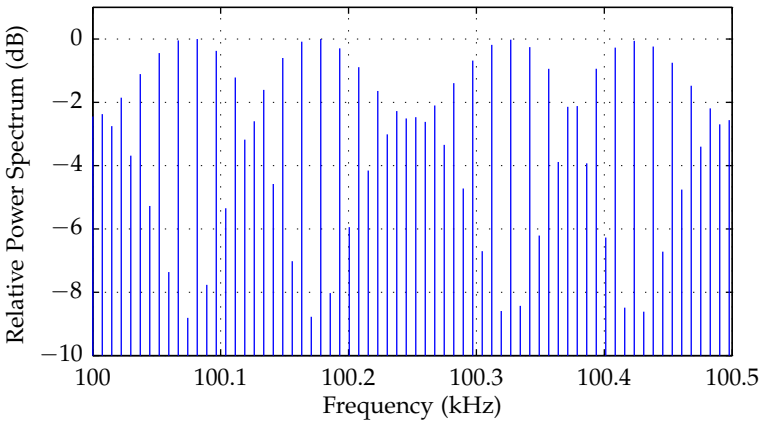

Figure 9: Close-up of the relative power spectrum of the RF eLoran signal; master phase code, GRI 6731.

2.2.2 *Complex Envelope and its Spectrum*

The concept of the Complex Envelope (CE) is introduced in Section A.2.1 in the Appendices. Using the equations in Section A.2.1, it can be shown that the complex envelope of the eLoran signal is given by[9]

$$s\left(t;\tau,\theta,\mathcal{C},T_{\mathrm{GRI}}\right)=\underbrace{e\left(t-\tau\right)\cdot\mathrm{e}^{\mathrm{j}\theta}}_{a(t;\tau,\theta)}\star b\left(t;\mathcal{C},T_{\mathrm{GRI}}\right)\star d\left(t;T_{\mathrm{GRI}}\right). \quad (2.10)$$

The spectrum of the complex envelope can then be calculated by applying the Fourier transform to the above equation and using the results obtained in the previous section:

$$S_s\left(f\right)=\frac{S_e\left(f\right)S_b\left(f\right)\mathrm{e}^{-\mathrm{j}2\pi f\tau+\mathrm{j}\theta}}{2T_{GRI}}\sum_{p=-\infty}^{\infty}\delta\left(f-\frac{p}{2T_{GRI}}\right).$$

Similarly as in the case of the RF signal, the spectrum of the complex envelope can be written more compactly as

$$S_s\left(f\right)=\sum_{p=-\infty}^{\infty}c_s\left[p\right]\delta\left(f-\frac{p}{2T_{GRI}}\right), \quad (2.11)$$

where

$$c_s\left[p\right]=\frac{\mathrm{e}^{-\mathrm{j}2\pi\frac{p}{2T_{GRI}}\tau+\mathrm{j}\theta}}{2T_{GRI}}S_e\left(\frac{p}{2T_{GRI}}\right)S_b\left(\frac{p}{2T_{GRI}}\right)$$

are the Fourier series coefficients of the signal's complex envelope.

2.3 BASIC SIGNAL CHARACTERISTICS

Some problems encountered in this work can be solved without knowledge of the complete signal structure. In many cases, basic first and second order characteristics provide enough information about the signals and their use often simplifies the calculations. This section examines the basic time-domain characteristics of eLoran signals and presents some intermediate results for use in subsequent analyses.

2.3.1 *Correlation Characteristics*

When investigating multipath (sky wave) rejection capability of the eLoran signal in Chapter 5, it will be necessary to evaluate the autocorrelation of the eLoran phase code sequences. The *time-averaged autocorrelation of a finite-length real sequence* $\mathcal{C}=\{C_m\}_{m=0}^{M-1}$ is usually defined as [48]

$$R_{\mathcal{C}}^{\mathrm{t}}\left[l\right]=\sum_m C_m C_{m+l}=\sum_m C_m C_{m-l},\quad m,l\in\mathbb{Z}.$$

9 The results assume that $T_p f_c$ and $T_{GRI} f_c$ are integers, which is always true with the current system configuration.

The autocorrelation of the GRI-A master code sequence $\mathcal{C}_{\mathrm{MA}} = \{C_{\mathrm{M},m}\}_{m=0}^{7}$ can therefore be calculated as

$$R_{\mathcal{C}_{\mathrm{MA}}}[l] = \begin{cases} \sum_{m=l}^{7} C_{\mathrm{M},m} C_{\mathrm{M},m-l} & 0 \leq l < 8, \\ R_{\mathcal{C}_{\mathrm{MA}}}[-l] & -8 < l < 0, \\ 0 & \text{otherwise}, \end{cases} \tag{2.12}$$

and that of the GRI-B master code sequence, $\mathcal{C}_{\mathrm{MB}} = \{C_{\mathrm{M},m}\}_{m=8}^{15}$, as

$$R_{\mathcal{C}_{\mathrm{MB}}}[l] = \begin{cases} \sum_{m=l+8}^{15} C_{\mathrm{M},m} C_{\mathrm{M},m-l} & 0 \leq l < 8, \\ R_{\mathcal{C}_{\mathrm{MB}}}[-l] & -8 < l < 0, \\ 0 & \text{otherwise}. \end{cases} \tag{2.13}$$

Calculations for the secondary phase code ($\mathcal{C}_{\mathrm{SA}}$, $\mathcal{C}_{\mathrm{SB}}$) are analogous to those above.

Figure 10 and Figure 11 show the autocorrelation of the GRI-A and GRI-B sequences for the two eLoran phase codes in use (see [47] or Table 3). Also plotted are the sums $R_{\mathcal{C}_{\mathrm{MA}}}[l] + R_{\mathcal{C}_{\mathrm{MB}}}[l]$ and $R_{\mathcal{C}_{\mathrm{SA}}}[l] + R_{\mathcal{C}_{\mathrm{SB}}}[l]$ which will be of special importance in Chapter 5. Note that both of these evaluate to 0 for $l \neq 0$. As will be shown later, this property of the codes enables eLoran receivers to mitigate effects of sky wave interference.

2.3.2 *Signal Power*

Signal power is a crucial parameter in determining the ranging performance of eLoran receivers. Due to the pulsed nature of the signal, power can be defined in a number of different ways.

Peak Power

The peak power of the eLoran signal is defined as the power of a sinusoid having amplitude equal to the eLoran pulse envelope at the pulse peak (i.e. 65 μs into the pulse for the ideal waveform). Thus, an eLoran signal $\tilde{x}(t)$ with pulse amplitude A has a peak power of $P_{\tilde{x}}^{\mathrm{p}} = A^2/2$.

Peak values are typically used to specify eLoran transmitter power. Note that this definition is independent of the pulse duty cycle (GRI).

Average Power

The average power of eLoran signal $\tilde{x}(t) = A \cdot \tilde{s}(t; \tau, \theta, \mathcal{C}, T_{\mathrm{GRI}})$ can be calculated as

$$\begin{aligned} P_{\tilde{x}}^{\mathrm{a}} &= \mathrm{Av}\left[|A \cdot \tilde{s}(t; \tau, \theta, \mathcal{C}, T_{\mathrm{GRI}})|^2 \right] \\ &= \frac{8A^2 E_{\tilde{a}}}{T_{\mathrm{GRI}}}, \end{aligned} \tag{2.14}$$

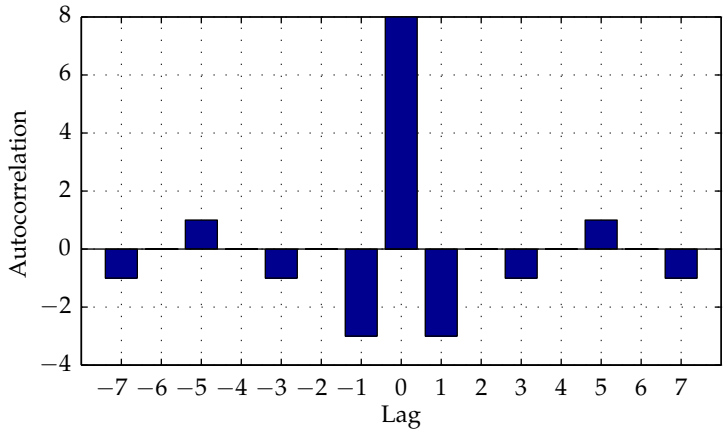

(a) GRI-A, $R_{\mathcal{C}_{\mathrm{MA}}}[l]$.

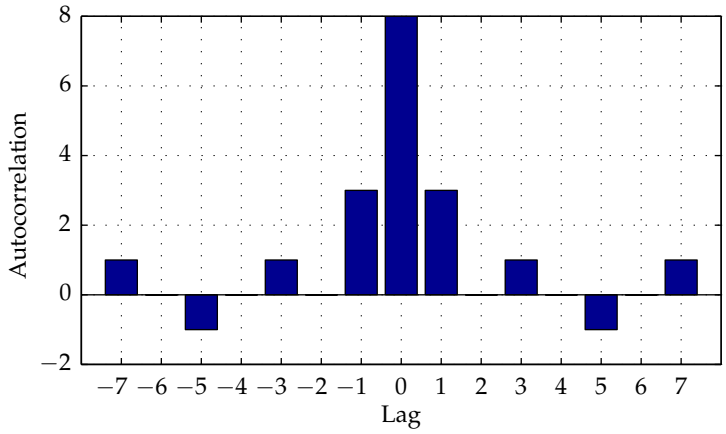

(b) GRI-B, $R_{\mathcal{C}_{\mathrm{MB}}}[l]$.

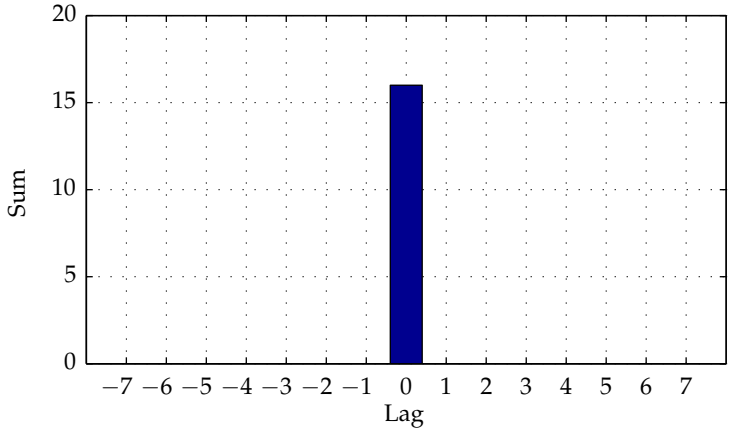

(c) GRI-A and GRI-B, $R_{\mathcal{C}_{\mathrm{MA}}}[l]+R_{\mathcal{C}_{\mathrm{MB}}}[l]$.

Figure 10: Autocorrelation sequences of the master phase code.

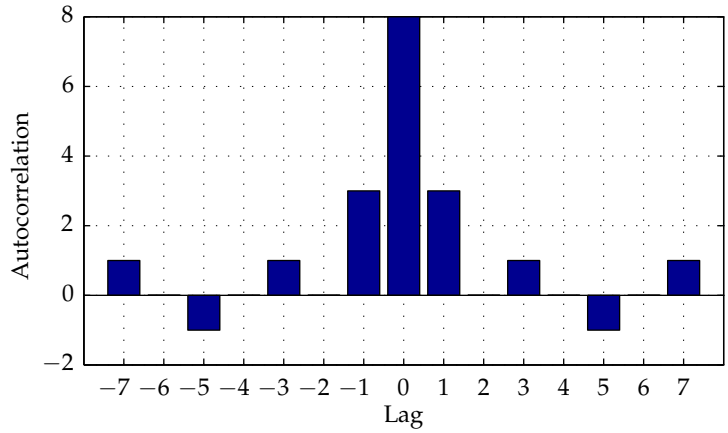

(a) GRI-A, $R_{\mathcal{C}_{\mathrm{SA}}}[l]$.

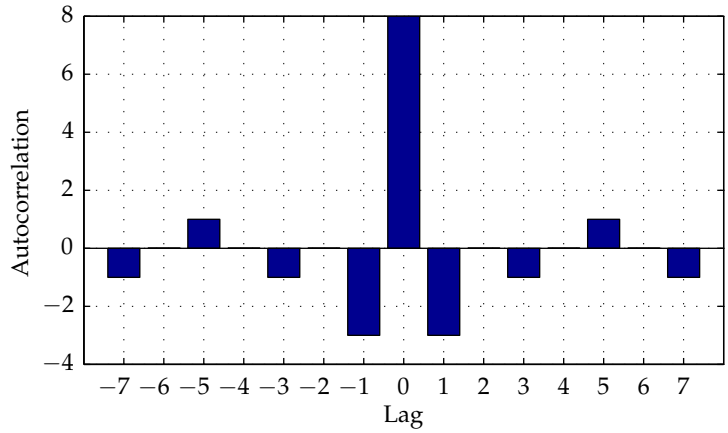

(b) GRI-B, $R_{\mathcal{C}_{\mathrm{SB}}}[l]$.

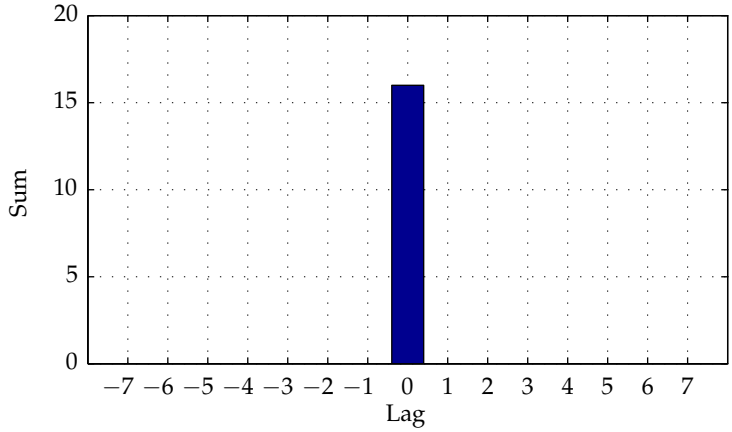

(c) GRI-A and GRI-B, $R_{\mathcal{C}_{\mathrm{SA}}}[l]+R_{\mathcal{C}_{\mathrm{SB}}}[l]$.

Figure 11: Autocorrelation sequences of the secondary phase code.

where $E_{\tilde{a}}$ is the energy of a single RF eLoran pulse (having unit amplitude)

$$\begin{aligned} E_{\tilde{a}} &= \int_0^{t_e} |\tilde{a}(t;\tau,\theta)|^2 \, dt \\ &= \int_0^{t_e} |e(t-\tau)\cos(2\pi f_c t + \theta)|^2 \, dt \\ &= \int_0^{t_e} |e(t-\tau)|^2 \frac{1+\cos(4\pi f_c t + 2\theta)}{2} dt. \end{aligned}$$

Since $t_e \gg 1/f_c$, the above can be simplified as follows:

$$\begin{aligned} E_{\tilde{a}} &\approx \frac{1}{2} \underbrace{\int_0^{t_e} |e(t-\tau)|^2 \, dt}_{E_e} \\ &= \frac{1}{2} \int_0^{t_e} \left(\frac{t}{t_p}\right)^4 \exp\left(4 - 4\frac{t}{t_p}\right) dt. \end{aligned}$$

This last integral can be solved by parts. Simplifying further the expression for $E_{\tilde{a}}$ and inserting into Equation 2.14 yields

$$P_{\tilde{x}}^a \approx \frac{3A^2 e^4 t_p}{32 T_{GRI}} = \frac{3e^4 P_{\tilde{x}}^p t_p}{16 T_{GRI}}.$$

Thus, a transmitter with a peak power of 1 MW has an average power of "only" 7 kW to 17 kW, depending on the GRI[10].

Sampling-Point Power

Except in transmitter design, the peak and average power are of little importance. For reasons that will become clear later, only the first 30 μs or so of each received eLoran pulse are useful for ranging. Receivers sample the pulses at a carefully chosen sampling point on the leading edge. The sampling-point power is then defined as the power of a sinusoid having the same amplitude as the pulse envelope at the chosen sampling point.

Specification [47] defines the *Standard Sampling Point* (SSP) to which far-field calculations or measurements should be referenced as the point 25 μs after the beginning of the pulse. For the standard eLoran pulse, the amplitude at the SSP is 0.506 times the peak amplitude (corresponding to an approx. 6dB drop relative to the peak power). Signal-to-Noise Ratio (SNR), as defined in Specification [47], should also be referenced to the SSP.

In practice, the received pulses are always distorted to some degree, for example as a result of the receiver input filtering. Consequently, the actual location of the sampling point (and therefore the useful signal power) may differ between receiver makes, and this often leads to inconsistencies in reported SNRs. The knowledge of the actual sampling point power is crucial for accurate receiver performance modelling and the issue is discussed further in Chapter 5.

10 According to Specification [47] GRI may range from 40,000 μs to 99,990 μs.

2.4 SUMMARY AND CONCLUSIONS

This chapter has defined a basic eLoran signal model, capturing the underlying structure of the signal in space. The signal definition used in this work is based on Specification [47]. However, some simplifying assumptions have had to be made in order to obtain a tractable representation, suitable for use in subsequent analyses. These are summarised below:

1. eLoran signal waveforms are modelled as deterministic functions of time; channel imperfections are not considered in this chapter (relevant imperfections will be introduced in the following chapter or at a later stage of this study).

2. Both master and secondary stations are assumed to transmit eight pulses in a GRI; the pulse length assumed throughout this work is 300 μs and the effects of possible data modulation of the pulses (e.g. Eurofix PPM) are ignored.

3. Envelope-to-Cycle Difference at the transmitter is assumed to be zero.

The signal model has been used to derive expressions for some equivalent representations and basic signal characteristics. It has been shown that the spectrum of eLoran signals is formed by discrete spectral lines, $1/\left(2T_{\mathrm{GRI}}\right)$ Hz apart. The lines are weighted by the spectrum of the corresponding phase code function, and the bandwidth occupied by the signal is governed by the shape of the pulse envelope.

Analytical expressions for the signal's complex envelope and its spectrum have been obtained. The use of the complex envelope representation significantly simplifies analyses conducted further in this work.

The autocorrelation sequences of eLoran phase codes have been shown to have properties that can help mitigate the effects of sky wave interference (the problem will be further explored in Chapter 4).

Finally, three definitions of signal power commonly used in eLoran have been provided and the relations between these definitions have been discussed.

With the knowledge of the eLoran signal structure and signal characteristics derived in this chapter, the next step is to examine the characteristics of the LF radio channel that determine signal quality at the receiver.

3 CHANNEL CHARACTERISTICS

The previous chapter developed a model of the transmitted eLoran waveform. The model forms the first building block of this thesis and allows for the basic characteristics of eLoran signals to be studied. The current chapter expands on this work by exploring the characteristics of the eLoran radio channel, and including in the model the key channel impairments. The resulting model provides a basis for investigations into eLoran signal processing, which will be the subject of Chapter 4 and Chapter 5. The current chapter begins with a discussion of possible sources of error at the transmitter, and then follows the signal path through the radio channel to the receiver. The new model is then compared with real-world RF data to demonstrate its validity.

3.1 TRANSMITTER IMPERFECTIONS

There are broadly three generations of Loran transmitters. Early Loran transmitters were based on vacuum tube amplifier technology [49]. These were gradually replaced by solid-state transmitters[1], providing considerable benefits in terms of reliability, longevity, and running costs [50]. A new transmitter design for eLoran has recently been unveiled [51] which is based around a Class D amplifier and, when compared to the previous design, demonstrates a considerably higher efficiency, smaller size, scalability, and improved waveform stability.

This section discusses how technological imperfections at the transmitter influence the signal waveforms, and highlights some of the achievements of modern eLoran transmitter design.

3.1.1 *Synchronisation Error*

Any error in the timing of eLoran transmissions translates directly into a ranging, and potentially positioning, error. Accurate and precise timekeeping at each eLoran transmitting station is therefore crucial to the performance of the system. To this end, eLoran transmitters are usually equipped with multiple Caesium clocks. Caesium clock offers an excellent frequency stability, however, it is also essential that all transmitter clocks within the system maintain synchronicity with UTC (or some other time base of choice). This can be achieved in a number of ways, some of which are briefly discussed below (details are given in reference [30]).

At present, transmitting stations in North-West Europe are synchronised using two-way Loran measurements. By using this method, the timing of the stations is maintained within 100 ns of UTC (Brest) [30]. The current synchronisation method works with discrete, 10 ns, timing steps, so-called Local Phase Adjustments (LPAs). Because of its coarse resolution, the transmitter time control mechanism effectively acts as a source of noise and can become one of the performance-limiting factors when using modern eLoran receivers. However, due to the high

1 The world's most powerful (1.6 MW peak) vacuum tube Loran-C transmitter at the U.S. Coast Guard station at George, WA, was shut down on 8th December 2003.

frequency stability of the Caesium clock, the LPAs are introduced relatively[2] infrequently, and it is believed that the residual timing error is largely compensated for by using eLoran differential corrections.

The preferred synchronisation method for eLoran is Two-Way Satellite Time Transfer (TWSTT) using a geostationary satellite. This method can achieve sub-nanosecond time-transfer accuracy [30]. Further, eLoran time control systems should apply timing corrections by frequency steering[3] [5], eliminating the need for using the LPAs. It is therefore concluded that synchronisation errors in eLoran will be negligible and do not need to be considered further.

3.1.2 *Pulse-to-Pulse Timing and Amplitude Jitter*

Various implementation imperfections can cause high-frequency pulse-to-pulse jitter in the transmitted signal. The draft eLoran system specification [47] permits a tolerance of ± 25 ns and ± 50 ns in the timing of individual pulses within a group for a single-rate and dual-rate station, respectively. The maximum acceptable amplitude deviation between any two pulses in a group is 5% for a single rate station and 10% for a dual-rate station [47]. Pelgrum [30] states that Loran signals can jitter on a pulse-to-pulse basis by 50 ns in time and 2% in amplitude[4]. It is reported that modern eLoran transmitter equipment can achieve better timing and amplitude stability (Hardy [51] states that, with the new Class D transmitter, pulse-to-pulse timing jitter should be in the order of 1 ns or better). However, it should be borne in mind that some short-term uncertainty in the transmitted signal also arises due to the fact that the transmitter output network is constantly stressed as the antenna sways[5] or environmental conditions change(changing impedance and phase centre location).

The timing jitter has the potential to affect the precision of the timing (and hence position) measurements at the receiver. However, the effect is practically cancelled out[6] by averaging of a large number of pulses prior to making the timing measurements. The amplitude jitter has, by definition, no impact on the carrier phase of the received pulses, and therefore it does not directly affect the positioning performance of the receiver. This would suggest that there is no need to consider the pulse-to-pulse jitter in this study. However, as will be shown in Chapter 6, both the timing and amplitude jitter can substantially reduce the effectiveness of some CRI mitigation algorithms and thus indirectly affect the receiver performance. The jitter will therefore be included in the signal model later in this work, when studying these specific CRI mitigation algorithms. In the absence of experimental data, it seems reasonable to assume that both the timing and amplitude jitter is statistically independent from pulse to pulse, Gaussian distributed, zero-mean, and with standard deviations as stated by Pelgrum or Hardy (see above).

2 Relative to the differential correction update rate.
3 Sub-nanosecond timing control can be achieved via frequency changes (rather than phase steps), as described e.g. in [52], [53].
4 The uncertainties stated by Pelgrum are understood as one sigma values.
5 Van Willigen et al. [54] state that, in adverse weather conditions, a typical Loran lattice tower antenna can sway by aproximately 1 m. Wire antennas, such as that used at the Anthorn station, UK, are less stable.
6 Assuming that the timing jitter is zero mean, and given the relatively small variance of the jitter.

3.2 LOW-FREQUENCY SIGNAL PROPAGATION

LF radio waves transmitted over the surface of the Earth propagate in two distinct modes – *ground wave*, which follows the curvature of the Earth's surface, and *sky wave*, which travels up into the ionosphere where it is reflected[7] back to Earth. Propagation characteristics of the ground wave are predictable and reasonably stable in time, which makes it well suited for estimating distances, as it had been demonstrated in numerous radionavigation systems (e.g. DECCA-Navigator, Omega, or Datatrak). Sky wave propagation, on the contrary, is determined by the constantly changing state of the ionosphere; the sky waves are therefore less predictable and generally considered a source of interference.

Ground wave and sky wave signal parameters are crucial inputs for modelling eLoran coverage and performance, and they also play an important role in determining the effects of CRI. This section describes the basic characteristics of the two main LF wave propagation modes and gives an overview of the propagation modelling techniques used in this work. The section also touches on the issue of re-radiation, which affects radio wave propagation in the proximity of large metallic structures.

3.2.1 *Ground Wave*

Ground wave propagation occurs as a result of refraction of the radiated wave in the atmosphere, diffraction at the Earth's surface, and absorption in the ground. These factors cause the wave to travel along the interface between the ground and the air (hence its name). On propagation from the transmitter to the receiver ground wave signals are also subject to attenuation, delay, and dispersion.

Attenuation and Field Strength

Ground waves are attenuated at a rate that depends on the conductivity of the surface over which they propagate – the lower the surface conductivity, the higher the rate of attenuation. Other factors that influence the attenuation are the surface permittivity, temperature, antenna heights above the terrain, and the frequency and polarisation of the wave [55].

As an illustration, Figure 12 shows a set of ground wave field strength curves applicable in the eLoran frequency band, drawn from data published by the ITU-R [55]. The figure plots the field strength as a function of the distance from the transmitter for different values of ground conductivity and permittivity (see also Table 4); the plots assume an Effective Monopole Radiated Power (EMRP)[8] of 1 kW. It is worth noting at this point the extremely wide range of signal strengths that an eLoran receiver may encounter in use. Assume, for example, that the receiver is required to process signals from transmitters located as close as 3 km (so that the receiver is just outside the near-field region) and up to 800 km from the receiver (commonly quoted distance beyond which early sky wave issues[9] can occur at mid-latitudes). As can be seen from

7 The term 'reflection' is often used in connection with sky waves, although the phenomenon is in fact a combination of several complicated effects, and may be more accurately described as refraction.

8 For definition of EMRP see [56].

9 See Section 3.2.2.

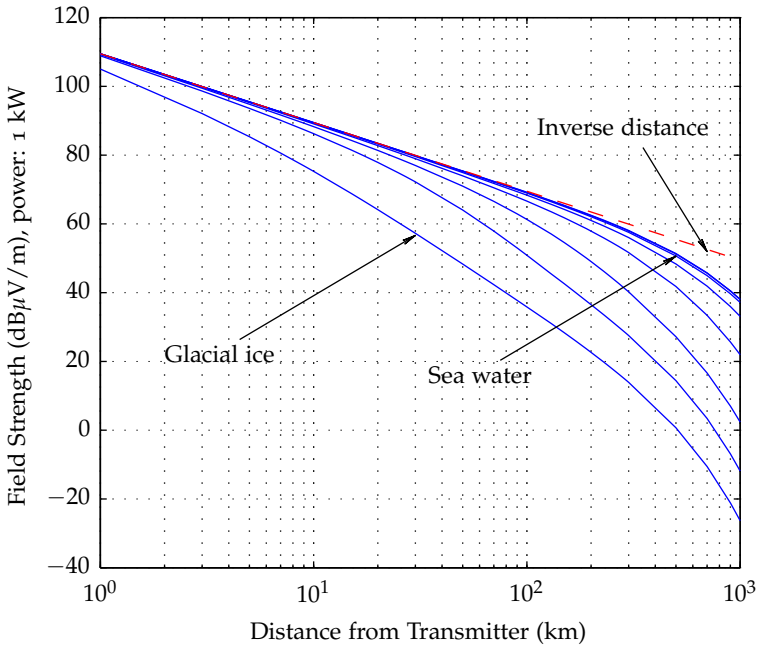

Figure 12: Ground wave field strength as a function of distance for a 1 kW transmission and different ground types (see Table 4).

Figure 12, the received signal strengths may then vary by as much as 120 dB. This places considerable demands on the design of the receiver front end and signal processing algorithms (see the near-far problem[10]). In terms of CRI, the wide range of received signal strengths necessitates the use of different interference mitigation strategies depending on the relative strength of the signal of interest with respect to the strength of the interference, as will be discussed later in this work. Ground wave (as well as sky wave) field strength modelling is therefore of crucial importance to understanding the effects of CRI.

Methods of modelling the ground wave field strength[11] are well established. A comprehensive overview of the existing methods was presented by Pelgrum [30]. In this study, ground wave field strengths will be modelled using the Millington's method as described in the ITU-R Recommendation [55] and implemented in the GLA eLoran Coverage Prediction Tool (see Chapter 9). The Millington's method is a semi-empirical approach that can be used for determining propagation over mixed paths (i.e. paths made up of sections of different ground conductivity and permittivity). It employs a set of propagation curves for different ground types (see Table 4) and combines these according to the conductivity profile along the propagation path. In this work, ground conductivity data will be drawn from a digital ground conductivity database developed at the University of Wales, Bangor, based on the ITU World Atlas of Ground Conductivities [58]. For illustration, Figure 13 shows the predicted ground wave field strength for the An-

10 The near-far problem is a condition in which a receiver captures a strong signal and thereby makes it impossible for the receiver to detect a weaker signal[57].

11 In accordance with Chapter 2, the ground wave signal field strength is defined here as the RMS value of a sinusoid having the same amplitude as the eLoran pulse envelope at the SSP.

GROUND TYPE	CONDUCTIVITY (mS/m)	RELATIVE PERMITTIVITY
Sea water	5000	70
Very good ground	30	40
Wet ground; good dry soil	10	30
Fresh water; cultivated ground	3	22
Medium dry, average ground; mountainous areas	1	15
Dry ground; permafrost; snow covered mountains	0.3	7
Extremely poor, very dry ground	0.1	3
Glacial ice	0.01	3

Table 4: Standard ground types as defined by ITU-R.

thorn transmitter, which operates within the GLA prototype eLoran system as a secondary station on GRI 6731.

Propagation Delay and Signal Time Offset

In order to obtain position and time, an eLoran receiver estimates the time offset of the ground wave eLoran signals in view (see τ in Equation 2.5 in the preceding chapter). The time offset of a signal from a particular station at a given location can be modelled as a sum of the station's Emission Delay (ED) τ_{ED}, the transmitter-to-receiver propagation delay τ_{prop}, and the receiver clock bias relative to the system clock τ_b:

$$\tau = \tau_{ED} + \tau_{prop} + \tau_b. \tag{3.1}$$

The ED is a (known) system constant. The clock bias is calculated in the receiver as part of the position solution (see Chapter 5) and for the purpose of this modelling it can be assumed known (in much of what follows, it will be useful to assume that $\tau_b = 0$ or $\tau_b = -\tau_{ED} - \tau_{prop}$). The propagation delay is a function of the distance between the transmitter and the receiver (i.e. the quantity of interest). However, it also depends on electric parameters of the Earth's surface along the signal path[12] and physical parameters of the atmosphere[13]. Due to these factors the propagation velocity of eLoran signals is lower than the velocity of light in vacuum ($c = 299792458\,\mathrm{m/s}$). Terrain

12 Mainly the ground conductivity.
13 Temperature, pressure, humidity.

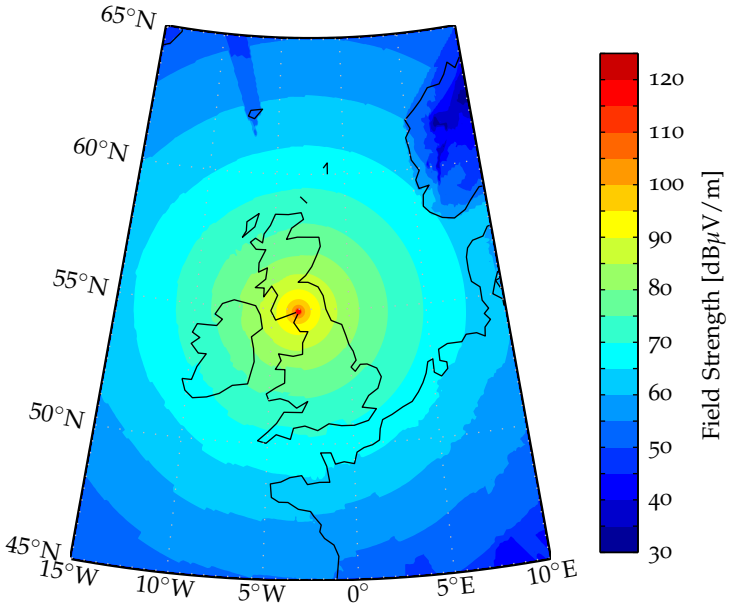

Figure 13: Predicted ground wave field strength for the Anthorn station.

elevation can also affect the signal propagation time, as eLoran ground waves follow the Earth's surface and therefore travel a longer path than the theoretical point-to-point distance over an assumed smooth Earth. Timing measurements made by the receiver thus need to be corrected to compensate for the additional delay before they are used in the position calculations. In eLoran, this is done through the use of three correction factors, as described below (the following is adapted from reference [59]).

The Primary Factor (PF), τ_{PF}, accounts for the fact that eLoran signals travel through air rather than vacuum. It is calculated as

$$\tau_{\mathrm{PF}} = \frac{r}{v_{\mathrm{atm}}},$$

where r is the ellipsoidal distance between the transmitter and the receiver as calculated by the Vincenty algorithm [59], and v_{atm} is the propagation velocity of the eLoran signal through the standard atmosphere ($v_{\mathrm{atm}} = 299691162\,\mathrm{m/s}$ is assumed, which corresponds to a refractive index[14] of 1.000338). It is also useful to define a *Delta Primary Factor*, $\tau_{\Delta\mathrm{PF}}$ - the difference in propagation time between propagation through the atmosphere and free-space propagation:

$$\tau_{\Delta\mathrm{PF}} = \frac{r}{v_{\mathrm{atm}}} - \frac{r}{c}.$$

The Secondary Factor (SF), τ_{SF}, represents the additional delay of a signal propagating over sea water with conductivity of 5000 mS/m. The SF can be well modelled. Reference [59] gives equations that permit

14 The refractive index of a medium is defined here as the ratio of the velocity of light in vacuum, c, and the phase velocity of a 100 kHz radio wave in the propagation medium.

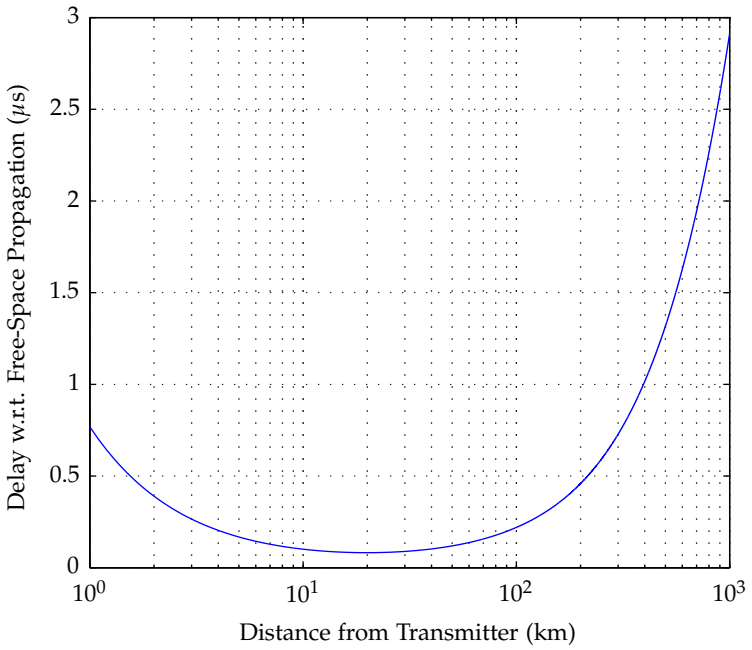

Figure 14: Delay with respect to free-space propagation experienced by a 100 kHz signal travelling over a sea water path ($\tau_{\Delta PF} + \tau_{SF}$).

the calculation of the combined contribution of $\tau_{\Delta PF} + \tau_{SF}$. One of these equations was adapted from [59] for use in this work as shown below:

$$\tau_{\Delta PF} + \tau_{SF} = \frac{1}{c} \cdot \left[B_1 + B_2 r' + \left(B_3 r' + B_4 \right) \mathrm{e}^{-\frac{r'}{2}} + \frac{2.277}{r'} \right]. \qquad (3.2)$$

Here, $r' = r \cdot 10^{-5}$, and the values of the constants in Equation 3.2 are as follows: $B_1 = -111.0$, $B_2 = 98.2$, $B_3 = 13.0$, $B_4 = 113.0$. Figure 14 plots the delay $\tau_{\Delta PF} + \tau_{SF}$ as a function of the distance from the transmitter. It can be seen from the figure that the additional delays are on the other of microseconds (equivalent to hundreds of meters in distance) and it is therefore essential that eLoran receivers compensate for the PF and SF.

The PF and SF are used to model the signal propagation in the Earth's atmosphere over an all-sea water path. Any additional delay due to propagation over land can then be taken into account using the so-called Additional Secondary Factor (ASF), τ_{ASF}. The ASFs are by definition zero over an all-sea-water path. ASF values for a heterogeneous propagation path can be modelled based on surface conductivity and topography data [30]. However, for such applications as aviation NPA or maritime HEA measured ASFs must be used [60]. These can be stored in the receiver in the form of an *ASF map*. In order to achieve the highest possible positioning accuracy, temporal variations in the ASF values can be monitored by differential Loran reference stations and broadcast to the user in the form of *differential corrections*, e.g. using the eLoran data channel. Note that not taking ASFs into account can lead to significant ranging errors of up to several kilometres [61]. Applying them correctly, on the other hand, gives the full eLoran accuracy, which approaches the repeatable accuracy of the system (Chapter 9).

Taking the three correction factors into account, the ground wave propagation delay can be modelled as:

$$\tau_{\text{prop}} = \frac{r}{c} + \tau_{\Delta\text{PF}} + \tau_{\text{SF}} + \tau_{\text{ASF}}. \tag{3.3}$$

In this work, the PF and SF will be modelled when deemed necessary (e.g. when generating RF signals for receiver performance testing as described in Chapter 6); ASFs will either be assumed known (a reasonable assumption when ASF maps are available and the receiver is operating in the differential mode) or equal to zero (an all-sea water path assumption).

Dispersion

A dispersive character of the propagation medium means that different frequency components of the eLoran signal travel at different velocities, which causes a slight distortion of the pulse shape as the signal propagates through the coverage area; some distortion is also introduced due to the fact that the ground wave attenuation varies slightly across the eLoran band.

The propagation-related distortion is usually described by a change in the ECD of the pulse, i.e. by a time-shift between the pulse envelope and the underlying 100 kHz carrier-wave signal[15]. The ECD shows a very predictable behaviour over sea water, changing in a negative direction with distance from the transmitter with a rate of change of approximately 2.5 μs per thousand miles [62]. Prediction of the ECD for mixed paths is also possible. Sherman [62] presented an empirical model which divides the propagation path into segments of constant ground conductivity and applies different ECD lapse rates in each of these segments. Williams and Last [63] described an analytical approach to modelling the pulse distortion, which also takes into account the effect of terrain. However, the accuracy of both these methods is limited by the accuracy of the available ground conductivity and topography data.

The important point to note here is that changes in ECD have practically no effect on the accuracy performance of eLoran receivers, as long as the ECD of the received pulse[16]stays within approximately $\pm 5\,\mu$s (i.e. a half-cycle of the eLoran carrier) of its nominal value ($\pm 2.5\,\mu$s if an H-field antenna is used due to the phase ambiguity associated with the loop antenna). This is because eLoran employs carrier-phase positioning and the receivers only use the pulse envelope to resolve the ambiguity inherent in the carrier phase measurements (for more detail on eLoran receiver operation see Chapter 4 and Chapter 5). Larger changes in ECD may cause the ambiguity resolution algorithm to fail. This results in a timing error which is an integer multiple of the eLoran cycle (equivalent to approximately 3 km error in the ranging measurement). It can therefore be seen that propagation-related changes in

15 For definition of the ECD see Chapter 2. Note that the actual distortion may be of a more complex nature, however using the ECD to describe the propagation-related changes in the pulse waveform is a common practice.

16 Strictly speaking, the ECD has only been defined for the ideal pulse as described in Chapter 2. The term 'ECD of the received pulse' is to be understood here as the time-difference between a reference point within the pulse determined based on the shape of the pulse envelope, and the true reference point determined by the zero crossings of the carrier wave signal.

ECD present an integrity, rather than accuracy, issue. Since integrity investigations are out of the scope of this work, it is concluded that the effects of propagation on the shape of the pulse do not need to be modelled.

3.2.2 *Sky Wave*

Given the 3 km wavelength of the eLoran signal, any practical eLoran transmitting antenna acts as a short vertical monopole over a conducting ground plane. The radiation pattern of such an antenna allows a substantial portion of the transmitted energy to be radiated above the horizon. A sky wave is formed which travels up into the ionosphere, where it is attenuated, refracted and eventually returned back to the Earth's surface. The down-coming wave may again be reflected at the surface and the process can be repeated one or more times, giving rise to *multihop sky waves*.

The ionosphere, which enables sky wave propagation, begins at an altitude of approximately 50 km and extends to beyond 1000 km [64]. It is created and sustained mainly by solar radiation which drives dissociation and ionisation processes in the upper layers of the Earth's atmosphere. The ionosphere consists of layers of different ion and electron density, commonly denoted by letters D, E and F[17]. The redirection of the sky wave back towards the Earth is a result of a varying refractive index of the ionosphere which is a function of the ion and electron densities. For LF waves, the redirection occurs in the D and E layers. Generally, higher-frequency signals are reflected at higher altitudes, and signals at frequencies above approximately 30 MHz penetrate to space.

The reflection coefficient of the ionosphere varies greatly with length and geographic and geomagnetic coordinates of the transmission path. Electrical characteristics of the ground at the transmitting and receiving sites also play an important role, as the finite conductivity of the Earth affects the vertical radiation pattern of the antennas [66].

The ionosphere is a dynamic system that constantly changes. In addition to the factors mentioned above, the proportion of energy reflected back to the Earth's surface is also a function of time of day, season of the year and epoch of the 11-year solar cycle.

Short-term variations, measured in minutes, arise due to continuous turbulence in the ionosphere [67]. The diurnal variation in field strength is considerable. During the day the sky wave is attenuated by the D-layer. After sunset the D-layer fades away and allows the LF signals to pass through it and be reflected by the E-layer. Consequently, day time annual median field strength is typically at least 20 dB lower than the night-time annual median [66]. Night-time LF sky waves are particularly strong in summer and winter [68]. Usually the night-time ionosphere also has a higher effective height, which results in a longer propagation delay of the night-time sky wave as compared to daytime conditions.

The variability of sky wave propagation makes it impossible to predict the parameters of the sky wave signals with an accuracy sufficient for absolute positioning; the sky wave is normally considered a form

17 The idea that the atmosphere contains a conducting layer was first proposed in 1839 by Carl Friedrich Gauss. The term 'ionosphere' was introduced in 1926 by Sir Robert Watson-Watt, and the names of the different layers in the ionosphere, D, E, and F were proposed by another British physicist, Sir Edward Appleton [65, 64].

of interference, causing signal fading and carrier phase distortion. In eLoran, own-sky wave interference[18] is largely prevented by the pulsed nature of the signal. The sky wave always arrives later than its ground wave counterpart; the leading edge of the pulses is thus usually free from own-sky wave interference and can be used for timing measurements.

The effective height may be significantly reduced during periods of severe solar weather, resulting in the occurrence of *early sky waves*. Anomalous sky wave propagation at LF is mainly caused by two solar-induced ionospheric conditions: the Sudden Ionospheric Disturbance (SID), which is a result of X-ray events on the Sun, and the Polar Cap Disturbance (PCD), which is caused by proton bursts conveyed to the Earth via the solar wind. A study conducted by the GLA suggests that the probability of early sky waves occurring over North-West Europe is very low [69].

However, sky waves originating from other eLoran chains transmitting at different GRIs can freely interfere (no matter what the delay) and cause considerable distortion of the wanted signals. Therefore, when introducing a new eLoran station, great attention should be paid to sky wave modelling. Two parameters of the sky wave signals will be of interest in this work - field strength and propagation delay.

Field Strength

ITU provides three methods for estimating the sky wave field strength at frequencies below 2 MHz:

1. The waveguide method; this technique is applicable at frequencies below about 60 kHz, where the distance between the Earth and the ionosphere is only a few wavelengths and the cavity tends to act as a waveguide. The propagation in the Earth-ionosphere waveguide can then be analysed using methods analogous to those used in the microwave region [66]. The waveguide method estimates the total field strength, including the ground wave.

2. The wave-hop method; this technique models the transmission as taking place along paths defined by one or more ionospheric reflections. It can be used at frequencies between about 60 kHz and 150 kHz [66] and for path lengths up to 16000 km. The method allows both night-time and day time sky wave field strengths to be estimated and it can provide signal strength values for each available sky wave mode (first-hop, second-hop, etc.). It also allows the modelling of seasonal variations and the effects of solar activity.

3. An empirical method based on Recommendation ITU-R P.1147 [68]; this method is intended for use at frequencies between 150 kHz and 1700 kHz and for path lengths between 50 km and 12000 km. It provides predictions for the composite night-time signal field strength for all available sky wave modes.

The third method was implemented in the GLA' eLoran Coverage Prediction Tool, and therefore it is this method that will be used in this

18 I.e. interference between the ground wave and sky wave signal components from the same station.

PERCENTILE	DB ABOVE MEDIAN
90	6.5
95	8.4
99	11.9

Table 5: Difference (dB) between the annual median night-time sky wave field strength and nigh time sky wave field strength not exceeded for the specified percentage of time.

study, although it is noted that the wave-hop method may be more suitable for these investigations.

As discussed above, sky wave field strengths in the LF band vary on timescales ranging from minutes to years. The empirical model used in this work predicts the annual median night-time field strength. Midday field strengths are typically 7 dB to 45 dB lower than the midnight values [68]. Short-term variations of the night-time sky wave about the median value are well approximated by a log-normal distribution with a standard deviation of 5.1 dB [68, 70]. Using this approximation, the night-time field strength not exceeded for any given percentage of time can be estimated (see Table 5).

For illustration, Figure 15 plots ground wave and sky wave field strength for a 1 kW transmission versus distance from the transmitter. Figure 16 then shows the predicted night-time sky wave field strength not exceeded 95% of the time for the Anthorn station. Because of the shape of the radiation pattern of the transmitting antenna and the geometry of sky wave propagation very little sky wave energy is received close to the transmitter, as can be seen from both figures. The sky wave field strength reaches its peak at a distance of approximately 100 km to 200 km. As can also be seen from Figure 15, the ground wave is attenuated at a considerably higher rate than the sky wave and depending on the ground type, the sky wave signal can dominate the ground wave signal at distances from about 55 km upwards. Sky wave rejection was therefore a major concern in the design of the Loran system. The sky wave rejection capability of the eLoran signal will be further discussed in Chapter 5.

Differential Delay

The sky wave signal component always travels a longer distance than the ground wave. The differential delay between the received sky wave and ground wave signal can be estimated from the effective height of the ionosphere, h, and the distance between the transmitter and receiver, r. The geometry of the problem is illustrated in Figure 17, assuming for simplicity a spherical Earth model and single-hop sky wave only. From Figure 17, the differential delay can be calculated as [71]:

$$\tau_{\mathrm{dif}} = \frac{2\sqrt{h^2 + 4R_{\mathrm{E}}\left(R_{\mathrm{E}} + h\right)\sin^2\left(\frac{r}{4R_{\mathrm{E}}}\right)}}{c} - \frac{r}{v_{\mathrm{atm}}}, \tag{3.4}$$

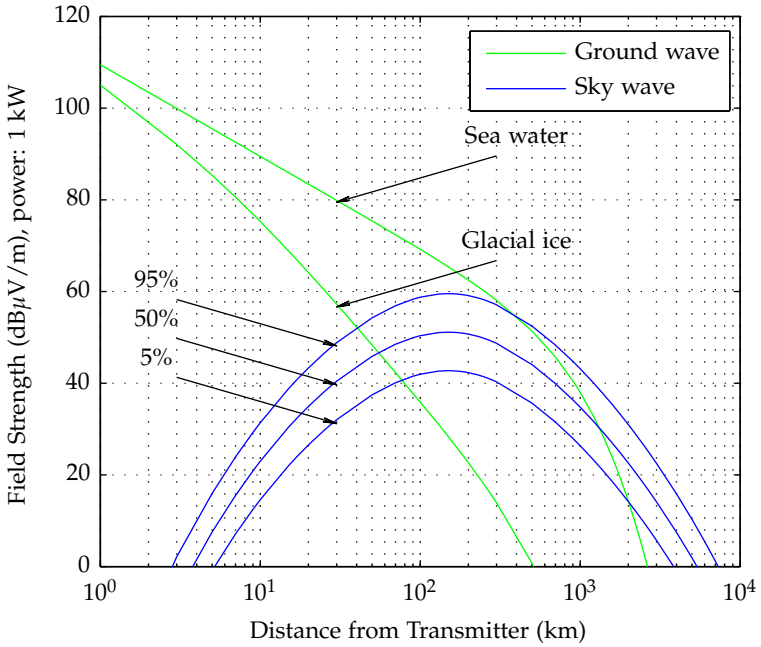

Figure 15: Comparison of ground wave field strength and night-time sky wave field strength not exceeded for the specified percentage of time; radiated power of 1 kW is assumed.

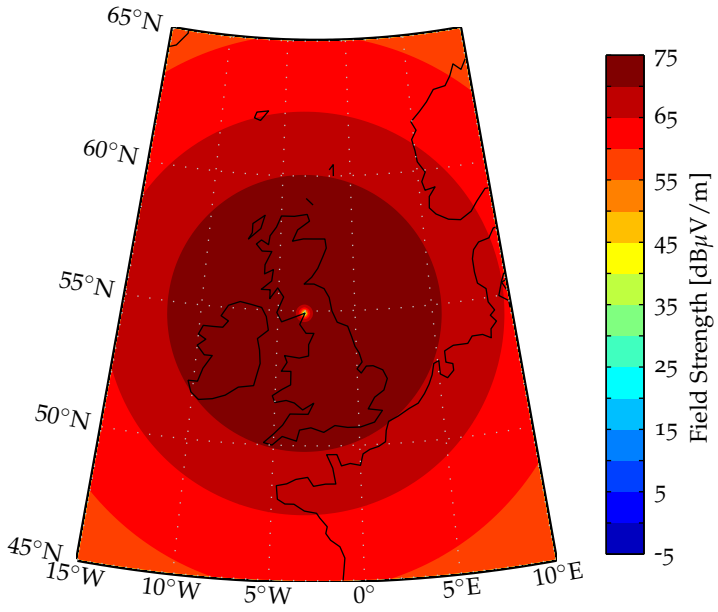

Figure 16: Predicted night-time sky wave field strength not exceeded 95% of the time for the Anthorn station.

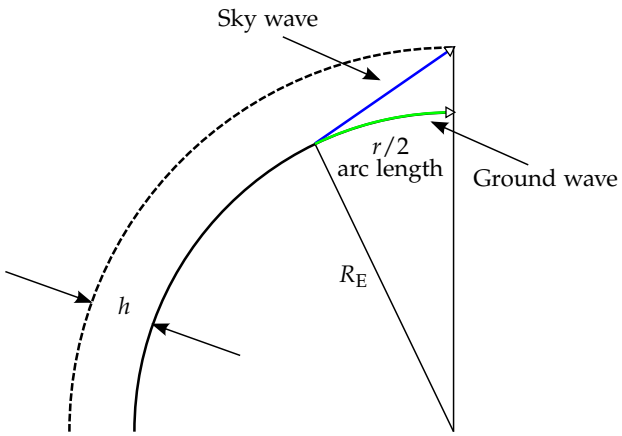

Figure 17: Calculation of the sky wave delay with respect to the ground wave (spherical Earth model); h is the effective height of the ionosphere, r is the great circle distance between the transmitter and the point of reception, $R_E \approx 6738$ km is the radius of the Earth.

PROPAGATION CONDITIONS	EFFECTIVE HEIGHT (km)
Night	89 – 99
Winter day	69 – 81
Summer day	60 – 72
Solar-active (PCD)	44 – 56

Table 6: Effective height of the ionosphere for different propagation conditions [71].

where propagation velocity of the sky wave signal through the ionosphere has been approximated by the velocity of light in vacuum, c, and propagation velocity of the ground wave has been set equal to the velocity of the signal through the standard atmosphere, v_{atm}, as defined above.

The delay is significantly affected by the effective height of the ionosphere. As discussed, the height is subject to considerable diurnal and seasonal variations and may be substantially reduced during periods of severe solar weather, such as PCD. Typical ionosphere height values for different propagation conditions are shown in Table 6.

Figure 18 plots the differential delay as a function of the distance from transmitter. As can be seen from the figure, under standard propagation conditions, the sky wave is at least 35 μs delayed with respect to the ground wave; the Loran pulse was designed with this in mind and receivers can mitigate most sky waves by using only the early portion of the received pulse, which is dominated by the ground wave. However, receiver input bandpass filtering may bring the sky wave and ground wave components closer to each other and some sky wave induced error may arise even under standard propagation conditions. This is further discussed in Chapter 5.

As mentioned earlier, early sky waves caused, for example, by PCD may result in substantial measurement errors; these anomalous condi-

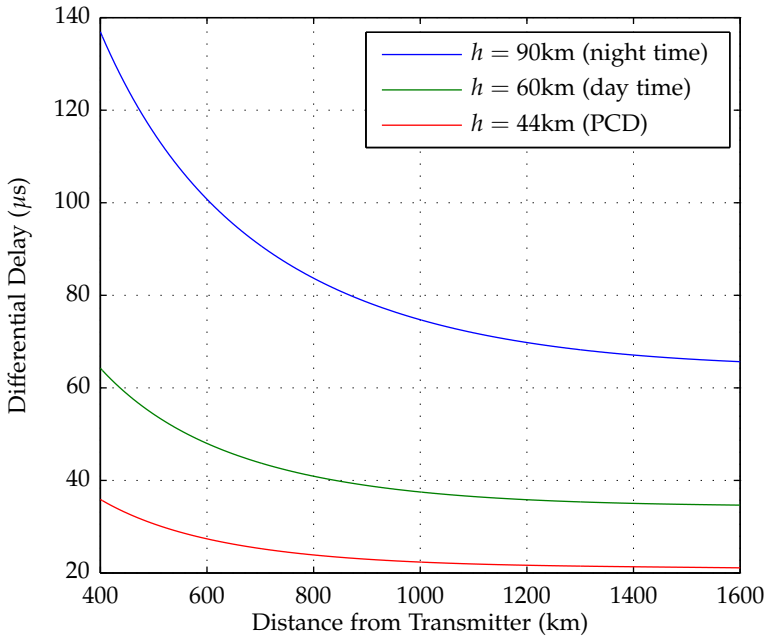

Figure 18: Sky wave delay for typical night-time ($h = 90\,\text{km}$), daytime ($h = 60\,\text{km}$), and PCD ($h = 44\,\text{km}$) ionosphere conditions.

tions should, however, be detected and flagged by integrity monitoring stations [5].

3.2.3 *Re-radiation*

eLoran signal propagation may be adversely affected by the presence of nearby conducting structures whose dimensions are an appreciable fraction of the signal carrier wavelength (e.g. bridges and power lines). Such structures can locally distort the electro-magnetic field and cause substantial positioning errors. Pelgrum [30] conducted an initial analysis of the phenomenon and its impact on eLoran positioning. He concluded that while correction of the effects at the receiver does not seem feasible, it is possible, for an appropriately equipped receiver, to detect the occurrence of re-radiation and provide timely warnings to the user. The integrity of the position solution can thus be retained at the cost of a reduced availability.

Since re-radiation is a separate problem from CRI which has only a localised effect on the system's performance, and given the possibility of detecting the measurements corrupted by re-radiation, it is concluded that the phenomenon does not need to be modelled here.

3.3 EXTERNAL NOISE

Noise is an integral part of any radio system. Noise in radio systems can originate from sources external to the receiving system, or from the receiving system itself. External sources include: lightning discharges (atmospheric noise); electrical machinery, electronics, power transmission lines, etc. (man-made noise); celestial bodies (galactic noise); and emissions from atmospheric gases and hydro-meteors. An example of a

noise source internal to the receiving system is thermal noise generated in the receiver antenna and front end.

Noise limits the performance of the receiver in the absence of interference, and although it may not be immediately obvious, it also affects the residual error due to CRI. This section therefore aims to identify the main sources of noise in eLoran and present noise models suitable for use in subsequent investigations. The focus here is on external noise, as this is the dominant source of noise in the LF band.

3.3.1 *Modelling External Noise*

The traditional source of information on radio noise is the ITU-R Recommendation P.372 [72]. Several types of external noise are described in the document, including atmospheric noise and man-made noise. The different noise sources are characterised in terms of the *noise figure* and its statistical properties. The noise figure gives the noise power level above thermal noise at the terminals of an equivalent loss-free receiving antenna having the same characteristics (except efficiency) as the actual antenna. A reference temperature of 290 K is assumed.

Depending on the frequency of interest, one or more noise sources need to be considered. ITU-R P.372 provides a method for combining noise contributions from different sources, and determining an overall external noise figure, here denoted F_e. From this noise figure, the available noise power in bandwidth b_{Hz} (Hz) at the output of the equivalent loss-free antenna can be calculated using the following equation:

$$P_e = F_e + B - 204 \quad \text{dBW}, \tag{3.5}$$

where $B = 10 \log b_{Hz}$. The recommendation also provides the following expression for the noise equivalent field strength corresponding to the noise power available at the output of an electrically short monopole antenna:

$$E_e = F_e + 20 \log f_{MHz} + 10 \log B - 95.5 \quad \text{dB}\mu\text{V/m}, \tag{3.6}$$

where f_{MHz} is the operating frequency expressed in MHz. The values of P_e or E_e can then be used as a basis for the calculation of the *Signal-to-Noise Ratio* (SNR) which is a crucial parameter in determining system performance.

The rest of this section takes a closer look at the key external noise sources relevant in the LF band.

3.3.2 *Atmospheric Noise*

Atmospheric noise is generated by lightning discharges in the atmosphere and is considered to be the dominant noise source in the LF band. Most of the energy produced by atmospheric discharges is radiated at frequencies below about 30 MHz and can be detected thousands of kilometers away from the source due to sky wave propagation [72]. The characteristics of the atmospheric noise vary with location on the globe, season of the year, and the time of day. The patterns are complex but, in general, the median noise power is higher near the equator than in polar regions and greater in summer than in winter. The noise is also

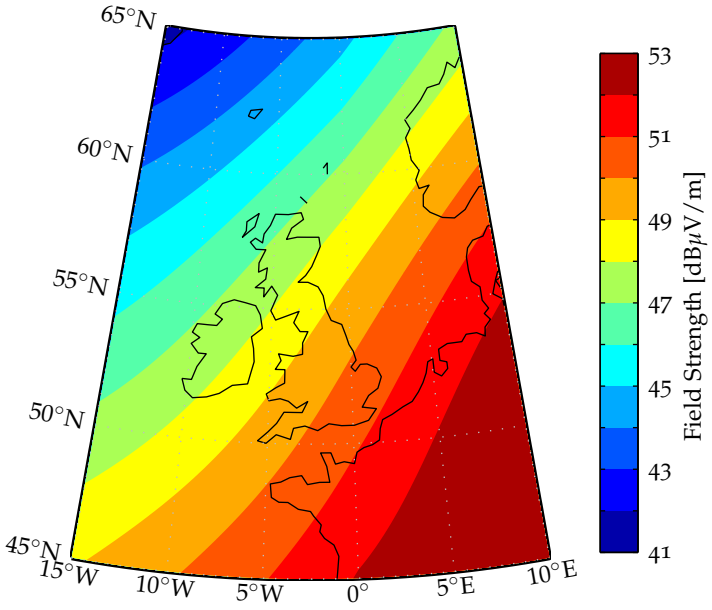

Figure 19: Annual atmospheric noise at 95th percentile.

generally stronger at night than during the day. A great number of statistical models for atmospheric noise were presented in the past. The traditional approach to atmospheric noise modelling for Loran makes use of ITU-R Recommendation P.372 [72] mentioned earlier. A brief description of the ITU model follows.

Noise Figure Statistics

The ITU model of atmospheric noise is a result of statistical evaluations of several years' worth of data from monitoring stations around the world. It provides information on the available noise power at a particular location and its fluctuation over time, and also on the amplitude probability distribution of the noise.

In order to tackle the spatial variability and the non-stationary nature of the noise, the ITU compiled a set of charts showing contours of the median value, F_{am}, of the atmospheric noise figure, F_a, at 1 MHz for each season of the year and each four-hour time block of the day. The ITU also published curves allowing the F_{am} figure to be converted to any frequency in the range between 10 kHz and 30 MHz. Further, for each season and time block, the ITU model gives statistical data on the variation of the atmospheric noise figure, F_a, about the median value. Interestingly, the model assumes that the variation can be represented by two normal distributions - one is used above the median value and one below. The distributions are described by the upper and lower decile values, D_u and D_l, respectively.

In order to account for year-to-year variations and uncertainty in the geographic variation of F_{am}, the standard deviation of the median noise figure $\sigma_{F_{am}}$ is also given. Values of the standard deviation of D_u and D_l, σ_{D_u} and σ_{D_l}, respectively, can also be obtained[19]. Based on

19 Only one value of D_u and D_l is given for the entire Earth's surface and each season-time block; σ_{D_u} and σ_{D_l} then account for the geographic variation of the deciles.

these statistics, the value of F_a not exceeded for any given percentage of time p of a given season-time block b, denoted here as $F_{a,p,b}$, can be calculated.

Finally, if an observation bandwidth is specified, the available noise power at the output of an equivalent loss-free receiving antenna as well as the equivalent RMS noise field strength not exceeded for the given percentage of time can be calculated, using Equation 3.5 and Equation 3.6 above[20].

Boyce [73] recently investigated the applicability of the ITU model to atmospheric noise in the Loran frequency band. Based on noise field strength data collected during a period of high storm activity, he concluded that the ITU model does predict the RMS noise field strengths[21] well up to about the 99.5% level (i.e. for $p \leq 99.5$). Above that level, the ITU model provides an over-bound of the actual atmospheric noise data measured by Boyce.

As explained in detail in Chapter 9, this study uses the ITU model to determine average noise field strengths, rather than using percentile values. In calculating the average annual RMS values, statistical data from all season-time blocks of the ITU model are combined in an attempt to obtain values representative of average noise conditions during the year.

Probability Distribution of Instantaneous Noise Envelope Field Strength

As mentioned above, the atmospheric noise is caused by electrical discharge activity in the atmosphere. At any time, a receiver is subject to the combined effect of a large number of atmospheric noise sources scattered around the world. The combination of contributions from distant storms received via sky wave propagation results in a noise process that has an approximately Gaussian probability distribution [74]. However, noise from nearby thunderstorms has an impulsive character and, as a result, the probability distribution of the atmospheric noise deviates, to a greater or lesser extent, from Gaussian. Properly designed receivers can exploit the non-Gaussian nature of the noise and achieve a significant processing gain by eliminating the impulsive component [30, 73]. The achievable gain is proportional to the noise impulsivity[22], and consequently the noise power (or SNR) alone is not sufficient to accurately determine the system performance.

For this reason, the ITU also provides information on the probability distribution of the instantaneous noise envelope field strength (in addition to the distribution of the RMS field strength treated in the previous section). The atmospheric noise is modelled as a bandpass process (see Section A.2) and described by a phase process and an envelope process. It is assumed that the phase is uniformly distributed between 0 and 2π. The noise envelope statistics can then be obtained from ITU-R Recommendation [72] in the form of *Amplitude Probability Distribution* (APD) curves.

20 However, it is not clear from the ITU document [72] whether the field strength calculated according to the recommendation corresponds to the RMS value of the noise field strength itself or to the RMS envelope field strength (which is what the ITU scientists actually measured). It should be noted that the former is 3 dB lower than the latter.

21 In accordance with the ITU method, the RMS value in Boyce's work was calculated over a 15 minute interval and the probability distribution of this RMS value was estimated from the data for each 4-hour time block of the day.

22 Voltage deviation, V_d, defined below can be considered as a measure of impulsivity of a noise process.

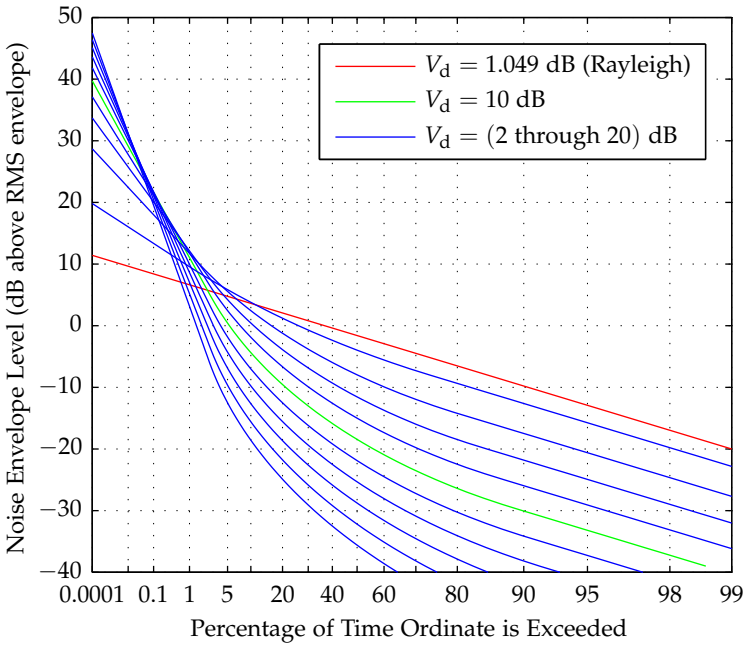

Figure 20: Amplitude Probability Distribution of Rayleigh-distributed noise (magnitude of a complex Gaussian random variable) and impulsive noise for different values of the voltage deviation, V_d.

The APD curves published by the ITU were constructed by analysing numerous 15 minute intervals of recorded instantaneous noise envelope voltages. The APD is given by the probability of the instantaneous noise envelope level exceeding a given value relative to the RMS value of the measurement interval. The ITU publishes sets of APD curves parametrised by the *voltage deviation*, V_d. This is calculated as the ratio of the RMS noise envelope to the average envelope voltage. The appropriate value of V_d for a given season-time block, frequency and receiver bandwidth can be determined from charts that can also be found in Recommendation [72].

To illustrate the concept, Figure 20 shows the APD of impulsive noise for different values of the voltage deviation, compared to the APD of Rayleigh distributed noise (representing the envelope of thermal-type, Gaussian noise). Two important observations can be made here:

Firstly, taking the APD for $V_d = 10\,\text{dB}$ as an example[23] (shown in green), it can be seen that the instantaneous noise envelope exceeds the RMS value for only about 5% of the time, while for 50% of the time the noise level is at least 18 dB below the RMS value (recall that the APD is normalised relative to the RMS value of the measurement interval). Compare this with the APD of the Rayleigh noise, having $V_d = 1.049$, where the noise level exceeds the RMS value for about 36% of the time. It should be clear from this example that describing impulsive atmospheric noise by its RMS statistic alone is of limited value.

Secondly, it is worth noticing that the coordinate system of the APD is such that the Rayleigh distribution plots as a straight line of negative slope. This makes it possible to use the APD to gauge the extent to

23 $V_d = 10\,\text{dB}$ is a typical value for LF according to data in ITU-R P.372 [72]; this assumes a bandwidth of 200 Hz.

which the impulsive noise data follow the Rayleigh distribution. Using again the APD curve for $V_d = 10\,\text{dB}$ as an example, it can be seen that the part of the curve above approximately the 70% ordinate is parallel to the Rayleigh line. This implies that approximately 30% of the time interval the noise follows the Rayleigh distribution, and 70% of the time the noise is more impulsive.

The latter observation is the basis of atmospheric noise mitigation algorithms used in eLoran receivers. It suggests that the noise can be separated into a Rayleigh, low power, component and an impulsive component, which can be eliminated from the data. The achievable processing gain depends on how often the noise is impulsive, and how much lower the Rayleigh portion of the noise is relative to the RMS value. Specific mitigation algorithms will be discussed in Chapter 4.

Boyce [73] explored the applicability of the ITU published APD data to atmospheric noise in the Loran frequency band. He confirmed experimentally that the APDs predicted by the ITU model for a given V_d provide an accurate representation of the actual noise data. However, he expressed concerns[24] as to how well the ITU model predicts the voltage deviation, V_d. Based on his measurements Boyce proposed a new model for V_d which allowed him to quantify the processing gain that can be achieved for any given noise level by eliminating the impulsive component of the noise. This then led to a significant improvement in the predicted system performance.

Boyce provides the following expression for the achievable gain due to atmospheric noise mitigation:

$$G_a = 1.8V_d - 1.1 \quad \text{dB}, \tag{3.7}$$

which can also be expressed in terms of the RMS noise field strength as:

$$G_a = 0.54E_a - 28.1 \quad \text{dB}. \tag{3.8}$$

Equation 3.8 is only valid for values of $E_a > 70\,\text{dB}\mu\text{V/m}$[73].

Equation 3.7 and Equation 3.8 provide a justification for modelling the atmospheric noise as a white Gaussian process (Rayleigh distributed envelope). The power of the process within the Loran band can either be set to the value predicted by the ITU model (resulting in conservative estimates of performance), or to the ITU-predicted value minus G_a (thus taking into account the effects of using atmospheric noise mitigation algorithms). Since the ITU voltage deviation data required to calculate G_a does not appear to be reliable in the Loran band (see [73]), and since Equation 3.8 above was derived based on measurements made in the United States and would have to be validated for use in Europe, the candidate decided to follow the former approach.

3.3.3 *Man-Made Noise*

Many common electrical devices, such as fluorescent tubes, switched-mode power supplies, computer systems and other electronic equipment produce a substantial amount of radio noise in the LF band. The

24 Note that ITU Recommendation [72] states that caution should be exercised when applying the voltage deviation data to LF, and its earlier version also warns that the predictions tend to overestimate V_d for larger bandwidths (such as those employed in eLoran).

noise emitted from such devices may severely affect the performance of eLoran if the receiver antenna is located close to the source of the noise. Some mitigation of the effects of the man-made noise by signal processing is possible but requires the use of sophisticated, computationally demanding techniques, some of which also require an advanced (multi-channel) receiver structure and the use of multiple antenna elements [30].

The simplest and most effective mitigation approach, however, is through spatial separation. The small electrical dimensions[25] of most sources of man-made noise luckily make them poor emitters of LF radiation. Consequently, the radiation from such sources is only likely to present a problem when the receiving antenna is located in the near field of the emitter. As is well known, field intensity in the far-field of an infinitesimally small radiating element is approximately proportional to the inverse of the distance r from the element, but in the near-field, the field is dominated by higher-order terms; in the case of an elemental dipole the relations are as follows ($k = \frac{2\pi}{\lambda}$):

$$E_\theta \sim \frac{j}{kr} + \frac{1}{(kr)^2} - \frac{1}{(kr)^3},$$

$$H_\phi \sim \frac{j}{kr} + \frac{1}{(kr)^2}.$$

The higher-order terms cause the intensity to fall off rapidly with increasing distance. The power received by an E-field and H-field antenna at distance r from the emitter is proportionate to $|E_\theta|^2$ and $|H_\phi|^2$, respectively. This, for example, means that increasing the distance from the noise source from 3 m to 30 m reduces the theoretical received noise power by approximately 60 dB in case of an E-field antenna and by 40 dB when an H-field receiving antenna is used (if the radiating element is a small loop, the power relations are interchanged). This effect is illustrated in Figure 21.

This work focuses on the use of eLoran in the maritime sector. Due to the rapid fall-off of the interfering field strength with increasing distance, it seems reasonable to assume that man-made noise from sources located on the shore will have a negligible impact on the performance of ship-borne receivers. However, noise generated by machinery and electronic systems on board ships can significantly affect eLoran reception, and should therefore be included in the signal model.

ITU-R Recommendation M.1467 [75] gives representative figures of the *topside noise*, P_t, for three categories of vessels, as summarised in Table 7. The Australian Advisory Group for Aeronautical Research and Development (AGARD) figure represents a naval vessel under normal cruise conditions, whilst the Department of Defence (DOD) figure represents the maximum noise level under battle conditions. The figure adopted by the Ionospheric Prediction Service of the Australian Department of Industry (IPS) is generally accepted as representing the noise level encountered on container vessels, pleasure cruisers and utility ships, and is also the value that will be used throughout this thesis.

The values of P_t given in Table 7 are referenced to a frequency of 3 MHz. Conversion to 100 kHz is achieved here using the method des-

25 Meaning physical dimensions expressed as multiples of the wavelength of the radiation.

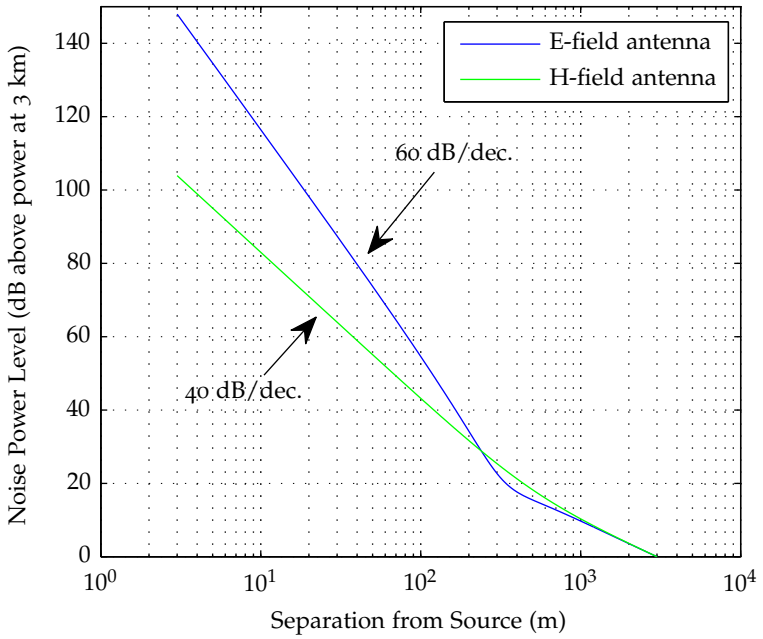

Figure 21: Power received in the near-field of an elemental dipole; $\lambda = 3\,\text{km}$; power level referenced to the power received at distance $r = \lambda$.

ENVIRONMENTAL CAT.	TOPSIDE NOISE (dBW/Hz @ 3 MHz)	c	d
AGARD ship	−148.0	69.2	27.7
IPS ship	−142.0	75.2	27.7
DOD Cat 1 mobile platform	−137.0	80.2	

Table 7: Naval environmental categories for topside noise as per ITU-R M.1467.

cribed in Paragraph 5 of ITU-R Recommendation P.372 [72]. Following the method in ITU-R P.372, the topside noise F_t (expressed as a noise figure) at the desired frequency f (given in MHz) can be calculated as follows:

$$F_t = c - d \log f,$$

where the coefficients c and d take the values shown in Table 7. The values of c given in the table were calculated from P_t, assuming that d takes on the same value as for the man-made noise curves published in ITU-R P.372. As an example, for the IPS vessel, $F_t \approx 103\,\text{dB}$ at $f = 100\,\text{kHz}$.

The noise figure can be converted into noise power or equivalent noise field strength using Equation 3.5 and Equation 3.6 above.

3.3.4 *Precipitation Static*

Electrically charged rain drops coming in contact with the antenna can increase noise levels at the receiver. This is usually referred to as precipitation static and is particularly a problem in the aviation sector. The impact of precipitation static on the E-field antenna can be mitigated by shielding the antenna elements from the environmental effects using a radome. Alternatively, an H-field antenna can be used which is not susceptible to precipitation static.

3.3.5 *Combination of Noise Sources*

In the LF band, the atmospheric noise and ship's topside noise are of comparable magnitude. When calculating the external noise power, it is therefore necessary to determine the statistics of the noise figure corresponding to the combination of the two noise sources. Since the noise figure representing the topside noise, F_t, is assumed to be a deterministic constant, this can easily be achieved as follows. The median external noise figure can be calculated as

$$F_{em} = 10 \log \left(10^{F_{am}/10} + 10^{F_t/10} \right).$$

As before, the noise figure can be converted into noise power or equivalent noise field strength using Equation 3.5 and Equation 3.6 above.

3.4 INTERFERENCE

Another important channel impairment in eLoran that needs to be taken into consideration is interference from other radio stations. Two broad categories of interference to eLoran can be distinguished - *Continuous Wave Interference* (CWI) caused by stations of other systems broadcasting on frequencies close to the Loran frequency band, and *Cross-Rate Interference* (CRI), which originates from Loran itself.

3.4.1 *Continuous Wave Interference (CWI)*

CWI occurs when signals from other (non-Loran) radio stations contain spectral components that appear close to, or overlap, the Loran frequency band. As shown earlier in Chapter 2, the shape of the eLoran pulses is such that 99% of the signal's energy is concentrated between (90 and 110) kHz. This frequency band is reserved for Loran [76] and it should be free from any intentional interference. Figure 23 in Section 3.6.1 below shows the relevant part of the LF spectrum as measured in the UK. The Loran band indeed appears to be free from CWI, however, the plot clearly shows a number of narrow-band transmissions in the immediate vicinity of the protected band. These signals may interfere to a greater or lesser extent depending on their frequency[26], the GRI of the eLoran signal, their relative strength (Signal-to-Interference Ratio), and the filtering applied in the receiver.

26 Note that, for simplicity, CWI is usually modelled as a pure sine wave with a constant amplitude and frequency. Although the actual interfering signal will in most cases have a more complex structure (e.g. ASK, FSK), this work follows the established model.

When the European Loran-C chains were planned in the early 1990's a great deal of attention was paid to the issue of CWI. Major work was carried out at Technical University (TU) Delft. Two key reports [77, 78] were produced in 1992 and 1993. Based on previous work of Remmerswaal, Arriens, van Willigen, and Beckmann [79, 80, 81, 82, 83, 38], the TU Delft reports model the impact of CWI on the performance of Loran-C receivers and explain how the effect can be minimised by judicious choice of GRIs. Report [84] prepared by the Loran Control Centre in Brest then contains experimental data supporting the TU Delft method. The issue of CWI was also extensively studied by Last and Bian of the University of Wales, Bangor. In [85] the authors proposed a deterministic model to quantify the error in timing and ECD measurements due to a single dominant CW interferer. In later work by the same authors [86] the method was extended to an arbitrary number of interferers using a statistical approach. The techniques developed at TU Delft and Bangor were then used in selecting the optimal set of GRIs for the North-West European chains [84] and in modelling the coverage and performance of the system [87, 88].

CWI posed a serious threat to Loran in the 1990's, since Europe was a particularly busy radio environment. Since then, however, many of the potential interferers, such as the Decca Navigator stations, have been decommissioned [44]. In addition, advances in receiver technology have allowed the use of sophisticated signal processing algorithms to detect and mitigate CWI. A variety of techniques have been proposed, such as adaptive notch filtering, adaptive cancelling, and weighted ensemble averaging [83, 89, 90, 30]. Consultations with eLoran receiver manufacturers [91, 92] have confirmed that CWI is much less of a threat to eLoran than it was to Loran-C, and that the major source of interference to eLoran currently is CRI. The residual effect of CWI on eLoran measurements is therefore not modelled in this study. However, some aspects of CWI will be considered later in Chapter 10 when developing a GRI selection procedure for eLoran.

3.4.2 *Cross-Rate Interference (CRI)*

The issue of CRI was described in Chapter 1 which also included a comprehensive literature review on this matter. CRI is the main subject of this study and will be dealt with in detail in subsequent chapters. Suffice to say at this point that CRI occurs whenever there are at least two detectable eLoran signals with different GRIs, and that it currently is the strongest source of interference to eLoran.

3.5 RECEIVER CONSIDERATIONS

3.5.1 *Thermal Noise*

Each resistive component in the receiving system contributes some thermal noise (see the Nyquist formula for thermal noise [93]). However, in a well designed LF system the total thermal noise contribution from the receiver and its antenna can be made lower than the external noise (which in the LF band is dominated by the atmospheric noise), as demonstrated e.g. in [30, 94]. The thermal noise is therefore of little concern and it will not be considered in this study.

3.5.2 *Clock Errors and Platform Dynamics*

As mentioned in Chapter 2, the time and carrier phase offsets of the received pulses can fluctuate over time due to the receiver's motion and local oscillator imperfections[27]. If left uncompensated, these effects can degrade the receiver's signal processing performance, effectively acting as additional sources of noise. In analysing the impact on the receiver performance it is convenient to express the time-variant offsets $\tau(t)$ and $\theta(t)$ using the Taylor's expansion:

$$\tau(t) = \tau(t_0) + \dot{\tau}(t_0)(t - t_0) + \frac{\ddot{\tau}(t_0)}{2!}(t - t_0)^2 + \dots. \tag{3.9}$$

The term $\tau(t_0)$ is the initial signal time offset at some reference time instant t_0. It can be modelled as a sum of the Emission Delay, τ_{ED} , transmitter-to-receiver propagation delay, $\tau_{\text{prop}}(t_0)$, and the (generally arbitrary) receiver clock bias relative to the system clock, $\tau_{\text{b}}(t_0)$. As discussed earlier, the propagation delay is a function of the transmitter-to-receiver distance, and it is one of the key quantities of interest when determining the position of the receiver.

The term[28] $\dot{\tau}(t_0)$, i.e. the rate of change of the time offset, arises due to non-zero radial velocity of the receiver with respect to the transmitter, and due to receiver clock drift (frequency error of the local oscillator). The effect of the clock drift can be substantial. Consider, as an example, a receiver whose time base is derived from a Temperature-Compensated Crystal Oscillator (TCXO). The TCXO is a common choice in consumer grade navigation receivers. The accuracy of this type of oscillator is typically of the order of 10^{-6} [95]. This means that over a 5 second interval (a typical observation interval used in eLoran receivers) the receiver clock can drift, with respect to the transmitter clock, by some 5 μs (corresponding to an apparent change in distance of 1.5 km). Luckily, the oscillator drift is usually predictable over short time intervals, and since it affects all measured signals by the same amount, it can be estimated in a similar way as the clock bias, and compensated for in signal processing (Chapter 4). The parameters of the receiver's motion are more difficult to predict than the clock fluctuations, however, the velocities typically encountered in the marine environment are relatively low, and the impact on the received signals is usually negligible. The effect of the higher order terms in Equation 3.9 can usually also be neglected. It is therefore concluded that, for the purpose of this analysis, the time offset can be considered constant over an observation interval of several seconds, $\tau(t) = \tau(t_0) = \tau$.

The carrier phase offset can be expressed similarly as:

$$\theta(t) = \theta(t_0) + \dot{\theta}(t_0)(t - t_0) + \frac{\ddot{\theta}(t_0)}{2!}(t - t_0)^2 + \dots$$

The term $\theta(t_0)$ is the initial carrier phase at the reference time instant t_0. It is a function of the same parameters as the time offset $\tau(t_0)$, but can only be measured modulo 2π. Carrier phase measurements are used in the receiver to precisely determine the timing of signal arrival (within one cycle of the carrier). The integer phase ambiguity is then resolved using the time offset measurements, which are based on the

27 Recall that the offsets are defined here with respect to the receiver clock.

28 A single\double dot above a symbol denotes the first\second derivative with respect to time, respectively.

shape of the pulse envelope. As will be clear, the analysis of eLoran positioning performance can be reduced to analysing the accuracy of the carrier phase measurements and geometry considerations.

The term $\dot{\theta}(t_0) = 2\pi f_{\text{CFO}}$ represents the Carrier Frequency Offset (CFO). Similar to the time-offset rate of change, the CFO can be caused by the receiver's motion (Doppler effect[29]) or by the local oscillator drift. Again, the effect of the oscillator drift in a consumer grade receiver can be serious. Following the same example as above, it can be seen that a typical TCXO can give rise to a CFO[30] of around 0.1 Hz, which corresponds to a carrier phase shift of 180° over 5 seconds; i.e. two eLoran pulses received just 5 seconds apart from each other would appear to have opposing carrier phase. In order to allow phase-coherent processing (which is crucial to eLoran) practical eLoran receivers, therefore, must compensate for the clock drift (see also Chapter 4). It will be assumed here that this compensation is perfect. The effect of motion in low-dynamic conditions (such as maritime environment) can usually be ignored; high-dynamic applications require that radial velocity vector for each eLoran station is estimated and the effects of motion are compensated for each station separately. The effect of the higher order terms in the Taylor expansion above can usually be neglected. Once again, it can be concluded that, for the purpose of this analysis, the carrier phase offset can be considered constant over the observation interval, $\theta(t) = \theta(t_0) = \theta$.

The assumptions made in this section allow the use of the original expressions for eLoran signal waveforms, as introduced in Chapter 2.

3.5.3 *Implementation Loss*

Other receiver related sources of noise such as quantisation noise, round-off errors in digital signal processing, or local oscillator phase noise are assumed to be a minor component of the overall measurement error in modern eLoran receivers [96]. The combined effect of the various receiver imperfections will be treated in this work as a loss in SNR. The implementation loss for a particular receiver model, L_{impl}, can be estimated experimentally using a signal simulator, as will be described in Chapter 6.

3.6 RECEIVED SIGNAL MODEL

In order to enable receiver performance analyses, simulation, and testing, a model for the received waveform needs to be developed that includes all the relevant channel impairments discussed above. Equation 3.10 below shows the received signal model used throughout this study. The signal at the output of the receiver antenna, $\tilde{x}(t)$, is modelled

29 The Austrian physicist Christian Doppler postulated his principle in his work 'On the coloured light of the binary stars and some other stars of the heavens' published in 1842 while he was working at the Prague Polytechnic (now Czech Technical University).

30 at the eLoran carrier frequency

as a sum of signals from N_{st} eLoran stations (for definition of $\tilde{s}(.)$ see Equation 2.5), contaminated by wide-band noise, $w(t)$, and CWI[31].

$$\tilde{x}(t) = \sum_{m=1}^{N_{st}} \Bigg[\underbrace{A_{m,1} \cdot \tilde{s}(t; \tau_{m,1}, \theta_{m,1}, \mathcal{C}_m, T_{GRI,m})}_{\text{ground wave}} + \underbrace{A_{m,2} \cdot \tilde{s}(t; \tau_{m,2}, \theta_{m,2}, \mathcal{C}_m, T_{GRI,m}) + \ldots}_{\text{first-hop sky wave}} \Bigg] + \underbrace{w(t)}_{\text{WGN}} + \sum_{i=1}^{N_{CWI}} \underbrace{B_i \cdot \cos(2\pi f_i t + \theta_i)}_{\text{CWI}}, \tag{3.10}$$

Each eLoran signal in the model has a ground wave component and a sky wave component. As shown in Chapter 2, five parameters need to be specified in order to define an eLoran signal waveform: amplitude, time offset, carrier phase, phase code and GRI. The amplitude of the ground wave signal components for a particular geographical location can be obtained using ITU-R model [55] described in Section 3.2.1. The model provides the RMS ground wave field strength at the receiving antenna, $E_{m,1}$. Dividing[32] by an antenna factor C_{ant} then gives the voltage at the output of an ideal loss-free receiving antenna terminated by an appropriate impedance. The antenna factor is a function of the antenna gain in the direction of the source and the wavelength, and can be defined for both E-field and H-field antennas. As will be seen later, the performance analyses carried out in this work do not require knowledge of the absolute signal voltages at the receiver input. Only relative signal and noise strengths are of importance. Since all signals received by the antenna will be subject to the same transformation, and since noise in a well-designed LF system is dominated by sources external to the receiver, the antenna factor plays no role in the analyses. For simplicity, it will be assumed that the receiving antenna is perfectly omnidirectional in the horizontal plane and that $C_{ant} = 1$ (units depending on the type of the antenna). The amplitude of the desired eLoran signal (i.e. the pulse envelope at the peak, 65 μs into the ideal pulse), $A_{m,1}$, can then be set to $A_{m,1} = \sqrt{2} \cdot E_{m,1}/C_{ant} = \sqrt{2} \cdot E_{m,1}$ (recall that $E_{m,1}$ is an RMS value).

The time offset of ground wave signals, $\tau_{m,1}$, can be calculated using Equation 3.1 above. Under the assumption of distortion-less transmission, the carrier phase of the signal can then be calculated from its time offset as

$$\theta_{m,1} = \text{mod}(-2\pi f_c \tau_{m,1}, 2\pi).$$

The phase code, $\mathcal{C}_m$, and GRI, $T_{GRI,m}$, are system constants and are not affected by signal propagation. Note that the eLoran signals may have different GRIs, therefore the signal model represented by Equation 3.10 inherently includes CRI.

31 When double indexing is used in denoting signal field strengths, amplitudes and other signal parameters, the first index value identifies the station from which the particular signal originates, while the second value identifies the propagation mode (i.e. 1 for ground wave, 2 for first-hop sky wave, 3 for second-hop sky wave, etc.).

32 Assuming the field strength is expressed in V/m, or A/m in the case of the H-field antenna, and that the receiving system is matched to the antenna impedance.

Sky wave borne CRI is of special importance as the amplitude of the sky wave signal component, $A_{m,2}$, is often comparable or higher than that of the corresponding ground wave, $A_{m,1}$ (see Figure 15 above). The sky wave signal amplitudes at a given distance from the transmitter can be estimated using ITU-R model [68] described in Section 3.2.1.

The time offset of the (first-hop) sky wave signal components for a given height of the ionosphere can be estimated as

$$\tau_{m,2} = \mathrm{mod}\left(\tau_{m,1} + \tau_{\mathrm{dif},m}, 2T_{\mathrm{GRI},m}\right),$$

where $\tau_{\mathrm{dif},m}$ are the corresponding differential delays obtained using Equation 3.4 above. The carrier phase of the sky wave components can then be calculated as

$$\theta_{m,2} = \mathrm{mod}\left(-2\pi f_c \tau_{m,2}, 2\pi\right).$$

Alternatively, because of the time-variant nature of the sky wave delay (Section 3.2.2), it may be appropriate to treat the carrier phase $\theta_{m,2}$ as a random variable with a uniform distribution between 0 and 2π.

The dominant source of noise in the LF band is the atmospheric noise. As explained above, the atmospheric noise process is in general non-stationary and non-Gaussian. For simplicity, it is modelled here as an Additive White Gaussian Noise (AWGN) process, $w(t)$. The power spectral density of $w(t)$ in subsequent analyses will be set such that the power of the noise within the noise bandwidth of the receiver (see Chapter 6) equals the power of the atmospheric noise within the same bandwidth, received by a short vertical monopole antenna, $P_{\mathrm{a},p,b}$, as predicted by the ITU model for a given probability level and season-time block ($p = 0.95$ is commonly used; see Section 3.3.2). The 'white noise' assumption seems reasonable given the wide-band nature of the atmospheric noise (over the bandwidth occupied by the eLoran signal) [72]. The assumption of Gaussian-distributed instantaneous noise voltages also is an acceptable simplification, as it results in a conservative estimate of the receiver performance (more impulsive noise can be mitigated to an extent by special signal processing algorithms, as discussed above).

CWI is modelled as a sum of N_{CWI} sine waves with a constant amplitude, B_i, and frequency, f_i. Signal amplitudes for a given location can be estimated in a similar manner as for the eLoran signals, as shown in an earlier publication by the author [44]. Information on the frequencies of the potential interferers and transmitter power can be drawn from the International Frequency List (IFL) published by the ITU [97]. The phase θ_i of the interference is commonly treated as a random variable with a uniform distribution between 0 and 2π [86]. CWI is included here for completeness; however, it is assumed that the interference falls outside the protected Loran frequency band ($f_i \notin [90; 110]$ kHz) and therefore can be suppressed by bandpass and notch filtering without significantly affecting the desired eLoran signal.

3.6.1 *Off-Air LF Signals*

In order to give more confidence in the signal model developed above, raw LF signal data was obtained and analysed. The data set used in these investigations was recorded using a digital wide-band LF receiver developed by Dr. Fullekrug of the University of Bath [98, 99]. Figure 22

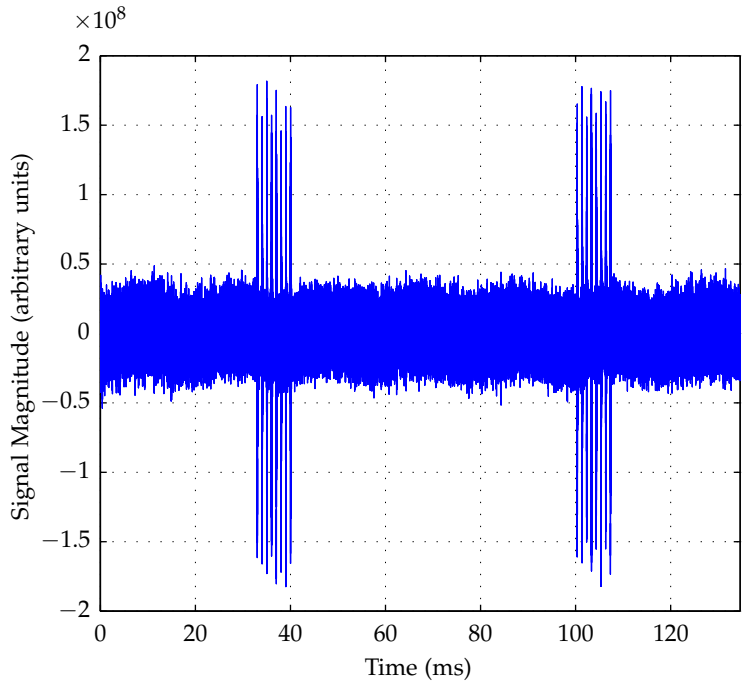

Figure 22: Off-air LF signals (time-domain view); raw signal data courtesy of Dr. Fullekrug, University of Bath.

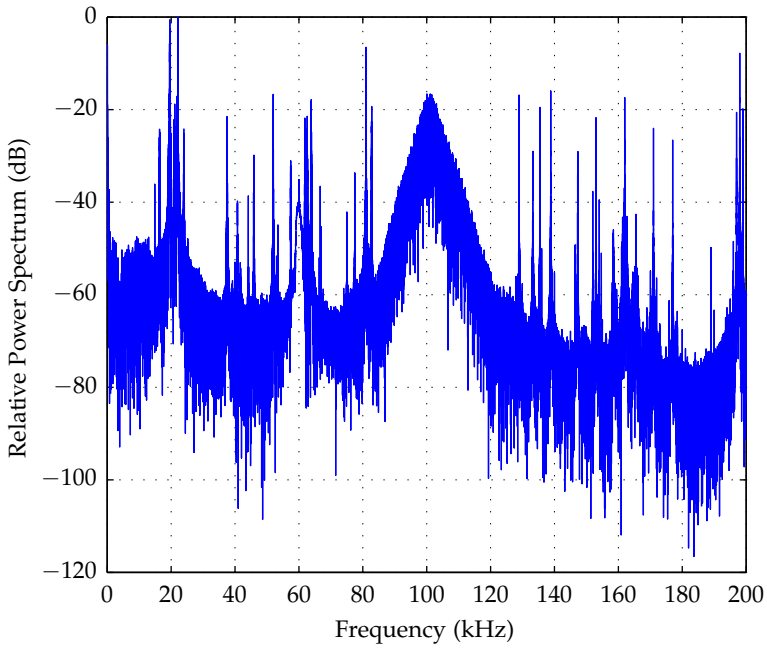

Figure 23: Off-air LF signals (frequency-domain view); raw signal data courtesy of Dr. Fullekrug, University of Bath.

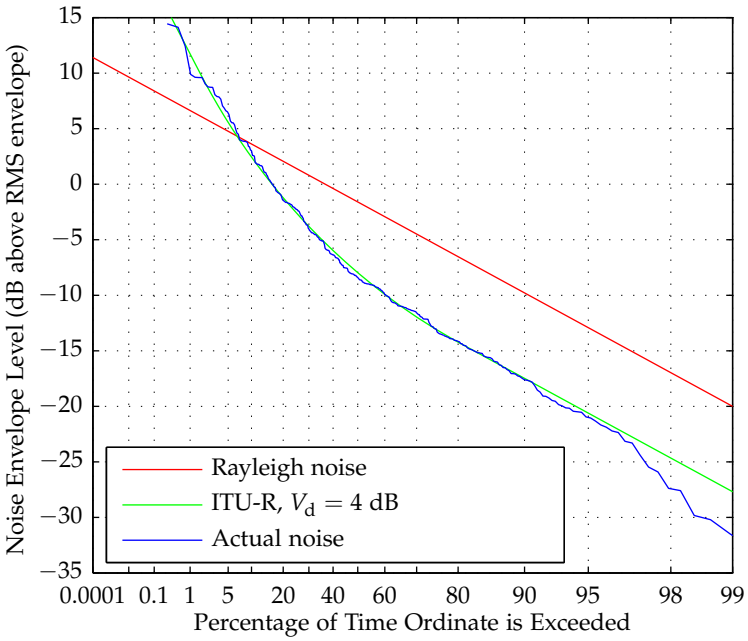

Figure 24: APD of the noise in the Loran band from a five second record during a quiet day; pulses from the North-West European Loran stations and the Western Chayka chain were removed; raw signal data courtesy of Dr. Fullekrug, University of Bath.

shows a short section of the raw signal and Figure 23 plots its spectrum (frequency components above 200 kHz were suppressed).

The time-domain plot clearly shows periodic pulsed transmissions from a nearby eLoran transmitter operating on GRI 6731. Transmissions from more distant stations are considerably weaker and are obscured by noise and interference[33]. The eLoran transmissions also stand out clearly in the frequency-domain plot (compare with the theoretical eLoran spectrum shown in Figure 8). The plot further shows that the signal is contaminated by wide-band noise, and also some CWI can be observed outside the protected Loran band. In the received signal model, the eLoran transmissions are represented by the first two terms on the r.h.s. of Equation 3.10. The wide-band noise is represented by the AWGN process denoted $w(t)$, and the CWI is modelled via the last term in Equation 3.10.

There were concerns whether the AWGN process is a suitable model for LF radio noise, which mainly is impulsive in nature. The data set recorded by Dr. Fullekrug was therefore processed to obtain the probability distribution of the background noise. Figure 24 gives the APD of the noise in the Loran band calculated from a five second signal snapshot recorded during a quiet day; pulses originating from the North-West European Loran stations and the Western Chayka chain were removed from the data set so as not to distort the results. As shown in the figure, the APD of the actual noise coincides remarkably well with the predicted APD curve for $V_d = 4$ dB constructed from the ITU-R data (see Section 3.3.2). According to Equation 3.7, a receiver that mitigates the impulsive component of the noise could in this case claim

33 Note that the plot shows the signals before being filtered by the standard eLoran bandpass filter.

a 6 dB processing gain. If the noise is modelled as a Gaussian (Rayleigh envelope) process (see the red line in Figure 24) this gain is not realised, which can lead to slightly conservative estimates of performance.

From the discussion in this section, it is concluded that the received signal model developed in this chapter and represented by Equation 3.10 provides a good approximation to real-world signal waveforms and can serve as a basis for further investigations.

3.7 SUMMARY AND CONCLUSIONS

This chapter has explored the characteristics of the eLoran radio channel, and identified the key channel impairments. A model for the received signal has been developed which includes the major sources of noise and interference to eLoran. A number of assumptions have been made to make the model suitable for further investigations. These can be summarised under the following headings:

1. Transmitter Imperfections
    a) Synchronisation related errors in modern eLoran transmitters will be negligible and therefore will not be modelled.
    b) High-frequency (pulse-to-pulse) timing and amplitude jitter of the transmitted signal is assumed to have a negligible impact on the performance of basic eLoran signal processing algorithms and it will not normally be modelled; however, it is recognised that the jitter can reduce the effectiveness of some CRI mitigation algorithms and thus may indirectly affect the performance; therefore, it will be considered when assessing the performance of these specific algorithms later in Chapter 6.
2. LF Signal Propagation
    a) It is assumed that ground wave propagation factors can be compensated for (by PF/SF modelling and through the use of ASF maps and differential corrections) and will not be considered here, unless it is necessary (e.g. for the purpose of receiver performance testing, where PF and SF need to be included).
    b) It is assumed that distortion of the eLoran pulses due to dispersion during propagation (and the associated change in ECD) has a negligible effect on the analysis and will not be modelled.
    c) Multi-hop sky waves are assumed to be substantially attenuated and delayed; only first-hop sky wave signals will be considered in this work.
    d) It is recognised that re-radiation is a separate problem from CRI and will not need to be considered in this work.
3. External Noise
    a) Atmospheric noise will be modelled as a white Gaussian process. The power spectral density of the noise will be set such that the power within the receiver's noise bandwidth equals the power of the atmospheric noise (within the same bandwidth) as predicted by ITU model [100].

b) It is assumed that man-made noise from sources ashore has a negligible impact on the performance of ship-borne receivers. Noise generated by machinery and electronic systems on board ships will be modelled according to ITU Recommendation [75].

c) It is also assumed that the impact of precipitation static is mitigated by using a radome or an H-field antenna.

4. Interference

a) It is assumed that CWI and any other inter-system interference fall outside the protected Loran frequency band and can be effectively suppressed by adequate signal processing.

5. Receiver Considerations

a) The receiving antenna is assumed to be omnidirectional in the horizontal plane (both its amplitude and phase response is assumed to be independent of the direction of arrival).

b) It is assumed that the receiver compensates for local oscillator drift and, if necessary, also for its motion; consequently, these effects are not considered in this analysis.

c) Internal noise (thermal and quantisation noise, round-off errors, etc.) is expected to be a minor component compared to external noise (dominated by atmospherics); the combined effect of the receiver imperfections will be modelled as a loss in SNR which will be determined experimentally.

Under the assumptions stated above, real-world eLoran waveforms can be approximated by Equation 3.10. The numerical values of the parameters in Equation 3.10 for a given geographical location can be estimated using methods summarised in Section 3.6.

The signal model introduced in this chapter provides an essential tool for the design of eLoran signal processing algorithms and their performance evaluation, which is the subject of the following chapters.

4 RECEIVER OVERVIEW

This chapter gives an overview of the basic building blocks of an eLoran receiver. It draws mainly on information from references [101, 102, 103, 104, 105, 30, 64] and personal discussions with eLoran receiver manufacturers [92, 91, 106, 107, 96, 108, 109]. Both hardware and software components are discussed in brief within this chapter. The next chapter then focuses on those parts of the receive chain that are of importance to the performance analyses that follow in Chapter 6 and Chapter 7.

4.1 HARDWARE

eLoran receiver manufacturers have widely adopted the Software Defined Radio (SDR) concept. This section provides a description of the key hardware components of an eLoran SDR.

A Software-Defined Radio is understood here as one where the signal is digitised early in the receive path and all subsequent signal processing is done in software. Due to the low centre frequency and relatively narrow bandwidth of the eLoran signal, the hardware architecture of an eLoran SDR is remarkably simple. The key components of an eLoran SDR are depicted in Figure 25. According to the diagram, eLoran signals are received by an active antenna, filtered and amplified in an analogue front-end, following which the signals are digitised and processed in a DSP unit. The results of the processing are then presented to the user via a standardised communication interface.

Some eLoran receivers can also be equipped with a (Differential) GNSS module, allowing them to produce an integrated (D)GNSS\eLoran position solution. Integrated positioning, however, is outside the scope of this work.

The rest of this section describes each of the hardware blocks in more detail.

4.1.1 *Antenna*

eLoran antennas are normally designed as active devices, comprising the actual antenna element(s), a bandpass filter to suppress signals outside the Loran band that may otherwise saturate the receiver's front-end, and an amplifier. The combination of the bandpass filter and amplifier is also sometimes referred to as the 'antenna coupler'. Both E-field and H-field antennas are being used in eLoran, each having its merits and limitations as described below.

E-field Antenna

E-field antennas have long been the sensors of choice in Loran systems for the relative simplicity of construction and operation. eLoran E-field antennas are typically designed as monopoles, consisting of a short vertical conductor, and the associated filter and amplifier.

As is well known, a vertical monopole antenna has an omnidirectional pattern in the horizontal plane. Since the antenna consists of only one

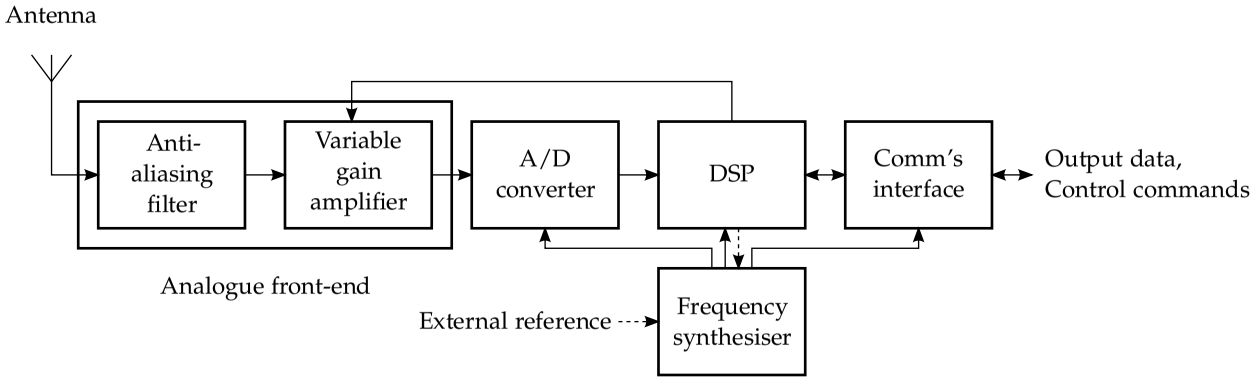

Figure 25: Hardware configuration of a single-channel software-defined eLoran receiver.

Figure 26: eLoran E-field antennas (photo courtesy of Reelektronika b.v. and UrsaNav Inc.).

element, a single-channel receiver architecture is used to process the output signal. Contrary to multi-element H-field antennas, there is no need for calibration of E-field antennas after installation.

A potential difficulty when using monopole E-field antennas is that they need to be grounded to provide adequate performance. This may be difficult to achieve in some applications, for example when used in tall buildings or in vehicles; it is less of an issue on ships, however, where the ground is well defined by the the metal body of the ship and the sea surface. In theory, it should also be possible to build a dipole E-field antenna that would differentially probe the electric field, and thereby remove the need for the grounding.

Another potential disadvantage of E-field antennas is their susceptibility to precipitation static (see Chapter 3). However, this problem can be alleviated by enclosing the antenna in a radome.

E-field antennas seem well suited for maritime use. Two examples of commercially available eLoran E-field antennas are shown in Figure 26. Further information on the design and properties of LF E-field antennas can be found for example in references [94, 74, 30].

H-field Antenna

H-field eLoran antennas are typically realised using several ferrite-loaded loop antenna elements. A single loop has a figure-eight antenna pattern in the horizontal plane. The phase response of an ideal loop is constant over the range of azimuths corresponding to each lobe of the figure-eight pattern, with a 180° degree phase transition between the two lobes. In order to obtain an omnidirectional characteristic, signals from two or more loop antenna elements need to be combined. This can be accomplished either in hardware, or in software. If the antenna outputs are combined in software, a two-channel receiver architecture is required. In either case, some calibration and additional signal processing has to be performed to achieve a truly omnidirectional antenna pattern.

Figure 27: A combined eLoran H-field\GPS antenna and the Reelektronika LORADD eLoran receiver (photo courtesy of Reelektronika b.v.).

An advantage of the two-channel approach is that it allows for a null to be created in the antenna characteristic at a given azimuth to suppress any interference coming from that direction. Further, the H-field antenna can be used to determine the signal angle of arrival, and consequently the heading of the carrying platform (electronic compass functionality). Another advantage of H-field antennas that is often mentioned is their inherent immunity to precipitation static.

Probably the main disadvantage of H-field antennas is the increased complexity of hardware design and signal processing. As explained above, a two-channel architecture is typically required. Parasitic coupling between the channels and between the antenna and the carrying platform causes heading-dependent errors which need to be calibrated after installation [30]. Further, an H-field antenna typically requires at least a single strong station with an ECD within $\pm 2.5\,\mu$s in order to be able to resolve the 180° phase ambiguity inherent to the loop antenna pattern [92]. It has also been reported that H-field antennas perform worse than E-field antennas in the presence of re-radiation [30].

Due to their immunity to preciptation static and the fact that no grounding is required, H-field antennas are suitable mainly for aviation use. A combined eLoran H-field\GPS antenna is shown in Figure 27 together with a state-of-the-art eLoran receiver.

Further information on eLoran H-field sensors can be found, for example, in reference [30].

4.1.2 *Analogue Front-end*

The receiver front-end encompasses all components between the antenna connector and the receiver's Analogue to Digital Converter (ADC). Its purpose is to make the received signal suitable for digitisation and further processing.

A receiver front-end typically consists of components such as frequency filters, downconverters and amplifiers. Since the Loran carrier frequency is only 100 kHz, there is no need for a downconverter in the analogue part of the receiver. The signal can directly be sampled at the carrier frequency and the downconversion can be accomplished later in the Digital Signal Processing (DSP) unit. Alternatively, the frequency conversion can be achieved through bandpass sampling.

The filtering stage in a front-end of a modern eLoran receiver is also relatively simple, typically consisting of only a low-pass anti-aliasing filter [109]. This filter rejects all frequency components above half the sampling frequency to ensure that the Nyqyist-Shannon sampling theorem is satisfied. Any out-of-band and in-band interference is suppressed by bandpass and notch filters implemented in the digital part of the receiver.

The front-end usually also contains a variable-gain amplifier. The gain of the amplifier would typically be controlled by the DSP unit to ensure that the signal at the output of the front-end drives the full range of the ADC, so that the amount of quantisation noise introduced during the subsequent digitisation process is minimised.

4.1.3 *A/D Converter*

The ADC digitises the output signal from the receiver's front-end and provides signal samples to the DSP unit. From this point on the receiver is fully digital, that is all subsequent processing is done in the discrete-time domain. The digitisation encompasses three steps: sampling, quantisation and coding.

Sampling (i.e. the discretisation in time) can be considered a lossless, reversible, operation. As long as the input signal satisfies the Nyquist-Shannon sampling criterion, no information is lost in the process and the time-continuous signal could, in theory, be perfectly recovered from the samples.

eLoran receivers typically sample the received signal at $f_s = 4f_c = 400\,\text{kHz}$. The advantage of using this particular sampling frequency is that the samples at the output of the ADC can then be interpreted as samples of the complex envelope, $x(t)$, of the received signal, $\tilde{x}(t)$ (see for example reference [110], p. 349).

Signal samples at the output of the ADC are encoded using a finite set of code words each expressed as an n-bit number. Clearly, only a finite set of discrete signal amplitude levels can be represented. The process of mapping the input signal values to a countable set of output values is called *quantisation*. Unlike sampling, quantisation is a lossy process in the sense that it introduces a quantisation noise into the output signal. The amount of noise that is added depends on the number of permissible amplitude levels used to represent the digitised signal, and on the signal amplitude with respect to the ADC's full scale range. The achievable Signal-to-Quantisation-Noise Ratio (SQNR) improves by 6 dB with each additional quantisation bit.

As discussed in Chapter 3, the receiver may be required to process eLoran signals that differ in level by as much as 120 dB. This necessitates the use of high-resolution ADCs[1]. Typically, 16-bit ADCs are used which achieve Signal-to-Noise-and-Distortion Ratio (SINAD) in the region of 90 dB. Given that the gain of the front-end amplifier can be adjusted over a range of 40 dB [109], a modern receiver can achieve a dynamic range of around 130 dB, consistent with the requirement stated above.

1 Note that eLoran receivers process the received signals in a linear manner, as opposed to Loran-C receivers which often used a hard-limiting front-end.

4.1.4 *Frequency Synthesiser Unit*

The frequency synthesiser unit produces clock signals for the ADC and possibly also for other components in the digital part of the receiver. The clock signals are derived from a reference frequency standard which can be free-running, controlled by the DSP unit according to the received eLoran signals, or disciplined by another reference source such as GPS.

There are three types of frequency standards that are commonly found in eLoran receivers. Consumer grade navigation receivers typically contain a Temperature-Compensated Crystal Oscillator (TCXO). The frequency accuracy of this type of oscillator is of the order of 10^{-6} [111]. High-end receivers such as those found in eLoran reference stations and ASF surveying equipment or eLoran timing receivers typically use an Oven Controlled Crystal Oscillator (OCXO)[109], or a Rubidium oscillator [96] with accuracies of the order of 10^{-8} [111] and 10^{-12} to 10^{-11}, respectively.

4.1.5 *Digital Signal Processing Unit*

The DSP unit processes raw signal samples coming from the ADC to extract key signal parameters and estimate position, velocity and time. It can be implemented in one of the following ways:

Modern *general-purpose processors* provide sufficient computational power to perform basic signal processing tasks and may be suitable for implementing low-complexity receivers, or as a proof-of-concept platform. Among the advantages of using general purpose processors is the flexibility in reconfiguration and the availability of a wide range of programming languages and software frameworks, which allows reduced development time. The price paid can be a less efficient use of clock cycles and a higher power consumption as compared to some other alternatives described below.

Digital signal processors are optimised to efficiently perform operations that are typical of various signal processing tasks. They make optimal use of the hardware and clock cycle time, at the expense of flexibility. Code for signal processors is often simpler than that required for a general purpose processor.

Field-programmable gate arrays are integrated circuits whose structure can be configured by the developer using a hardware description language. The structure of these devices is programmable down to the logical gate level, which means they can be tailored to efficiently[2] perform highly specialised signal processing tasks. Among the disadvantages of this technology is high transistor redundancy and power consumption.

Application specific integrated circuits are chips that are custom-designed and optimised for a particular application. This technology optimises transistor count and the use of clock cycles and it therefore minimises chip size and power consumption; however the associated non-recurring engineering costs are high and the structure of the chip is fixed once it is manufactured. This means that this approach is only cost-effective for large-volume production.

An interesting alternative that has recently been introduced to the market are *all programmable systems-on-chip*. These devices tightly couple

2 In terms of clock cycle use.

high capacity programmable gate arrays with multi-core processors. This architecture makes it possible to implement any computationally intensive, time-critical, tasks using the programmable logic and higher-level computations using the processor cores, which can be running a convenient operating system. A major advantage of this approach is the tight, low latency, high throughput coupling between the logic and the processor and also the possibility to reconfigure the gate array using the inbuilt processor.

4.1.6 *Interfacing*

eLoran receivers are seldom used as standalone devices and therefore are not usually equipped with a display. Instead, the results of the processing are typically output on a serial (RS-232) or Ethernet port in the form of NMEA[3] type messages containing low-level signal parameter estimates as well as the position and time information. Usually a graphical user interface software is also provided that can be used to display the measurements and configure the receiver via a PC.

4.2 SIGNAL PROCESSING

As discussed in the previous section, eLoran receivers use the SDR approach where practically all signal processing is performed in the digital domain by the DSP unit. This section gives an overview of the key signal processing blocks typically implemented in the digital portion of an eLoran receiver.

At the time of writing and to the best of the author's knowledge, all commercially available eLoran receivers use the conventional two-step approach to estimating position, velocity and time. The two-step architecture is based around a bank of identical signal processing channels that first process the received signal so as to extract estimates of each of the station TOA, pseudorange and data. The pseudorange estimates and navigation data are then used as inputs to the Position, Velocity and Time (PVT) estimator. Each of the signal processing channels works independently of the other channels in this configuration.

A potential disadvantage of the two-step architecture is that it makes no use of the fact that the pseudoranges are correlated by the receiver-transmitter geometry. Several alternative receiver architectures have been described in the literature that exploit the correlation between different signals. One such concept is the Vector Tracking Loop (VTL) [110], where information from the PVT estimator is fed back to the individual signal processing channels. The main advantage of the VTL is that the channels support each other through the feedback from the PVT estimator and hence can operate at a considerably lower Signal-to-Noise Ratio (SNR). The VTL can even withstand momentary blockages of one or more signals, and it performs better than the conventional architecture in highly dynamic scenarios.

An even more general approach, termed Direct Position Estimation (DPE), has recently been proposed, in which the position solution is directly obtained from the received signal samples without generating independent intermediate estimates. Different versions of the algorithm based on the Weighted Least Squares (WLS) method, Maximum

3 National Marine Electronics Association (NMEA) specifies data structures for communication between marine electronics.

Likelihood (ML) method and particle filtering are described in references [112, 113, 114]. Similar to the VTL, DPE performs better than the conventional architecture when some of the signals have low SNR. The DPE also has some advantages in terms of multipath rejection. However, advanced receiver architectures such as VTL or DPE are not yet widely in use and therefore will not be considered here.

Figure 28 depicts the key signal processing blocks of an eLoran receiver that is based on the conventional two-step architecture. The rest of this section briefly describes each of the blocks.

4.2.1 *Signal Conditioning*

As discussed in Chapter 3, the Loran radio channel is subject to a large number of impairments including various types of noise and interference or frequency offset. The task for the signal conditioning block is to reverse or at least mitigate the effects of the major channel impairments.

Mitigation of Impulsive Noise

One of the specifics of the LF radio channel is the presence of atmospheric noise which typically dominates the noise floor. As explained before, atmospheric noise has a low-power Gaussian component, as well as a non-Gaussian, impulsive, component caused by atmospheric discharges in the relative proximity of the receiver's location. If left uncompensated, the noise spikes generated by these discharges can disrupt the operation of subsequent signal processing stages, potentially rendering the receiver outputs useless for periods comparable to the receiver's averaging time (see below).

It was shown for example in references [115, 116] that optimal processing of signals in non-Gaussian noise requires the use of non-linear operations, such as *clipping* or *hole-punching* (also referred to as *blanking* or *censoring*). Clipping limits the magnitude of all signal samples that are larger than a certain threshold determined by the statistics of the noise. Hole-punching replaces those samples by zeros. The probability density of the residual noise obtained by such non-linear processing can be assumed to be approximately Gaussian.

Clock Drift and Doppler Shift Compensation

Any practical radio receiver has to deal with frequency offsets in the received signal caused by local oscillator imperfections and receiver movement with respect to the transmitting stations (Doppler shift). The oscillator frequency offset as well as the Doppler offsets for each station can be obtained as part of the position\velocity\time solution. This makes it possible to accurately compensate for these imperfections. Reducing the frequency offset in the received signals is necessary to enable coherent processing.

There are two ways of correcting the frequency offsets that are commonly used in eLoran receivers. One option is to control the frequency of the receiver's reference oscillator from the DSP unit so that the estimated oscillator drift is minimised. This technique is usually referred to as *clock steering*. Clearly, this method cannot be used to compensate for the Doppler shifts, as these are generally different for each station.

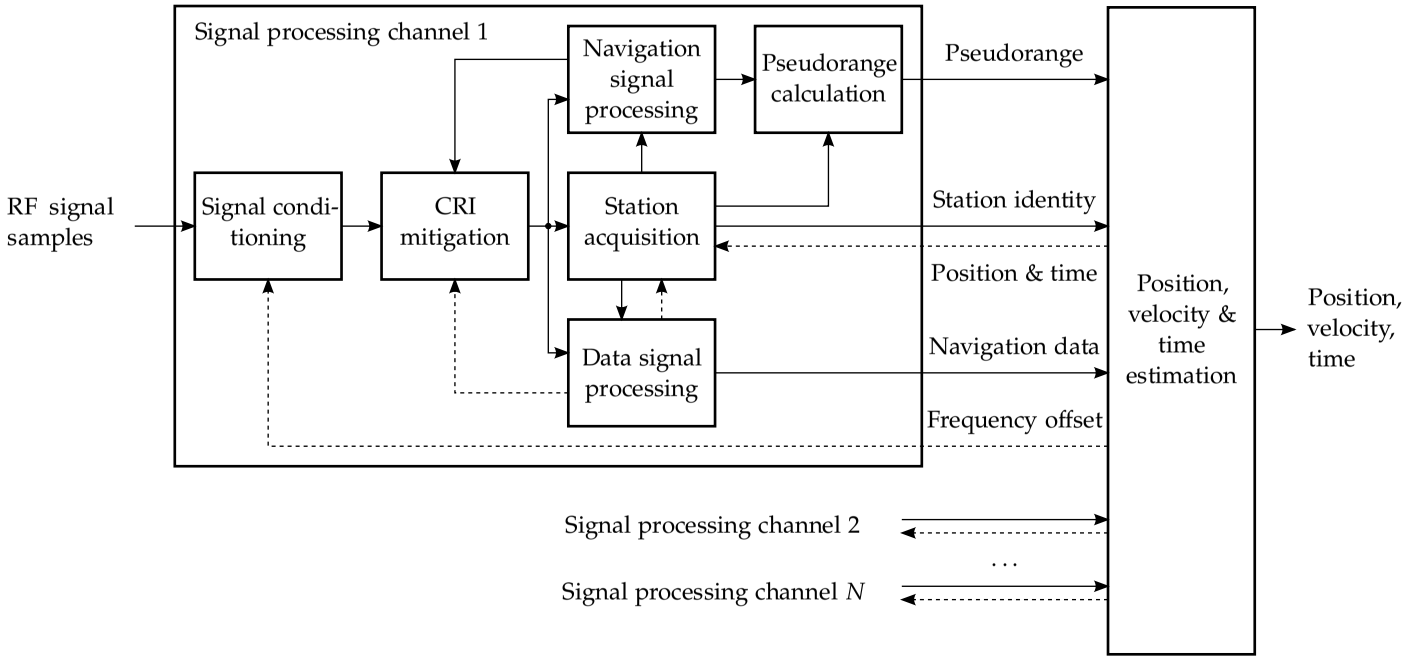

Figure 28: Schematic signal processing diagram of an eLoran receiver based on the two-step architecture; aiding data can be provided as shown by the dashed lines.

Another option is to use a fractional delay filter implemented in the DSP unit to correct for the frequency offset by *interpolation* of the incoming samples. If for the intended application the Doppler offsets are of a significant magnitude, then each signal processing channel will require a separate interpolating filter. For a low-dynamics application it may be sufficient to implement only a single interpolating filter, common to all signal processing channels, to correct only for the oscillator drift.

If there is not enough stations to form a position solution (i.e. the clock drift and Doppler offsets cannot be resolved), the receiver can be synchronised to one (normally the strongest) of the received eLoran signals which then allows for coherent processing to be performed over a longer time period.

Out-of-Band Interference Rejection

Figure 23 in Chapter 3 shows the spectrum of signals received within the bandwidth of a typical eLoran receiver. The plot is based on actual off-air data as captured in the UK. It can clearly be seen in the figure that there is a considerable number of potential interfering signals outside the Loran band. These signals must be suppressed as they would otherwise affect the accuracy of the receiver's measurements, or even make the processing of weaker signals impossible. This can easily be achieved by inserting a *bandpass filter* in the receive path.

Traditionally, an analogue Butterworth filter was used. In modern receivers the input bandpass filter is implemented in the DSP unit, however, eLoran receiver manufacturers retained the original filter specification so that the frequency response of the digital filter approximates that of the analogue Butterworth one (see also Chapter 5 and Appendix B).

In-Band (Non-Loran) Interference Mitigation

The removal of any narrow-band interfering signals (CWI) within the Loran band or close to its borders is typically achieved by adaptive notch filtering. Contemporary receivers implement up to 30 notch filters per antenna channel [91]. These are normally tuned on the basis of average signal PSD observed after the input bandpass filter and after the removal of any Loran energy in the band. The depth and bandwidth of the notches can also be adjusted automatically according to the radio environment.

It should be noted that any distortion caused by the bandpass or notch filtering must be appropriately taken into account when estimating eLoran signal time of arrival and other signal parameters.

In-band interference from cross-rating Loran stations (CRI) is dealt with separately, as discussed in the following section.

4.2.2 *CRI Mitigation*

CRI is considered the strongest source of interference to eLoran. As will be shown later in this thesis, in order to meet the stringent eLoran performance standards, CRI levels in each signal processing channel must be substantially reduced using special CRI mitigation algorithms. Several techniques for mitigating the effects of CRI are known. These can be summarised under the following headings:

- *CRI blanking* - this method discards signal samples that are likely to be hit by CRI (detection and censoring);
- *CRI cancelling* - this technique uses a replica waveform of the cross-rating signal to cancel the interference from the composite received signal (estimate and subtract algorithms);
- *Null steering* - this method can suppress interference coming from a given direction by creating a null in the antenna pattern at the required azimuth (only applicable to receivers equipped with a dual-channel H-field antenna).

The two most prevalent CRI mitigation techniques, CRI blanking and CRI cancelling, will be studied in detail in the following chapters.

It can be seen from the schematic diagram of Figure 28 that, in addition to the raw signal, the CRI mitigation block also receives information from the navigation signal and data signal processing blocks. This information may include Signal-to-Interference Ratios, signal time of arrival, estimates of the cross-rating waveforms and data carried by the cross-rating signals. As will be shown later, all this information is required to perform CRI mitigation effectively.

4.2.3 *Station Acquisition*

Having mitigated the effects of the major channel impairments on the received signal, the receiver can start extracting information on the eLoran signals. The initial phase of this process is usually referred to as *station acquisition*. Its aim is to identify a group of eLoran stations whose signals can be received at the receiver's location and produce initial estimates of the key signal parameters.

Acquisition is a composite detection\estimation problem. First, the receiver selects a specific GRI to be processed. In most cases the receiver has approximate knowledge of its position on the globe that allows it to considerably reduce the set of GRIs that need to be searched. It then detects and identifies individual stations and generates coarse estimates of the time of arrival of their pulse groups.

The pulse groups can be pulled out of noise by averaging signal samples separated in time by $2T_{\mathrm{GRI}}$ (note that signal samples separated by $2T_{\mathrm{GRI}}$ that contain eLoran pulses will be strongly correlated, whereas samples containing only noise will be uncorrelated; consequently the noise will tend to average out, revealing the eLoran pulse groups). This operation acts as a comb filter in the frequency domain and the terms *averaging* and *comb-filtering* will be used interchangeably throughout this thesis.

After averaging, the individual signals in a chain can be identified based on the correlation properties of the eLoran phase codes and known timing relations between the master station and each secondary station (the emission delays). Signal detection is typically accomplished by comparing the results of the correlation processing to a threshold determined based on a statistical analysis of the noise present in the processed signal. The process is repeated for all GRIs that are likely to be available at the receiver's location.

The acquisition process can be aided in two ways. If the receiver has already acquired UTC and knows its approximate position, it can directly calculate the approximate arrival times of signals from any

eLoran station[4]. This way, secondary stations can be identified even if the master station cannot be received. Further, the identity of a station can also be confirmed based on the data messages carried by the station's signal.

For more information on signal acquisition see, for example, reference [64].

4.2.4 *Navigation Signal Processing*

Once the station acquisition is complete, each active signal processing channel starts estimating parameters of one particular eLoran station's signal. This is accomplished in several steps, as briefly described below and detailed in Chapter 5.

First, it is necessary to suppress any remaining transmission channel impairments, such as in-band noise, residual CRI and CWI and own sky wave interference. Given the periodic nature of eLoran signals, the in-band noise and residual interference (or any source of noise\interference that is uncorrelated from PCI to PCI) can be mitigated by comb-filtering, as described earlier. The comb filter is likely to have a shorter averaging time than that used for signal acquisition to allow the receiver to track platform dynamics.

Further suppression of noise and interference is achieved by passing the signal through a *phase-decoding filter*, which works by correlating the incoming signal with the master or secondary phase code sequence[5]. This also removes the phase coding from the received pulses. The combination of the comb-filter and the phase-decoding filter effectively performs coherent averaging of all pulses received over the past averaging period. Thanks to the correlation properties of the eLoran phase codes, the phase-decoding filter also suppresses any *long-delay sky wave interference*.

The next step involves estimating the *time offsets* of the ground wave components of all stations in view. This is accomplished by inspecting the shape of the envelope of the averaged pulse. Since the peak of the pulse is usually distorted by short-delay sky waves, eLoran receivers use only the leading edge of the pulse in this processing.

eLoran transmits phase-coherent pulses which makes it possible to use *carrier phase measurements* to precisely determine the timing of signal arrival (within one cycle of the carrier). The integer phase ambiguity is resolved by using the time offset measurements obtained in the previous step. To prevent interference from *short-delay sky waves*, the carrier phase is measured at a carefully selected sampling point on the leading edge of the averaged pulse. The carrier phase estimators are typically based on the Maximum Likelihood method and will be examined closer in Chapter 5.

Based on the (coarse) time offset estimates and (precise but ambiguous) carrier phase measurements, the receiver then calculates the accurate TOA of each signal in view. Finally, the TOAs are converted into *pseudoranges* by taking into account the signal emission delays and signal velocity in free space, and the results are passed to the PVT estimator.

Besides the key signal parameters mentioned above, the receiver normally also estimates a number of additional parameters to facilitate

4 Recall that eLoran signals are synchronised to UTC.
5 See $b\,(t; \mathcal{C}, T_{\mathrm{GRI}})$ in Chapter 2.

signal processing and analysis. For example, signal strength can be estimated based on the signal level at the chosen sampling point. Noise power is commonly measured by sampling the incoming signal at time instants where there is no significant eLoran energy. This then allows SNR to be calculated which can be used to weight the individual signals in the position solution. ECD is often estimated and used as a measure of confidence in the correct carrier phase ambiguity resolution. The receiver can also estimate sky wave signal parameters or even whole waveforms and use the information to minimise sky wave induced measurement error.

4.2.5 *Data Signal Processing*

The Loran Data Channel (LDC) allows the system to meet the stringent performance requirements of the maritime sector by conveying to the user real-time differential Loran corrections, integrity and UTC messages and other data. First experiments with data modulation of Loran signals were done in the late 1960s [117]. Since then, a variety of data transmission methods have been proposed as detailed in references [105, 37, 118] . The following three methods in particular were considered for use in eLoran:

The *Eurofix Data Link* was originally conceived and developed at the Technical University (TU) Delft in the Netherlands as part of an integrated GPS\Loran-C navigation system [105]. It uses a Pulse Position Modulation (PPM) of the last six pulses in a GRI (first two pulses remain unmodulated) and can achieve effective data rates between 18.7 bit/s and 46.7 bit/s depending on the GRI.

A method called *Ninth Pulse Communications* was the favoured solution for the proposed U.S. eLoran system [6]. It uses a PPM of an additional pulse in a group (i.e. the navigation pulses are not affected, except by a slight increase in CRI). The effective data rates are comparable with those of the Eurofix Data Link.

Finally, the *High Speed Loran Data Channel* method was designed for data broadcast trials at the request of the U.S. Federal Aviation Administration [118]. It demonstrates the capability of Loran to broadcast the full 250 bit/s Wide Area Augmentation System (WAAS) message using the Intra-pulse Frequency Modulation, which works by altering the carrier frequency of the Loran pulses after the rise time of the pulse.

The European implementation of eLoran uses Eurofix for data transmission and the rest of this section will therefore focus on this technique. The Eurofix Data Link uses a form of a tri-state PPM that is said to be *balanced*, i.e. the average time shift of the pulses constituting a Eurofix symbol[6] equals zero. This means that the modulation is effectively transparent to the navigation signal processing as the time shifts due to the modulation are averaged out in the comb filter. This fact also provides justification for omitting the data modulation in the eLoran signal model used in this work (Chapter 2). The only signal processing algorithm that is affected by the presence of the modulation is CRI cancelling. As will be discussed in later chapters, when cancelling data-modulated eLoran signals it is necessary to re-modulate the replica waveform with the received data. For simplicity[7] it will be assumed

6 A Eurofix symbol is carried by the last six pulses in an eLoran pulse group. Each symbol represents 7 bits of information, and a Eurofix message consists of 30 symbols.

7 A performance analysis of the Loran Data Channel is out of the scope of this work.

throughout that the receiver has perfect knowledge of the Eurofix data carried by each received signal so that CRI cancelling can be applied.

The information transmitted via Eurofix is protected by a *Reed-Solomon error correction code* capable of correcting up to 10 consecutive symbol errors. Further, the code can withstand a loss of up to 55% of the pulses in a message [105]. A *Cyclic Redundancy Check* can also be performed on the decoded messages to confirm data integrity. Such a robust coding scheme was required in order to be able to cope with burst errors caused by transmitter dual-rate blanking and CRI in general. The maximum error-correcting capability of the code should be taken into consideration when selecting GRIs for new eLoran stations by ensuring that the overlaps between any two cross-rating signals do not last longer than 10 consecutive repetition intervals (Chapter 10).

As far as signal processing is concerned, there are some fundamental differences between navigation and data communications. Since each of the six modulated pulses in a group carries information, averaging of the pulses as a means of increasing SNR and Signal-to-Interference Ratio (SIR) is not possible in Eurofix. On the other hand, the Eurofix signal processing does not require measuring absolute signal TOA but only relative time shifts of the last six pulses in a group with respect to the first two (unmodulated) pulses. The receiver can therefore make use of all the energy in each pulse, including the sky waves.

One of the major sources of error in Eurofix data transfer is CRI. CRI mitigation algorithms discussed above are equally applicable to Eurofix signal processing. CRI blanking can be used to flag corrupted pulses as *erasures*, which helps the Reed-Solomon decoder in decoding the Eurofix message. CRI cancelling can also be applied although, as mentioned above, the replica waveform needs to be re-modulated with the received Eurofix data. Null steering using a two-channel H-field antenna was also proved effective [119].

For further detail on Eurofix communications and associated signal processing algorithms see reference [105].

4.2.6 *Position, Velocity and Time Estimation*

The PVT estimation block receives pseudorange measurements and navigation data from the individual signal processing channels and generates estimates of the receiver's position, velocity and UTC time. Each pseudorange can be modelled as a nonlinear equation in three unknowns (two position coordinates[8] and the range equivalent of the receiver's clock offset with respect to the system time). A minimum of three equations (i.e. three simultaneous pseudorange measurements) are therefore required to solve for the unknown parameters.

The calculations also require that the PF and SF propagation factors are taken into account (Chapter 3). For the best achievable positioning accuracy, surveyed ASF data also need to be supplied. This data is typically provided in the form of ASF maps stored in the receiver, supplemented by real-time differential corrections obtained via the LDC. The LDC also provides messages that enable the receiver to recover absolute UTC time and date.

Finally, pseudorange rates can be generated by differencing successive pseudorange observables and used to estimate the receiver's

8 Note that eLoran can only provide a 2D position fix as all eLoran transmitters are land based.

velocity vector and local oscillator drift. This is accomplished in a similar manner as the estimation of the receiver's position and clock offset.

4.3 SUMMARY AND CONCLUSIONS

This chapter has discussed the key aspects of eLoran receiver hardware and signal processing in order to provide the reader with context for interpreting subsequent chapters. Based on a literature review and consultations with eLoran receiver manufacturers, the following high-level conclusions can be drawn:

1. eLoran receivers are software defined radios in which practically all signal processing is done digitally.
2. Contemporary receivers are based around the conventional two-step architecture where the receiver first produces a set of pseudorange measurements which are then used as inputs to a PVT estimation algorithm.
3. While several alternative data transmission schemes have been proposed, the European implementation of eLoran uses the Eurofix data link and for the rest of this thesis the focus will be on this technique. For simplicity, it will be assumed throughout this thesis that the receiver has perfect knowledge of the Eurofix data carried by each received signal. Consequently, and due to its balanced nature, the Eurofix modulation can be assumed to have a negligible impact on the performance of the navigation signal processing algorithms examined in this thesis.
4. For use in the maritime domain, E-field antennas are preferred over H-field.

The following chapter deals in detail with those parts of the receive chain that are relevant to the performance analyses presented later in this thesis.

Part II

MAIN CONTRIBUTION

5 RECEIVER SIGNAL PROCESSING MODEL

The previous chapter gave an overview of eLoran receivers and signal processing techniques. The current chapter focuses on those aspects of receiver signal processing that are crucial in determining eLoran ranging performance. The aim of this chapter is to develop a signal processing model that will allow the evaluation of the effects of radio noise and interference on the receiver performance. The main difficulty encountered in the development of such a model is the lack of published information on eLoran receivers. Receiver manufacturers carefully guard their intellectual property and the use of proprietary integrated circuits and digital signal processing further obscures details of operation of modern receivers. However, even the most sophisticated designs must obey the laws of physics, statistics and information theory. In this chapter, receiver design is considered as an estimation theory problem. An optimal receiver structure is proposed based on the principles of Maximum Likelihood estimation. This structure will then be used in the following chapter to determine performance bounds, which any practical receiver should approach. The algorithms described here should therefore be regarded as basic concepts rather than an accurate description of a particular receiver design.

5.1 CARRIER PHASE ESTIMATION

As explained earlier, eLoran uses carrier based positioning, and carrier phase estimation is therefore at the heart of eLoran receiver signal processing. In this section, some of the basic concepts of estimation theory are introduced, and a carrier phase estimator for a channel with AWGN is derived which then becomes the basis of the signal processing model developed further in this chapter.

5.1.1 *Elements of Estimation Theory*

Estimation theory is a branch of statistics that deals with estimating values of parameters from observed data sets. The *observations*[1], $\mathbf{x} = [x_1, x_2, \ldots, x_N]$, are considered to be random in nature, with a Probability Density Function (PDF) $p(\mathbf{x}; \theta)$, dependent on the *parameter of interest*, θ. For simplicity, it is assumed here that the unknown parameter is a time-invariant scalar. The purpose of estimation theory is to arrive at an *estimator*, i.e. a function, $g(\cdot)$, that assigns to the observations, $\mathbf{x}$, an estimate $\hat{\theta}$ of the parameter θ:

$$\hat{\theta} = g(\mathbf{x}).$$

Due to the random nature of the observations, there are many possible approaches to the estimation problem (see e.g. reference [120]).

1 In this work, the observations represent samples of the continuous-time received signal waveform.

For example, a natural requirement would be that the estimator should minimise the Mean Square Error (MSE) of the estimates[2]:

$$\varepsilon_{\text{MSE}} = \text{E}\left[\left(\hat{\theta} - \theta\right)^2\right].$$

Interestingly, adoption of this criterion usually leads to unrealizable estimators that require knowledge of the value of the parameter that is to be estimated.

The way around this problem is to restrict the estimator to be *unbiased* (an estimator is termed unbiased, if on average, it yields the true value of the unknown parameter, i.e. $\text{E}\left[\hat{\theta}\right] = \theta$ for all values of θ), and find the one that minimises the variance. This is termed the Minimum Variance Unbiased (MVU) estimator. Unfortunately, the MVU estimator may not always exist, and even if it does, it is usually difficult to find. Nevertheless, it is a useful theoretical concept as its variance can be lower-bounded by the Cramer-Rao Lower Bound (CRLB) [120]. For this reason it is often used as a benchmark for the performance evaluation of practical estimators. Estimators that achieve the CRLB are called *efficient estimators*.

An approach often used in practice is to force the estimator to be linear in the data, and find the one that is unbiased and has minimum variance. This is termed the Best Linear Unbiased Estimator (BLUE). This technique is well suited for position estimation in pseudoranging systems (see Section 7.2.4).

Arguably the most popular approach to parameter estimation in signal processing is based on the ML principle. The following section provides a brief overview of ML estimation and derives an ML carrier phase estimator for an AWGN channel.

5.1.2 *Maximum Likelihood Estimation*

ML estimation is widely used in practice as it provides a straightforward procedure for designing estimators. The method does not require prior knowledge of the statistical properties of the parameter θ, and for many problems, an ML estimator can be found as an explicit function of the observed data, $\mathbf{x} = [x_1, x_2, \ldots, x_N]$. Although the ML estimator has no optimal properties for finite data records, it has a number of desirable asymptotic properties. It can be shown that the ML estimator is *asymptotically unbiased*, meaning that for large data sets ($N \to \infty$) the estimator yields on average the true value of θ. It is also *asymptotically efficient* which means that for $N \to \infty$ its variance approaches that of the MVUB (i.e. the CRLB). For signal in noise problems, the ML estimator also achieves the CRLB for high SNRs [120].

In ML estimation, the parameter θ is treated as a deterministic (but unknown) value. The relation between the unknown parameter and the observed data is modelled by a PDF $p(\mathbf{x}; \theta)$. The ML estimate is then defined to be the value of θ that maximises the (assumed) PDF of the observations for $\mathbf{x}$ fixed:

$$\hat{\theta}_{ML} = \arg\max_{\theta} p(\mathbf{x}; \theta).$$

2 Throughout this document, $\text{E}[\cdot]$ denotes the statistical expectation of a random variable.

In the following, the ML approach is applied to the problem of estimating the value of a parameter of a known waveform corrupted by AWGN.

ML Estimation for a Deterministic Signal in an AWGN Channel

Consider the case of a known, deterministic RF signal waveform $\tilde{s}(t;\theta)$ corrupted by WGN:

$$\tilde{x}(t) = \tilde{s}(t;\theta) + w(t).$$

The signal $\tilde{x}(t)$ is observed over a time interval $t \in \langle 0; T_i \rangle$ and the task is to find the ML estimate $\hat{\theta}_{ML}$ of the unknown parameter θ.

First, the observation vector $\mathbf{x}$ must be formed. The observations can be obtained by equidistant sampling of the continuous-time waveform $\tilde{x}(t)$ with a sampling frequency that satisfies the Nyquist-Shannon sampling theorem with respect to the desired signal, $\tilde{s}(t;\theta)$; it is assumed that $\tilde{x}(t)$ is appropriately filtered in order to avoid aliasing; it is also assumed that the anti-aliasing filter has sufficiently large bandwidth so that the desired signal passes through the filter undistorted. In the following, $\tilde{x}_n$ and $\tilde{s}_n(\theta)$, where $n = 1, 2, \ldots N$, denote the samples of the respective waveforms.

Next, a model of the PDF of the observed samples must be created. Since, in this example, the only source of randomness in the observations comes from the additive noise $w(t)$, which is assumed to be white, zero-mean and Gaussian distributed, the PDF of the data can be expressed as

$$p(\mathbf{x};\theta) = \left(\frac{1}{\sqrt{2\pi}\sigma}\right)^N \exp\left\{-\sum_{n=1}^{N} \frac{[\tilde{x}_n - \tilde{s}_n(\theta)]^2}{2\sigma^2}\right\}, \tag{5.1}$$

where σ^2 is the variance of the noise present in the sampled signal. As explained above, the ML estimate $\hat{\theta}_{ML}$ is found by maximising the PDF with respect to θ:

$$\hat{\theta}_{ML} = \arg\max_{\theta} p(\mathbf{x};\theta).$$

From Equation 5.1 it can be seen that this is equivalent to the following minimisation problem:

$$\hat{\theta}_{ML} = \arg\min_{\theta} \sum_{n=1}^{N} [\tilde{x}_n - \tilde{s}_n(\theta)]^2,$$

which can also be expressed using the continuous-time signal waveforms, as follows [121]:

$$\hat{\theta}_{ML} = \arg\min_{\theta} \int_{T_i} [\tilde{x}(t) - \tilde{s}(t;\theta)]^2 \, \mathrm{d}t, \tag{5.2}$$

where T_i is the observation time over which the signal is being evaluated; throughout this work T_i will also be referred to as the *integration time* as it is also the length of the integration interval in Equation 5.2. Note that the maximisation of the modelled PDF of the observed data is in fact equivalent to minimising the mean square error between the estimated signal waveform and the actual received signal.

ML Carrier Phase Estimation in an AWGN Channel

The ML principle will now be applied to the problem of estimating the phase offset, θ, of a signal from an eLoran station. As discussed in Chapter 2 and Chapter 3, actual eLoran signals have a rather complex structure; nevertheless, for the purpose of this derivation, it is considered sufficient to model the received signal as a pure harmonic waveform (representing the carrier signal of a single eLoran station) corrupted by AWGN:

$$\tilde{x}(t) = \underbrace{A\cos(2\pi f_c t + \theta)}_{\tilde{s}(t;\theta)} + w(t).$$

Measuring the phase of noisy sine waves is indeed the essence of eLoran positioning. The complexity associated with the actual eLoran signal structure (the pulsed nature of the signal, the phase codes, interference, etc.) will be dealt with in the following sections of this chapter.

The ML estimate $\hat{\theta}_{ML}$ of the carrier phase is obtained by substituting for $\tilde{s}(t;\theta)$ into Equation 5.2 above:

$$\begin{aligned}\hat{\theta}_{ML} &= \arg\min_{\theta} \int_{T_i} \left[\tilde{x}(t) - A\cos(2\pi f_c t + \theta)\right]^2 \mathrm{d}t \\ &= \arg\min_{\theta} \left[-2A\int_{T_o} \tilde{x}(t)\cos(2\pi f_c t + \theta)\,\mathrm{d}t + \right. \\ &\qquad \left. \underbrace{\int_{T_i} \tilde{x}^2(t)\,\mathrm{d}t}_{\text{not a function of } \theta} + A^2 \underbrace{\int_{T_i} \cos^2(2\pi f_c t + \theta)\,\mathrm{d}t}_{\approx T_i/2 \text{ for } T_i \gg 1/f_c}\right].\end{aligned}$$

Clearly, the second and third terms in the above expression are not functions of θ and therefore can be ignored in the derivation (it has been assumed that $T_i \gg 1/f_c$, which always holds in practice, as the integration time is typically of the order of seconds). The first term then involves correlation of the received signal $\tilde{x}(t)$ with the estimated carrier waveform. This can further be rewritten as

$$\begin{aligned}\hat{\theta}_{ML} &= \arg\min_{\theta} \left[-2A\int_{T_i} \tilde{x}(t)\cos(2\pi f_c t + \theta)\,\mathrm{d}t\right] \\ &= \arg\max_{\theta} \left[\underbrace{\int_{T_i} \tilde{x}(t)\cos(2\pi f_c t + \theta)\,\mathrm{d}t}_{\Lambda(\theta)}\right].\end{aligned}$$

The term denoted $\Lambda(\theta)$ is normally referred to as the *likelihood function*. The ML estimate is found by maximising $\Lambda(\theta)$ with respect to θ. A necessary condition for a maximum is that

$$\frac{\mathrm{d}\Lambda(\theta)}{\mathrm{d}\theta} = 0,$$

that is

$$\int_{T_i} \tilde{x}(t)\sin\left(2\pi f_c t + \hat{\theta}_{\mathrm{ML}}\right)\mathrm{d}t = 0. \tag{5.3}$$

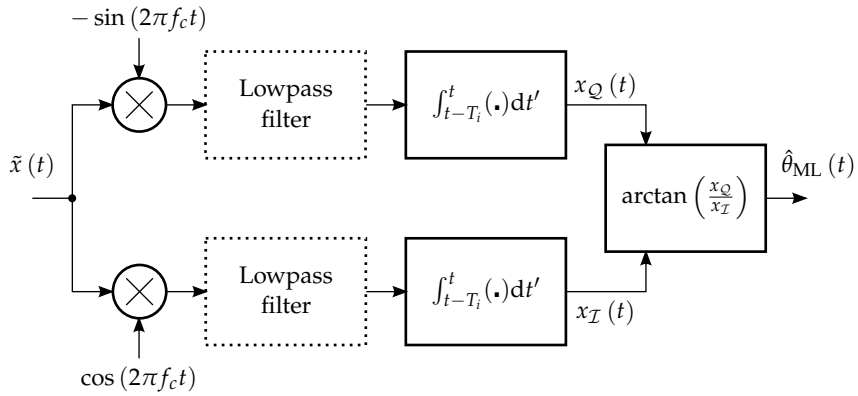

Figure 29: Feed-Forward estimator structure for the ML estimation of the carrier phase; based on Equation 5.4.

Upon expanding the sine function, using basic trigonometric identities and rearranging the terms, the ML estimate of the carrier phase can be expressed explicitly as[3]

$$\hat{\theta}_{\mathrm{ML}} = \arctan\left[-\frac{\int_{T_i}\tilde{x}(t)\sin(2\pi f_c t)\,\mathrm{d}t}{\int_{T_i}\tilde{x}(t)\cos(2\pi f_c t)\,\mathrm{d}t}\right]. \tag{5.4}$$

Feed-Forward vs. Feed-Back Estimators

Equation 5.4 implies the use of a structure shown in Figure 29. Such a structure directly estimates the unknown parameter from a single observation interval and is usually referred to in the literature as a one-shot, batch-processing, open loop, or Feed-Forward (FF) estimator.

Note that the multiplication by the quadrature carriers in the FF implementation shown in Figure 29 effectively provides the real and imaginary part of the *complex envelope*[4] of the received signal. The process of generating the complex envelope normally also requires a pair of low-pass filters to suppress the double-frequency components produced by the multiplication (these are shown by a dashed line in Figure 29). However, the integrators employed in the estimator act as low-pass filters with a cut-off frequency of approximately $1/2T_i$. Since in practical situations $1/2T_i \ll f_c$, the integrators can take over the function of the low-pass filters. This means that the estimator structure can be simplified as shown in Figure 30; the block that transforms the RF signal $\tilde{x}(t)$ into its complex envelope, $x(t)$, is called the *frequency downconverter*; the block denoted $\angle$ calculates the polar angle of the complex-valued signal and will be referred to here as the *phase detector*.

In practical receivers, carrier phase estimation is often performed using Feed Back (FB) systems (tracking loops). FB estimators work by synchronising a locally generated reference signal to the received signal, as illustrated in Figure 31. The basic structure of an FB estimator can be derived from Equation 5.3 above. The estimator is based on the fact that the integral in Equation 5.3 is zero when the phase offset of the reference signal equals the ML estimate $\hat{\theta}_{\mathrm{ML}}$. The output of the

3 Note that the one-argument arctan(.) function used in Equation 5.4 produces estimates in the range $\left(-\frac{\pi}{2}, \frac{\pi}{2}\right)$ only. This can be overcome by using the four-quadrant arctan2(.,.) function instead (for definition see Section A.4 in the Appendices).

4 For definition of the complex envelope see Appendix A.

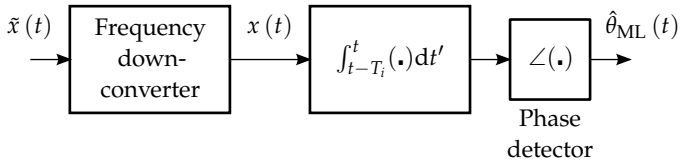

Figure 30: Feed-Forward carrier phase estimator operating on the complex envelope of the received signal.

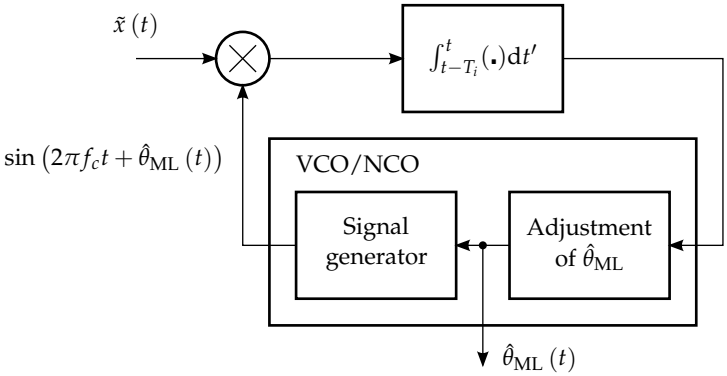

Figure 31: Feed-Back estimator structure for the ML estimation of the carrier phase; based on Equation 5.3.

integrator in Figure 31 can therefore be used as an error signal to control the phase offset of the local generator in such a way that the magnitude of the estimation error is reduced, and eventually the ML estimate is obtained. The theory of FB systems is discussed thoroughly e.g. in reference [122].

A decision now needs to be taken as to which of the two structures will be adopted in the following investigations. FB estimators are often used in practice due to their low computational complexity and their inherent ability to track slowly varying parameter changes. However, FF estimators prove useful in performance analyses of ML estimation, and since their performance can be related to the performance achieved by FB systems, it is the candidate's choice to use the FF structure in this study. Note that the FF and FB structures shown above were derived from the same likelihood function $\Lambda(\theta)$, and their performance in AWGN should indeed be the same or comparable. It is also noted that consultations with an eLoran receiver manufacturer [91] confirmed that their products used direct estimation rather than tracking loops.

5.2 SKY WAVE REJECTION AND CHANNEL SHARING

For the sake of clarity, the previous section modelled the received eLoran signal as a single sinusoid embedded in noise. In reality there will, of course, always be multiple transmitting stations in the coverage area of an eLoran system. Also, as discussed in Chapter 3, each eLoran signal can contain multiple sky wave modes, each acting as a source of interference. This section deals with the problems of channel sharing and sky wave rejection in eLoran. As will be clear from the discussion

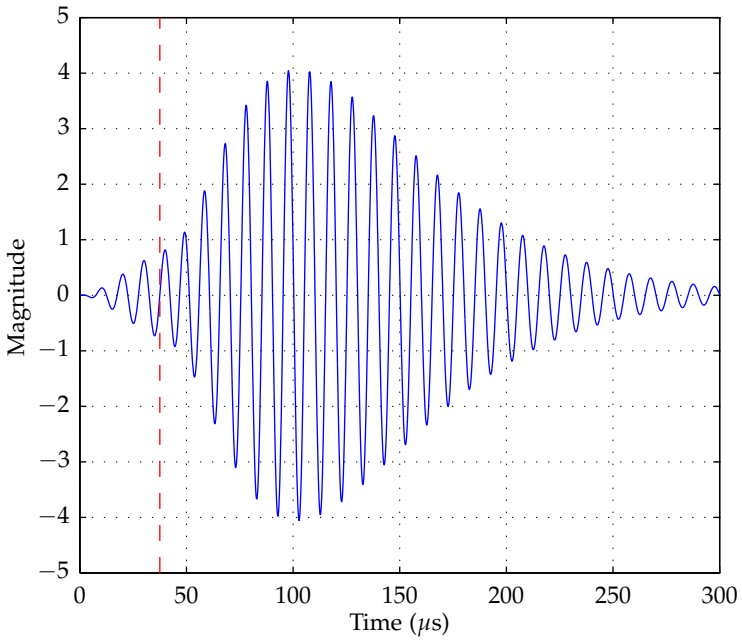

Figure 32: Composite eLoran pulse as sensed in the far E-field; the ground wave component is interfered with a short delay sky wave with a differential delay of 37.5 μs and power 12 dB above that of the ground wave (worst-case sky wave conditions expected according to the draft Minimum Performance Standards for Marine eLoran Receiving Equipment [123]); area to the left of the dashed line shows the sky wave-free part of the pulse, usable for absolute positioning.

below, the two problems are closely interlinked and therefore are treated here together.

5.2.1 *Short Delay Sky Wave Rejection*

As was shown in Chapter 3, under standard propagation conditions the first-hop sky wave arrives at the receiver at least 35 μs later than the ground wave signal component. In the following, sky waves with a differential delay τ_{diff} of 35 μs to 700 μs will be referred to as *short delay sky waves*. As described below, such sky waves can be mitigated by transmitting pulsed rather than continuous wave signals.

Pulse Sampling

Short delay sky waves are mitigated in eLoran receivers by using, in the carrier phase estimation process, only the early (sky wave free) part of the received pulses (see Figure 32). With classical Loran signal processing the receiver effectively takes only *one signal sample per pulse*[5]. The carrier phase estimator derived in the preceding section then needs to be modified in order to take the pulsed nature of the eLoran signal into account.

5 Some researchers [30, 124] considered the possibility of using the energy in the sky wave portion of the pulse to aid in the tracking of the ground wave signal. However, to the best of author's knowledge, no such algorithms have been described in sufficient detail in the open literature and this possibility will therefore not be considered here.

Assume for the moment that the transmitted signal consists of a sequence of eLoran pulses spaced $2T_{\mathrm{GRI}}$ apart (i.e. it is assumed that there is only one pulse per PCI)[6]

$$\begin{aligned}\tilde{s}\left(t;\tau,\theta,T_{\mathrm{GRI}}\right) &= \tilde{a}\left(t;\tau,\theta\right) \star d\left(t;T_{\mathrm{GRI}}\right) \\ &= \sum_{n=-\infty}^{\infty} \tilde{a}\left(t-2nT_{\mathrm{GRI}};\tau,\theta\right).\end{aligned}$$

Assume further that the received signal after downconversion can be modelled as[7]

$$x\left(t\right) = \underbrace{A_1 s\left(t;\tau_1,\theta_1,T_{\mathrm{GRI}}\right)}_{\text{ground wave}} + \underbrace{A_2 s\left(t;\tau_2,\theta_2,T_{\mathrm{GRI}}\right)}_{\text{sky wave}} + \underbrace{w_{\mathrm{b}}\left(t\right)}_{\text{CE of band-limited WGN}},$$

where $s\left(t;\tau_1,\theta_1,T_{\mathrm{GRI}}\right)$ is the complex envelope of $\tilde{s}\left(t;\tau,\theta,T_{\mathrm{GRI}}\right)$, τ_1 and θ_1 will be assumed to be equal to zero[8], and $\tau_2 \in \left\langle 35\cdot 10^{-6}, 700\cdot 10^{-6}\right)$. The impact of the sky wave can then be mitigated by making the following modifications to the estimator structure (see also Figure 33):

First, the incoming signal will be sampled at time instants given by $t_{n'} = 2n'T_{\mathrm{GRI}} + \tau_{\mathrm{sp}}$, $n' \in \mathbb{Z}$. It is assumed that an appropriate value for the sampling offset, τ_{sp}, is determined by an independent algorithm, based on the shape of the pulse leading edge. Clearly, there are two conflicting requirements that affect the choice of the optimal sampling point. From an SNR point of view, the pulse should be sampled at its peak, i.e. 65 μs into the pulse (assuming the ideal waveform). The presence of the sky wave, on the other hand, requires that the receiver samples early in the pulse. In practice, the pulses need to be sampled at least $(4-6)$ dB below the peak if sky wave interference is to be avoided. The process of determining the value of τ_{sp} will be discussed in more detail later in this chapter.

Next, it will be assumed that a new phase estimate is generated and sent for further processing once per given *update interval*, T_{up}, where $T_{\mathrm{up}} \leq T_{\mathrm{i}}$. This is represented by an additional sampler placed before the phase detector, as shown in Figure 33. It is further assumed that the update interval, T_{up}, as well as the integration interval, T_{i}, are both integer multiples of the pulse repetition interval, $2T_{\mathrm{GRI}}$, and that the input and output samplers act in synchronism, i.e. the output sampler takes samples at time instants $t_u = uT_{\mathrm{up}} + \tau_{\mathrm{sp}}$. These assumptions allow some simplification in the derivation of the signal processing model and in the performance analysis that will follow, without affecting the validity of the results.

6 For definition of $\tilde{a}\left(t;\tau,\theta\right)$ and $d\left(t;T_{\mathrm{GRI}}\right)$ see Chapter 2.
7 For definition of $\tilde{w}_{\mathrm{b}}\left(t\right)$see Appendix A.
8 Recall that the time and carrier phase offsets are defined here relative to the (arbitrary set) receiver clock; therefore it can be assumed that the offsets for the signal of interest take any suitable value.

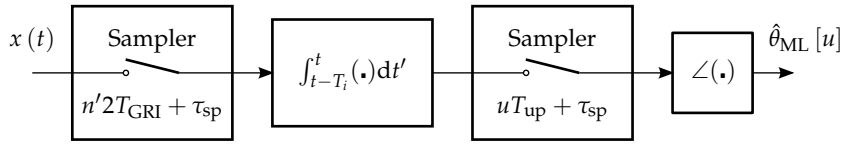

Figure 33: Carrier phase estimation for a pulsed signal waveform; the pulse repetition interval is given by $2T_{\mathrm{GRI}}$, $\tau_{\mathrm{sp}} \in \langle 0, 2T_{\mathrm{GRI}})$ determines the position of the sampling point, $T_i = N_{\mathrm{i}} \cdot 2T_{\mathrm{GRI}}$ is the integration interval, $N_{\mathrm{i}} \in \mathbb{N}$, $T_{\mathrm{up}} = N_{\mathrm{up}} \cdot 2T_{\mathrm{GRI}}$ is the update interval, $N_{\mathrm{up}} \in \mathbb{N}$, $N_{\mathrm{up}} \leq N_{\mathrm{i}}$, and $n' \in \mathbb{Z}$, $u \in \mathbb{Z}$.

Comb Filtering

Before proceeding to the next signal processing stage, it is worthwhile to re-examine the structure shown in Figure 33. The signal at the output of the integrator in Figure 33 can be written as

$$\begin{aligned} x_{\mathrm{i}}(t) &= \int_{t-T_i}^{t} x(t')\, d(t' - \tau_{\mathrm{sp}}; T_{\mathrm{GRI}})\, \mathrm{d}t' \\ &= \int_{t-T_i}^{t} x(t') \sum_{n' \in \mathbb{Z}} \delta(t' - 2n'T_{\mathrm{GRI}} - \tau_{\mathrm{sp}})\, \mathrm{d}t' \\ &= \sum_{n' \in \mathcal{S}_{t,T_i}^{(n)}} x(2n'T_{\mathrm{GRI}} + \tau_{\mathrm{sp}}), \end{aligned} \tag{5.5}$$

where $\delta(.)$ is the Dirac delta, and $\mathcal{S}_{t,T_i}^{(n')}$ is the set of all $n' \in \mathbb{Z}$ such that $(2n'T_{\mathrm{GRI}} + \tau_{\mathrm{sp}}) \in (t - T_i, t\rangle$. In words, to calculate the output value of the integrator at time t one needs to add samples of all pulses from a given GRI that have arrived since $t - T_i$. Since in Loran systems T_{GRI} is always an integer multiple of the carrier cycle (see signal specifications [14, 88]), the algorithm described by Equation 5.5 effectively performs *coherent integration* on the received signal, thereby reducing the impact of noise and interference.

The sum in Equation 5.5 can be put into a more convenient form by realising that it only needs to be evaluated at time $t_u = uT_{\mathrm{up}} + \tau_{\mathrm{sp}}$, where $u \in \mathbb{Z}$, and T_{up} is an integer multiple of $2T_{\mathrm{GRI}}$ (see the output sampler). With this in mind, it should be clear that the combination of the input sampler and the integrator in Figure 33 can be replaced by a block performing a moving average operation described by the following equation:

$$x_{\mathrm{c}}(t) = \frac{1}{N_{\mathrm{i}}} \sum_{n'=0}^{N_{\mathrm{i}}-1} x(t - 2n'T_{\mathrm{GRI}}), \tag{5.6}$$

where $N_{\mathrm{i}} = {}^{T_i}/_{2T_{\mathrm{GRI}}}$. The factor ${}^{1}/_{N_{\mathrm{i}}}$ was added purely for scaling purposes so that the amplitude of the useful signal remains unchanged. Note that the above modification will not affect the carrier phase estimates in any way, as long as the output sampler remains synchronised with the incoming signal.

Equation 5.6 implies the use of a structure commonly called the *comb filter*. The filter owes its name to the shape of its magnitude response. By taking the Fourier transform on both sides of Equation 5.6, rearranging

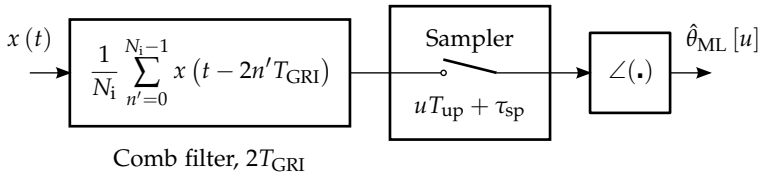

Figure 34: Carrier phase estimator for a pulsed signal utilising a comb filter; the pulse repetition interval is given by $2T_\mathrm{GRI}$, $\tau_\mathrm{sp} \in \langle 0, 2T_\mathrm{GRI})$ determines the position of the sampling point, $T_i = N_\mathrm{i} \cdot 2T_\mathrm{GRI}$ is the integration interval, $N_\mathrm{i} \in \mathbb{N}$, $T_\mathrm{up} = N_\mathrm{up} \cdot 2T_\mathrm{GRI}$ is the update interval, $N_\mathrm{up} \in \mathbb{N}$, $N_\mathrm{up} \leq N_\mathrm{i}$, and $n' \in \mathbb{Z}$, $u \in \mathbb{Z}$.

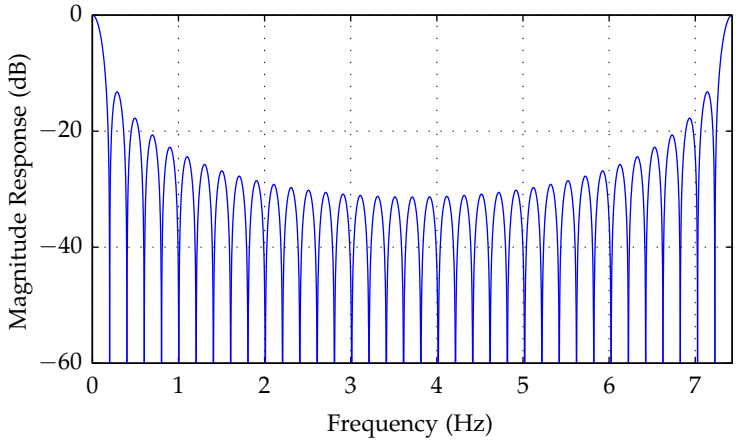

Figure 35: Magnitude response of a comb filter, $|H_\mathrm{c}(f)|$; $T_\mathrm{GRI} = 6731 \cdot 10^{-5}$, $N_\mathrm{i} = 37$.

the terms, and applying some straightforward algebra, the frequency response of the filter is found to be

$$H_\mathrm{c}(f) = \frac{S_{x_\mathrm{c}}(f)}{S_x(f)} = \frac{1}{N_\mathrm{i}} \sum_{n'=0}^{N_\mathrm{i}-1} \mathrm{e}^{-\mathrm{j}2\pi f n' 2T_\mathrm{GRI}} = \frac{1}{N_\mathrm{i}} \frac{1 - \mathrm{e}^{-\mathrm{j}2\pi f T_\mathrm{i}}}{1 - \mathrm{e}^{-\mathrm{j}2\pi f 2T_\mathrm{GRI}}}. \quad (5.7)$$

Figure 35 shows the magnitude response of this filter, $|H_\mathrm{c}(f)|$, for $T_\mathrm{GRI} = 6731 \cdot 10^{-5}\,\mathrm{s}$ and $N_\mathrm{i} = 37$ (corresponding to an integration time of approximately 5 s). As can be seen from the figure, the filter accentuates spectral components at integer multiples of $1/2T_\mathrm{GRI}$, thus allowing the estimator to be "tuned" for the reception of signals with a given GRI (recall from Chapter 2 that the spectrum of an eLoran signal is formed by discrete lines, $1/2T_\mathrm{GRI}$ apart). It can therefore be concluded that the combination of the comb filter and the sampler fulfills the following three basic functions:

- Short-delay sky wave mitigation;
- Coherent integration;
- eLoran rate selection.

An estimator structure utilising the comb filter is shown in Figure 34.

5.2.2 *Long Delay Sky Wave Rejection*

As explained in Chapter 2, in order to increase the average signal power, eLoran transmitters send pulses in groups of eight. Pulses in a group are separated by 1 ms (T_p). Since the pulse length is approximately 250 μs to 300 μs, there is a danger that sky wave components delayed by more than 700 μs or so can interfere with pulses sent later in the group. For the purpose of this work sky wave components arriving at the receiver with a differential delay greater than 700 μs will be referred to as *long delay sky waves*. Such sky waves are mitigated through the use of carefully designed phase codes, as discussed in this section.

Multiple Pulsing and eLoran Phase Codes

Consider one period (i.e. one PCI) of the full eLoran navigation signal as defined in Chapter 2. After downconversion in the receiver, the signal can be written as[9]

$$\begin{aligned} x(t) &= a(t;\tau,\theta) \star b(t;\mathcal{C},T_{\mathrm{GRI}}) \\ &= \sum_{m=0}^{7} \left[C_m a(t - mT_p;\tau,\theta) + C_{m+8} a\left(t - mT_p - T_{GRI};\tau,\theta\right) \right], \end{aligned} \tag{5.8}$$

where $a(\cdot)$ is the complex envelope of the eLoran pulse, and $C_m = \pm 1$ represents the Master or Secondary phase code values (Chapter 2). The phase coding takes the form of a carrier phase reversal in some of the pulses. The purpose of the coding will become clear later; however, it is immediately clear that before carrier phase estimation can be performed, the coding must be wiped off. As above, it is assumed that the receiver takes one sample per each received pulse and accumulates the samples in an integrator. The effect of the phase coding can then easily be reversed by multiplying the samples by the appropriate phase code values (note that $C_m^2 = 1, \forall m$). The process of sampling the incoming signal, phase-decoding and integrating the samples can be written as follows:

$$\begin{aligned} x_p(t) &= \int_{t-2T_{\mathrm{GRI}}}^{t} x(t') \cdot b\left(t' - \tau_{sp};\mathcal{C},T_{\mathrm{GRI}}\right) \mathrm{d}t' \\ &= \int_{t-2T_{\mathrm{GRI}}}^{t} x(t') \sum_{m'=0}^{7} \left[C_{m'} \delta\left(t' - m'T_p - \tau_{sp}\right) + \right. \\ &\left. + C_{m'+8} \delta\left(t' - m'T_p - T_{\mathrm{GRI}} - \tau_{sp}\right) \right] \mathrm{d}t'. \end{aligned} \tag{5.9}$$

Following the same reasoning as in the previous section, it can be shown that the operation described by Equation 5.9 above can be replaced by a moving average filter defined in the time domain by the following expression[10]:

$$x_p(t) = \frac{1}{16} \sum_{m'=0}^{7} \left[C_{m'} x\left(t - 2T_{\mathrm{GRI}} + m'T_p\right) + C_{m'+8} x\left(t - T_{\mathrm{GRI}} + m'T_p\right) \right]. \tag{5.10}$$

9 For definition of $b(t;\mathcal{C},T_{\mathrm{GRI}})$ see Chapter 2.

10 The $1/16$ factor was added for scaling purposes so that the pulse amplitude remains unchanged after the filtering.

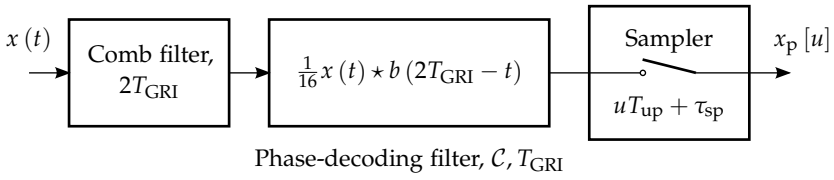

Figure 36: Position of the phase-decoding filter in the signal processing chain.

Alternatively, the filtering operation can be viewed as a correlation of the incoming signal with the phase-code function, $b(t; \mathcal{C}, T_{GRI})$, or as a convolution of the signal with a time-reversed copy of the phase-code function:

$$\begin{aligned} x_p(t) &= \frac{1}{16} \int_{-\infty}^{\infty} x(t' + t) \cdot b(t' + 2T_{GRI}; \mathcal{C}, T_{GRI}) \, dt' \\ &= \frac{1}{16} x(t) \star b(2T_{GRI} - t; \mathcal{C}, T_{GRI}). \end{aligned}$$

The latter form of the expression allows the frequency response of this signal processing block to be expressed as

$$H_p(f) = \frac{1}{16} S_b^*(f) \, e^{-j4\pi f T_{GRI}},$$

where $S_b(f)$ was calculated in Chapter 2.

The filter described by the above equations will be referred to throughout this work as the *phase decoding filter*. Figure 36 shows its position within the proposed signal processing model.

Sky Wave Rejection through Phase-Decoding

Consider now what happens if the phase decoding filter is fed with a combination of a ground wave and a long delay sky wave signal. For clarity, attention is again limited to a time-interval of length one PCI[11]. The complex envelope of the composite signal can then be written as

$$\begin{aligned} x(t) = & \underbrace{A_1 \sum_{m=0}^{7} \left[C_m a(t - mT_p; \tau_1, \theta_1) + C_{m+8} a(t - mT_p - T_{GRI}; \tau_1, \theta_1) \right]}_{\text{ground wave}} \\ & + \underbrace{A_2 \sum_{m=0}^{7} \left[C_m a(t - mT_p; \tau_2; \theta_2) + C_{m+8} a(t - mT_p - T_{GRI}; \tau_2; \theta_2) \right]}_{\text{sky wave}}, \end{aligned} \tag{5.11}$$

where τ_1 and θ_1 will be assumed equal to zero[12], and $\tau_2 = \tau_{diff} \geq 700 \cdot 10^{-6}$ (long-delay sky wave). In the following, it will be convenient

11 Note that the phase decoding filter always operates on an interval of length one PCI.

12 Recall that the time and carrier phase offsets are defined here relative to the (arbitrary set) receiver clock.

to express the sky wave delay τ_2 as a sum of an integer multiple of the pulse spacing T_p and a fractional part τ_2^f:

$$\tau_2 = lT_p + \tau_2^f, \quad l \in \mathbb{N}.$$

The integer part is calculated here as

$$l = \left\lfloor (\tau_2 + t_e) / T_p \right\rfloor,$$

where t_e is the eLoran pulse width; this implies that $\tau_2^f \in (-t_e, T_p - t_e >$.

Upon inserting $x(t)$ from Equation 5.11 into Equation 5.10 above and simplifying the expression by limiting attention to $t \in \langle 2T_{GRI}, 2T_{GRI} + T_p \rangle$, the output signal of the phase decoding filter can be expressed in the following form[13]:

$$\begin{aligned} x_p(t) &= A_1 a(t - 2T_{GRI}; 0, 0) \\ &+ \frac{A_2}{16} \Big(\underbrace{\sum_{m'=l}^{7} C_{m'} C_{m'-l}}_{R_{C_A}[l]} + \underbrace{\sum_{m'=l}^{7} C_{m'+8} C_{m'+8-l}}_{R_{C_B}[l]} \Big) \\ &\cdot a\left(t - 2T_{GRI}; \tau_2^f; \theta_2\right). \end{aligned} \tag{5.12}$$

It can be seen that the output signal is a combination of the wanted ground wave pulse and a scaled sky wave pulse. The scaling is given by the autocorrelation function of the GRI-A and GRI-B pulse groups, which was evaluated in Chapter 2.[14]It was shown in Chapter 2 that

$$R_{C_A}[l] + R_{C_B}[l] = \begin{cases} 16, & l = 0; \\ 0, & \text{otherwise.} \end{cases}$$

The above holds for both the Master and the Secondary phase code. The case when $l = 0$ corresponds to a short delay sky wave which is mitigated as described in Section 5.2.1. For $l > 0$ (i.e. for sky wave delay greater than $T_p - t_e$), however, any sky wave contamination is cancelled out due to the correlation properties of the phase codes, that is

$$x_p(t) = A_1 a(t - 2T_{GRI}; 0, 0), \quad t \in \langle 2T_{GRI}, 2T_{GRI} + T_p \rangle, \, l > 0.$$

Consider now the full form of the eLoran navigation signal as described by Equation 2.10. Since the signal is periodic in $2T_{GRI}$ and since the phase decoding filter is a Linear Time-Invariant (LTI) system, the output of the filter will also be periodic and since the impulse

13 In the derivation use was made of the fact that T_p and T_{GRI} are integer multiples of the eLoran carrier cycle and therefore shifting the pulses in time by T_p or T_{GRI} does not cause any carrier phase shift, i.e. $\exp(-j2\pi f_c q T_p) = 1$, $\exp(-j2\pi f_c q T_{GRI}) = 1$ for any $q \in \mathbb{Z}$.

14 Note that it was assumed above that the filter and the input signal utilised the same phase code. In the general case, the output signal would contain cross-correlation terms involving the filter\signal phase codes.

response of the filter is equal to zero for $t > 2T_{\mathrm{GRI}}$, the output signal for $t \in \langle 2n'T_{\mathrm{GRI}}, 2n'T_{\mathrm{GRI}} + T_{\mathrm{p}} \rangle$, $n' \in \mathbb{Z}$ can be written as follows:

$$x_{\mathrm{p}}(t) = \begin{cases} \sum_{n=-\infty}^{\infty} [A_1 a(t - 2nT_{GRI}; 0, 0) + \\ \quad A_2 a(t - 2nT_{GRI}; \tau_2; \theta_2)], & l = 0 \\ A_1 \sum_{n=-\infty}^{\infty} a(t - 2nT_{GRI}; 0, 0), & l > 0. \end{cases} \tag{5.13}$$

This section has focused on the primary function of the eLoran phase codes, i.e. the rejection of long delay sky waves. The codes are also used in station acquisition and identification. These receiver functions, however, are outside the scope of this work and will not be discussed here.

5.2.3 *Early Sky Wave Rejection*

Sky waves with a differential delay of less than 35 μs will be referred to here as *early sky waves*. Early sky waves are very rare, but can cause severe measurement errors.

Unfortunately, the eLoran navigation signal has no early sky wave rejection capability. However, in a fully-implemented eLoran system, the occurrence of early sky wave conditions is detected by integrity monitoring stations operating throughout the coverage area, and timely warnings are provided to users, e.g. through the Loran Data Channel [5]. Hardening of eLoran receivers through the use of Receiver Autonomous Integrity Monitoring (RAIM) algorithms exploiting redundant measurements can also help reduce the risks associated with this rare phenomenon.

5.3 CRI MITIGATION

As shown in Section 5.2, an eLoran receiver selects signals of a particular rate by performing a comb filtering operation on the received signal. There are, however, several reasons why the comb filtering never provides perfect rejection of cross-rating signals, as discussed below.

The comb filter works by accentuating frequency components of the received signal at integer multiples of $1/2T_{\mathrm{GRI}}$ (i.e. those of the signal of interest), while attenuating others. Since the filtering is performed on a finite observation interval T_{i} (typically 5 s), the filter actually accentuates a range of frequencies approximately $1/2T_{\mathrm{i}}$ (i.e. typically 0.1 Hz) around each of the spectral lines (see Figure 35). Frequency components of a cross-rating signal that appear close to the spectral lines of the signal of interest then may not be sufficiently suppressed.

Further, any two rates share spectral lines at integer multiples of the reciprocal of the greatest common divisor of the two PCIs. In theory, the common lines could be suppressed through the use of balanced phase codes[15] and appropriate GRI selection. However, the primary consideration in the design of Loran phase codes was the sky wave rejection capability discussed above, and this resulted in the use of unbalanced phase codes. Therefore, with the current system configuration it is impossible to completely suppress a cross-rating signal through phase decoding and comb filtering alone.

15 i.e. phase codes that contain the same number of positive and negative code values

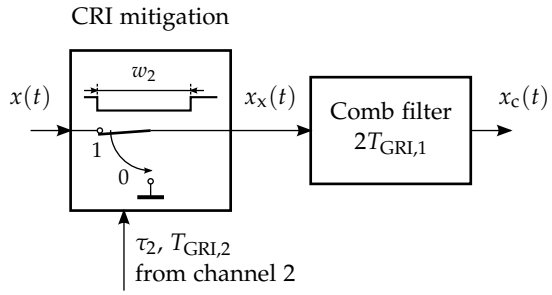

Figure 37: CRI mitigation by blanking.

The measurement error due to CRI is a complicated function of the GRIs, signal time and phase offsets, amplitudes, integration time and other signal and receiver parameters. A rigorous quantification of the effects of CRI will be presented in Chapter 7. It will be shown that in order to meet the stringent eLoran accuracy performance standards, additional forms of CRI mitigation are needed. The Loran literature describes several CRI mitigation techniques [29]. The rest of this section presents two of these techniques, considered as the most common ones.

5.3.1 *Detect-and-Drop Algorithms (CRI Blanking)*

One of the simplest yet effective ways of mitigating CRI is the detection and censoring of the pulses likely corrupted by the interference. This is also referred to in the literature as *CRI blanking*. Two methods are known which can be used to detect the corrupted pulses [105]. The first method compares each received pulse against a reference shape obtained by averaging of the received (phase-decoded) pulse waveforms. The second method assumes that the receiver is processing signals from both cross-rating stations, which makes it possible to predict the time when the pulses from different rates overlap based on the known timing relations between the signals.

Figure 37 shows a signal processing model for CRI blanking adopted in this study. The block works by simply substituting zeros for the input signal when a cross-rating pulse group arrives. The model assumes that the position of the cross-rating pulses is known by the receiver, which is a reasonable assumption for an all-in-view eLoran receiver.

By discarding all eLoran pulses that overlap, it is possible to completely suppress the interference; however, the price paid is a (sometimes excessive) loss of useful signal energy which in turn leads to poorer performance in noise. The impact of CRI blanking on the ranging performance of eLoran receivers will be analysed in Chapter 7.

5.3.2 *Estimate and Subtract Algorithms (CRI Cancelling)*

Estimate and subtract algorithms may provide a viable alternative in situations where CRI blanking leads to an excessive loss of signal energy. These algorithms are also referred to in the Loran literature as *CRI cancelling*. Some authors distinguish between time-domain and frequency-domain cancelling, or CRI filtering [29, 105]. Although the specifics of the implementation may vary between different receiver

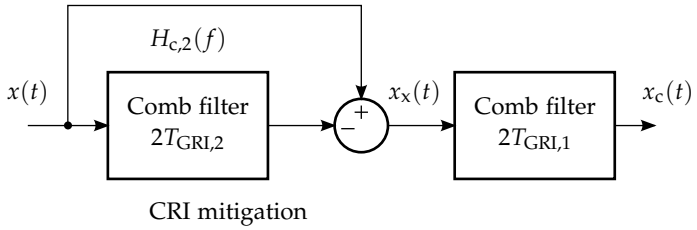

Figure 38: CRI cancelling as implemented by Peterson [28].

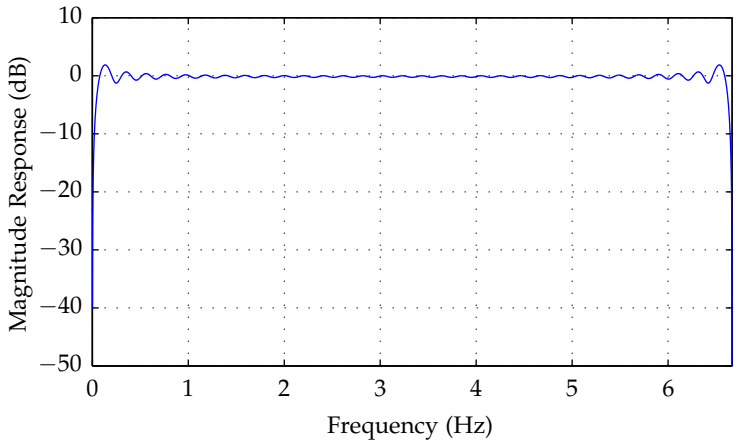

Figure 39: Magnitude response of the CRI filter.

models, the underlying principle is the same - the receiver reconstructs a replica waveform of the interference and subtracts it from the composite received signal, effectively cancelling the interference while leaving the useful signal (largely) intact.

The signal processing model for CRI cancelling used in this study is based on a receiver implementation by Peterson [28] and is shown in Figure 38. The model uses a comb filter to generate a replica of all signals from a given GRI, which is then subtracted from the input signal in order to eliminate the interference. This structure will be referred to here as the *CRI filter*. Referring back to Equation 5.7, the frequency response of the CRI filter can be expressed as

$$H_x(f) = 1 - H_{c,2}(f).$$

Figure 39 shows a close-up of the magnitude response $|H_x(f)|$ of the filter. As expected, the filter produces notches at integer multiples of the reciprocal of the PCI of the cross-rating signal that is to be suppressed. If there are several cross-rating signals, multiple CRI filters can be cascaded.

Clearly, the effectiveness of CRI cancelling depends on the accuracy of the replica signals. In practice, there are a number of reasons why the cancellation is never perfect. First, the replicas are obtained by averaging of the received, noisy, signals and are therefore contaminated by some residual noise and interference. Pulse-to-pulse timing and amplitude stability of the eLoran signals is another important factor (see Chapter 3). Since the cancelling algorithm works with averaged waveforms, the pulse-to-pulse fluctuations in the cross-rating signal

cannot be reproduced, and consequently the effectiveness of the algorithm is reduced. Further complications may arise when the cross-rating signal is data modulated. In that case, the digital information has to be recovered and re-modulated onto the replica signal (data channel considerations are, however, out of the scope of this analysis). A quantitative analysis of the effectiveness of CRI cancelling will be presented in Chapter 7.

5.4 INPUT FILTERING

The last signal processing block examined in this chapter is the input bandpass filter. This filter is required in order to suppress out-of-band interference and limit the bandwidth of the noise entering the receiver. Unfortunately, the filter also affects the pulse shape, which has implications for the selection of an optimal sampling point and the achievable Sky wave-to-Ground wave Ratio (SGR) and SNR. It is therefore important to consider the characteristics of the input filter and its impact on the received waveforms.

5.4.1 *Standard Input Bandpass Filter*

Filter Definition

The input filter designs used by different receiver manufacturers may vary slightly. This analysis assumes an 8th order Butterworth filter with a $-3\,\mathrm{dB}$ bandwidth of $28\,\mathrm{kHz}$ and the passband centred at $100\,\mathrm{kHz}$. This appears to be a commonly accepted standard for modern eLoran receivers [125]. It is noted that the passband of this filter is wider than the protected Loran band. A wider bandwidth was chosen in order to minimise the distortion of the received pulses. This, however, means that some out-of-band interference can leak through the filter. It will be assumed here that any inter-system interference that falls within the passband of the filter is suppressed by adaptive notch filters (see Chapter 4).

Transfer Function

The properties of an Linear Time Invariant (LTI) filter are conveniently described by its transfer function, $\widetilde{H}_{\mathcal{L}}(p)$. Finding the transfer function for one of the standard classes of filters is a well-established process in filter design theory. Some aspects of filter design are discussed in Appendix B, which considers three different forms of the transfer function: rational polynomial, zero-pole-gain, and the residue form. Each of these forms will be useful at a different stage of this study.

Frequency Response

The frequency response of the input bandpass filter, $\widetilde{H}_{\mathrm{b}}(f)$, can be calculated from its transfer function, $\widetilde{H}_{\mathrm{b},\mathcal{L}}(p)$, as described in Appendix B. Figure 40 shows the magnitude response, $|\widetilde{H}_{\mathrm{b}}(f)|$, and phase response, $\angle\widetilde{H}_{\mathrm{b}}(f)$, of the filter, and Figure 41 plots its group and phase delay. It can be seen from Figure 40 that the phase response is significantly non-linear in the Loran band and therefore some distortion of the pulse waveforms can be expected. The impact of the filtering on the pulse shape is investigated in detail in Section 5.4.3.

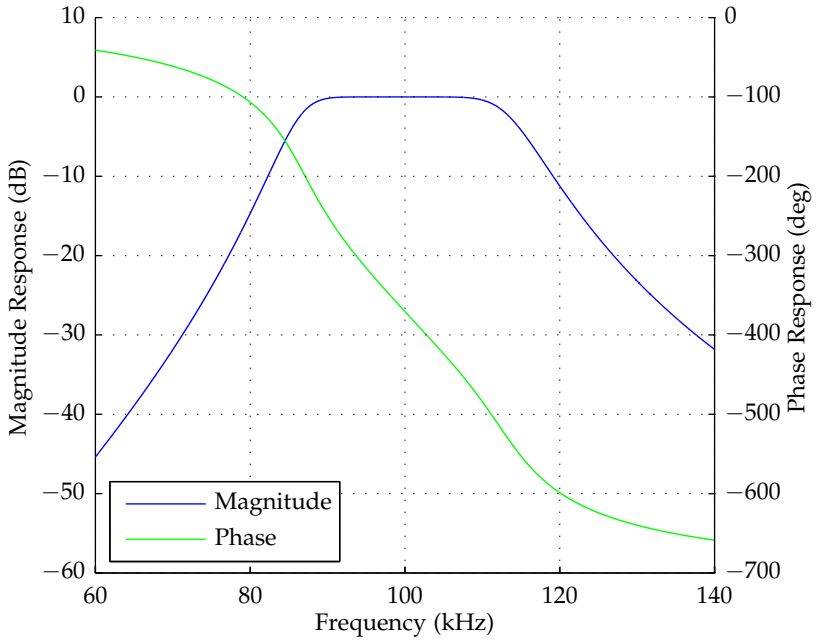

Figure 40: Frequency response of the standard input bandpass filter.

It is also noted that the phase response indicates a non-zero phase shift at the carrier frequency, $\angle\widetilde{H}_{\mathrm{b}}(f_{\mathrm{c}}) = \theta_{\mathrm{b}} \approx -10.5°$. The same phase shift is applied to the received signal from all eLoran stations, and as such it does not affect the position estimate. However, since the performance analysis presented later in this work also aims to assess biases in carrier phase measurements caused by CRI, it is necessary to compensate for θ_{b}. This can be done as shown in Section 5.5.

Noise Bandwidth

The concept of noise bandwidth is introduced in Appendix A. Applying Equation A.11 to the frequency response of the standard bandpass filter gives a noise bandwidth of

$$B_{\mathrm{b,n}} \doteq 28.733\,\mathrm{kHz}.$$

The noise bandwidth of the input bandpass filter will be of importance mainly when evaluating receiver performance through simulations.

5.4.2 *Characteristics of the Filtered Signal*

Autocorrelation Function of a Band-Limited WGN Process

The noise at the receiver input is modelled in this work as a WGN process. After filtering by the input bandpass filter the noise is no longer uncorrelated over time. Since the time of correlation is an important factor in the receiver performance analysis, it will be worthwhile to examine the ACF of the filtered noise.

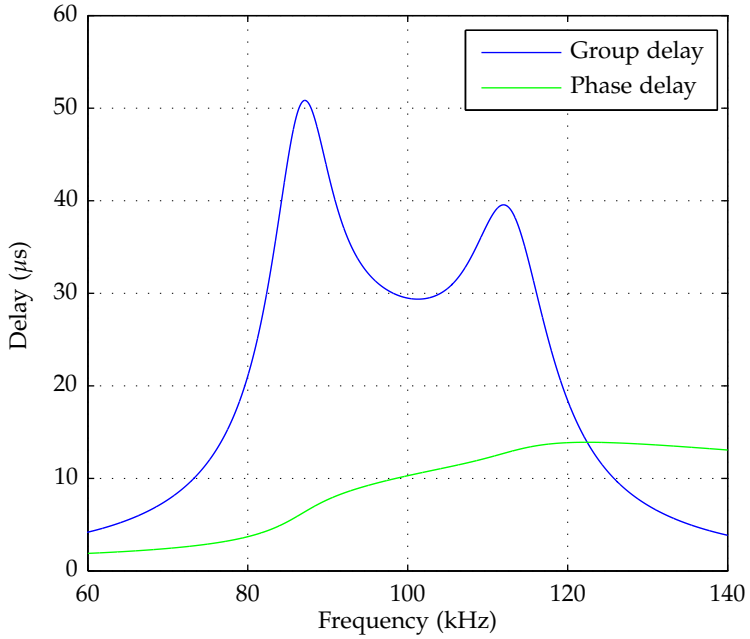

Figure 41: Group and phase delay of the standard input bandpass filter.

The ensemble averaged ACF of the noise at the output of the standard bandpass filter, $R^{\mathrm{e}}_{\widetilde{w}_{\mathrm{b}}}(\tau)$, is easily obtained from its PSD, $D^{\mathrm{e}}_{\widetilde{w}_{\mathrm{b}}}(f)$, as follows:

$$R^{\mathrm{e}}_{\widetilde{w}_{\mathrm{b}}}(\tau) = \mathcal{F}^{-1}_{f,\tau}\left\{D^{\mathrm{e}}_{\widetilde{w}_{\mathrm{b}}}(f)\right\} = \frac{N_0}{2}\mathcal{F}^{-1}_{f,\tau}\left\{\left|\widetilde{H}_{\mathrm{b}}(f)\right|^2\right\},$$

where $N_0/2$ is the double-sided PSD of the white noise at the input of the filter. If the filter's magnitude response is approximated by an ideal brick-wall characteristics the ACF of the filtered noise takes on the following form[16]:

$$R^{\mathrm{e}}_{\widetilde{w}}(\tau) = N_0 B_{\mathrm{b,n}} \mathrm{sinc}\left(B_{\mathrm{b,n}}\tau\right)\cos\left(2\pi f_0 \tau\right).$$

Similarly, the ACF of the real and imaginary part of the complex envelope of the filtered noise, $R^{\mathrm{e}}_{w_{\mathcal{I}}}(\tau)$ and $R^{\mathrm{e}}_{w_{\mathcal{Q}}}(\tau)$, respectively, can be shown to be given by

$$R^{\mathrm{e}}_{w_{\mathcal{I}}}(\tau) = R^{\mathrm{e}}_{w_{\mathcal{Q}}}(\tau) = N_0 B_{\mathrm{b,n}} \mathrm{sinc}\left(B_{\mathrm{b,n}}\tau\right).$$

The ACFs are plotted in Figure 42; from the figure it can be seen that while the filtered noise is strongly correlated on time-scales of tens of microseconds, values spaced 1 ms apart (the separation between two pulses in a group) are practically uncorrelated. This supports the earlier assumption that an eLoran receiver utilises in the phase estimation process only a *single sample per each received pulse*. Taking more samples on the pulse leading edge would be of little benefit, as the noise in these samples would be strongly correlated. If the receiver takes one sample per pulse, the noise can safely be considered *uncorrelated from sample to sample*.

16 For definition of the sinc (.) function see Appendix A.

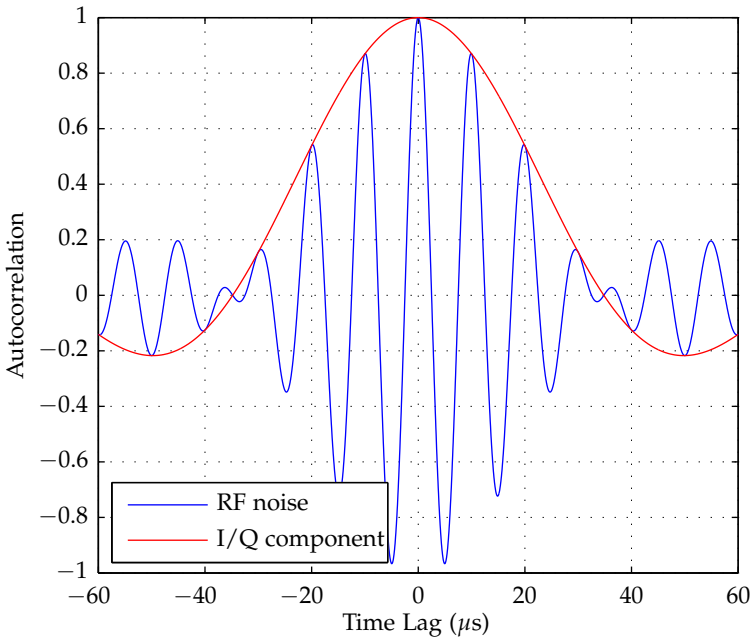

Figure 42: Autocorrelation function of noise after filtering by the standard bandpass filter (blue) and after conversion to baseband.

Pulse Envelope Distortion Due to Bandpass Filtering

Unfortunately, the input filtering also affects the useful eLoran signal. The pulse leading edge becomes less steep and the pulses are stretched in time. Envelope distortion caused by the filtering has important implications for optimal sampling point selection (see Section 5.4.3), which in turn affects the achievable performance of the receiver. The aim of this section is to find the shape of the filtered pulse envelope so that the impact of the filtering on the performance can be precisely quantified. The approach is to first find the frequency response of a lowpass filter equivalent, $H_{\mathrm{b}}(f)$, of the standard bandpass filter (see Appendix A), and then apply this filter to the complex envelope of the ideal pulse, $a(t;\tau,\theta)$.

As shown in Appendix B, the transfer function of the standard input bandpass filter can be expressed in the residue form as

$$\widetilde{H}_{\mathrm{b},\mathcal{L}}(p) = \sum_{i=1}^{8} \frac{r_i}{p - p_i}.$$

The values of the r_i coefficients and the filter poles, p_i, are listed in Appendix B. Since the filter is stable, the frequency response of the filter, $\widetilde{H}_{\mathrm{b}}(f)$, can be obtained by substituting $p = \mathrm{j}2\pi f$ in the transfer function, i.e. $\widetilde{H}_{\mathrm{b}}(f) = \widetilde{H}_{\mathrm{b},\mathcal{L}}(\mathrm{j}2\pi f)$. The frequency response of the equivalent lowpass filter, $H_{\mathrm{b}}(f)$, is then obtained as

$$H_{\mathrm{b}}(f) = \widetilde{H}_{\mathrm{b}}(f + f_c) = \sum_{i=1}^{8} \frac{r_i}{\mathrm{j}2\pi(f - f_c) - p_i},$$

where f_c is the Loran carrier frequency.

The complex envelope of the eLoran pulse, $a(t;\tau,\theta)$, is given by Equation 2.10. For the purpose of this derivation it can be assumed that $\tau = \theta = 0$, in which case

$$a(t;\tau,\theta) = e(t),$$

where $e(t)$ is the "real" envelope of the pulse, as described by Equation 2.1. The spectrum of this waveform, $S_e(f)$, was calculated earlier in Chapter 2 and is given by Equation 2.7. The spectrum of the filtered complex envelope can then be calculated as

$$S_{e_b}(f) = H_b(f)\, S_e(f).$$

$S_{e_b}(f)$ can be resolved into partial fractions and these can easily be transformed back into the time domain. The complex envelope of the filtered pulse can then be expressed in the following form:

$$\begin{aligned} e_b(t) = \left(\frac{e}{t_p}\right)^2 \sum_{i=1}^{8} \{ & A_i \exp\left[(p_i - j2\pi f_c)\, t\right] \\ & + \left(B_i + C_i t + \frac{D_i t^2}{2}\right) \exp\left(-\frac{2t}{t_p}\right) \Big\}\, u(t), \end{aligned} \tag{5.14}$$

in which

$$A_i = \frac{2r_i}{\left(p_i - j2\pi f_c + \frac{2}{t_p}\right)^3},$$

$$B_i = -A_i,$$

$$C_i = \frac{-2r_i}{\left(p_i - j2\pi f_c + \frac{2}{t_p}\right)^2},$$

$$D_i = \frac{-2r_i}{p_i - j2\pi f_c + \frac{2}{t_p}},$$

and $u(t)$ is the unit step function defined in Appendix A. Note that the input filter has to be stable for the above expressions to hold, i.e. it was assumed that $\mathrm{Re}[p_i] < 0$, $i = 1, 2, \ldots, 8$. Finally, the real envelope of the filtered pulse is calculated as $|e_b(t)|$. This function is plotted in Figure 43 together with the ideal pulse shape as defined in the signal specification.

5.4.3 *Position of the Sampling Point*

According to the proposed signal processing model, the received signal (after downconversion and the necessary filtering) is sampled at time instants given by $t_u = uT_{up} + \tau_{sp}$, where $u \in \mathbb{Z}$, T_{up} is the update interval (assumed to be an integer multiple of $2T_{GRI}$), and $\tau_{sp} \in \langle 0, 2T_{GRI}\rangle$ is the sampling offset relative to the start of a PCI. The *time into pulse* at which the samples are taken, τ_p, is defined by

$$\tau_p = \mathrm{mod}\left(\tau_{sp} - \tau, 2T_{GRI}\right),$$

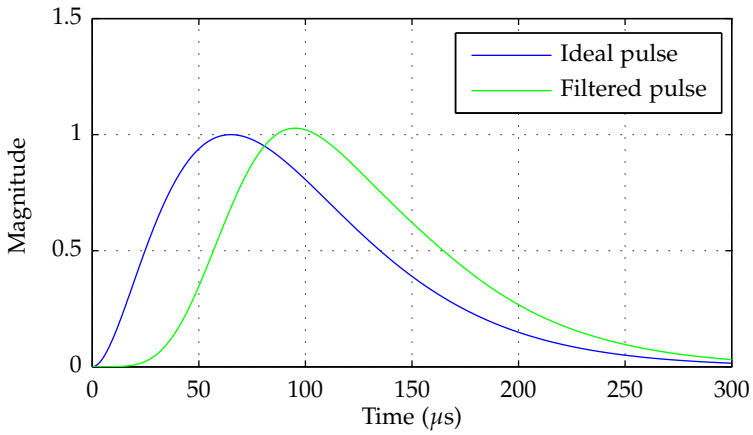

Figure 43: Ideal eLoran pulse envelope compared with the envelope of a filtered pulse.

where τ is the time offset of the signal of interest. The value of τ_p is the receiver designer's choice and it is the aim of this section to find an optimal value for this parameter.

All signal timing measurements in an eLoran receiver must be made with respect to a common reference point within the pulse. It is usually (and rather vaguely) stated in the Loran literature that the received pulses are "tracked [at the zero crossing] around the 30 μs point"[17] [126, 30]. The "30 μs point" of an undistorted pulse can easily be found by matching its shape to that of the ideal pulse defined in the signal specification (see also HCPR below). However, as shown above, the received pulses get considerably distorted during receiver input filtering and, consequently, it is not entirely clear how the reference point should be chosen and where in the filtered pulse should the samples be taken. Unfortunately, receiver manufacturers do not generally disclose information of this kind. The rest of this section discusses this problem from three different points of view in an attempt to justify the choices made by the candidate.

Half-Cycle Peak Ratio and Signal Time Offset Estimation

The usual method of identifying a reference point within the eLoran pulse makes use of a metric called *Half-Cycle Peak Ratio* (HCPR). HCPR is defined in reference [30] as follows:

$$\text{hcpr}\{x(t)\} = \frac{|x(t + 2.5 \cdot 10^{-6})|}{|x(t - 2.5 \cdot 10^{-6})|},$$

where $|x(\cdot)|$ denotes the signal envelope and t is time in seconds[18]. At each epoch u, the receiver can adjust the sampling point offset τ_{sp}

17 This does not necessarily mean that the signal samples must be taken at this particular point in the pulse. The carrier phase can be measured at any (sky wave free) part of the received pulse.

18 HCPR defined in this way in fact is a misnomer as the spacing between adjacent peaks of the RF waveform varies slightly throughout the pulse due to the shape of the pulse envelope.

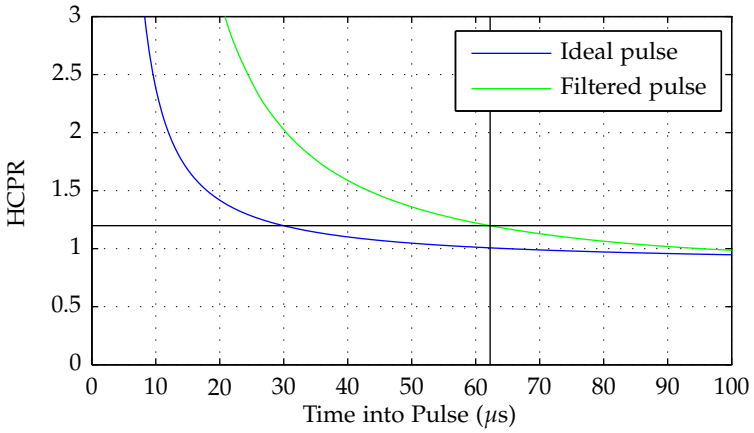

Figure 44: HCPR for the ideal pulse and a pulse filtered by the standard input filter.

so that the HCPR at the sampling point matches a pre-defined target value, h_{tgt}:

$$\text{hcpr}\left\{x\left(uT_{\text{up}} + \tau_{\text{sp}}\left[u\right]\right)\right\} = h_{\text{tgt}},$$

where h_{tgt} is a function of τ_{p} and the shape of the filtered pulse. This assures that signal samples are consistently taken at approximately the same point within the pulse. From $\tau_{\text{sp}}\left[u\right]$, the receiver can also easily estimate the signal time offset:

$$\hat{\tau}\left[u\right] = \text{mod}\left(\tau_{\text{sp}}\left[u\right] - \tau_{\text{p}}, 2T_{\text{GRI}}\right).$$

As mentioned above, when defining the target HCPR value, h_{tgt}, any distortion of the pulse caused by the receiver antenna, input circuitry and filtering must be taken into account. Since the antenna and receiver front end can be designed in such a way that they have a negligible impact on the pulse shape, the focus here will be on the input bandpass filter.

Figure 44 plots the HCPR for the ideal pulse ($\text{hcpr}\left\{e\left(t\right)\right\}$) and a pulse filtered by the standard input bandpass filter ($\text{hcpr}\left\{e_{\text{b}}\left(t\right)\right\}$). It can be seen from the figure that the HCPR at 30 μs into the ideal pulse (the usually quoted tracking point) is approximately 1.198. The same value of HCPR is observed at approximately 62 μs into the filtered pulse. This means that the receiver may need to sample the pulses significantly later than expected.

Filtering Loss

As shown above, after filtering by the standard input filter the leading edge of the pulse becomes less steep, with the peak being reached at around 95 μs after the start of the pulse. The signal amplitude 30 μs into the filtered pulse is considerably lower than the amplitude at the 30 μs point on the ideal pulse. This is illustrated in Figure 45 which shows the signal loss throughout the filtered pulse relative to the signal level 30 μs into the ideal pulse. Again, it is seen that sampling the ideal pulse at the 30 μs point is equivalent to sampling approximately 62 μs into the filtered pulse (where the filtering loss approaches 0 dB). The

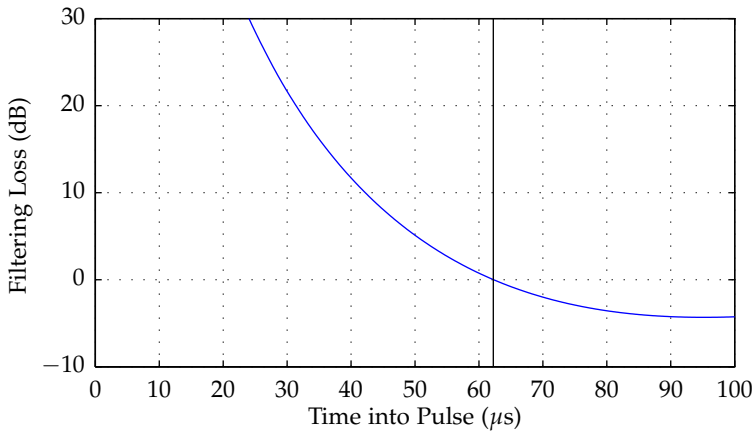

Figure 45: Filtering loss for the standard input bandpass filter as a function of time into pulse.

following section investigates the consequences that sampling later in the pulse has in terms of sky wave interference.

Worst-Case Error due to Own Sky Wave Interference

The draft Minimum Performance Standards for Marine eLoran Receiving Equipment (MPS) [123] require that

> '... The receiver shall acquire and track, in the presence of sky wave interference with delays from 37.5 μsec and greater. The acquisition and tracking must occur with sky wave signals having signal levels (SGR) of up to 12 dB to 26 dB relative to the desired signal for sky wave delays of 37.5 and 60 μsec, respectively. For sky waves with values of delay between 37.5 and 60 μsec, the maximum relative sky wave level is linearly interpolated from the values at 37.5 and 60 μsec. For delays greater than 60 μsec, 26 dB is specified. This tracking shall be achieved without any change in the overall performance from the case where no sky wave exists. ...'.

If the incoming signal was passed through the input stages of the receiver undistorted, the above requirements would easily be met by sampling the pulses at the 30 μs point. However, input filtering in a practical receiver stretches the pulses in time, makes the leading edge of the pulses less steep and therefore makes it necessary to move the sampling point further into the pulse. This is illustrated in Figure 46. Hence, the question arises of how the input filtering affects the sky wave rejection capability of the signal and whether the above requirements can be met in practice. In the following the maximum carrier phase estimation error due to own sky wave interference will be derived.

Consider the output signal of the phase decoding filter as described by Equation 5.13 and assume, as above, that $\tau_1 = \theta_1 = 0$; assume further that $\tau_2 = \tau_1 + \tau_{\text{diff}} = \tau_{\text{diff}} < 700 \cdot 10^{-6}$ (short delay sky wave, $l = 0$), and that $\theta_2 = \theta_w$, i.e. the sky wave will be assumed to have the worst-case phase offset that maximises the phase measurement error, as depicted in Figure 47; finally assume that the signal is sampled at

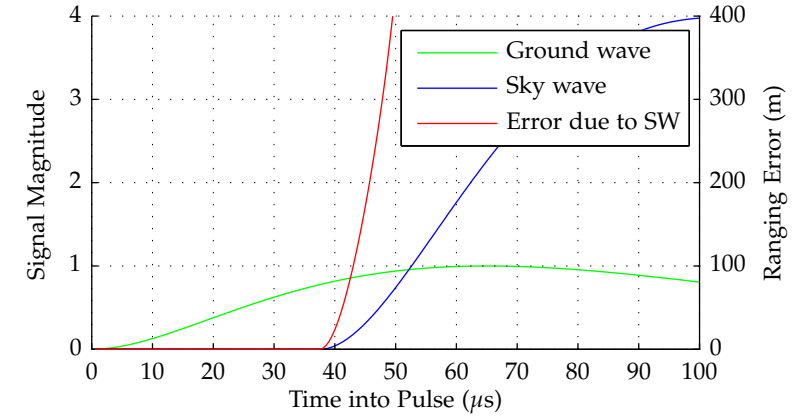

(a) Ideal pulse shape.

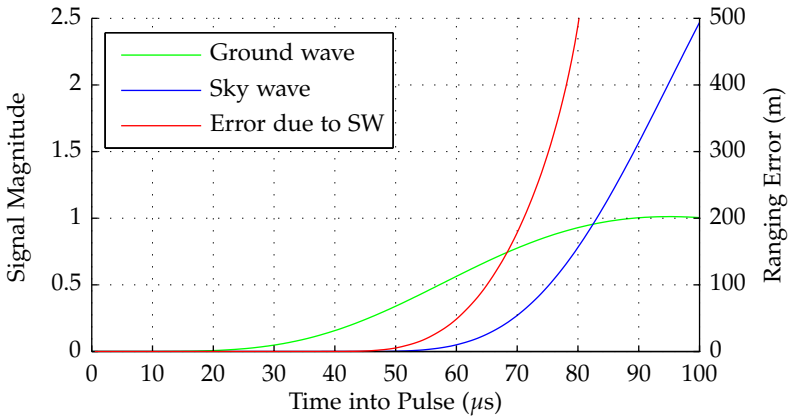

(b) Filtered pulse.

Figure 46: Envelope of a ground wave and worst-case expected sky wave pulse according to the MPS.

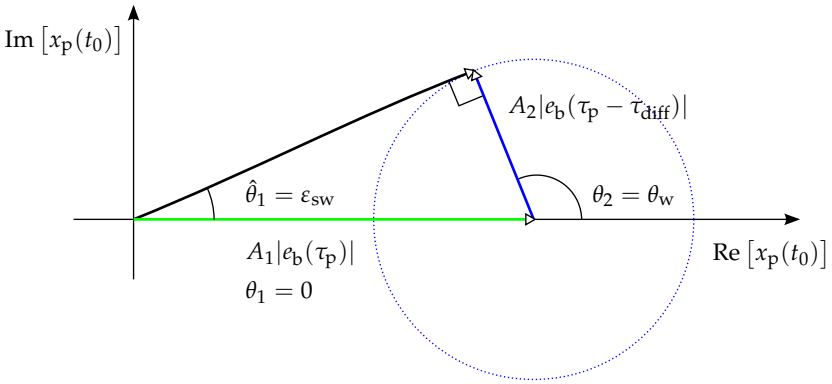

Figure 47: Vector representation of the ground wave and sky wave components of the complex signal (worst-case sky wave carrier phase offset assumed).

time instant $t_0 = \tau_{sp} = \tau_1 + \tau_p = \tau_p$. The signal at the output of the phase decoding filter can then be written as

$$\begin{aligned} x_p(t_0) &= A_1 a(\tau_p; 0; 0) + A_2 a(\tau_p; \tau_{diff}; \theta_w) \\ &= \underbrace{A_1 e(\tau_p)}_{\text{useful signal}} + \underbrace{A_2 e(\tau_p - \tau_{diff}) \cdot e^{j\theta_w}}_{\text{sky wave interference}}. \end{aligned}$$

As can be seen from Figure 47. the worst-case carrier phase measurement error due to the sky wave interference, $\varepsilon_{sw} = \hat{\theta}_1 - \theta_1 = \hat{\theta}_1$, can easily be expressed as

$$\begin{aligned} \varepsilon_{sw} &= \arcsin \frac{A_2 e(\tau_p - \tau_{diff})}{A_1 e(\tau_p)} \\ &= \arcsin \left[\sqrt{SGR} \frac{e(\tau_p - \tau_{diff})}{e(\tau_p)} \right], \end{aligned} \tag{5.15}$$

where $SGR = A_2^2/A_1^2$ is the sky wave to ground wave ratio. Equation 5.15 holds for the ideal pulse shape. The effect of the input bandpass filtering can be taken into account by substituting $|e_b(\cdot)|$ (Equation 5.14) for $e(\cdot)$ in the above equation. The phase measurement error directly translates into a pseudorange measurement error, as given by the following expression (see Equation 5.16 and Equation 5.17 below):

$$\varepsilon_{sw}^{pr} = -\frac{c}{2\pi f_c} \varepsilon_{sw}.$$

Figure 46 above plots the worst-case range error, ε_{sw}^{pr}, for SGR = 12 dB and sky wave delay $\tau_{diff} = 37.5\,\mu s$ (see the MPS requirements) as a function of the position of the sampling point, τ_p. Results for both the ideal and filtered pulse waveforms are shown. It can be seen from the figure that the worst-case measurement error can be substantial. The receiver can mitigate the sky wave interference in two ways.

First, as discussed earlier, the receiver can use only the early, sky wave free, part of the pulse. In a practical receiver, however, this results in a substantial loss of useful signal energy (see Figure 45 above).

Alternatively, the receiver can estimate and subtract the sky wave waveform from the composite received signal. In this case, the carrier phase measurements can be performed at a later point in the pulse, providing a higer SNR. The sampling point position, τ_p, can also be adjusted adaptively as the sky wave conditions change. Various techniques for sky wave estimation are described in the following references [30, 127, 128, 129].

Optimal Sampling Point Position

It should be clear from the discussion above that the optimal choice of the sampling point position is a trade-off between SNR and SGR. Table 8a shows the useful signal amplitude (relative to pulse peak) and worst-case range measurement error due to sky wave interference for a signal sample taken 30 μs into the ideal pulse. The table also shows the value of HCPR that can be used to identify the sampling point. Table 8b then lists the same parameters for three sampling point positions within the filtered pulse. As mentioned above, there is very little ground wave energy at 30 μs into the filtered pulse; the signal will clearly have to be sampled further into the pulse. The furthest point that guarantees error-free measurement under the worst-case sky wave conditions expected is at 37.5 μs. However, as can be seen from Table 8b, useful signal amplitude at that point is still very low. The last option considered in Table 8b assumes sampling at 62.25 μs into the pulse. This value was chosen because the HCPR and signal level at this point are the same as for the 30 μs point on the ideal pulse (this also corresponds with the fact that the group delay of the input bandpass filter in the passband is in the region of 30 μs to 40 μs). The ranging error due to sky wave interference for this sampling point, however, can reach up to 69 m.

In the following it will be assumed that the receiver samples the signal 62.25 μs into the pulse, i.e. $\tau_p = 62.25 \cdot 10^{-6}$, which is equivalent to sampling at the 30 μs point on the ideal pulse. It will further be assumed that short-delay own sky wave interference is estimated and cancelled out using one of the methods referenced above.

It should be noted that correct phase relations within the pulse are only guaranteed by the signal specification in the vicinity of the SZC, which is defined on the transmitter current waveform (see Chapter 2). The measurements should therefore take place at a point in the processed pulse that is equivalent to the SZC on the transmitter pulse.

5.5 DEVELOPING THE SIGNAL PROCESSING MODEL

Figure 48 shows a signal processing model for a single channel of an eLoran receiver. The input RF signal, $\tilde{x}(t)$, is modelled by Equation 3.10 presented in Chapter 3. The first block in the proposed model is the *standard input bandpass filter*, whose characteristics have been thoroughly discussed above.

The bandpass filtered RF signal, $\tilde{x}_b(t)$, is converted to baseband in the *frequency down-converter*. At the output of the down-converter is the complex envelope, $x_b(t)$, of the filtered signal.

TIME INTO PULSE (μS)	HCPR	AMPLITUDE (REL. TO PEAK)	RANGE ERROR SKY WAVE (m)
30.00	1.198	0.6253	0

(a) Ideal pulse

TIME INTO PULSE (μS)	HCPR	AMPLITUDE (REL. TO PEAK)	RANGE ERROR SKY WAVE (m)
30.00	2.025	0.05177	0
37.50	1.669	0.1275	0
62.25	1.198	0.6242	68.73

(b) Filtered pulse.

Table 8: Selected pulse characteristics and ranging error due to sky wave; the error is the maximum error experienced under the worst case sky wave conditions expected (see MPS [123]).

The receiver then needs to select signals of a particular rate (GRI) and suppress those of other rates that may also be present. This can be achieved by averaging over the repetition interval of the station of interest, $2T_{\mathrm{GRI},m}$, in the *comb filter*. To further reduce the effects of CRI, eLoran receivers employ special *CRI mitigation* algorithms. These algorithms are represented in the proposed model by an additional signal processing block inserted between the downconverter and the main comb filter[19]. This study deals with two CRI mitigation methods, commonly referred to as CRI blanking and CRI cancelling. Signal processing models for both can be found in Section 5.3.

The next block is the *phase decoding filter*, which allows the receiver to identify individual signals within a chain and helps suppress long delay sky waves and some other forms of interference. The combination of the phase-decoding filter and the comb filter effectively performs *coherent integration* of pulses received within an integration interval T_{i} (typically around 5 s).

To avoid own interference from short-delay sky waves, eLoran receivers use for absolute positioning only the early portion of the received pulses. In the proposed signal processing model, this is achieved by *sampling* the averaged signal at the output of the phase-decoding filter, $x_{\mathrm{p}}(t)$, at time instants defined by $t_u = uT_{\mathrm{up}} + \tau_{\mathrm{sp}}$, where $u \in \mathbb{Z}$, $T_{\mathrm{up}} \leq T_{\mathrm{i}}$ is an update interval (typically around 1 s), and τ_{sp} is a carefully chosen sampling point offset. At the output of the sampler is a discrete-time signal, here denoted as $x_{\mathrm{p}}[u] = x_{\mathrm{p}}(t_u)$.

The next block in the model compensates for the phase shift θ_{b} introduced by the input bandpass filter by performing a *phase rotation* of the complex samples. The final block is the *phase detector*, which transforms the pulse samples into carrier phase estimates, $\hat{\theta}_{m,1}[u]$.

19 Note that the CRI mitigation must take place before the signal is processed by the comb filter.

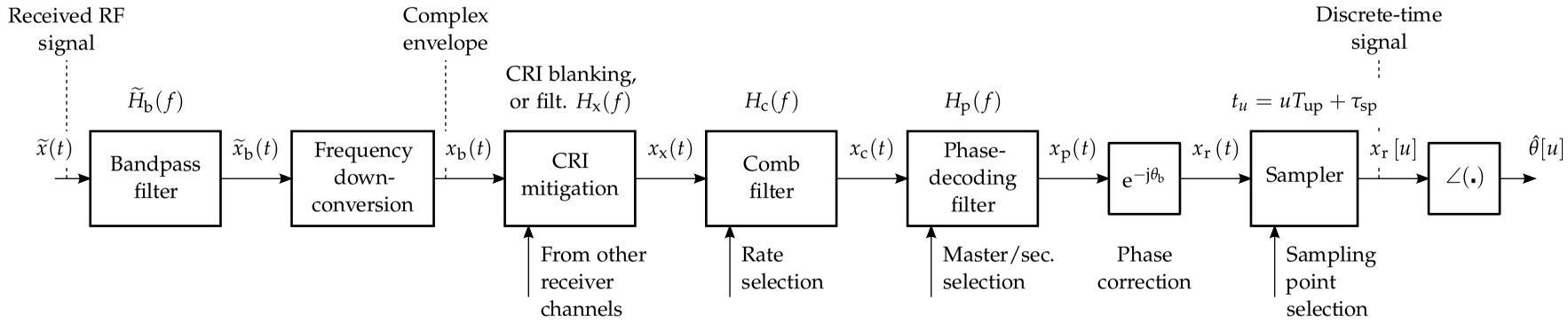

Figure 48: Signal processing model for a single channel of an eLoran receiver.

5.6 SIGNAL TIME OF ARRIVAL AND PSEUDORANGE CALCULATION

At each epoch u, the receiver estimates the signal time offset, $\hat{\tau}_m[u]$, and carrier phase, $\hat{\theta}_m[u]$, for each station in view, $m = 1, 2, \ldots, N_{\text{st}}$, as described in Section 5.4.3 and Section 5.5. Based on these measurements the receiver then calculates the accurate time of arrival of each signal with respect to the receiver clock.

Unfortunately, the author has struggled to find a satisfactory definition of signal time of arrival in the Loran literature. Loran-C related documents and standards generally do not define time of arrival, as Loran-C was a time-difference (hyperbolic) system. The draft MPS for Marine eLoran Receiving Equipment [123] gives the following definition:

> "The time of arrival of the pulse group from a transmitting station is the time of occurrence of the electric field of the standard zero crossing of the 1st pulse, in a pulse group at the receiving antenna, with respect to the local receiver clock."

This definition seems rather ambiguous as the standard zero crossing is defined on the transmitter antenna current and not on the far-field waveform (see Chapter 2 and recall the transmitter current to far-field transformation). The author interpreted the definition as follows:

> "The time of arrival of the pulse group from a transmitting station is the time of occurrence of the electric field of the positive zero crossing closesest to the 30 μs point on the envelope of the 1st pulse, in a pulse group at the receiving antenna, with respect to the local receiver clock."

Note that due to the transformation between transmitter current and far E-field, the zero crossing referred to in the above definition occurs 27.5 μs after the start of the pulse (assuming undistorted waveform). Bearing this in mind, the TOA can be calculated from the observations as given below:

$$\hat{t}_{\text{a},m}[u] = \text{mod}\left(\frac{I+F}{f_{\text{c}}} + 27.5 \cdot 10^{-6}, 2T_{\text{GRI},m}\right), \tag{5.16}$$

where

$$I = \text{round}\left[f_{\text{c}}\left(\hat{\tau}_m[u] + \frac{\hat{\theta}_m[u]}{2\pi f_{\text{c}}}\right)\right]$$

is the integer number of carrier cycles within the TOA, and

$$F = -\frac{\hat{\theta}_m[u]}{2\pi}$$

is the fractional part, which determines the accuracy of the TOA measurement. Note that F depends only on the carrier phase estimates and not on the time offset.

Next, the receiver produces a set of N_{pr} pseudoranges ($N_{\text{pr}} \leq N_{\text{st}}$), one for each station to be included in the position solution. For simplicity of notation, it will be assumed that the active stations are those

with indexes $m = 1, 2, \ldots, N_{\text{pr}}$. The pseudorange observations can then be written as:

$$\hat{\rho}_n[u] = c\left[\text{mod}\left(\hat{t}_{\text{a},n}[u] - \tau_{\text{ED},n}, 2T_{\text{GRI},n}\right)\right], \; n = 1, 2, \ldots, N_{\text{pr}}, \quad (5.17)$$

where c is the velocity of light in free space. The pseudoranges are then passed as inputs to the PVT estimation algorithm.

5.7 POSITION ESTIMATION

Literature on positioning systems commonly distinguishes between *single-point* and *filtered position solutions*. A single-point positioning algorithm uses pseudorange measurements from the current epoch u only. A filtered position solution also makes use of data from previous epochs. Both approaches are briefly discussed below.

5.7.1 *Single-Point Solution*

Single-point eLoran positioning algorithms take as an input a set of N_{pr} pseudoranges $\hat{\rho}_n[u]$, $n = 1, 2, \ldots, N_{\text{pr}}$ each calculated from a corresponding TOA measurement using Equation 5.17 above (for simplicity of notation, the epoch index u will be dropped in the following). The pseudorange measurements can each be modelled as a nonlinear equation in three unknowns

$$\rho_n = r(\lambda, \varphi; \lambda_n, \varphi_n) + \rho_{\text{f},n}(\lambda, \varphi) + \rho_{\text{b}}, \quad (5.18)$$

where r is the ellipsoidal distance between the receiver position (λ - latitude,φ - longitude) and the (known) transmitter position (λ_n, φ_n), $\rho_{\text{b}} = c\tau_{\text{b}}$ is the range equivalent of the receiver clock bias, and $\rho_{\text{f},n}(\lambda, \varphi)$ accounts for the PF, SF and ASF factors (see Chapter 3):

$$\rho_{\text{f},n}(\lambda, \varphi) = c\left[\tau_{\Delta\text{PF},n}(\lambda, \varphi) + \tau_{\text{SF},n}(\lambda, \varphi) + \tau_{\text{ASF},n}(\lambda, \varphi)\right].$$

The propagation factors are obtained by modelling (PF, SF) and through the use of ASF maps and real-time differential corrections, which can be carried by the eLoran signal itself (see Loran Data Channel). The unknown receiver position and clock offset can then be found by solving the following set of equations:

$$r(\lambda, \varphi; \lambda_n, \varphi_n) + \rho_{\text{f},n}(\lambda, \varphi) + \rho_{\text{b}} = \hat{\rho}_n, \; n = 1, 2, \ldots, N_{\text{pr}} \quad (5.19)$$

Least Squares

eLoran receivers typically find the position by iteratively solving a linearised version of the above problem. The method starts with an approximate position and clock offset estimate, $\hat{\mathbf{q}} = \left[\hat{\lambda}, \hat{\varphi}, \hat{\rho}_{\text{b}}\right]^{\text{T}}$, and refines the initial estimate in stages so that it better fits the receiver pseudorange observations,$\{\hat{\rho}_n\}_{n=1}^{N_{\text{pr}}}$. In each stage, pseudorange predictions based on the current position estimate are obtained from Equation 5.18:

$$\rho_n = r\left(\hat{\lambda}, \hat{\varphi}; \lambda_n, \varphi_n\right) + \rho_{\text{f},n}\left(\hat{\lambda}, \hat{\varphi}\right) + \hat{\rho}_{\text{b}}, \; n = 1, 2, \ldots, N_{\text{pr}},$$

and a vector of measurement residuals is calculated

$$\Delta\boldsymbol{\rho} = \begin{bmatrix} \hat{\rho}_1 - \rho_1 \\ \hat{\rho}_2 - \rho_2 \\ \vdots \\ \hat{\rho}_{N_{\text{pr}}} - \rho_{N_{\text{pr}}} \end{bmatrix}.$$

The residual vector can be linearly related to a difference in the estimated position solution, $\Delta\mathbf{q}$, as shown below[20]. For reasons that will become clear later (see the performance analysis of Chapter 9), it will be convenient at this point to use a local coordinate system centred at the current position estimate, rather than the geodetic coordinates:

$$-\underbrace{\begin{bmatrix} \mathbf{i}_1 & 1 \\ \mathbf{i}_2 & 1 \\ \vdots & \vdots \\ \mathbf{i}_{N_{\text{pr}}} & 1 \end{bmatrix}}_{\mathbf{A}} \underbrace{\begin{bmatrix} \Delta x \\ \Delta y \\ \Delta b \end{bmatrix}}_{\Delta\mathbf{q}} = \Delta\boldsymbol{\rho}. \tag{5.20}$$

Matrix $\mathbf{A}$ in the above equation is usually referred to as the *direction cosine matrix* or the *geometry matrix*. It contains unit vectors pointing from the current position estimate to the individual transmitting stations

$$\mathbf{i}_n = [\sin(\beta_n), \cos(\beta_n)],$$

where β_n are bearings of the stations from the receiver. The differences Δx, Δy and Δb represent corrections (expressed in meters) to be applied to the current position and receiver clock bias estimates.

Clearly, a minimum of three pseudorange measurements are required to solve for the unknown parameters. If there are only three pseudoranges ($N_{\text{pr}} = 3$), Equation 5.20 above can be solved directly by matrix inversion:

$$\Delta\mathbf{q} = \mathbf{A}^{-1}\Delta\boldsymbol{\rho}. \tag{5.21}$$

If the system is overdetermined ($N_{\text{pr}} > 3$), the Least Squares (LS) method is commonly used to find a solution that best fits the measurements:

$$\Delta\mathbf{q} = \left(\mathbf{A}^{\text{T}}\mathbf{A}\right)^{-1}\mathbf{A}^{\text{T}}\Delta\boldsymbol{\rho}. \tag{5.22}$$

The correction vector $\Delta\mathbf{q}$ is then used to update the position solution estimate, $\hat{\mathbf{q}}$ (using an appropriate conversion between meters and degrees of latitude and longitude), and another iteration of the algorithm starts. The calculation is stopped when the magnitude of the correction vector $\|\Delta\mathbf{q}\|$ becomes negligible.

It can be shown [120] that if the errors in the pseudorange measurements are zero mean, uncorrelated with each other and have equal

20 Note that in the linearisation process, the correction factor term $\rho_{\text{f},n}(\hat{\lambda}, \hat{\varphi})$ is ignored as negligible compared to the range and clock offset terms; however, the term has to be included in the calculation of predicted pseudoranges in each iteration.

variance, then the LS method implements the BLUE estimator. If the measurement errors are also Gaussian distributed, the estimator is MVU.

Weighted Least Squares

If the measurement errors are uncorrelated but have different variance (which is usually the case in practice), the optimum solution is given by the WLS method:

$$\Delta\mathbf{q} = \left(\mathbf{A}^{\mathrm{T}}\mathbf{W}\mathbf{A}\right)^{-1}\mathbf{A}^{\mathrm{T}}\mathbf{W}\Delta\boldsymbol{\rho}, \tag{5.23}$$

where the weight matrix $\mathbf{W}$ is given by:

$$\mathbf{W} = \left(\mathrm{var}\left[\Delta\boldsymbol{\rho}\right]\right)^{-1}.$$

In order to improve the position solution further, it is necessary to tie measurements over time by including a model of the system dynamics in a solution filter, as discussed in the following section.

5.7.2 *Filtered Solution*

A disadvantage of the single-point solution is that it does not make use of information from previous measurement epochs. The previous position and velocity estimates clearly provide some indication of the current position, and similarly with the receiver clock bias and drift. This motivates the use of *solution filters* in navigation receivers. A solution filter maintains an estimate of the receiver state (which typically includes the receiver position, velocity, clock bias, and clock drift) by combining the previous solution (propagated forward in time) with information obtained from current measurements. A classical example of this approach is the Kalman filter, whose many forms are widely described in the literature (see e.g. [120, 130]).

The filtered solution has a number of benefits, including greater availability of the position solution and reduced noise in the position output. The use of a solution filter can also facilitate multi-system integration. However, the success of this approach depends upon accurate modelling of the system dynamics and the measurement process. Mismodelled dynamics and measurements can seriously degrade the performance of the filter. The filtered solution can also be problematic from an integrity point of view, as the filtering propagates integrity risk from one epoch to the next. Successive single-point solutions, on the other hand, are independent and therefore can highlight corrupted measurements more quickly.

For the purpose of this analysis, it seems appropriate to assume that the receiver uses a single point positioning algorithm. Specifically, it will be assumed throughout this thesis that the WLS method is used, as described in the previous section. This approach should provide a conservative estimate of the achievable accuracy for most practical receivers.

5.8 SUMMARY AND CONCLUSIONS

In this chapter, an eLoran receiver signal processing model has been developed based on the principles of ML estimation (Figure 48). Various aspects of eLoran signal processing have been discussed including channel sharing and CRI mitigation, sky wave rejection, and carrier phase estimation. The effects of input bandpass filtering have also been investigated and implications for the optimal choice of the sampling point have been considered.

As in previous chapters, a number of assumptions had to be made. These can be summarised as follows:

1. Antenna and receiver front-end
    a) The antenna and receiver front-end are assumed to have a negligible impact on the received signal.
2. Input bandpass filter
    a) This analysis assumes an 8th order Butterworth filter with a -3 dB bandwidth of 28 kHz and the passband centred at 100 kHz.
    b) It is assumed that any inter-system interference that falls within the passband of the filter is suppressed by adaptive notch filters. The notch filtering is assumed to have a negligible effect on the useful signal.
3. CRI Mitigation
    a) Two CRI mitigation algorithms are considered, namely CRI blanking and CRI cancelling. With CRI blanking it is assumed that the receiver has perfect knowledge of the time offset of the cross-rating signal.
4. Comb filtering
    a) The integration time, T_i, is assumed to be an integer multiple of the PCI of the signal of interest.
5. Pulse sampling
    a) It is assumed that the receiver uses, in the phase estimation process, one sample per pulse. The samples are taken at a point 62.25 μs into the (filtered) pulse. The pulse amplitude at this point is the same as the amplitude at the 30 μs point on the ideal pulse, i.e. approximately 4 dB less than the peak value.
    b) Noise in successive pulse samples can be considered uncorrelated.
    c) It is also assumed that short-delay sky waves interfering with the chosen sampling point are estimated and cancelled, so that receiver performance is not affected.
6. Phase estimation
    a) Direct estimation is used rather than tracking loops.
    b) A phase estimate is generated once per update interval, T_{up}, where $T_{up} \leq T_i$; it is assumed that T_{up} is an integer multiple of the PCI of the signal of interest.

7. Position solution
    a) A single point WLS position solution algorithm is used.

The receiver signal processing model developed here is one of the key building blocks of this work. It will be used in the following chapter, along with the results of Chapter 2 and 3, to determine bounds on the achievable ranging and positioning performance of eLoran under noise and interference conditions.

6 PSEUDORANGE ERROR MODEL

This chapter aims to develop analytical models of the pseudorange measurement error in the presence of RF noise and CRI, taking into account state-of-the-art eLoran signal processing algorithms. The chapter consists of two main parts. The first one introduces some of the key terms and definitions used throughout the rest of this work. The second part contains the actual analysis and is further divided into several sections, each of which deals with a particular source of measurement error.

6.1 DEFINITIONS

This section reviews the definitions of the two key signal parameters that determine receiver performance, namely the SNR, and the SIR, and defines the receiver performance metrics used in this thesis.

6.1.1 *Signal-to-Noise Ratio*

The SNR is the key determinant of receiver performance. Yet there is no universally accepted definition of SNR in eLoran. Due to the pulsed nature of the signal and differences in receiver design, SNRs have traditionally been a matter of confusion in Loran systems. Engineers from different sectors of the Loran industry approached the problem from different perspectives, which gave rise to a number of different SNR definitions. This section reviews some of the definitions used by the Loran community and presents a definition of SNR that will be used throughout this work.

Overview of Definitions

The United States Coast Guard (USCG) Signal Specification [14] defines SNR as:

> 'The ratio of the RMS amplitude of the Loran pulse at the Standard Sampling Point[1] (SSP) to the RMS value of the noise present at that time.'

The USCG definition is not satisfactory as it does not state where in the receive chain the measurements should be taken and neither does it specify the measurement bandwidth.

The RTCM Loran-C Receiver MPS document [131] gives the following definition:

> 'SNR is the ratio of the Loran-C signal level at the SSP to the RMS level of simulated noise. SNR can be expressed as a dimensionless number indicating RMS voltage\RMS voltage or as a ratio in dB.'

The definition refers to simulated noise, as its primary use in the RTCM document was to set standard conditions for receiver performance testing. The noise is characterised in the document as follows:

1 For the definition of the SSP see Chapter 2

> 'The simulated noise (Gaussian) is considered to have a uniform power spectral density prior to filtering. After filtering by a single resonator L-C filter having a center frequency of 100 kHz and a 3 dB bandwidth of 30 kHz, the noise level is the voltage generated across a 50 Ω resistive load, measured on a true RMS voltmeter.'

Practically the same definitions of SNR are also used in later documents issued by Radio Technical Commission for Aeronautics (RTCA) [132] and the FAA [133, 134], and in the British Standard [135]. The RTCA standard [132] allows the use of either Gaussian noise (as described above) or simulated atmospheric noise defined in FAA document [134]. If Gaussian noise is used, the standard allows adjusting the level of the noise generator to compensate for the differences between atmospheric and Gaussian noise amplitude distributions (see Appendix H of document [132]).

Unfortunately, the above definition is not suitable for implementation in receivers as it refers to the ideal Loran waveform and a particular kind of noise; the actual, real-world, waveforms and noise characteristics will always differ to some extent from the ideal ones. Also, as discussed earlier, the signal and noise levels seen by the receiver will be affected by input filtering and possibly other signal processing. Some of these aspects are reflected in the draft MPS for Marine eLoran Receiving Equipment [123], which gives the following SNR definition:

> 'Signal to noise ratio (SNR) is the ratio of the root mean square (RMS) amplitude, of the envelope, of the eLoran pulse, at the standard zero crossing point, to the RMS value of the noise present at that time.
>
> It is recognized that measuring signal and noise in the context of a receiver inherently requires some amount of processing. It is also recognized that this processing is not limited to, but may include different forms of signal averaging, and different amounts of filtering prior to a signal measurement or a noise measurement. It is also recognized that SNR measurements are heavily influenced by the design of the receive antenna, the analog front end, and a receiver's digital filters. This document attempts to standardize the definition of SNR in an attempt to reduce the variability of reported SNR values, between various receivers.
>
> With regard to an SNR measurement, signal level shall be normalized to a level equal to that of a single eLoran pulse.
>
> With regard to an SNR measurement, noise level shall be measured at a point where there are no tracked eLoran stations, and any averaging that has been performed, must be accurately compensated for.
>
> The noise measurement shall be taken after interference mitigation including, but not limited to CWI, impulse noise, crossrate mitigation, and notch filtering.'

An example of a definition employed by a receiver manufacturer [136] is then given below:

> 'The SNR of a station on a Loran receiver is calculated as the Loran pulse amplitude, divided by the RMS noise ahead

> of the pulse (in a region very roughly 50 μs long) that is observed after pulse subtraction, interferer notching, and ensemble averaging, corrected back to the ADC input. The amplitude is the nominal pulse amplitude, so conceptually it's measured at the 30 μs point, and it's roughly half the peak amplitude of the pulse. [...] Since the SNR is also inversely proportional to the square root of the receiver bandwidth, and there is no accepted way to normalize for this, SNR will vary somewhat according to the Loran receiver brand and model.'

Although the above definitions acknowledge that there is a variability in reported SNRs across different receiver makes and models, they still leave some ambiguity as to how the SNR should be measured. For example, neither of the definitions specifies the measurement bandwidth. Note also that, strictly speaking, the standard zero crossing, which is refered to above, is only defined on the transmitter antenna current waveform and not for a far-field waveform.

The matter of defining and measuring SNR has also been brought up in discussions within the International Loran Association (ILA) [137], [138].

Redefining SNR

From the discussion above it can be seen that neither of the presented definitions suits the needs of this study. The ideal definition should be suitable for theoretical receiver performance analyses. It should also allow the unambiguous specification of operating conditions for the purpose of receiver testing, and it should be easy to implement in a practical receiver. These requirements are somewhat contradictory, and therefore two different SNR definitions are proposed below. Note that (in contrast to the definitions stated above) SNR will be defined here as a power ratio, as is common in engineering practice.

SNR on a Matched Load

The first proposed definition is mainly suitable for the purpose of receiver testing in a controlled radio environment:

> SNR is the ratio of the eLoran signal power to the power of the noise delivered by the signal source to an impedance-matched load. For the purpose of this definition, 'eLoran signal power' means the average power that would be delivered to the load by a continuous wave signal with an amplitude equal to the envelope of the voltage generated by the incoming eLoran pulses across the load at a point having the same Half-Cycle Peak Ratio (HCPR) as the ideal eLoran waveform 30 μs into the pulse. The noise power is the average power delivered to the matched load after filtering the signal by the standard input bandpass filter[2]. It is assumed that the noise power is measured at a time when there is no significant eLoran energy present.

The definition refers to the 30 μs point rather than the SSP, which brings it in line with definitions used by receiver manufacturers [136, 108]. It

2 See Section 5.4.1 in Chapter 5.

allows the calibration of test signals at a clearly defined point outside the receiver. Such signals can then be used to assess the receiver's performance under exactly defined operating conditions. This definition could also be used to calibrate SNR measurement algorithms in eLoran receivers, which would contribute to reducing the variability of reported SNRs between different receiver models seen today.

Sampling Point SNR

This definition refers to the receiver signal processing model shown in Figure 48 in Chapter 5. It defines the SNR from a signal-theoretic point of view, so the quantities used in the definition do not have a direct physical meaning. In the context of the signal processing model of Figure 48, it is convenient to define SNR as follows:

> SNR is the ratio of the eLoran signal sampling point power to the power of the noise present in the signal. For the purpose of this definition, 'sampling point power' means the time-averaged power of an equivalent continuous wave signal, having an amplitude equal to the envelope of the eLoran pulse at the output of the sampler in Figure 48. The noise power is given by the average power of the noise process that would be observed at the output of the input bandpass filter (see Figure 48) after the removal of the eLoran waveforms.

This definition is suitable for theoretical performance analyses of eLoran receivers as it is tied to the signal level at the actual sampling point used in the carrier phase estimation process. SNR defined in this way may vary between different receiver designs, as the position of the sampling point is left at the designer's choice. Note however, that if the assumptions about signal processing made in Chapter 5 hold, then the two SNR definitions given above will be numerically equal.

6.1.2 *Signal-to-Interference Ratio*

The SIR is a crucial signal parameter in the study of CRI. It is a measure of the relative strength of the useful signal with respect to a cross-rating signal. In this work, SIR will be calculated as

$$\mathrm{SIR} = \frac{A_{1,1}^2}{A_{m,i}^2},$$

where $A_{1,1}$ is the amplitude of the ground wave component of the useful signal, and $A_{m,i}$ is the amplitude of the i-th component of the cross-rating signal $m = 2, 3, \ldots$, where $i = 1$ denotes the ground wave component, $i = 2$ the first-hop sky wave component, etc..

6.1.3 *Quantifying the Measurement Error*

One of the main aims of this work is to evaluate the impact of CRI on the accuracy of eLoran position. A key factor that determines the positioning accuracy is the pseudorange measurement error. It should be clear from previous discussions that the problem of evaluating the

pseudorange error is equivalent to that of establishing the accuracy of the signal carrier phase estimates.

Given the model of the received signal developed in Chapter 3, the phase estimation error, denoted $\varepsilon[u] = \hat{\theta}[u] - \theta$, can be assumed to have a random, as well as a deterministic component. The random component is mainly due to the RF noise, which is modelled here as AWGN. The deterministic component of the error is caused by CRI and possibly other sources of interference. Assuming that any non-Loran interference is sufficiently suppressed, the deterministic error component will be periodic with a period given by the least common multiple of the PCIs of the cross-rating signals. The carrier phase estimation error, $\varepsilon[u]$, will therefore be modelled as a *cyclostationary random process*.

Since the statistical properties of cyclostationary processes vary cyclically with time, the usual approach to dealing with such processes is through the use of average characteristics (i.e. both time- and ensemble-averaged, $\mathrm{Av}[\mathrm{E}[\cdot]] \equiv \mathrm{AvE}[\cdot]$; see also Appendix A). The following receiver performance metrics were therefore chosen for use in this work:

The *average carrier phase estimation error*

$$\mu_\varepsilon^{\mathrm{a}} = \mathrm{AvE}[\varepsilon[u]],$$

the *average variance of the carrier phase estimation error*

$$\mathrm{var}^{\mathrm{a}}[\varepsilon[u]] \equiv \overline{\sigma_\varepsilon^2} = \mathrm{AvE}\left[|\varepsilon[u] - \mu_\varepsilon^{\mathrm{a}}|^2\right],$$

and, alternatively, the *average power of the carrier phase estimation error*[3]

$$P_\varepsilon^{\mathrm{a}} = \mathrm{E}\left[P_\varepsilon^t\right] = \mathrm{AvE}\left[|\varepsilon[u]|^2\right].$$

The equivalent time of arrival and pseudorange measurement errors can be estimated by applying error propagation to Equation 5.16 and Equation 5.17 in Chapter 5.

6.2 PSEUDORANGE ERROR ANALYSIS

The following sections develop a set of models to analyse and assess the performance of eLoran receivers under a variety of conditions: Section 6.2.1 quantifies the pseudorange measurement error due to RF noise in the received signal; Section 6.2.2 to Section 6.2.4 analyse the errors due to uncompensated CRI; Section 6.2.5 to Section 6.2.8 assess the effectiveness of the two most prevalent CRI mitigation techniques - CRI blanking and CRI cancelling; and Section 6.2.9 considers the optimum approach to CRI mitigation in eLoran receivers.

The analyses presented here generally follow the following pattern: First, a model for the received signal is formulated. This will usually be a subset of the full signal model presented in Chapter 3. Only those components that are essential to the problem studied in each respective subsection are included. A receiver signal processing model is then specified. This, again, will be a subset of the full model developed in Chapter 5. The next step is to determine key statistical characteristics of the signal at the input to the phase detector (refer to the signal process-

3 P_ε^t denotes the time-averaged power of the estimation error; for definition see Appendix A.

ing model of Figure 48). Since the blocks in the signal processing model preceding the phase detector are linear, the analysis can be performed separately for the desired and interfering signal components and the resulting characteristics can be found by applying the superposition principle. Finally, the statistics of the measurement error at the output of the phase detector are found using error propagation. Each section is concluded by a discussion of the results obtained.

6.2.1 *Performance in White Gaussian Noise*

This section establishes a theoretical lower bound on the pseudorange measurement error in the presence of AWGN. Background noise limits receiver performance in the absence of interference. As will become clear later, noise is also an important consideration when determining the effects of CRI.

Received Signal Model

In this analysis, the received signal will be modelled as a sum of an eLoran waveform[4] $\tilde{x}_1(t) = A\tilde{s}(t;\tau,\theta,\mathcal{C},T_{\mathrm{GRI}})$ and an AWGN process $w(t)$ with doublesided PSD of $N_0/2$:

$$\tilde{x}(t) = \underbrace{A\tilde{s}(t;\tau,\theta,\mathcal{C},T_{\mathrm{GRI}})}_{\tilde{x}_1(t)} + w(t).$$

Since, in a practical receiver, the clock is subject to an arbitrary offset, and since $w(t)$ is a stationary process, the choice of time origin is not important and it can be assumed (without loss of generality) that $\tau = 0$. Assuming that the useful signal waveform is not distorted during propagation (see assumptions made in Chapter 3), this means that also $\theta = 0$.

Signal Processing Model

Since the signal model does not include any cross-rating eLoran signals, the signal processing model of Figure 48 (Chapter 5) can be simplified for the purpose of this analysis by leaving out the 'CRI mitigation' block. The model will, therefore, consist of the standard input bandpass filter, frequency downconverter, comb filter, phase-decoding filter, the phase correction block to compensate for the phase shift introduced by the input bandpass filter, the sampler, and the phase detector.

Measurement Error Process

As discussed above, the phase measurement error can be represented by a cyclostationary random process, which can be described by average performance characteristics. In this particular analysis, the only source of disturbance is the AWGN, which is a stationary process. As will be shown below, this means that also the measurement error is stationary. This removes the need for time-averaging when evaluating the performance metrics, and the expressions reduce to ensemble-averaged characteristics:

$$\mu_\varepsilon^{\mathrm{a}} = \mathrm{AvE}\left[\varepsilon\left[u\right]\right] \overset{\text{stat.}}{=} \mathrm{E}\left[\varepsilon\right] = \mu_\varepsilon,$$

4 For definition of $\tilde{s}(\cdot)$ see Chapter 2.

$$\begin{aligned}\mathrm{var}^{\mathrm{a}}\left[\varepsilon\left[u\right]\right] &= \mathrm{AvE}\left[\left|\varepsilon\left[u\right]-\mu_{\varepsilon}^{\mathrm{a}}\right|^2\right] \overset{\text{stat.}}{=} \\ &= \mathrm{E}\left[\left|\varepsilon-\mu_{\varepsilon}\right|^2\right] = \mathrm{var}\left[\varepsilon\right].\end{aligned}$$

Desired Signal Component at the Phase Detector

Since the desired component of the received signal, $\tilde{x}_1(t)$, is assumed to be deterministic, the receiver's response to $\tilde{x}_1(t)$ will also be a deterministic function of time. The task here is to find this function.

The first block in the signal processing model is the standard input bandpass filter. The effects of bandpass filtering on the eLoran signal waveform were examined in Chapter 5. As shown in the chapter, the filtering causes a carrier phase shift θ_{b}, and some distortion of the pulse envelope. The phase shift affects all signals by the same amount and can easily be compensated for using the phase correction block. The envelope distortion can be described by Equation 5.14. It affects the available SNR and SGR at the sampling point and as such, it needs to be taken into account in this analysis. Recalling Equation 5.14 and Equation 2.10, the desired signal after bandpass filtering and frequency downconversion can be expressed as

$$\begin{aligned}x_{1,\mathrm{b}}(t) \overset{\tau=0}{=} A\sum_{n=-\infty}^{\infty}\sum_{m=0}^{7}\big[&C_m e_{\mathrm{b}}\left(t-mT_p-2nT_{GRI}\right) \\ &+C_{m+8}e_{\mathrm{b}}\left(t-mT_p-(2n+1)\,T_{GRI}\right)\big].\end{aligned}$$

The signal is then averaged in the comb filter over an interval of length $2T_{\mathrm{GRI}}$ (Equation 5.6). Since $x_{1,\mathrm{b}}(t)$ is periodic in $2T_{\mathrm{GRI}}$, the comb filter has no effect on this signal component; the response of the filter to the desired signal is thus given by

$$x_{1,\mathrm{c}}(t) = x_{1,\mathrm{b}}(t).$$

The next step involves filtering by the phase-decoding filter, as described by Equation 5.10, Chapter 5. Upon inserting $x_{1,\mathrm{c}}(t)$ into Equation 5.10 and limiting attention to $t \in \bigcup_{n'\in\mathbb{Z}}\left\langle 2n'T_{\mathrm{GRI}}, 2n'T_{\mathrm{GRI}}+T_{\mathrm{p}}\right\rangle$, the output of the phase decoding filter can be written as

$$x_{1,\mathrm{p}}(t) = A\sum_{n=-\infty}^{\infty} e_{\mathrm{b}}\left(t-2nT_{GRI}\right).$$

Next, the carrier phase of the signal is adjusted to compensate for the phase shift introduced in the bandpass filter:

$$x_{1,\mathrm{r}}(t) = x_{1,\mathrm{p}}(t)\,\mathrm{e}^{-j\theta_{\mathrm{b}}}.$$

Although this step is not necessary from a functional point of view, compensating for the carrier phase shift ensures that the complex envelope of the desired signal component, $x_{1,\mathrm{r}}(t) = x_{1,\mathrm{r},\mathcal{I}}(t) + jx_{1,\mathrm{r},\mathcal{Q}}(t)$, is real for $\tau = 0$, which simplifies further computations.

According to the signal processing model, the signal is then sampled at $t = uT_{\mathrm{up}} + \tau_{\mathrm{sp}}$, where $u \in \mathbb{Z}$, T_{up} is the update interval, which is assumed to be an integer multiple of $2T_{\mathrm{GRI}}$, and τ_{sp} is the sampling point offset, which is determined based on the shape of the pulse envelope. Assuming that the signal has been correctly acquired, i.e. $\tau_{\mathrm{sp}} \approx \mathrm{mod}\left(\tau+\tau_{\mathrm{p}}, 2T_{\mathrm{GRI}}\right)$, where τ_{p} is a parameter whose value is

selected by the receiver designer (see Chapter 5), the sampled signal is given simply by

$$\begin{aligned} x_{1,\mathrm{r}}[u] &\equiv x_{1,\mathrm{r}}\left(uT_{\mathrm{up}}+\tau_{\mathrm{sp}}\right) \\ &= |\tau=0| = Ae_{\mathrm{b}}\left(\tau_{\mathrm{p}}\right)\mathrm{e}^{-j\theta_{\mathrm{b}}} = A\left|e_{\mathrm{b}}\left(\tau_{\mathrm{p}}\right)\right|,\ \forall u\in\mathbb{Z}. \end{aligned} \tag{6.1}$$

In words, the desired signal component at the input to the phase detector is equal to the envelope of the filtered pulse at the sampling point.

Noise at the Phase Detector

This part of the analysis determines the receiver's response to the noise process $w(t)$. The aim is to find the basic first-order and second-order statistics of the random process at the input to the phase detector to enable the evaluation of the phase measurement error.

Noise at the input to the receiver is modelled as an AWGN process with a doublesided PSD of $N_0/2$. Passing $w(t)$ through the input bandpass filter results in a noise process $\widetilde{w}_{\mathrm{b}}(t)$, whose power spectral density is concentrated around $\pm f_c$. The noise now has a finite power of $P^{\mathrm{e}}_{\widetilde{w}_{\mathrm{b}}} = \mathrm{var}\left[\widetilde{w}_{\mathrm{b}}(t)\right] = N_0 B_{\mathrm{b,n}}$, where $B_{\mathrm{b,n}}$ is the noise bandwidth of the filter, as calculated in Chapter 5.

It can be shown [48] that the band-limited noise $\widetilde{w}_{\mathrm{b}}(t)$ is a Wide-Sense Stationary (WSS) signal. Further, the complex envelope of the noise at the output of the down-converter, $w_{\mathrm{b}}(t) = w_{\mathrm{b},\mathcal{I}}(t) + \mathrm{j}w_{\mathrm{b},\mathcal{Q}}(t)$, is again a WSS process, its I and Q components are uncorrelated, zero mean and have equal power (see Appendix A):

$$\mathrm{E}\left[w_{\mathrm{b},\mathcal{I}}(t)\, w_{\mathrm{b},\mathcal{Q}}(t)\right] = 0, \tag{6.2}$$

$$\mathrm{E}\left[w_{\mathrm{b},\mathcal{I}}(t)\right] = \mathrm{E}\left[w_{\mathrm{b},\mathcal{Q}}(t)\right] = 0, \tag{6.3}$$

$$P^{\mathrm{e}}_{w_{\mathrm{b},\mathcal{I}}} = P^{\mathrm{e}}_{w_{\mathrm{b},\mathcal{Q}}} = \mathrm{var}\left[w_{\mathrm{b},\mathcal{I}}(t)\right] = \mathrm{var}\left[w_{\mathrm{b},\mathcal{Q}}(t)\right] = P^{\mathrm{e}}_{\widetilde{w}_{\mathrm{b}}}. \tag{6.4}$$

Next, the signal is passsed through the comb filter, phase-decoding filter, and the sampler. The output signal from these blocks will be denoted $w_{\mathrm{c}}(t)$, $w_{\mathrm{p}}(t)$, and $w_{\mathrm{p}}[u]$, respectively; the respective I and Q components will be denoted as $w_{\mathrm{c},\mathcal{I}}(t)$, $w_{\mathrm{c},\mathcal{Q}}(t)$, etc. The following discussion makes use of Equation 5.6 and Equation 5.10 presented in Chapter 5, and the following two observations:

1. The output signal of an LTI system driven by a WSS signal is a WSS signal [48].

2. Uniform sampling of a WSS signal results in a WSS signal; the mean and variance of the sampled signal are the same as those of the original signal.

The mean and variance of the noise signals at the output of the individual blocks can then be found as follows. Since $\mathrm{E}\left[w_{\mathrm{b},\mathcal{I}}(t)\right] = \mathrm{E}\left[w_{\mathrm{b},\mathcal{Q}}(t)\right] = 0$, it follows immediately that $\mathrm{E}\left[w_{\mathrm{c},\mathcal{I}}(t)\right] = \mathrm{E}\left[w_{\mathrm{c},\mathcal{Q}}(t)\right] = \mathrm{E}\left[w_{\mathrm{p},\mathcal{I}}(t)\right] = \mathrm{E}\left[w_{\mathrm{p},\mathcal{Q}}(t)\right] = 0$.

The variance of the noise at the output of the comb filter can be found from Equation 5.6 and Equation 6.4 using error propagation

$$\begin{aligned}\text{var}\left[w_{\text{c},\mathcal{I}}\left(t\right)\right] &= \text{var}\left[w_{\text{c},\mathcal{Q}}\left(t\right)\right] \\ &= \frac{1}{N_{\text{i}}^2}\sum_{n'=0}^{N_{\text{i}}-1}\text{var}\left[w_{\text{b},\mathcal{I}}\left(t-2n'T_{\text{GRI}}\right)\right] \\ &= \frac{1}{N_{\text{i}}}\text{var}\left[w_{\text{p},\mathcal{I}}\left(t\right)\right] = \frac{P^{\text{e}}_{\widetilde{w}_{\text{b}}}}{N_{\text{i}}},\end{aligned}$$

where it has been assumed that noise values $2T_{\text{GRI}}$ (or more) apart are mutually uncorrelated (see also discussion in Section 5.4.1 of Chapter 5).

Similarly, it follows from Equation 5.10 and the above result that

$$\begin{aligned}\text{var}\left[w_{\text{p},\mathcal{I}}\left(t\right)\right] &= \text{var}\left[w_{\text{p},\mathcal{Q}}\left(t\right)\right] \\ &= \frac{1}{16^2}\sum_{m=0}^{7}\Big\{C_m^2\text{var}\left[w_{\text{c},\mathcal{I}}\left(t-2T_{\text{GRI}}+mT_{\text{p}}\right)\right] \\ &+C_{m+8}^2\text{var}\left[w_{\text{c},\mathcal{I}}\left(t-T_{\text{GRI}}+mT_{\text{p}}\right)\right]\Big\} \\ &= \frac{1}{16}\text{var}\left[w_{\text{c},\mathcal{I}}\left(t\right)\right] = \frac{P^{\text{e}}_{\widetilde{w}_{\text{b}}}}{16N_{\text{i}}},\end{aligned}$$

where it has been assumed that noise values T_{p} (or more) apart are uncorrelated.

The multiplication by the complex exponential in the phase correction block does not affect the statistical properties of the noise. Further, since $w_{\text{p},\mathcal{I}}\left(t\right)$, $w_{\text{p},\mathcal{Q}}\left(t\right)$ are WSS, the statistics of the residual noise after sampling are the same as those of the continuous-time waveform. The mean and variance of the noise at the output of the sampler, $w_{\text{r}}\left[u\right]$, are therefore given by

$$\begin{aligned}&\text{E}\left[w_{\text{r},\mathcal{I}}\left[u\right]\right] = \text{E}\left[w_{\text{r},\mathcal{Q}}\left[u\right]\right] = \text{E}\left[w_{\text{p},\mathcal{I}}\left(t\right)\right] = 0, \\ &\text{var}\left[w_{\text{r},\mathcal{I}}\left[u\right]\right] = \text{var}\left[w_{\text{r},\mathcal{Q}}\left[u\right]\right] = \text{var}\left[w_{\text{p},\mathcal{I}}\left(t\right)\right] = \frac{P^{\text{e}}_{\widetilde{w}_{\text{b}}}}{16N_{\text{i}}}.\end{aligned} \tag{6.5}$$

By similar reasoning as above it can also be shown that

$$\text{cov}\left[w_{\text{r},\mathcal{I}}\left[u\right], w_{\text{r},\mathcal{Q}}\left[u\right]\right] = \text{E}\left[w_{\text{r},\mathcal{I}}\left[u\right]\cdot w_{\text{r},\mathcal{Q}}\left[u\right]\right] = 0. \tag{6.6}$$

In summary, the residual noise at the input to the phase detector is a WSS process, its I and Q components are uncorrelated, zero mean and have equal power. The noise power in the I and Q components is equal to the power of the RF noise that passes through the input bandpass filter, reduced by a factor equal to the number of pulses received within the integration interval.

Measurement Error Statistics

The results developed in the previous sections will now be combined to derive the statistics of the phase estimation error. Assuming, as above, that $\tau = 0$ and applying the superposition principle, the input signal to the phase detector can be expressed as

$$x_{\text{r}}\left[u\right] = x_{1,\text{r}}\left[u\right] + w_{\text{r}}\left[u\right] = \left|\tau = 0\right| = A\left|e_{\text{b}}\left(\tau_{\text{p}}\right)\right| + w_{\text{r},\mathcal{I}}\left[u\right] + \text{j}w_{r,\mathcal{Q}}\left[u\right].$$

The in-phase and quadrature components of $x_\mathrm{r}[u]$ are therefore given by

$$x_{r,\mathcal{I}}[u] \equiv \mathrm{Re}[x_\mathrm{r}[u]] = A\left|e_\mathrm{b}(\tau_\mathrm{p})\right| + w_{\mathrm{r},\mathcal{I}}[u],$$

$$x_{r,\mathcal{Q}}[u] \equiv \mathrm{Im}[x_\mathrm{r}[u]] = w_{\mathrm{r},\mathcal{Q}}[u],$$

and the carrier phase estimates are obtained from $x_\mathrm{r}[u]$ as

$$\hat{\theta}[u] = \angle x_\mathrm{r}[u] = \arctan 2\left(x_{r,\mathcal{Q}}[u], x_{r,\mathcal{I}}[u]\right). \tag{6.7}$$

Note that the assumption that $\tau = \theta = 0$, made at the beginning of the analysis, means that $\hat{\theta}[u]$ directly corresponds to the instantaneous phase estimation error $\varepsilon[u] = \hat{\theta}[u] - \theta$ (which is the main subject of this analysis). Under the additional assumption that $P^\mathrm{e}_{x_{r,\mathcal{I}}} \gg P^\mathrm{e}_{x_{r,\mathcal{Q}}}$ (a high SNR assumption), the phase estimation error $\varepsilon[u]$ is limited to the range of $\left(-\frac{\pi}{2}, \frac{\pi}{2}\right)$ almost certainly and the four-quadrant arctan2(.,.) in Equation 6.7 can be replaced by the one-argument arctan (.) function

$$\hat{\theta}[u] = \varepsilon[u] = \arctan\left(\frac{x_{r,\mathcal{Q}}[u]}{x_{r,\mathcal{I}}[u]}\right). \tag{6.8}$$

The statistics of the measurement error $\varepsilon[u]$ can then be found by applying multivariate error propagation to the above equation.

Restricting attention to high-SNR signals is a reasonable simplification as eLoran aims at providing 10 m level positioning accuracy, which is only achievable with sufficiently strong received signals. Note also that measurements of weak signals are likely to be weighted out in the position solution or will not be used at all.

Under the high SNR assumption, the multivariate analysis can be avoided by further simplifying Equation 6.8 as follows:

$$\varepsilon[u] = \arctan\left(\frac{x_{r,\mathcal{Q}}[u]}{x_{r,\mathcal{I}}[u]}\right) \approx \frac{x_{r,\mathcal{Q}}[u]}{x_{r,\mathcal{I}}[u]} \approx \frac{w_{\mathrm{r},\mathcal{Q}}[u]}{A\left|e_\mathrm{b}(\tau_\mathrm{p})\right|}.$$

The calculation of the statistics of the measurement error than becomes remarkably easy:

$$\mu_\varepsilon = \mathrm{E}\left[\frac{w_{\mathrm{r},\mathcal{Q}}[u]}{A\left|e_\mathrm{b}(\tau_\mathrm{p})\right|}\right] = \frac{\mathrm{E}[w_{\mathrm{r},\mathcal{Q}}[u]]}{A\left|e_\mathrm{b}(\tau_\mathrm{p})\right|} = 0,$$

$$\begin{aligned}\mathrm{var}[\varepsilon] = \mathrm{var}\left[\frac{w_{\mathrm{r},\mathcal{Q}}[u]}{A\left|e_\mathrm{b}(\tau_\mathrm{p})\right|}\right] &= \frac{\mathrm{var}[w_{\mathrm{r},\mathcal{Q}}[u]]}{A^2\left|e_\mathrm{b}(\tau_\mathrm{p})\right|^2} \\ &= \frac{P^\mathrm{e}_{\tilde{w}_\mathrm{b}}}{16N_\mathrm{i}A^2\left|e_\mathrm{b}(\tau_\mathrm{p})\right|^2} = \frac{1}{2N_\mathrm{p}\cdot\mathrm{SNR}_{\tau_\mathrm{p}}},\end{aligned} \tag{6.9}$$

where

$$N_\mathrm{p} = 16N_\mathrm{i} = \frac{8T_i}{T_\mathrm{GRI}}$$

is the number of eLoran pulses received within the receiver integration time[5], and

$$\mathrm{SNR}_{\tau_\mathrm{p}} = \frac{A^2 \left| e_\mathrm{b}\left(\tau_\mathrm{p}\right)\right|^2}{2P^\mathrm{e}_{\widetilde{w}_\mathrm{b}}}$$

is the sampling point SNR, as defined in Section 6.1.1.

Referring to Equation 5.16 in Chapter 5, the equivalent *error in signal time of arrival measurement* can be expressed (in seconds squared) as

$$\mathrm{var}\left[\varepsilon_\mathrm{t}\right] = \left(\frac{1}{2\pi f_\mathrm{c}}\right)^2 \mathrm{var}\left[\varepsilon\right] = \frac{1}{8\left(\pi f_\mathrm{c}\right)^2 N_\mathrm{p}\cdot \mathrm{SNR}_{\tau_\mathrm{p}}}, \tag{6.10}$$

where f_c is the eLoran carrier frequency of 100kHz, and the equivalent *pseudorange measurement error* in meters squared can be expressed, using Equation 5.17, as

$$\mathrm{var}\left[\varepsilon_\rho\right] = c^2 \mathrm{var}\left[\varepsilon_\mathrm{t}\right] = \frac{c^2}{8\left(\pi f_\mathrm{c}\right)^2 N_\mathrm{p}\cdot \mathrm{SNR}_{\tau_\mathrm{p}}} = \frac{c_0}{N_\mathrm{p}\cdot \mathrm{SNR}_{\tau_\mathrm{p}}}, \tag{6.11}$$

where

$$c_0 = \frac{c^2}{8\left(\pi f_\mathrm{c}\right)^2} \approx 337.4^2.$$

This agrees with an expression given earlier by Lo et al. 139, and the same result can also be obtained using the theory of Cramer-Rao lower bounds 120.

It should be noted that the above expressions represent theoretical lower bounds on the measurement error. Due to receiver implementation imperfections, real-world performance is likely to be slightly worse than the theoretical predictions. The effect can be calibrated out using an additional multiplicative factor, L_impl:

$$\mathrm{var}\left[\varepsilon_\rho\right] \equiv \sigma_\rho^2 \approx L_\mathrm{impl}\frac{337.4^2}{N_\mathrm{p}\cdot \mathrm{SNR}_{\tau_\mathrm{p}}}. \tag{6.12}$$

The exact value of the implementation loss factor L_impl for a specific receiver model can be found experimentally using a signal simulator (see Chapter 8). This approach also allows the effects of other, generally unknown, receiver parameters (such as the exact location of the sampling point) to be calibrated out.

Discussion of Results

Figure 49 plots the RMS pseudorange measurement error σ_ρ as a function of SNR for the shortest and longest admissible GRI [14] and a typical integration time of $T_\mathrm{i} \approx 5\,\mathrm{s}$. The figure also shows results obtained by computer simulations (see also Chapter 8) which are in perfect agreement with the analytical predictions. The effect of implementation losses is not considered here (L_impl set equal to 1) and therefore the plots in Figure 49 should be interpreted as theoretical lower bounds on the measurement error.

5 Recall that T_i is assumed to be an integer multiple of $2T_\mathrm{GRI}$.

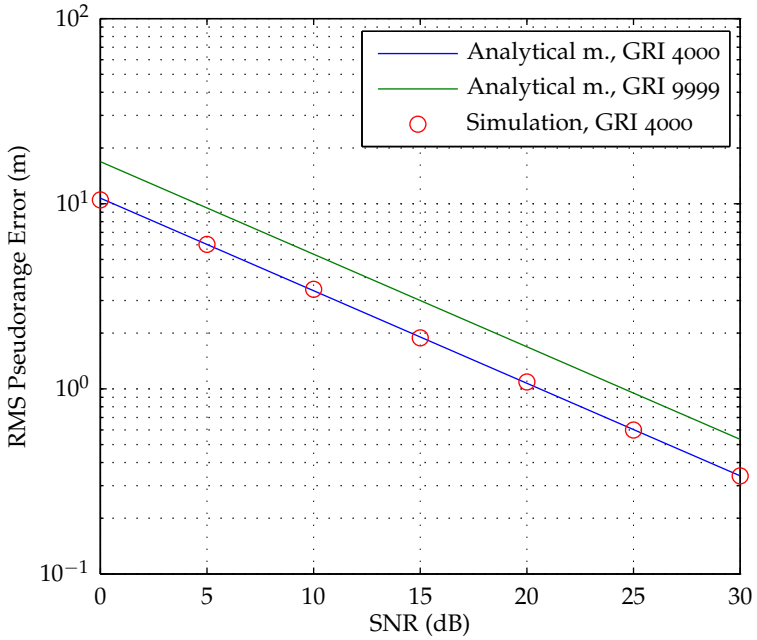

Figure 49: RMS pseudorange error due to AWGN as a function of SNR (theoretical lower bound vs. computer simulation); implementation loss factor $L_{\text{impl}} = 1$; integration time $T_{\text{i}} \approx 5\,\text{s}$;

6.2.2 *Performance in CRI: Deterministic Frequency Domain Model*

This section develops an analytical model to quantify the measurement error in the presence of a single cross-rating signal. The analysis in this section presents a worst case scenario in that it assumes that no CRI mitigation algorithms (except from the inherent averaging) are used at the receiver to suppress the cross-rating signal. The main contribution of this analysis is that it gives insight into the intricate structure of CRI and the way how different signal parameters affect the measurement error. Note also that in practice it may not be viable to apply CRI mitigation algorithms to all cross-rating signals in view. A certain portion of the signals is likely to be left uncompensated, and the results of the current and the following section can then be used to quantify the impact on the measurement error.

Received Signal Model

In this section, the received signal will be modeled as a sum of two cross-rating eLoran waveforms[6]

$$\tilde{x}(t) = A_1 \tilde{s}(t; \tau_1, \theta_1, \mathcal{C}_1, T_{\text{GRI},1},) + A_2 \tilde{s}(t; \tau_2, \theta_2, \mathcal{C}_2, T_{\text{GRI},2}),$$

where $T_{\text{GRI},1} \neq T_{\text{GRI},2}$. RF noise or any other channel impairmants discussed earlier will not be considered as they are irrelevant to the problem at hand. It will be convenient to simplify the model further, as follows.

First, as in the previous section, it will be assumed that $\tau_1 = 0$ (recall that, in practice, the receiver time base is subject to an arbitrary bias;

6 For definition of $\tilde{s}(\cdot)$ see Chapter 2.

the time offset of the signal of interest can therefore be conveniently chosen to be equal to zero). In order to preserve the timing relationship between the cross-rating signals, the time offset of the interfering signal then needs to be adjusted accordingly. To signify this fact, the adjusted offset will be denoted in the following as $\Delta\tau_2$. For any two values of τ_1, τ_2, the adjusted offset is calculated simply as

$$\Delta\tau_2 = \mathrm{mod}\left(\tau_2 - \tau_1, 2T_{\mathrm{GRI},2}\right).$$

Next, under the assumption that the transmission channel is without distortion (see discussions in Section 3.2.1, Chapter 3), the carrier phase offsets of the two signals can be expressed as a function of the respective time offsets. Since $\tau_1 = 0$, also $\theta_1 = 0$. The (adjusted) phase offset of the interfering signal can then be expressed as

$$\Delta\theta_2 = -2\pi f_c \Delta\tau_2.$$

Further, as will become clear later in the analysis, the CRI-induced error is proportionate to the ratio of the signal amplitudes (i.e. the SIR), rather than to the absolute signal amplitudes, A_1, A_2. Taking into account all the above points, $\tilde{x}(t)$ can, for the purpose of this analysis, be redefined as follows:

$$\tilde{x}(t) = \underbrace{\tilde{s}\left(t; 0, 0, \mathcal{C}_1, T_{\mathrm{GRI},1}\right)}_{\tilde{x}_1(t)} + \underbrace{\frac{1}{\sqrt{\mathrm{SIR}}}\tilde{s}\left(t; \Delta\tau_2, \overbrace{-2\pi f_c \Delta\tau_2}^{\Delta\theta_2}, \mathcal{C}_2, T_{\mathrm{GRI},2}\right)}_{\tilde{x}_2(t)}, \quad (6.13)$$

where $\tilde{x}_1(t)$ represents the desired signal component, $\tilde{x}_2(t)$ is considered as interference, and $\mathrm{SIR} = A_1^2/A_2^2$ is the signal to interference ratio.

Signal Processing Model

This analysis will use the same signal processing model as was used in the previous section for analysing performance in AWGN (i.e. eLoran CRI mitigation algorithms will not be considered; refer also to Figure 48 in Chapter 5).

Measurement Error Process

Since the received signal model described by Equation 6.13 is fully deterministic, also the measurement error will be a deterministic function of time. This removes the need for ensemble-averaging when evaluating the performance metrics, and the expressions reduce to time-averaged characteristics:

$$\mu_\varepsilon^{\mathrm{a}} = \mathrm{AvE}\left[\varepsilon[u]\right] \overset{\mathrm{det.}}{=} \mathrm{Av}\left[\varepsilon[u]\right] = \mu_\varepsilon^{\mathrm{t}},$$

and

$$\begin{aligned}\mathrm{var}^{\mathrm{a}}[\varepsilon[u]] &= \mathrm{AvE}\left[\left|\varepsilon[u]-\mu_{\varepsilon}^{\mathrm{a}}\right|^2\right] \overset{\text{det.}}{=} \\ &= \mathrm{Av}\left[\left|\varepsilon[u]-\mu_{\varepsilon}^{\mathrm{t}}\right|^2\right] = \mathrm{var}^{\mathrm{t}}[\varepsilon[u]]\,.\end{aligned}$$

Desired Signal at the Phase Detector

Following the same steps as in Section 6.2.1, it can be shown that the desired signal component at the input to the phase detector, $x_{1,\mathrm{r}}[u]$, is given by

$$x_{1,\mathrm{r}}[u] = \left|e_{\mathrm{b}}\left(\tau_{\mathrm{p}}\right)\right|,\ \forall u \in \mathbb{Z},$$

i.e. it is a real constant equal to the envelope of the desired signal pulse at the sampling point.

Interference at the Phase Detector

This subsection aims to characterise the interfering signal component observed at the input to the phase detector. Early attempts at modelling the interference in the time domain led to considerable mathematical complications caused mainly by the pulsed, periodic nature of the signals. In this analysis the problem will be formulated in the frequency domain. Since the signal parameters are treated here as deterministic, the resulting model will be referred to as the Deterministic Frequency Domain (DFD) model of CRI.

Upon reception, eLoran signals are converted to baseband and passed through a series of LTI filters (recall the signal processing model of Figure 48). The spectrum of the signal after frequency down conversion, filtering, and correction of the carrier phase shift introduced by the input bandpass filtering can be written as

$$S_{x_{2,\mathrm{r}}}(f) = \underbrace{H_{\mathrm{b}}(f)\,H_{\mathrm{c}}(f)\,H_{\mathrm{p}}(f)\,\mathrm{e}^{-j\theta_{\mathrm{b}}}}_{H_{\mathrm{f}}(f)}\,S_{x_2}(f)\,,$$

where $S_{x_2}(f)$ is the spectrum of the complex envelope of the interfering signal component at the receiver input; $H_{\mathrm{b}}(f) = \widetilde{H}_{\mathrm{b}}(f+f_c)$ is the frequency response of the equivalent low-pass filter representing the input bandpass filter $\widetilde{H}_{\mathrm{b}}(f)$ (see Chapter 5); θ_{b} is the carrier phase shift due to the input bandpass filtering; $H_{\mathrm{c}}(f)$ and $H_{\mathrm{p}}(f)$ represent the comb and phase-decoding filters and were defined in Section 5.2.2; and $H_{\mathrm{f}}(f)$ then collects the effects of the three filters (including the carrier phase correction).

The spectrum $S_{x_2}(f)$ can be obtained using Equation 2.11 in Chapter 2. By substituting for $S_{x_2}(f)$ in the above equation, the spectrum of the filtered interference signal can be expressed in the form

$$S_{x_{2,\mathrm{r}}}(f) = \sum_{n=-\infty}^{\infty} c_{x_{2,\mathrm{r}}}[n]\,\delta\left(f-\frac{n}{2T_{GRI,2}}\right), \tag{6.14}$$

where

$$c_{x_{2,\mathrm{r}}}[n] = \frac{\mathrm{e}^{-\mathrm{j}2\pi\Delta\tau_2\left(\frac{n}{2T_{GRI,2}}+f_\mathrm{c}\right)}}{2T_{GRI,2}\sqrt{\mathrm{SIR}}} \cdot S_e\left(\frac{n}{2T_{GRI,2}}\right) S_b\left(\frac{n}{2T_{GRI,2}}\right) H_\mathrm{f}\left(\frac{n}{2T_{GRI,2}}\right),\ n \in \mathbb{N} \quad (6.15)$$

are the Fourier series coefficients of the filtered interference component; $\Delta\tau_2$, $T_{\mathrm{GRI},2}$, and SIR are the respective signal parameters as defined above; and $S_e(f)$ and $S_b(f)$ were calculated in Chapter 2.

The next signal processing step inolves sampling of the interference waveform (GRI $T_{\mathrm{GRI},2}$) by a sampler synchronised to the desired signal (GRI $T_{\mathrm{GRI},1}$). This operation in particular is what makes the analysis of CRI difficult to accomplish in the time domain. The process of sampling the filtered signal can be described by the following expression:

$$x_{2,\mathrm{r}}[u] = x_{2,\mathrm{r}}\left(uT_\mathrm{up} + \tau_\mathrm{sp}\right),\ u \in \mathbb{Z}. \quad (6.16)$$

Here, $x_{2,\mathrm{r}}[u]$ are the samples of the filtered signal, T_up is the measurement update interval which is assumed to be an integer multiple of the PCI of the desired signal, $T_\mathrm{up} = N_\mathrm{up} \cdot 2T_{\mathrm{GRI},1}$, $N_\mathrm{up} \in \mathbb{N}$, and τ_sp is a conveniently chosen sampling point offset. Note that since the sampler is synchronised with the desired signal, i.e. $\tau_\mathrm{sp} \approx \mathrm{mod}\left(\tau_1 + \tau_\mathrm{p}, 2T_\mathrm{GRI}\right)$ where τ_p is a parameter selected by the receiver designer (see Chapter 5), and since it was assumed that $\tau_1 = 0$, τ_sp can be replaced by τ_p in the following discussion. Further, denote[7]

$$T \equiv \mathrm{lcm}\left(T_\mathrm{up} \cdot 10^5, 2T_{\mathrm{GRI},2} \cdot 10^5\right) \cdot 10^{-5}, \quad (6.17)$$

$$N_1 \equiv \frac{T}{T_\mathrm{up}},$$

and

$$N_2 \equiv \frac{T}{2T_{\mathrm{GRI},2}}.$$

It should then be clear that $x_{2,\mathrm{r}}[u]$ is periodic in N_1, and its spectrum can therefore be represented by a discrete Fourier series with coefficients

$$c^\mathrm{d}_{x_{2,\mathrm{r}}}[n] = \frac{1}{N_1}\sum_{u=0}^{N_1-1} x_{2,\mathrm{r}}[u]\,\mathrm{e}^{-\mathrm{j}un\frac{2\pi}{N_1}},\ n \in \mathbb{N}. \quad (6.18)$$

The value for $x_{2,\mathrm{r}}[u]$ in the above equation is given by the continuous-time signal $x_{2,\mathrm{r}}(t)$ evaluated at $t = uT_\mathrm{up} + \tau_\mathrm{p}$. Since this signal is periodic in $2T_{\mathrm{GRI},2}$ it can also be expressed using the Fourier series expansion. It will be convenient to assume in the following that $x_{2,\mathrm{r}}(t)$

7 $\mathrm{lcm}(a, b)$ is the least common multiple of a and b.

is periodic in $T = 2T_{\mathrm{GRI},2}N_2$, rather than just $2T_{\mathrm{GRI},2}$. In that case, the expansion takes on the form

$$\begin{aligned} x_{2,\mathrm{r}}[u] &= \sum_{l'=-\infty}^{\infty} c'_{x_{2,\mathrm{r}}}\left[l'\right] \mathrm{e}^{\mathrm{j}l'\frac{2\pi}{T}\left(uT_{\mathrm{up}}+\tau_{\mathrm{p}}\right)} \\ &= \sum_{l'=-\infty}^{\infty} c'_{x_{2,\mathrm{r}}}\left[l'\right] \mathrm{e}^{\mathrm{j}l'u\frac{2\pi}{N_1}} \mathrm{e}^{\mathrm{j}l'\frac{2\pi}{T}\tau_{\mathrm{p}}}, \end{aligned} \tag{6.19}$$

where the series coefficients can be obtained using Equation 6.15 above as

$$c'_{x_{2,\mathrm{r}}}\left[l'\right] = \begin{cases} c_{x_{2,\mathrm{r}}}[l], & \text{for } l' = lN_2,\ l \in \mathbb{Z} \\ 0, & \text{otherwise.} \end{cases} \tag{6.20}$$

Substituting Equation 6.19 and Equation 6.20 into Equation 6.18 yields

$$\begin{aligned} c^{\mathrm{d}}_{x_{2,\mathrm{r}}}[n] &= \frac{1}{N_1}\sum_{u=0}^{N_1-1}\sum_{l'=-\infty}^{\infty} c'_{x_{2,\mathrm{r}}}\left[l'\right] \mathrm{e}^{\mathrm{j}l'u\frac{2\pi}{N_1}} \mathrm{e}^{\mathrm{j}l'\frac{2\pi}{T}\tau_{\mathrm{p}}} \mathrm{e}^{-\mathrm{j}un\frac{2\pi}{N_1}} \\ &= \frac{1}{N_1}\sum_{l=-\infty}^{\infty} c_{x_{2,\mathrm{r}}}[l]\, \mathrm{e}^{\mathrm{j}l\frac{2\pi}{2T_{\mathrm{GRI},2}}\tau_{\mathrm{p}}} \underbrace{\sum_{u=0}^{N_1-1} \mathrm{e}^{\mathrm{j}u(lN_2-n)\frac{2\pi}{N_1}}}_{\substack{N_1,\ \text{for } (lN_2-n)=mN_1, \\ 0,\ \text{for } (lN_2-n)\neq mN_1.}}. \end{aligned} \tag{6.21}$$

It can be seen from the above equation that in order to calculate the n-th coefficient in the discrete Fourier series expansion, $c^{\mathrm{d}}_{x_{2,\mathrm{r}}}[n]$, one first needs to find all $l \in \mathbb{Z}$ for which $lN_2 - n$ is divisible by N_1. This requires some number theory.

The problem described above can be treated as a linear congruence equation[8]

$$lN_2 \equiv n \pmod{N_1}.$$

Methods of solving linear congruences can be found, for example, in reference [140]. As shown in [140], the above congruence has a solution for l if and only if n is divisible by the Greatest Common Divisor (GCD), d, of N_1 and N_2,

$$d = \gcd\left(N_1, N_2\right).$$

If a solution exists, it can be found using the extended Euclidean algorithm [140]. This algorithm yields integers w and z such that $wN_1 + zN_2 = d$. One solution to the congruence is then

$$l_0 = \frac{zn}{d},$$

and the other solutions are the numbers congruent to l_0 modulo $\frac{N_1}{d}$, i.e. the set of all solutions is given by

$$\mathcal{L}_n = \left\{ l \in \mathbb{Z}; l = l_0 + m\frac{N_1}{d}, m \in \mathbb{Z} \right\}. \tag{6.22}$$

8 For definition of the congruence relation see Appendix A.

The coefficients of the discrete Fourier series of the interference component can then be obtained from Equation 6.21 as

$$c^{\mathrm{d}}_{x_{2,\mathrm{r}}}[n] = \sum_{l \in \mathcal{L}_n} c_{x_{2,\mathrm{r}}}[l]\, \mathrm{e}^{\mathrm{j}l \frac{2\pi}{2T_{\mathrm{GRI},2}} \tau_{\mathrm{p}}}.$$

It is useful to note that the spectral coefficients $c_{x_{2,\mathrm{r}}}[l]$ in the above equation diminish with increasing $|l|$. Consequently, in practical calculations, l can be restricted to a range $|l| \leq \lceil 2T_{\mathrm{GRI},2} B_{x_{2,\mathrm{r}}} \rceil$, where $B_{x_{2,\mathrm{r}}}$ is a suitably chosen constant consistent with the bandwidth of the interfering signal. Recall also that $x_{2,\mathrm{r}}[u]$ is periodic in N_1. *This means that the CRI component at the phase detector is completely described by a set of N_1 Fourier coefficients*

$$\left\{ c^{\mathrm{d}}_{x_{2,\mathrm{r}}}[n] \right\}_{n=0}^{n=N_1-1}.$$

Finally, the Fourier coefficients of the real and imaginary parts of $x_{2,\mathrm{r}}[u]$, $c^{\mathrm{d}}_{x_{2,\mathrm{r},\mathcal{I}}}[n]$ and $c^{\mathrm{d}}_{x_{2,\mathrm{r},\mathcal{Q}}}[n]$, can be calculated from $c^{\mathrm{d}}_{x_{2,\mathrm{r}}}[n]$ as follows (see Equation A.1 and Equation A.2 in Appendix A):

$$c^{\mathrm{d}}_{x_{2,\mathrm{r},\mathcal{I}}}[n] = \frac{1}{2}\left[c^{\mathrm{d}}_{x_{2,\mathrm{r}}}[n] + \left(c^{\mathrm{d}}_{x_{2,\mathrm{r}}}[-n] \right)^* \right],$$

$$c^{\mathrm{d}}_{x_{2,\mathrm{r},\mathcal{Q}}}[n] = \frac{1}{2j}\left[c^{\mathrm{d}}_{x_{2,\mathrm{r}}}[n] - \left(c^{\mathrm{d}}_{x_{2,\mathrm{r}}}[-n] \right)^* \right].$$

Measurement Error Statistics

The signal at the input to the phase detector can be expressed as a superposition of the responses to the desired and interfering signal components:

$$x[u] = x_{1,\mathrm{r}}[u] + x_{2,\mathrm{r}}[u] = |\tau = 0| = \left| e_{\mathrm{b}}\left(\tau_{\mathrm{p}}\right) \right| + x_{2,\mathrm{r}}[u].$$

The in-phase and quadrature components of $x[u]$ are then given by

$$x_{\mathcal{I}}[u] \equiv \mathrm{Re}\left[x[u]\right] = \left| e_{\mathrm{b}}\left(\tau_{\mathrm{p}}\right) \right| + x_{2,\mathrm{r},\mathcal{I}}[u], \tag{6.23}$$

$$x_{\mathcal{Q}}[u] \equiv \mathrm{Im}\left[x[u]\right] = x_{2,\mathrm{r},\mathcal{Q}}[u],$$

and the carrier phase estimates (which in this setting correspond to the instantaneous phase estimation error, $\varepsilon[u]$) are obtained as

$$\hat{\theta}[u] = \varepsilon[u] = \angle x[u] = \arctan\left(\frac{x_{\mathcal{Q}}[u]}{x_{\mathcal{I}}[u]} \right). \tag{6.24}$$

As in the previous section, some simplifying assumptions will be made. Under high to moderate SIR conditions (SIR $>$ 10 or so) the power of the useful signal in the inphase component, $P^{\mathrm{t}}_{x_{1,\mathrm{r}}} = \left| e_{\mathrm{b}}(\tau_{\mathrm{p}}) \right|^2$, is significantly higher than the power of the interference component,

$$P^{\mathrm{t}}_{x_{2,\mathrm{r},\mathcal{I}}} = \sum_{n=0}^{N_1-1} \left| c^{\mathrm{d}}_{x_{2,\mathrm{r},\mathcal{I}}}[n] \right|^2,$$

and the interference term $x_{2,r,\mathcal{I}}[u]$ in Equation 6.23 can therefore be neglected. Equation 6.24 then becomes

$$\hat{\theta}[u] = \varepsilon[u] \approx \arctan\left(\frac{x_{2,r,\mathcal{Q}}[u]}{|e_b(\tau_p)|}\right) \approx \frac{x_{2,r,\mathcal{Q}}[u]}{|e_b(\tau_p)|}.$$

The spectrum of the phase measurement error can then be approximated by the following set of Fourier coefficients

$$c_\varepsilon^d[n] = \frac{c_{x_{2,r,\mathcal{Q}}}^d[n]}{|e_b(\tau_p)|},\ n = 0, 1, \ldots, N_1 - 1,$$

and finally, the time-averaged characteristics of the measurement error can be calculated as

$$\mu_\varepsilon^t = \mathrm{Av}[\varepsilon[u]] \approx \mathrm{Av}\left[\frac{x_{2,r,\mathcal{Q}}[u]}{|e_b(\tau_p)|}\right] = c_\varepsilon^d[0], \tag{6.25}$$

$$\begin{aligned} P_\varepsilon^t &= \mathrm{Av}\left[|\varepsilon[u]|^2\right] \\ &\approx \mathrm{Av}\left[\left|\frac{x_{2,r,\mathcal{Q}}[u]}{e_b(\tau_p)}\right|^2\right] \\ &= \sum_{n=0}^{N_1-1}\left|c_\varepsilon^d[n]\right|^2, \end{aligned} \tag{6.26}$$

and

$$\mathrm{var}^t[\varepsilon[u]] = P_\varepsilon^t - \left|\mu_\varepsilon^t\right|^2.$$

Referring to Equation 5.16 and Equation 5.17 in Chapter 5, the spectrum of the equivalent pseudorange measurement error and the basic pseudorange error statistics can be estimated as follows:

$$c_{\varepsilon_\rho}^d[n] = -\frac{c}{2\pi f_c} c_\varepsilon^d[n],\ n = 0, 1, \ldots, N_1 - 1, \tag{6.27}$$

$$\mu_{\varepsilon_\rho}^t = \mathrm{Av}\left[\varepsilon_\rho[u]\right] \approx c_{\varepsilon_\rho}^d[0], \tag{6.28}$$

$$P_{\varepsilon_\rho}^t = \mathrm{Av}\left[\left|\varepsilon_\rho[u]\right|^2\right] \approx \sum_{n=0}^{N_1-1}\left|c_{\varepsilon_\rho}^d[n]\right|^2. \tag{6.29}$$

The above results were derived under the assumption of high to moderate SIR. The simplifications applied during the derivation cannot be used under low SIR conditions (SIR < 10). This does not present a problem, however, as under such conditions eLoran receivers typically use CRI blanking to mitigate the interference, as will be described later in this chapter.

Discussion of Results

Figure 50 and Figure 51 below give the predicted pseudorange measurement error due to uncompensated CRI as a function of SIR and signal time offset, $\Delta\tau_2$, for coprime[9] and non-coprime GRIs, respectively. The plots show the mean error $\mu^{\mathrm{t}}_{\varepsilon_\rho}$ (bias) and RMS error

$$\mathrm{rms}^{\mathrm{t}}\left[\varepsilon_\rho\right] = \sqrt{P^{\mathrm{t}}_{\varepsilon_\rho}}$$

obtained using Equation 6.28 and Equation 6.29 above.

As would be intuitively expected, the measurement error is inversely proportional to the square root of the SIR. From the figures it can be seen that uncompensated CRI can cause pseudorange errors in the region of 1 m at a relatively moderate SIR of around 10 dB.

The error is highly sensitive to the time alignment between the cross-rating pulse trains, represented here by the time offset $\Delta\tau_2$. The fast, sinusoidal, variations are caused by the changing carrier phase relationship between the signals (recall that the time and carrier phase offsets are assumed to be related as $\Delta\theta_2 = -2\pi f_c \Delta\tau_2$). The slow variation in the magnitude of the error, which is only apparent for the non-coprime GRIs (Figure 51), is related to the pulsed nature of the signal and the phase codes used. It can also be seen from the figures that the pattern is periodic in the time offset, with a period given by the GCD of the cross-rating stations' PCIs (i.e. 20 μs and 200 μs in the examples given here). Note that, with coprime GRIs, the error is uniformly distributed across the whole range of time offsets (i.e. approximately uniformly distributed in space); however, with non-coprime GRIs, the distribution is not uniform and the peak error can be significantly higher than if coprime GRIs were used.

The error patterns show very little sensitivity to the master vs. secondary phase codes. In the examples chosen here, the desired station uses the secondary phase code and the interfering station uses the master code.

As can be seen from Figure 52 and Figure 53 below, the CRI-induced error is a complicated function of the cross-rating GRIs. Figure 52 shows the error when a GRI 6731 signal is interfered with a cross-rating signal which has the same phase code as the desired station; Figure 53 assumes different phase codes. There is a general decreasing trend in the magnitude of the error with increasing GRI of the interfering station. This is in line with expectations, as there are less interfering pulses per unit time. However, there are a large number of outliers that result in errors considerably above the main trend line. As also indicated in the figures, these outliers are mostly GRIs that are not coprime with the desired station's GRI. Apart from non-coprime GRIs, there are also other combinations of GRIs that cause excessive measurement error and these will be studied in the following section.

Interestingly, Figure 53 also shows a significant portion of the GRIs falling below the trend line. However, the reader should bear in mind that this plot was generated for a particular value of the time offset between the interfering signals, $\Delta\tau_2$. With a different value of $\Delta\tau_2$ the same GRIs may appear above the trend line, and when the error is averaged over the whole range of possible time offsets, all of the

9 Two GRIs are said to be *coprime*, or *mutually prime*, when the GCD of the GRI identifiers is equal to 1.

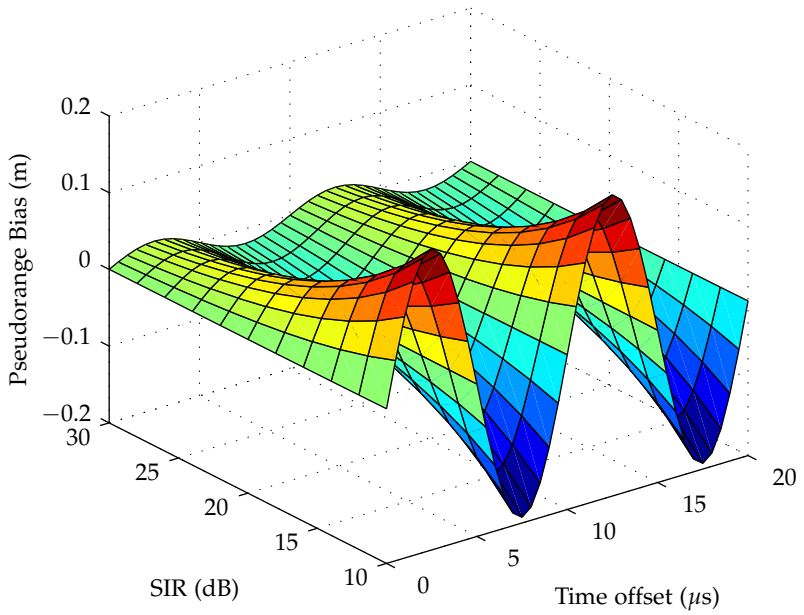

(a) Bias (max: 0.2 m)

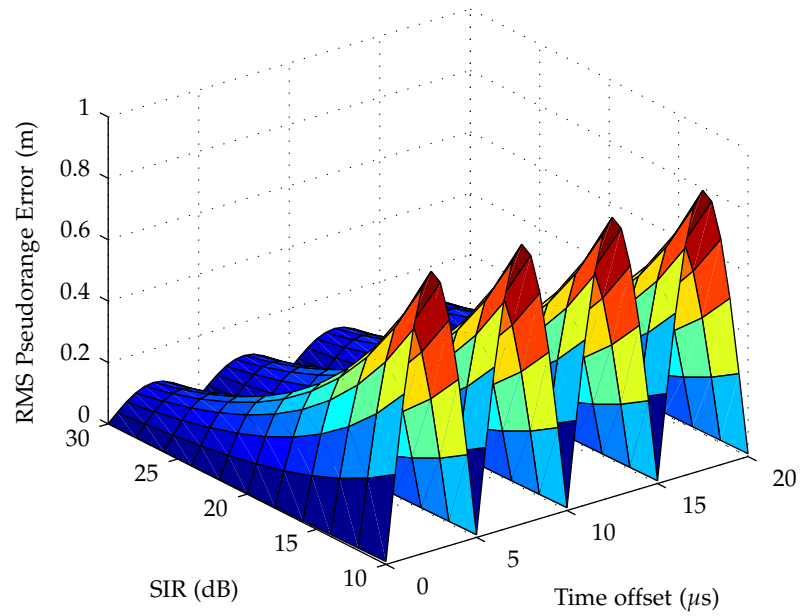

(b) RMS error (max: 1.0 m)

Figure 50: Pseudorange measurement error due to uncompensated CRI as a function of SIR and signal time offset $\Delta\tau_2$ for *coprime GRIs* as predicted by the DFD model; desired station: GRI 6731, secondary; interfering station: GRI 7499, master.

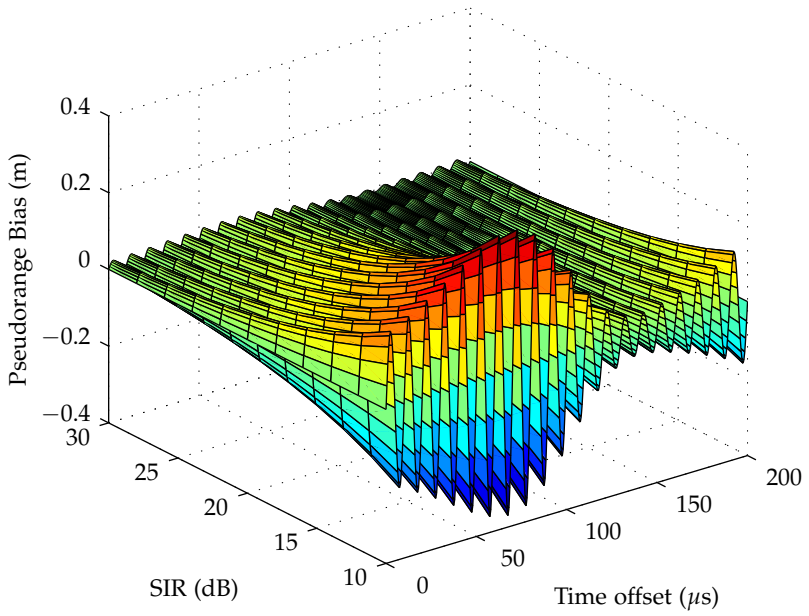

(a) Bias (max: 0.4 m)

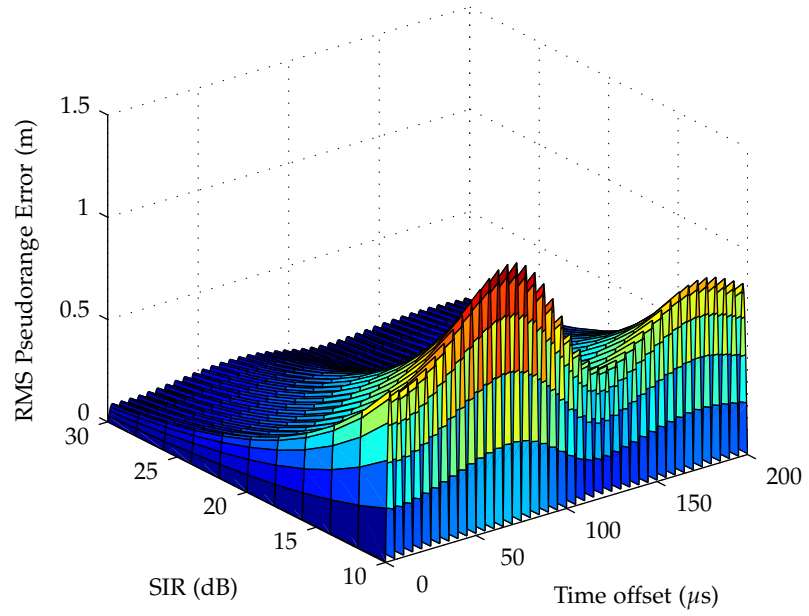

(b) RMS error (max: 1.3 m)

Figure 51: Pseudorange measurement error due to uncompensated CRI as a function of SIR and signal time offset $\Delta\tau_2$ for *non-coprime GRIs* as predicted by the DFD model; desired station: GRI 6730, secondary; interfering station: GRI 7490, master.

non-coprime GRIs will lie close to the trend line, as will be shown in Section 6.2.3.

Figure 54 is a close-up of the error vs. GRI plot in the area where the interfering GRI approaches that of the desired signal. As would be expected, a sharp increase in the measurement error can be seen in this region. The figure also compares the analytical predictions with results obtained by numerical simulations. As can be seen in the figure, there is a perfect agreement between the theory and simulation (more information on the methods of verification used in this thesis can be found in Chapter 8).

Figure 55 shows the power spectrum of the measurement error,

$$\left\{ \left| c_{\varepsilon_\rho}^{\mathrm{d}}[n] \right|^2 \right\}_{n=0}^{N_1-1},$$

obtained using Equation 6.27 above and expressed in dB relative to the strongest spectral component. Since the spectrum is an even and periodic function in frequency, only spectral components corresponding to frequencies between 0 Hz and half the sampling frequency, $1/(2T_{\mathrm{up}})$, are shown. It can be seen from the figure that, when the cross-rating GRIs are coprime, the error power is relatively homogeneously distributed over the whole range of frequencies, i.e. the error signal will have a noise-like character. On the contrary, when the GRIs are not coprime, the power is concentrated in a small number of frequency components, giving rise to a strong periodic error signal component.

Another noteworthy feature of uncompensated CRI, illustrated in Figure 56, is that the error does not average out. There is a certain maximum integration time beyond which further averaging does not improve performance. This is due to the fact that the eLoran phase codes are not balanced. This effect may be of particular importance in static monitoring receivers (e.g. for timing or reference station applications) where long integration periods may be used, and it confirms the need for additional receiver CRI mitigation algorithms. It should be noted that, in order to illustrate the peculiar nature of CRI, the GRIs in this example were intentionally selected so that the longer GRIs show a higher error (contrary to what would intuitively be expected).

6.2.3 *Performance in CRI: Stochastic Frequency Domain Model*

The deterministic model developed in the previous section can predict the measurement error at a single point in the coverage area, assuming that all signal parameters are time-invariant. The model provides a valuable insight into the nature of CRI but is of limited practical use - particularly the application to system coverage and performance prediction would be problematic. Coverage prediction models typically divide the area of interest into a grid of regularly spaced points and examine in turn the system's performance at each point. A point in the grid may represent an area of several hundreds or thousands km^2. While signal amplitudes can be considered constant within an area of this size, signal time offset and carrier phase may vary substantially within the grid cell (recall that the wavelength of the eLoran carrier is 3 km). Additional variability in signal timing arises when sky wave borne interference is considered (see Figure 18 in Chapter 3), and also ASFs may contribute to the spatial and temporal variability of the signal

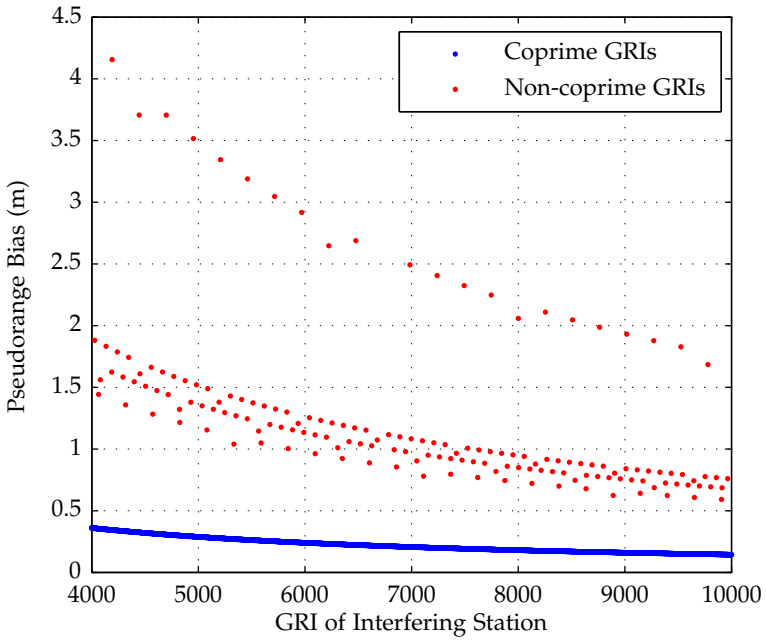

(a) Bias

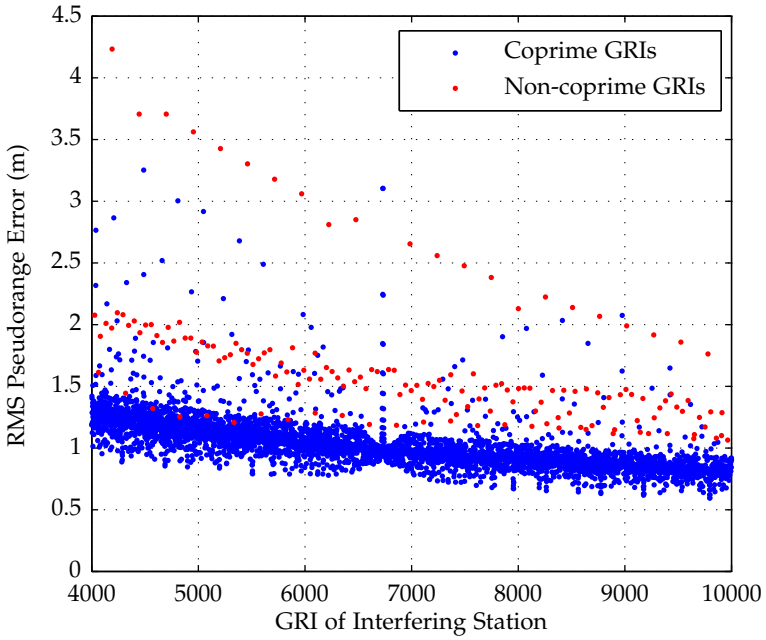

(b) RMS error

Figure 52: Pseudorange measurement error due to uncompensated CRI as a function of the interfering signal GRI as predicted by the DFD model; desired station: GRI 6731, secondary; interfering station: GRI as per horizontal axis, secondary; $\Delta\tau_2 = 2.5\,\mu$s; SIR $= 10$ dB.

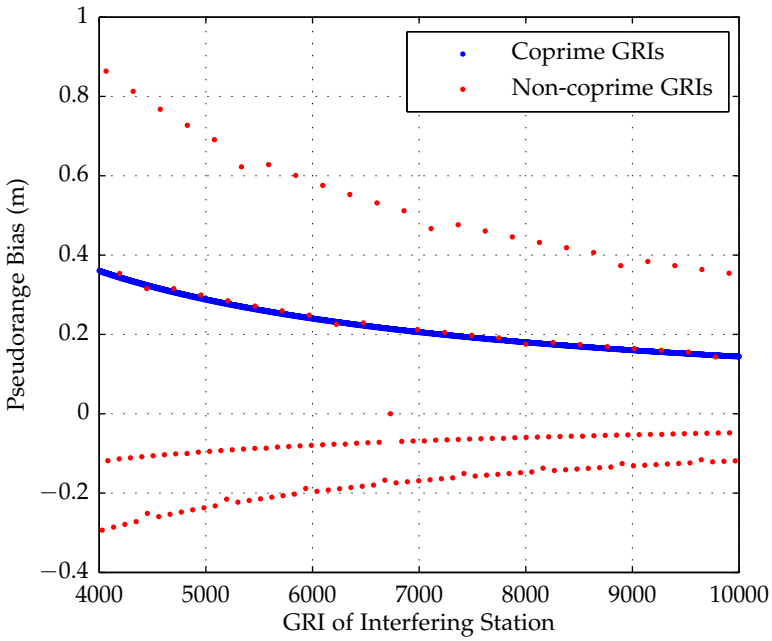

(a) Bias

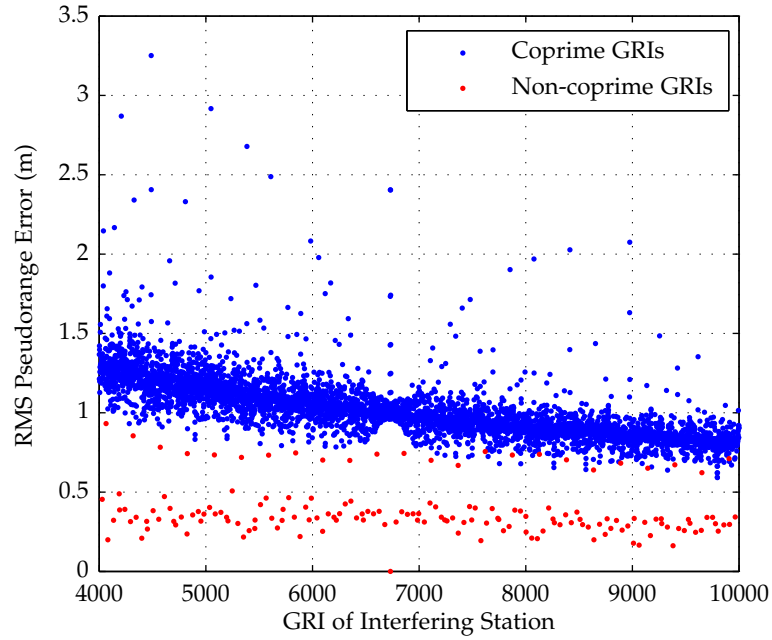

(b) RMS error

Figure 53: Pseudorange measurement error due to uncompensated CRI as a function of the interfering signal GRI as predicted by the DFD model; desired station: GRI 6731, secondary; interfering station: GRI as per horizontal axis, master; $\Delta\tau_2 = 2.5\,\mu$s; SIR $= 10$ dB.

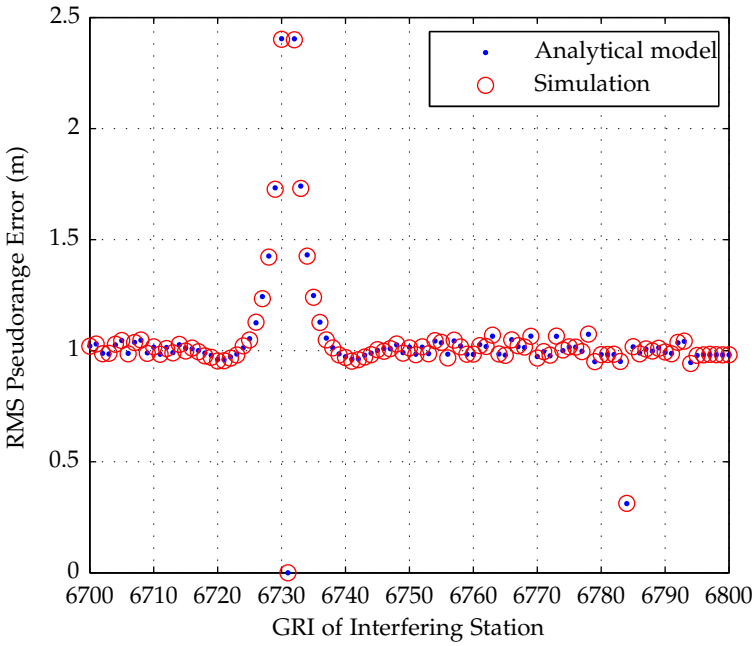

Figure 54: Pseudorange measurement error due to uncompensated CRI as a function of the interfering signal GRI as predicted by the DFD model (verification by simulation); desired station: GRI 6731, secondary; interfering station: GRI as per horizontal axis, master.

parameters. This motivates the development of a model in which the signal time (and carrier phase) offset is treated as a random variable, and the measurement error is calculated as the average error over the range of all possible time offsets. The resulting model will be referred to as the Stochastic Frequency Domain (SFD) model of uncompensated CRI.

Received Signal Model

Similarly as in the previous section, the received signal will be modeled as a sum of two cross-rating eLoran waveforms

$$\tilde{x}(t) = \underbrace{\tilde{s}(t;0,0,\mathcal{C}_1,T_{\mathrm{GRI},1})}_{\tilde{x}_1(t)} + \underbrace{\frac{1}{\sqrt{\mathrm{SIR}}}\tilde{s}\left(t;\Delta\tau_2,\overbrace{-2\pi f_c\Delta\tau_2}^{\Delta\theta_2},\mathcal{C}_2,T_{\mathrm{GRI},2}\right)}_{\tilde{x}_2(t)},$$

where $\tilde{x}_1(t)$ represents the desired signal component, and $\tilde{x}_2(t)$ is considered as interference ($T_{\mathrm{GRI},1} \neq T_{\mathrm{GRI},2}$). In line with the discussion above, the time offset $\Delta\tau_2$ will be treated as a random variable. For the sake of simplicity, it will be assumed that $\Delta\tau_{.2}$ is uniformly distributed between 0 and $2T_{\mathrm{GRI},2}$ (i.e. all possible values of the time offset are considered equally probable).

Signal Processing Model

For the purpose of this study, the signal processing model of Figure 48 (Chapter 5) will be modified slightly by moving the frequency down-

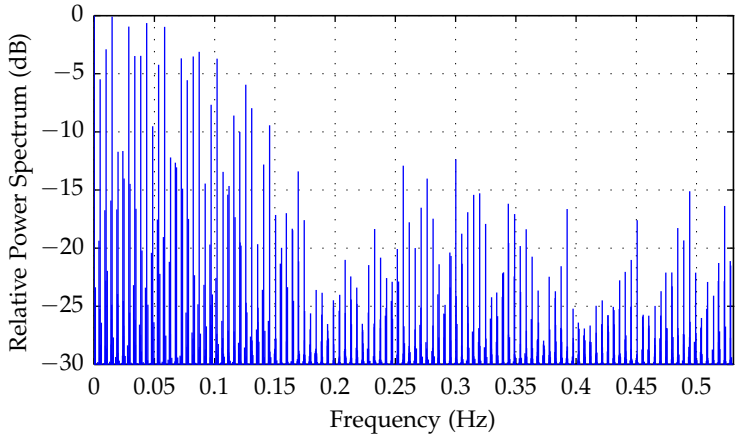

(a) Coprime GRIs; desired station: GRI 6731, secondary; interfering station: GRI 7499, master.

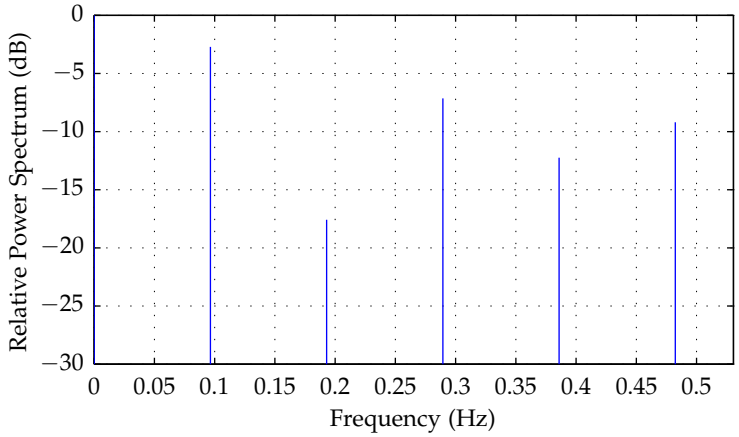

(b) Non-coprime GRIs; desired station: GRI 6731, secondary; interfering station: GRI 4081, master.

Figure 55: Power spectrum of the pseudorange measurement error due to uncompensated CRI as predicted by the DFD model.

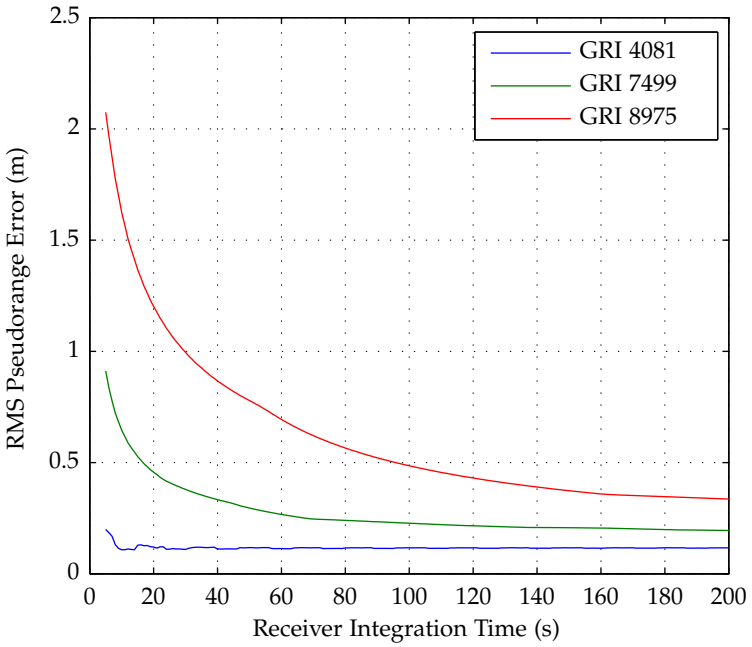

Figure 56: Pseudorange measurement error due to uncompensated CRI as a function of the receiver integration time as predicted by the DFD model; $\Delta\tau_2 = 2.5\,\mu$s; SIR $= 10$ dB; desired station: GRI 6731, secondary; interfering station: master.

conversion block behind the comb and phase-decoding filters and the phase correction block. Note that the order in which these operations are carried out does not matter as the frequency response of the filters and the correction block is invariant to a shift by f_c in frequency. As in the previous section, eLoran CRI mitigation algorithms will not be considered.

Measurement Error Process

The only source of measurement error in the present model is the cross-rating signal $\tilde{x}_2(t)$. For $\Delta\tau_2$ fixed, $\tilde{x}_2(t)$ is periodic in $2T_{\mathrm{GRI},2}$ (this case was investigated in detail in the previous section). It can be shown that if $\Delta\tau_2$ is considered random and uniformly distributed between 0 and $2T_{\mathrm{GRI},2}$, then $\tilde{x}_2(t)$ becomes a WSS random process [141]. Consequently, also the measurement error process will be stationary, and it can therefore be characterised by ensemble-averaged statistics (i.e. there is no need for time averaging):

$$\mu_\varepsilon^{\mathrm{a}} \overset{\text{stat.}}{=} \mathrm{E}[\varepsilon] = \mu_\varepsilon,$$

$$\mathrm{var}^{\mathrm{a}}[\varepsilon[u]] \overset{\text{stat.}}{=} \mathrm{E}\left[|\varepsilon - \mu_\varepsilon|^2\right] = \mathrm{var}[\varepsilon],$$

$$P_\varepsilon^{\mathrm{a}} \overset{\text{stat.}}{=} P_\varepsilon^{\mathrm{e}}$$

Desired Signal Component at the Phase Detector

As in the previous sections, the desired signal component at the input to the phase detector, $x_{1,\mathrm{r}}[u]$, can be shown to be given by

$$x_{1,\mathrm{r}}[u] = \left|e_{\mathrm{b}}\left(\tau_{\mathrm{p}}\right)\right|, \ \forall u \in \mathbb{Z},$$

i.e. it is equal to the (real) envelope of the filtered, desired, pulse at the sampling point.

Interference at the Phase Detector

As explained above, if $\Delta\tau_2$ is assumed to be uniformly distributed between 0 and $2T_{\mathrm{GRI},2}$ then the interference signal at the receiver input, $\tilde{x}_2(t)$, can be considered as a WSS random process. It is also easy to see that this process would have zero mean and, consequently, the signal after receiver filtering and phase correction, $\tilde{x}_{2,\mathrm{r}}(t)$, can also be considered as zero mean and WSS.

The next signal processing operation is the frequency down-conversion. It can be shown (see for example [48]) that the complex envelope $x_{2,\mathrm{r}}(t)$ obtained by the down-conversion of $\tilde{x}_{2,\mathrm{r}}(t)$ is again a zero mean WSS process, and that the I and Q components of the down-converted signal, $x_{2,\mathrm{r},\mathcal{I}}$ and $x_{2,\mathrm{r},\mathcal{Q}}$, resp. are uncorrelated, zero mean and their power is equal to the power of the filtered RF signal $\tilde{x}_{2,\mathrm{r}}(t)$:

$$\mathrm{E}\left[x_{2,\mathrm{r},\mathcal{I}}(t)\, x_{2,\mathrm{r},\mathcal{Q}}(t)\right] = 0, \tag{6.30}$$

$$\mathrm{E}\left[x_{2,\mathrm{r},\mathcal{I}}(t)\right] = \mathrm{E}\left[x_{2,\mathrm{r},\mathcal{Q}}(t)\right] = 0, \tag{6.31}$$

$$P^{\mathrm{e}}_{x_{2,\mathrm{r},\mathcal{I}}} = P^{\mathrm{e}}_{x_{2,\mathrm{r},\mathcal{Q}}} = \mathrm{var}\left[x_{2,\mathrm{r},\mathcal{I}}(t)\right] = \mathrm{var}\left[x_{2,\mathrm{r},\mathcal{Q}}(t)\right] = P^{\mathrm{e}}_{\tilde{x}_{2,\mathrm{r}}}. \tag{6.32}$$

Finally, the baseband signal $x_{2,\mathrm{r}}(t)$ is sampled at time instants defined by $t = uT_{\mathrm{up}} + \tau_{\mathrm{sp}}$, where T_{up} is the measurement update interval, τ_{sp} is a suitably selected sampling offset, and $u \in \mathbb{Z}$. Since the I and Q components of the baseband signal are stationary, the ensemble averaged statistics of the sampled signals, $x_{2,\mathrm{r},\mathcal{I}}[u]$, $x_{2,\mathrm{r},\mathcal{Q}}[u]$, are the same as those of the respective continous-time signals. It has been shown above that the I and Q components are zero mean. All that remains to be calculated is the power of the filtered RF signal, $P^{\mathrm{e}}_{\tilde{x}_{2,\mathrm{r}}}$. This can be done as follows.

Recall that, for $\Delta\tau_2$ fixed, the interference signal component $\tilde{x}_2(t)$ at the receiver input is periodic in $2T_{\mathrm{GRI},2}$, and can be described by a Fourier series with coefficients given by (see Chapter 2)

$$\begin{aligned} c_{\tilde{x}_2}[n] = &\left[S_e\left(\frac{n}{2T_{\mathrm{GRI},2}} - f_c\right)\mathrm{e}^{-\mathrm{j}2\pi\frac{n}{2T_{\mathrm{GRI},2}}\Delta\tau_2} + \right. \\ &\left. S_e\left(\frac{n}{2T_{\mathrm{GRI},2}} + f_c\right)\mathrm{e}^{-\mathrm{j}2\pi\frac{n}{2T_{\mathrm{GRI},2}}\Delta\tau_2}\right] \cdot \frac{S_b\left(\frac{n}{2T_{\mathrm{GRI},2}}\right)}{4T_{\mathrm{GRI},2}\sqrt{\mathrm{SIR}}} \\ \approx &\, S_e\left(\frac{|n|}{2T_{\mathrm{GRI},2}} - f_c\right) S_b\left(\frac{n}{2T_{\mathrm{GRI},2}}\right) \frac{\mathrm{e}^{-\mathrm{j}2\pi\frac{n}{2T_{\mathrm{GRI},2}}\Delta\tau_2}}{4T_{\mathrm{GRI},2}\sqrt{\mathrm{SIR}}}, \ n \in \mathbb{Z}. \end{aligned} \tag{6.33}$$

If $\Delta\tau_2$ is considered as a random variable uniformly distributed between 0 and $2T_{\text{GRI},2}$ then $\tilde{x}_2(t)$ becomes a WSS process. The (ensemble-averaged) PSD of $\tilde{x}_2(t)$ can then be shown to be (see e.g. [141])

$$D^{\text{e}}_{\tilde{x}_2}(f) = \sum_{n=-\infty}^{\infty} \text{E}\left[\left|c_{\tilde{x}_2}[n]\right|^2\right] \delta\left(f - \frac{n}{2T_{\text{GRI},2}}\right). \tag{6.34}$$

The PSD of signal $\tilde{x}_{2,\text{r}}(t)$ obtained from $\tilde{x}_2(t)$ by the receiver filtering is then given by

$$D^{\text{e}}_{\tilde{x}_{2,\text{r}}}(f) = \underbrace{\left|\tilde{H}_{\text{b}}(f) H_{\text{c}}(f) H_{\text{p}}(f)\right|^2}_{\left|\tilde{H}_{\text{f}}(f)\right|^2} D^{\text{e}}_{\tilde{x}_2}(f), \tag{6.35}$$

and consequently the power of $\tilde{x}_{2,\text{r}}(t)$ is

$$P^{\text{e}}_{\tilde{x}_{2,\text{r}}} = \int_{-\infty}^{\infty} D^{\text{e}}_{\tilde{x}_{2,\text{r}}}(f)\,\text{d}f = \sum_{n=-\infty}^{\infty} \left|\tilde{H}_{\text{f}}\left(\frac{n}{2T_{GRI,2}}\right)\right|^2 \text{E}\left[\left|c_{\tilde{x}_2}[n]\right|^2\right].$$

By substituting from Equation 6.33, noting that $|c_{\tilde{x}_2}[n]|$ does not depend on $\Delta\tau$ (and therefore there is no need for the ensemble averaging) and using the fact that $\tilde{H}_{\text{f}}(f)$, $S_e(f)$, and $S_b(f)$ are even functions of frequency, the expression for the interference power becomes

$$P^{\text{e}}_{\tilde{x}_{2,\text{r}}} \approx \sum_{n=0}^{\infty} \frac{\left|\tilde{H}_{\text{f}}\left(\frac{n}{2T_{GRI,2}}\right) S_e\left(\frac{n}{2T_{\text{GRI},2}} - f_c\right) S_b\left(\frac{n}{2T_{\text{GRI},2}}\right)\right|^2}{8 \cdot \text{SIR} \cdot T^2_{\text{GRI},2}}. \tag{6.36}$$

Measurement Error Statistics

By the same reasoning as in Section 6.2.2, assuming again that SIR > 1, and using the results derived above, the statistics of the phase measurement error $\varepsilon[u]$ can be determined as

$$\mu_\varepsilon \approx \text{E}\left[\frac{x_{2,\text{r},\mathcal{Q}}[u]}{|e_{\text{b}}(\tau_{\text{p}})|}\right] = 0, \tag{6.37}$$

$$P^{\text{e}}_\varepsilon = \text{var}[\varepsilon[u]] = \text{E}\left[|\varepsilon[u]|^2\right] \approx \text{E}\left[\left|\frac{x_{2,\text{r},\mathcal{Q}}[u]}{e_{\text{b}}(\tau_{\text{p}})}\right|^2\right] = \frac{P^{\text{e}}_{\tilde{x}_{2,\text{r}}}}{\left|e_{\text{b}}(\tau_{\text{p}})\right|^2}, \tag{6.38}$$

where $P^{\text{e}}_{\tilde{x}_{2,\text{r}}}$ is calculated using Equation 6.36 above.

The equivalent pseudorange error characteristics can be calculated in the same manner as before:

$$\mu_{\varepsilon_\rho} = -\frac{c}{2\pi f_{\text{c}}}\mu_\varepsilon = 0,$$

$$P^{\text{e}}_{\varepsilon_\rho} = \left(\frac{c}{2\pi f_{\text{c}}}\right)^2 P^{\text{e}}_\varepsilon. \tag{6.39}$$

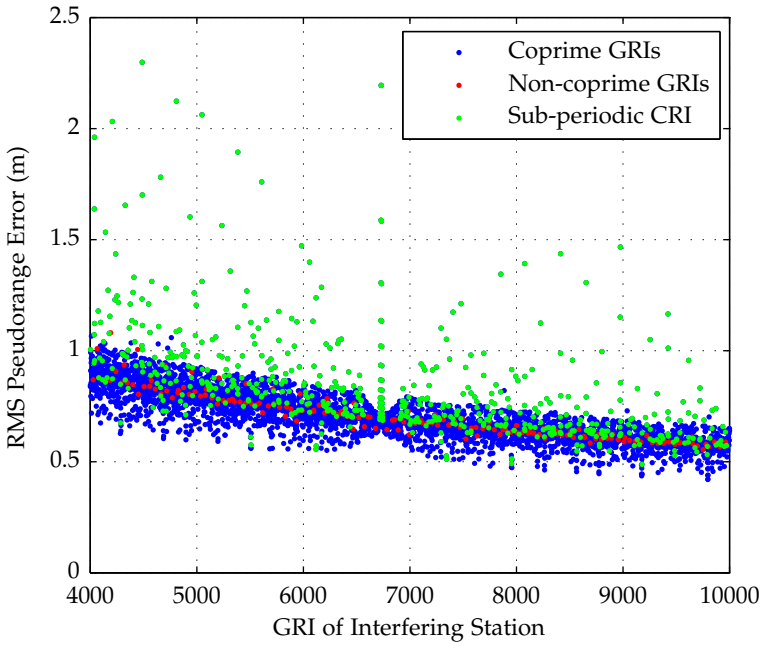

Figure 57: RMS pseudorange measurement error due to uncompensated CRI as a function of the interfering signal GRI as predicted by the SFD model; desired signal: GRI 6731, secondary; interfering signal: GRI as per horizontal axis, secondary; SIR = 10 dB.

Discussion of Results

Figure 57 gives the pseudorange measurement error due to uncompensated CRI as a function of the interfering signal GRI, as predicted by the stochastic (SFD) model developed in this section. The figure shows the RMS error

$$\text{rms}\left[\varepsilon_\rho\right] = \sqrt{P^{\text{e}}_{\varepsilon_\rho}}$$

for a GRI 6731 station and SIR = 10 dB, calculated using Equation 6.39 (the measurement bias, μ_{ε_ρ}, is zero for any combination of GRIs, as shown above). The SFD model assumes that the cross-rating pulse trains are randomly aligned in time and calculates the average measurement error over all possible time-alignments between the pulse trains. The results presented here are therefore independent of the signal time offset.

Figure 58 shows a close-up of the measurement error vs. GRI plot in the area where the interfering GRI approaches that of the desired signal. The figure compares the predictions of the SFD model with results obtained by averaging the error calculated using the DFD method developed in the previous section over the whole range of possible time offsets. As can be seen in the figure, there is a perfect agreement between the two approaches.

Figure 57 bears a strong resemblance to Figure 52 and Figure 53 of the previous section. As expected, the error shows a decreasing trend with increasing GRI of the interfering signal. The only substantive difference is that all non-coprime GRIs (shown in red) now appear close

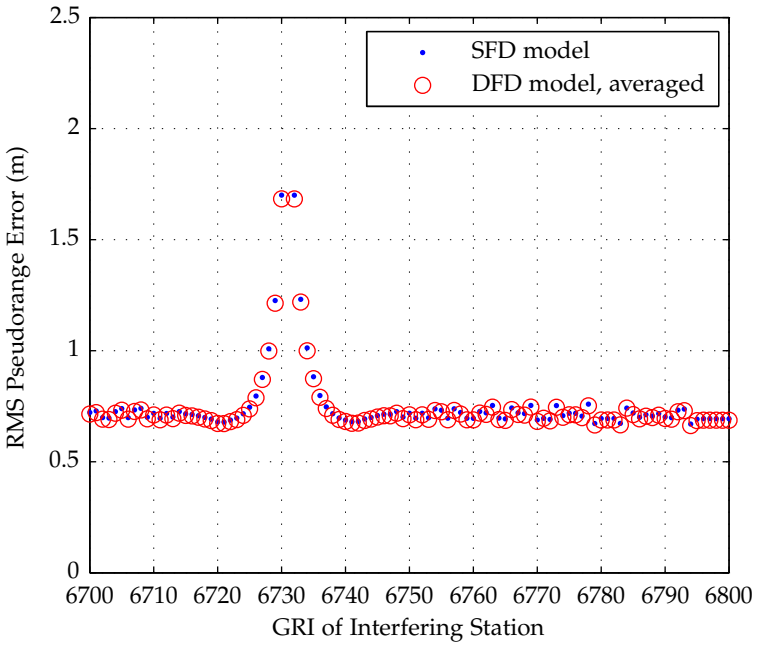

Figure 58: RMS ranging error due to uncompensated CRI as a function of the interfering signal GRI as predicted by the SFD model (verification against the DFD model); desired station: GRI 6731, secondary; interfering station: GRI as per horizontal axis, master; SIR = 10 dB.

to the trend line and there are no outliers below the line. This is an expected result of the averaging applied in the SFD model.

However, it can be seen from Figure 57 that there are still a considerable number of coprime GRIs that can give rise to excessive measurement error. What exactly is the cause of this error? On closer examination, it can be seen that the error peaks occur when the ratio of the GRIs in question is close to a simple fraction, such as $1/2$, $2/3$, $3/4$, etc. The reason for this is best understood by an example. Consider GRIs 4001 and 6001. These GRIs are coprime, and so their common period is several hundred seconds, however, their ratio is very close to $2/3$. This means that when the pulse groups overlap then after only three repetitions of GRI 4001 (two repetitions of 6001) they overlap again and the time offset of one pulse group with respect to the other changes by only 10 μs (one Loran carrier cycle) between the two overlap situation. Moreover, after six GRIs of 4001 (four GRIs of 6001), the overlapping pulses can colide with exactly the same phase codes (recall that the phase codes repeat after two GRIs). This *sub-periodic interference* pattern will persist until the cross-rating pulse groups separate or the phase coding suppresses the interference.

Farey Sequences

The above example explains the mechanism that causes the sub-periodic CRI. A question that remains to be answered is how to effectively identify the GRIs that are likely to result in this kind of interference. A possible algorithm is proposed below that makes use of a mathematical construct called the *Farey sequence*.

The Farey sequence φ_N of order N is the ascending sequence of irreducible fractions between 0 and 1 whose denominators do not exceed N [142]. For example, the Farey sequences of order 1 to 4 are:

$$\varphi_1 = \left\{ \frac{0}{1}, \frac{1}{1} \right\},$$

$$\varphi_2 = \left\{ \frac{0}{1}, \frac{1}{2}, \frac{1}{1} \right\},$$

$$\varphi_3 = \left\{ \frac{0}{1}, \frac{1}{3}, \frac{1}{2}, \frac{2}{3}, \frac{1}{1} \right\},$$

$$\varphi_4 = \left\{ \frac{0}{1}, \frac{1}{4}, \frac{1}{3}, \frac{1}{2}, \frac{2}{3}, \frac{3}{4}, \frac{1}{1} \right\}.$$

A MATLAB code to generate Farey sequences of any given order is given in Appendix A. The sequences can be used for the identification of sub-periodic CRI as follows:

1. Generate a Farey sequence of order N. The sequence order determines the maximum separation between the overlapping pulse groups (expressed in multiples of GRIs) that is considered potentially harmful. GRIs that result in sub-periodic overlaps separated in time by more than N group repetition intervals will not be included in the analysis. For simplicity, this example assumes $N = 4$. In practise, the order needs to be considerably higher in order to highlight all the harmful GRI combinations, as discussed further below.

2. Modify the Farey sequence by omitting the first element (0) and including the reciprocals of all remaining elements.

   In this example, the modified sequence would be given by

   $$\varphi'_4 = \left\{ \frac{1}{4}, \frac{1}{3}, \frac{1}{2}, \frac{2}{3}, \frac{3}{4}, \frac{1}{1}, \frac{4}{3}, \frac{3}{2}, \frac{2}{1}, \frac{3}{1}, \frac{4}{1} \right\}.$$

3. The GRIs that may result in sub-periodic CRI can then be found by taking

   $$T_{\mathrm{GRI},\varphi'_N}[m] = \mathrm{round}\left(\varphi'_N[m] \cdot T_{\mathrm{GRI},1} \cdot 10^5 \right) \cdot 10^{-5}, \quad m \in \left\{ 1, 2, \ldots, \left\| \varphi'_N \right\| \right\},$$

   and excluding all values that fall outside the range of GRIs prescribed by the signal specification. $T_{\mathrm{GRI},1}$ in the above is the GRI of the desired station (expressed in seconds).

   For example, based on the Farey sequence of order 4, the GRIs that can interfere with $T_{\mathrm{GRI},1} = 6731 \cdot 10^{-5}$ s would be predicted to be

   $$T_{\mathrm{GRI},\varphi'_4} = \{4487, 5048, 6731, 8975\} \cdot 10^{-5}.$$

4. The last step is to assess the change in time offset of the interfering pulse group with respect to the desired one between two successive overlap situations (denoted here $\Delta\tau_{\mathrm{sub}}$). If the magnitude of this change is greater than a certain threshold value $\Delta\tau_{\mathrm{sub,max}}$,

the interference is suppressed by phase codes and the GRI in question is not considered to interfere. On the basis of numerical experiments, a threshold value of $\Delta\tau_{\text{sub,max}} = 150\,\mu\text{s}$ (i.e. approximately half the pulse duration) is deemed appropriate. The time offset $\Delta\tau_{\text{sub}}$ for the m-th GRI in $T_{\text{GRI},\varphi'_N}$ can simply be calculated as follows:

$$\Delta\tau_{\text{sub}}[m] = a_m \cdot T_{\text{GRI},1} - b_m \cdot T_{\text{GRI},\varphi'_N}[m],$$

where a_m and b_m are the numerator and denominator of the m-th fraction in φ'_N.

For the example considered above, the time offsets $\Delta\tau_{\text{sub}}$ would be calculated to be $10\,\mu\text{s}$, $10\,\mu\text{s}$, $0\,\mu\text{s}$ and $-10\,\mu\text{s}$. Since all four values are below the threshold given by $\Delta\tau_{\text{sub,max}}$, the GRIs in $T_{\text{GRI},\varphi'_4}$ all have the potential to cause sub-periodic CRI. Indeed, looking at Figure 57, it can be seen that these GRIs give measurement errors far above the average (2.3 m, 2.1 m, 3.7 m and 1.5 m, respectively).

The above assessment also needs to be carried out for GRIs in the vicinity of those identified in step 3, as these will also produce ratios close to the Farey points, φ'_N, and may therefore also lead to sub-periodic interference. The number of adjacent GRIs that need to be considered is essentially determined by the value of $\Delta\tau_{\text{sub,max}}$.

For example, the examination of GRIs adjacent to the first interfering GRI identified above, GRI 4487, shows that all GRIs between 4483 and 4492 give $|\Delta\tau_{\text{sub}}| < 150\,\mu\text{s}$, and therefore the whole range should be considered as interference to the desired GRI.

In the above example a Farey sequence of order $N = 4$ was used, which resulted in only four GRIs being flagged as interferring in step 3 (and several adjacent GRIs identified in step 4). However, it is clear from Figure 57 that the actual number of GRIs that cause sub-periodic CRI is much higher, and therefore a higher order Farey sequence must be used. Numerical experiments suggest that all potential sub-periodic interference can be reliably identified when $N = 40$ and $\Delta\tau_{\text{sub,max}} = 150\,\mu\text{s}$; as such, these values are used in this analysis. This is also illustrated in Figure 57 by the green data points.

6.2.4 *Performance in CRI: Multiple Interferers*

In the previous sections, only a single interfering signal was considered. In a realistic scenario, one must deal with multiple cross-rating eLoran signals, as well as ground wave vs. sky wave borne interference. This section extends the SFD model of Section 6.2.3 to include these aspects of CRI.

Received Signal Model

The received signal will be modeled as a superposition of the desired eLoran signal, $\tilde{x}_1(t)$, and N_{CRI} interfering eLoran waveforms, $\tilde{x}_{m,1}(t)$,

$m = 2, 3, \ldots, N_{\text{CRI}} + 1$, including their respective first-hop sky waves, $\tilde{x}_{m,2}(t)$:

$$\tilde{x}(t) = \widetilde{x}_1(t) + \underbrace{\sum_{m=2}^{N_{\text{CRI}}+1} \left[\tilde{x}_{m,1}(t) + \tilde{x}_{m,2}(t)\right]}_{\tilde{x}_{\text{CRI}}(t)}. \tag{6.40}$$

Consistent with previous sections, it will be assumed that the desired signal has a unit amplitude and a zero time and carrier phase offset

$$\widetilde{x}_1(t) = \tilde{s}(t; 0, 0, C_1, T_{\text{GRI},1}).$$

The combined interference waveform is denoted

$$\tilde{x}_{\text{CRI}}(t) \equiv \sum_{m=2}^{N_{\text{CRI}}+1} \left[\tilde{x}_{m,1}(t) + \tilde{x}_{m,2}(t)\right].$$

The ground wave and sky wave components of the interfering signal, respectively, will be modelled as follows

$$\tilde{x}_{m,1}(t) = \frac{1}{\sqrt{\text{SIR}_{m,1}}}\tilde{s}\left(t; \Delta\tau_{m,1}, \overbrace{-2\pi f_c \Delta\tau_{m,1}}^{\Delta\theta_{m,1}}, C_m, T_{\text{GRI},m}\right),$$

$$\tilde{x}_{m,2}(t) = \frac{1}{\sqrt{\text{SIR}_{m,2}}}\tilde{s}\left(t; \Delta\tau_{m,2}, \overbrace{-2\pi f_c \Delta\tau_{m,2}}^{\Delta\theta_{m,2}}, C_m, T_{\text{GRI},m}\right).$$

The SIR values $\text{SIR}_{m,1}$, $\text{SIR}_{m,2}$ are assumed constant in this analysis (recall that the signal amplitudes are unlikely to change significantly over a small geographical area and short time periods comparable with the common period of the signals).

In accordance with the model developed in the previous section, the time offsets of the interfering signals, $\Delta\tau_{m,1}$ and $\Delta\tau_{m,2}$, are modelled as random variables uniformly distributed between 0 and $2T_{\text{GRI},m}$. It is assumed that the different time offsets are statistically independent of each other (for any combination of the variables).

The carrier phase offsets, $\Delta\theta_{m,1}$ and $\Delta\theta_{m,2}$, are assumed to be related to the time offsets as shown in Equation 6.40 above.

Finally, it is assumed that $T_{\text{GRI},1} \neq T_{\text{GRI},m}$, $m = 2, 3, \ldots, N_{\text{CRI}} + 1$.

Signal Processing Model

As in the previous section, the signal processing model of Figure 48 (Chapter 5) will be modified by moving the frequency down-conversion block behind the comb and phase-decoding filters and the phase correction block. eLoran CRI mitigation algorithms will not be considered.

Measurement Error Process

Since the time offsets $\Delta\tau_{m,1}$ and $\Delta\tau_{m,2}$, $m = 2, 3, \ldots, N_{\text{CRI}} + 1$, are assumed to be uniformly distributed between 0 and $2T_{\text{GRI},m}$, the respective interference components $\tilde{x}_{m,1}$ and $\tilde{x}_{m,2}$, can be considered as stationary processes. The sum of stationary processes is again a stationary process (see e.g. reference [143]). Since the disturbance is stationary,

also the measurement error will be stationary, and the receiver performance can therefore be adequately described by ensemble-averaged characteristics.

Desired Signal Component at the Phase Detector

As in the previous sections the desired signal component at the input to the phase detector, $x_{1,\mathrm{r}}[u]$, is given by

$$x_{1,\mathrm{r}}[u] = \left|e_{\mathrm{b}}\left(\tau_{\mathrm{p}}\right)\right|, \ \forall u \in \mathbb{Z}.$$

Interference at the Phase Detector

By the same reasoning as in the previous section, it can be shown that the I and Q components of the combined interference signal at the input to the phase detector, $x_{\mathrm{CRI,r},\mathcal{I}}[u]$ and $x_{\mathrm{CRI,r},\mathcal{Q}}[u]$, resp. are uncorrelated, zero mean, stationary processes, and their power is equal to the power of the combined interference waveform after filtering by the input bandpass filter, comb filter and phase decoding filter, $P^{\mathrm{e}}_{\tilde{x}_{\mathrm{CRI,r}}}$.

The PSD of a sum of independent, stationary, zero mean random processes is equal to the sum of the PSDs of the individual processes [143]. This means that the power of the filtered combined interference waveform, $P^{\mathrm{e}}_{\tilde{x}_{\mathrm{CRI,r}}}$, can be obtained simply by summing the power contributions of each interfering component

$$P^{\mathrm{e}}_{\tilde{x}_{\mathrm{CRI,r}}} = \sum_{m=2}^{N_{\mathrm{CRI}}+1} P^{\mathrm{e}}_{\tilde{x}_{m,1,\mathrm{r}}} + P^{\mathrm{e}}_{\tilde{x}_{m,2,\mathrm{r}}}, \tag{6.41}$$

where (see previous section)

$$P^{\mathrm{e}}_{\tilde{x}_{m.i,\mathrm{r}}} \approx \sum_{n=0}^{\infty} \frac{\left|\tilde{H}_{\mathrm{f}}\left(\frac{n}{2T_{GRI,m}}\right) S_e\left(\frac{n}{2T_{\mathrm{GRI},m}} - f_c\right) S_b\left(\frac{n}{2T_{\mathrm{GRI},m}}\right)\right|^2}{8\mathrm{SIR}_{m,i}\left(T_{\mathrm{GRI},m}\right)^2}, \ i = 1,2.$$

Measurement Error Statistics

By the same reasoning as in Section 6.2.2, assuming that $P^{\mathrm{e}}_{\tilde{x}_{\mathrm{CRI,r}}} \ll \left|e_{\mathrm{b}}\left(\tau_{\mathrm{p}}\right)\right|^2$ (a reasonable assumption for a high to moderate SIR and a limited number of interferers), and using the results derived above, the basic statistics of the phase measurement error $\varepsilon[u]$ can be determined as

$$\mu_\varepsilon \approx \mathrm{E}\left[\frac{x_{\mathrm{CRI,r},\mathcal{Q}}[u]}{\left|e_{\mathrm{b}}\left(\tau_{\mathrm{p}}\right)\right|}\right] = 0,$$

and

$$P^{\mathrm{e}}_{\varepsilon} = \mathrm{var}[\varepsilon[u]] = \mathrm{E}\left[\left|\varepsilon[u]\right|^2\right] \approx \mathrm{E}\left[\left|\frac{x_{\mathrm{CRI,r},\mathcal{Q}}[u]}{e_{\mathrm{b}}\left(\tau_{\mathrm{p}}\right)}\right|^2\right] = \frac{P^{\mathrm{e}}_{\tilde{x}_{\mathrm{CRI,r}}}}{\left|e_{\mathrm{b}}\left(\tau_{\mathrm{p}}\right)\right|^2},$$

where $P^{\mathrm{e}}_{\tilde{x}_{\mathrm{CRI,r}}}$ can be calculated using Equation 6.41 above. By substituting for $P^{\mathrm{e}}_{\tilde{x}_{\mathrm{CRI,r}}}$ from Equation 6.41, the phase measurement error can also be expressed simply as

$$P^{\mathrm{e}}_{\varepsilon} = \sum_{m=2}^{N_{\mathrm{CRI}}+1} P^{\mathrm{e}}_{\varepsilon,m,1} + P^{\mathrm{e}}_{\varepsilon,m,2},$$

where $P^{\mathrm{e}}_{\varepsilon,m,1}$ and $P^{\mathrm{e}}_{\varepsilon,m,2}$ is the power of the measurement error due to the ground wave and sky wave component of the m-th interferer, respectively, which can be calculated using the SFD model from the previous section.

The pseudorange measuerment error is calculated from the phase measurement error using Equation 6.39 above.

Discussion of Results

The above analysis shows that, under the assumption of uniformly distributed time offsets and high to moderate SIR, the combined effect of multiple interferers (incl. sky wave borne CRI) is simply the sum of their individual measurement error contributions (expressed in terms of power) which can be calculated using the SFD model presented in Section 6.2.3. The validity of this result has been verified against computer simulations (see Chapter 8).

6.2.5 *Mitigating CRI by Blanking: Evaluating the Blanking Loss*

As explained in Chapter 5, CRI blanking works by eliminating from the received data all eLoran pulses that are overlapped by signals from other rates. In this way it is possible to completely suppress the interference; however, the blanking also causes a loss of useful signal energy as there are less pulses to integrate over. This then affects the receiver performance in the presence of noise.

The aim of this section is to develop tools to evaluate the signal loss associated with CRI blanking. The results of this analysis will then be used in the following section to quantify the residual impact of CRI on the receiver performance.

Received Signal Model

For the purpose of this analysis, it will be sufficient to model the received eLoran signals as rectangular pulse trains, as illustrated in Figure 59. An eLoran pulse will be represented by a window of width w_1. In order to provide a conservative estimate of the blanking loss, w_1 will be set equal to the full pulse width $w_1 = 300\,\mu$s; however, it should be noted that a shorter window may be appropriate for some receiver designs as the blanking is only needed when the leading edge of the desired pulse is overlapped.

In the following, a rectangular pulse train having only one pulse per period will be referred to as *simple pulse train*.

Signal Processing Model

This analysis makes use of the signal processing model shown in Figure 37. It will be assumed that the receiver uses the same blanking strategy as is used on dual-rated Loran transmitters, i.e. that it discards

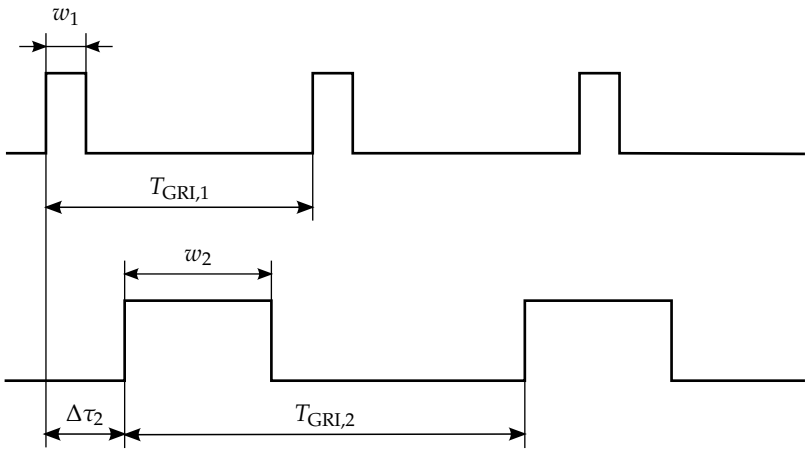

Figure 59: Received signal model for the blanking loss evaluation (not to scale).

all pulses of the desired signal that overlap any part of the blanking interval of the cross-rating signal.

In accordance with [47], it will be assumed that the blanking interval extends from 900 μs preceding the first pulse of the group of the cross-rating signal to 1600 μs after the last. This is illustrated in Figure 59 which shows the blanking interval as a rectangular window of width $w_2 = 9500\,\mu$s.

As is shown later in Chapter 8, this simple model provides results that are in a very good agreement with data obtained from a commercial eLoran receiver during laboratory simulator experiments.

Blanking Loss

The *blanking loss* is defined here as the proportion of pulses of the desired signal that are overlapped (fully or partially) by the blanking interval of the cross-rating signal, assuming that the observation interval grows without bound. The rest of this section considers three approaches to calculating this quantity.

Brute Force Approach to Blanking Loss Evaluation

As discussed earlier, in the first approximation CRI can be considered a deterministic phenomenon. The transmitter waveforms are periodic and consequently, the overlap patterns between eLoran pulse trains received at a particular location can also be considered periodic. This means that the analysis of the overlap patterns can be restricted to a well-defined time interval T_o, referred to here as the *overlap time*, after which the pattern starts to repeat[10]. The overlap time for two cross-rating signals with GRIs $T_{GRI,1}$ and $T_{GRI,2}$ (expressed in seconds) can be calculated as

$$T_o = \text{lcm}\left(2T_{GRI,1} \cdot 10^5, 2T_{GRI,2} \cdot 10^5\right) \cdot 10^{-5}. \tag{6.42}$$

10 Note however, that the CRI-induced phase estimation error may have a period which is longer than T_o, as the length of the receiver update interval, T_{up}, should also be taken into account.

Calculating the blanking loss is then equivalent to counting the number of overlapped pulses within the overlap time.

This calculation can be accomplished in a straightforward manner by generating the pulse arrival times for the two cross-rating pulse trains and directly counting the number of overlaps on a time interval equal to T_o. This brute force approach is simple to implement but it is computationally intensive and would be impractical for use in coverage and performance prediction.

Number-Theoretic Approach to Blanking Loss Evaluation

Finding an analytical solution to the pulse coincidence problem outlined above has proved to be a surprisingly challenging task, which had been tackled by several researchers before. The exact solution requires the application of some number theoretic methods, specifically, use will be made of the theory of *linear congruences*. The concept of linear congruences was successfully applied to the pulse coincidence problem by Miller and Schwarz in [144]. In that paper, the authors determined the coincidence time fraction for two pulse trains with both a fixed initial phase and a randomly varying phase. Their method was further refined by Friedman [145] and can be restated as follows, in a way that does not require any special knowledge of number theory.

Consider two simple pulse trains, as shown in Figure 59. The use of the number theoretic approach requires that all values in the analysis are integral multiples of some (arbitrary) number, p:

$$\begin{aligned} w_1 &= up, \quad T_{\mathrm{GRI},1} = mp, \quad \Delta\tau_2 = rp. \\ w_2 &= vp, \quad T_{\mathrm{GRI},2} = np, \end{aligned}$$

Let $g = \gcd(m,n)$ and $M = \operatorname{lcm}(m,n)$. Next, form all possible differences $x_2 - x_1$, where

$$\begin{aligned} x_1 &= 1, 2, \ldots, u \\ x_2 &= r+1, r+2, \ldots, r+v, \end{aligned} \tag{6.43}$$

and let N be the number of these differences which are divisible by g. The time fraction of coincidence of the two pulse trains is then [145]

$$f = \frac{N}{M}. \tag{6.44}$$

Friedman [145] derived an effective method of calculating N in Equation 6.44, following the pattern of Table 9. The table shows all differences $x_2 - x_1$, which satisfy the above condition, in the special case that $r = 0$ (i.e. zero initial time offset between the pulse trains). The quantities a_1, a_2, r_1 and r_2 in the table are defined by the following equations

$$\begin{aligned} u &= a_1 g + r_1 \quad 0 \leq r_1 < g, \\ v &= a_2 g + r_2 \quad 0 \leq r_2 < g, \end{aligned}$$

where $a_1, a_2 \in \mathbb{N}_0$.

More importantly for the purposes of this analysis, Friedman's technique can also be used to calculate the exact number of overlapped pulses per overlap time of the two pulse trains. This can be achieved by considering the following: The left edge of each overlap is determined

x_2	x_1	TOTAL PER ROW
1	$1, 1+g, 1+2g, \ldots, 1+a_1 g$	a_1+1
2	$2, 2+g, 2+2g, \ldots, 2+a_1 g$	a_1+1
⋮	⋮	⋮
r_1	$r_1, r_1+g, r_1+2g, \ldots, r_1+a_1 g$	a_1+1
r_1+1	$r_1+1, r_1+1+g, \ldots, r_1+1+(a_1-1)g$	a_1
⋮	⋮	⋮
g	$g, 2g, 3g, \ldots, a_1 g$	a_1
$g+1$	$1, 1+g, 1+2g, \ldots, 1+a_1 g$	a_1+1
⋮	⋮	⋮
	etc.	

Table 9: Friedman's pattern for the calculation of the coincidence fraction.

by the left edge of some pulse in one, or both, of our pulse trains. Since Table 9 is essentially a description of all units of coincidence of the two pulse trains [145], each occurrence of $x_1 = 1$ in that table can be interpreted as an overlap in which the left edge of a pulse from the first pulse train participates. Analogically for $x_2 = 1$ and the second pulse train. The total number of overlaps per overlap time, $N_{o,1,2}$, is then

$$N_{o,1,2} = n_1 + n_2 - 1,$$

where n_i, $i \in \{1, 2\}$ is the number of occurrences of $x_i = 1$ in Table 9. In the above equation it is necessary to subtract 1 from $n_1 + n_2$, as the overlap corresponding to $(x_1 = 1, x_2 = 1)$ has been counted twice. As shown in [145], the values of n_1 and n_2 for $r = 0$ can be deduced directly from Table 9.

Friedman's method will now be extended to allow for an arbitrary value of r, i.e. an arbitrary initial time offset between the pulse trains. This will be accomplished by constructing a pattern similar to Table 9 to enable the effective evaluation of n_1 and n_2; n_1 is again the number of occurrences of $x_1 = 1$ in the pattern, but n_2 is now the number of occurrences of $x_2 = r + 1$ (recall Equation 6.43).

For reasons that will be apparent later, the following quantities are defined:

$$\begin{aligned} u &= a_1 g + r_1 \quad 0 \leq r_1 < g, \\ r+1 &= a_1' g + r_1' \quad 0 \leq r_1' < g, \\ r+v &= a_2' g + r_2' \quad 0 \leq r_2' < g, \\ r &= a_2'' g + r_2'' \quad 0 \leq r_2'' < g, \end{aligned} \tag{6.45}$$

where $a_i, a_i', a_i'' \in \mathbb{N}_0$, $i \in \{1, 2\}$. First, the value of n_1 will be calculated. Recall that n_1 is the number of differences $x_2 - x_1$ which are divisible by

g and in which $x_1 = 1$ participates. The calculation of n_1 will proceed in two steps. From Equation 6.43, it can be seen that x_2 is in the range $r+1$ to $r+v$. Nevertheless, it will be assumed for the moment that x_2 can take on all integer values between 1 and $r+v$. In that case the values of x_2 that satisfy the above condition on the difference $x_2 - x_1$ can be written as

$$x_2 : 1, 1+g, 1+2g, \ldots, \begin{cases} 1 + a_2' g & \text{if } r_2' > 0, \\ 1 + (a_2' - 1)\, g & \text{if } r_2' = 0. \end{cases}$$

It can be seen from the above that the number of values of x_2 that satisfy the condition is given by

$$n_1' = \begin{cases} 1 + a_2' & \text{if } r_2' > 0, \\ a_2' & \text{if } r_2' = 0. \end{cases} \tag{6.46}$$

Assume now that x_2 takes on all integer values between 1 and r. In a similar fashion as above, it can be shown that there are n_1'' values that satisfy the condition on $x_2 - x_1$, where

$$n_1'' = \begin{cases} 1 + a_2'' & \text{if } r_2'' > 0, \\ a_2'' & \text{if } r_2'' = 0. \end{cases} \tag{6.47}$$

Hence, for x_2 in the range $r+1$ to $r+v$, the total number of differences that satisfy the condition is given by

$$n_1 = n_1' - n_1''. \tag{6.48}$$

The calculation of n_2 , i.e. the number of occurrences of $x_2 = r+1$ in the integer model of overlaps, proceeds in a similar manner as above. First, all permissible values of x_1 which result in differences $x_2 - x_1$ divisible by g will be enumerated. If $r_1' > 0$, these values are

$$x_1 : r_1', r_1' + g, r_1' + 2g, \ldots, \begin{cases} r_1' + a_1 g & \text{if } r_1 \geq r_1', \\ r_1' + (a_1 - 1)\, g & \text{if } r_1 < r_1'. \end{cases}$$

If $r_1' = 0$, then x_1 can take on values

$$x_1 : g, 2g, 3g, \ldots, a_1 g.$$

From the above it can be seen that

$$n_2 = \begin{cases} 1 + a_1 & \text{if } r_1 \geq r_1', \\ a_1 & \text{if } r_1 < r_1' \text{ or } r_1' = 0. \end{cases} \tag{6.49}$$

The total number of overlaps per overlap time of the two pulse trains, $N_{o,1,2}$, can then be calculated as

$$N_{o,1,2} = \begin{cases} n_1 + n_2 & \text{if } g \text{ does not divide } r, \\ n_1 + n_2 - 1 & \text{if } g \text{ divides } r. \end{cases} \tag{6.50}$$

(If r is divisible by g then the combination $(x_1 = 1, x_2 = r + 1)$ has been counted twice and therefore it is necessary to subtract 1 from $n_1 + n_2$).

Equation 6.45 to Equation 6.50 thus provide a method for the rapid evaluation of the total number of overlapped pulses over the common period of two pulse trains (i.e. the overlap time), eliminating the need for the computationally expensive iterations over individual pulses required by the brute force approach. The blanking loss is then calculated as the ratio of the number of overlapped pulses to the total number of pulses of the useful signal within the overlap time.

Figure 60 plots the blanking loss for three specific combinations of GRIs and different values of the time offset $\Delta\tau_2$ between the two cross-rating pulse trains as obtained using the number-theoretic method proposed by the candidate. Two important observations can be made here:

It can be seen from the figure that the blanking loss varies with the time offset between the pulse trains, i.e. with the user's position. The amount of variation in the pattern is proportionate to the GCD of the two GRIs. Note that the variation vanishes almost completely when the GRIs are coprime (GCD is 10 μs).

It is also apparent that the patterns in Figure 60 are periodic and it can be shown that the period is equal to the GCD of the GRIs. Similarly as in the preceding sections, it can be concluded that coprime GRIs should be favoured in the GRI selection as they spread the residual measurement error equally over all signal time offsets and are likely to give lower peak errors than non-coprime GRIs.

Stochastic Approach to Blanking Loss Evaluation

As discussed in Section 6.2.3, for the purpose of coverage and performance prediction it is appropriate to model the time offset between the cross-rating signals as a random variable with a uniform probability distribution. The quantity of interest is then the mean blanking loss obtained by averaging over all possible time offset values.

The pulse coincidence problem for random pulse trains has been studied by numerous researchers. In this study, the work of Stein and Johansen [146] and Self and Smith [147] was found to be especially useful. In reference [146] the authors presented a method for describing statistically the time coincidences among a set of random pulse trains. This method was later used in reference [147] to derive an expression for the mean period of simultaneous overlaps of multiple pulse trains, each of which is defined by a pulse duration, w_m, and a pulse period $T_{\mathrm{GRI},m}$. For two pulse trains, the expression takes the following form:

$$T_{\mathrm{c},1,2} = \frac{T_{\mathrm{GRI},1} T_{\mathrm{GRI},2}}{w_1 + w_2}.$$

Hence, on average, there is $1/T_{\mathrm{c},1,2}$ collisions per second; multiplying by the pulse period of the desired signal, $T_{\mathrm{GRI},1}$, then gives the percentage of overlapped pulses from pulse train 1, i.e. the blanking loss:

$$L_{\mathrm{b},1,2} = \frac{w_1 + w_2}{T_{\mathrm{GRI},2}}. \tag{6.51}$$

Note that the coincidence problem studied here is in fact equivalent to considering collisions between a pulse train with pulse duration of $(w_1 + w_2)$ and a pulse train with an infinitesimally small pulse duration

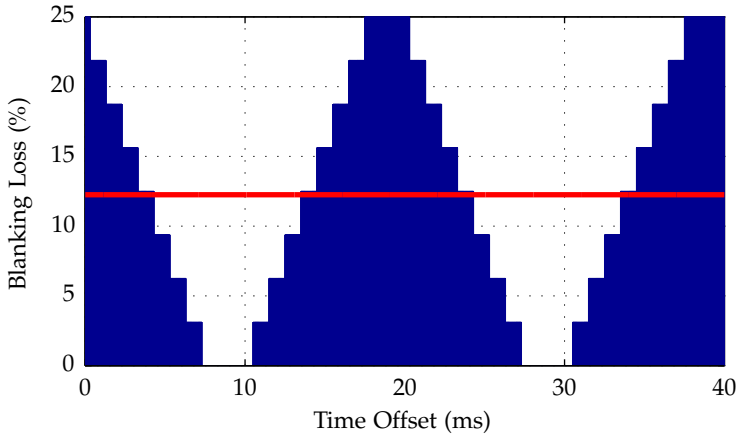

(a) Non-coprime GRIs; desired station: GRI 6000; interfering station: GRI 8000.

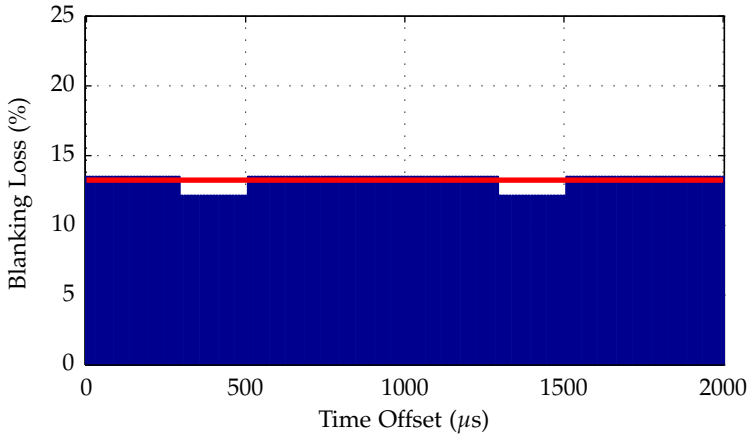

(b) Non-coprime GRIs; desired station: GRI 6700; interfering station: GRI 7400.

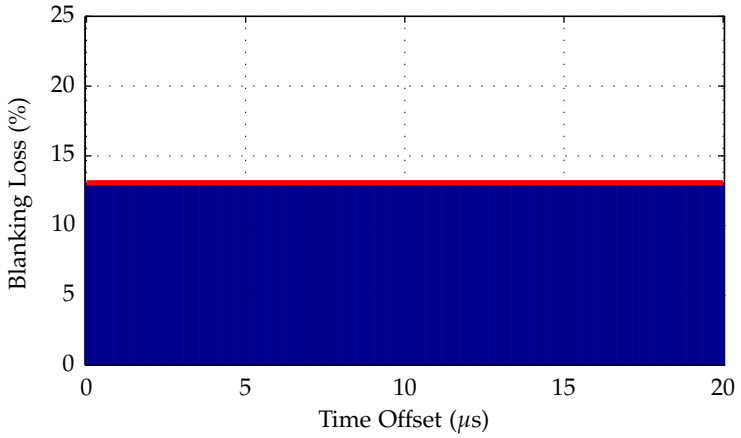

(c) Coprime GRIs; desired station: GRI 6731; interfering station: GRI 7499.

Figure 60: Blanking loss as a function of the time offset between the cross-rating signals, $\Delta\tau_2$; red line shows the mean value calculated using Equation 6.51.

and period $T_{\mathrm{GRI},2}$. Pulses from pulse train 2 occur every $T_{\mathrm{GRI},2}$, and it is then clearly seen that the probability of overlap for any given pulse from pulse train 1 must be given by Equation 6.51 above (see geometrical probability [148]). The rigorous derivation contained in references [146] and [147] proves that such a simplification is justified and it also shows that the above equations are equally valid for random and regular pulse trains (the latter meaning that $T_{\mathrm{GRI},m}$ and w_m are deterministic constants). For random pulse trains, $T_{\mathrm{GRI},m}$ and w_m are mean values; for regular trains, such as eLoran signals, they are specific, fixed values.

Equation 6.51 allows a considerable simplification of the blanking loss calculations compared to the brute force and number-theoretic methods introduced above. It should be noted that the results obtained using the statistical approach represent the *mean value* of the blanking loss over all possible time offsets between the cross-rating signals (see Figure 60). The exact blanking loss for a specific time alignment between the signals (i.e. specific location in the coverage area) cannot be calculated using this approach. However, this does not present a problem as GRIs are usually assigned so that they are mutually prime and in that case there is practically no variation in the blanking loss with varying time offsets, as shown above. The value for any specific time alignment is then very well approximated by the mean.

For the purpose of coverage and performance prediction it is also necessary to be able to evaluate the blanking loss in the presence of sky wave borne CRI, multiple interferers and transmitter dual-rate blanking. The statistical method described above can easily be extended to include the impact of all of these factors.

Sky wave propagation may increase the probability of collision between the interfering pulse trains, as the longer propagation time of the sky wave components means that the composite unwanted signal occupies a greater portion of time. However, this effect has already been accounted for by using a blanking interval that extends 1600 μs after the last pulse in the group (compare with typical sky wave delay values shown in Figure 18).

In the presence of *multiple cross-rating stations* the evaluation of the blanking loss needs to be broken down into two stages. First, the blanking loss due to stations of individual GRIs, $L_{\mathrm{b},g}^{\mathrm{GRI}}$, is calculated by summing the contributions of individual stations operating on a given GRI. In the following, g denotes the GRI of the interfering station, m identifies individual stations in view ($m = 1$ corresponds to the desired station), and $\mathcal{M}_g$ is the set of all cross-rating stations operating on GRI g:

$$L_{\mathrm{b},g}^{\mathrm{GRI}} = \sum_{m \in \mathcal{M}_g} L_{\mathrm{b},1,m}. \tag{6.52}$$

Simply summing the individual blanking loss values is justified, as signals of multiple interferers from a common chain cannot overlap.

Second, the combined blanking loss, L_{b}, is calculated, assuming that the effects of interference from stations operating on different GRIs are statistically independent:

$$L_{\mathrm{b}} = 1 - \prod_{g} \left(1 - L_{\mathrm{b},g}^{\mathrm{GRI}}\right). \tag{6.53}$$

As mentioned earlier, there is also some loss of signal due to *transmitter dual-rate blanking*. In Europe, dual-rated transmitters use *priority blanking*, where the same rate is always blanked at every overlap (the priority rate is not affected). As already explained, the transmitter blanks all pulses that overlap any part of the blanking interval extending over each pulse group of the priority signal [47]. The attendant blanking loss can again be calculated using Equation 6.51 above, and included into the overall budget through Equation 6.52.

6.2.6 *Mitigating CRI by Blanking: Achievable Performance*

This section aims to quantify the impact of CRI blanking on the accuracy of eLoran pseudorange measurements in the presence of AWGN.

Received Signal Model

As explained earlier, the use of CRI blanking reduces the available useful signal energy and consequently the receiver's ranging performance in noise is degraded. To demonstrate this effect, the received signal will be modelled as a sum of multiple cross-rating signals and an AWGN process.

Signal Processing Model

This analysis makes use of the signal processing model of Figure 48 (Chapter 5). CRI blanking will be modelled as shown in Figure 37 and discussed above.

Measurement Error Statistics

The impact of CRI blanking on eLoran accuracy can be estimated by using results from Section 6.2.5 and Section 6.2.1. First, Equations 6.51 to 6.53 should be used to evaluate the blanking loss, L_b. The blanking loss directly relates to the loss of energy available for the carrier phase estimation process.

The measurement error can then be estimated using Equation 6.12, where the number of pulses, N_p, has to be reduced accordingly, i.e. one uses $(1 - L_b) \cdot N_p$ instead of the nominal value.

Discussion of Results

Figure 61 illustrates the effect of CRI blanking on the pseudorange measurement error in the presence of AWGN. The figure plots the ranging error due to the AWGN for a GRI 6731 signal, assuming that up to three cross-rating GRIs are blanked. The eLoran signals in this example were assigned GRI values used in the North-West European system. SNR is the sampling point SNR, as defined in Section 6.1.1.

It can be seen from Figure 61 that when all the cross-rating signals are blanked, the blanking loss reaches 83% and the pseudorange error is approximately 2.4 times higher than if there was no CRI. Whether it is advantageous for the receiver to use blanking (and suffer some blanking loss) or not (and suffer some error due to uncompensated CRI) depends on the SIR and SNR, as will be further discussed in Section 6.2.9.

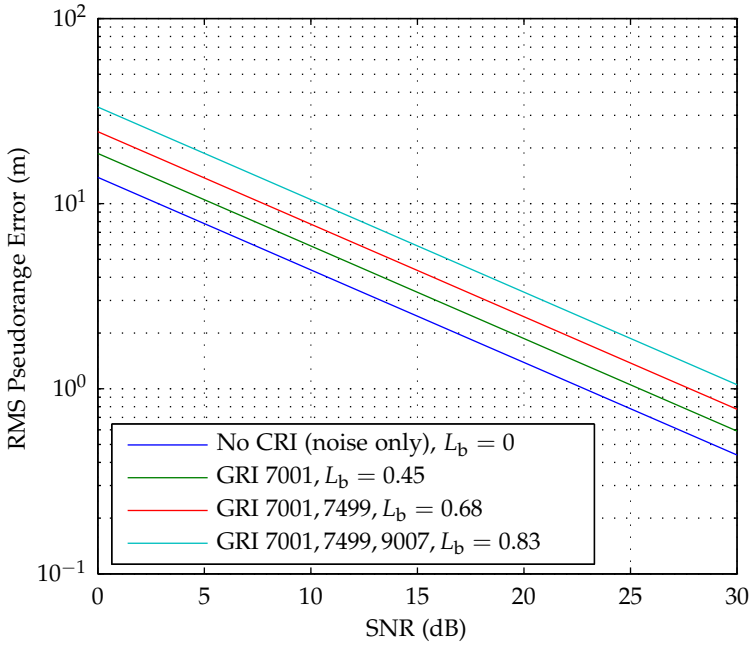

Figure 61: Residual pseudorange error after CRI blanking for a GRI 6731 signal interfered with other European GRIs.

6.2.7 *Mitigating CRI by Cancelling: Jittered Signal Spectrum*

As discussed in Chapter 3, due to a range of factors, eLoran signals suffer from pulse-to-pulse timing and amplitude jitter. The jitter does not significantly affect the performance of the receiver algorithms discussed so far (note that the jitter is assumed to be zero mean and its effects are therefore mitigated by averaging of a large number of pulses at the receiver) and therefore it has been ignored up to now. However, the jitter is an important performance limiting factor for CRI cancelling, as will be shown in the following section. In preparation for the analysis of this CRI mitigation algorithm, this section determines the effect of the jitter on the PSD of the eLoran signal.

Signal Model

Based on results presented by Macfarlane [149] it is expected that the effects of the amplitude and timing jitter on the performance of CRI cancelling algorithms are similar, therefore this analysis focuses only on the former. It will be assumed that the jitter is statistically independent from pulse to pulse, zero-mean, and with standard deviation σ_A (see also the discussion in Chapter 3). The received RF signal can then be modelled using the following expression:

$$\begin{aligned}&\tilde{s}\left(t;\tau,\mathcal{C},T_{\mathrm{GRI}},\sigma_A\right)\\&=\sum_{n=-\infty}^{\infty}\sum_{m=0}^{7}\left\{A_{16n+m}C_m e\left(t-mT_{\mathrm{p}}-2nT_{\mathrm{GRI}}-\tau\right)\right.\\&\left.+A_{16n+m+8}C_{m+8}e\left(t-mT_{\mathrm{p}}-(2n+1)\,T_{\mathrm{GRI}}-\tau\right)\right\}\cdot\\&\qquad\qquad\cos\left[2\pi f_{\mathrm{c}}\left(t-\tau\right)\right],\end{aligned}\tag{6.54}$$

where the amplitude jitter terms have the following properties:

$$\mathrm{E}\left[A_m\right] = 1,$$

and

$$\mathrm{E}\left[A_m A_n\right] = \begin{cases} \mathrm{E}\left[A_m\right]\mathrm{E}\left[A_n\right] = 1, & \text{if } m \neq n \\ \mathrm{E}\left[A_m^2\right] = \left(\mathrm{E}\left[A_m\right]\right)^2 + \sigma_A^2 = 1 + \sigma_A^2, & \text{if } m = n. \end{cases} \tag{6.55}$$

Similarly as in the previous section, the time offset τ will be considered a random variable with a uniform probability distribution between 0 and $2T_{\mathrm{GRI}}$.

PSD Calculation

The PSD of the jittered signal will be calculated from the ensemble-averaged autocorrelation function of the signal, $R_{\tilde{s}}^{\mathrm{e}}(t_1, t_2)$, which can be obtained as described below:

$$\begin{aligned}
&R_{\tilde{s}}^{\mathrm{e}}(t_1, t_2) \\
&= \mathrm{E}\left[\tilde{s}\left(t_1; \tau, \mathcal{C}, T_{\mathrm{GRI}}, \sigma_A\right) \tilde{s}\left(t_2; \tau, \mathcal{C}, T_{\mathrm{GRI}}, \sigma_A\right)\right] \\
&= \mathrm{E}\left[\sum_{n=-\infty}^{\infty} \sum_{m=0}^{7} \left\{A_{16n+m} C_m e\left(t_1 - mT_{\mathrm{p}} - 2nT_{\mathrm{GRI}} - \tau\right)\right.\right. \\
&\left. + A_{16n+m+8} C_{m+8} e\left(t - mT_{\mathrm{p}} - (2n+1)\, T_{\mathrm{GRI}} - \tau\right)\right\} \cdot \cos\left[2\pi f_{\mathrm{c}}\left(t_1 - \tau\right)\right] \\
&\cdot \sum_{l=-\infty}^{\infty} \sum_{k=0}^{7} \left\{A_{16l+k} C_k e\left(t_2 - kT_{\mathrm{p}} - 2lT_{\mathrm{GRI}} - \tau\right)\right. \\
&\left.\left. + A_{16l+k+8} C_{k+8} e\left(t_2 - kT_{\mathrm{p}} - (2l+1)\, T_{\mathrm{GRI}} - \tau\right)\right\} \cos\left[2\pi f_{\mathrm{c}}\left(t_2 - \tau\right)\right]\right].
\end{aligned}$$

To ease the calculation, $R_{\tilde{s}}^{\mathrm{e}}(t_1, t_2)$ will be decomposed into four terms denoted $R_{\tilde{s},1,1}^{\mathrm{e}}(t_1, t_2)$, $R_{\tilde{s},1,2}^{\mathrm{e}}(t_1, t_2)$, $R_{\tilde{s},2,1}^{\mathrm{e}}(t_1, t_2)$, and $R_{\tilde{s},2,2}^{\mathrm{e}}(t_1, t_2)$. The term $R_{\tilde{s},1,1}^{\mathrm{e}}(t_1, t_2)$ is formed by the product of the first term in the first double summation and the first term in the second double summation in the expression above; $R_{\tilde{s},1,2}^{\mathrm{e}}(t_1, t_2)$ is formed by the product of the first and second terms in the double summations, etc.:

$$\begin{aligned}
&R_{\tilde{s},1,1}^{\mathrm{e}}(t_1, t_2) \\
&= \mathrm{E}\left[\sum_{n=-\infty}^{\infty} \sum_{m=0}^{7} A_{16n+m} C_m e\left(t_1 - mT_{\mathrm{p}} - 2nT_{\mathrm{GRI}} - \tau\right)\right. \\
&\cdot \sum_{l=-\infty}^{\infty} \sum_{k=0}^{7} A_{16l+k} C_k e\left(t_2 - kT_{\mathrm{p}} - 2lT_{\mathrm{GRI}} - \tau\right) \\
&\qquad \left.\frac{1}{2}\left\{\cos\left[2\pi f_{\mathrm{c}}\left(t_1 - t_2\right)\right] + \cos\left[2\pi f_{\mathrm{c}}\left(t_1 + t_2 - 2\tau\right)\right]\right\}\right].
\end{aligned}$$

Considering that τ is assumed to be uniformly distributed between 0 and $2T_{\mathrm{GRI}}$ and statistically independent of the amplitude factors A_m, the expression for $R^{\mathrm{e}}_{\tilde{s},1,1}(t_1,t_2)$ can be rewritten as[11]

$$\begin{aligned}
&R^{\mathrm{e}}_{\tilde{s},1,1}(t_1,t_2)\\
&=\frac{1}{4T_{\mathrm{GRI}}}\sum_{n=-\infty}^{\infty}\sum_{m=0}^{7}\sum_{l=-\infty}^{\infty}\sum_{k=0}^{7}\mathrm{E}\left[A_{16n+m}A_{16l+k}\right]C_mC_k\\
&\cdot\int_0^{2T_{\mathrm{GRI}}} e\left(t_1-mT_{\mathrm{p}}-2nT_{\mathrm{GRI}}-\tau\right)e\left(t_2-kT_{\mathrm{p}}-2lT_{\mathrm{GRI}}-\tau\right)\mathrm{d}\tau\\
&\qquad\cdot\cos\left[2\pi f_{\mathrm{c}}\left(t_1-t_2\right)\right].
\end{aligned}$$

Consider now the case where $m=k$ and $n=l$:

$$\begin{aligned}
&R^{\mathrm{e}}_{\tilde{s},1,1}(t_1,t_2)\\
&=\left|(m=k)\wedge(n=l)\right|\\
&=\frac{1}{4T_{\mathrm{GRI}}}\sum_{n=-\infty}^{\infty}\sum_{m=0}^{7}\mathrm{E}\left[A^2_{16n+m}\right]\\
&\cdot\int_0^{2T_{\mathrm{GRI}}} e\left(t_1-mT_{\mathrm{p}}-2nT_{\mathrm{GRI}}-\tau\right)e\left(t_2-mT_{\mathrm{p}}-2nT_{\mathrm{GRI}}-\tau\right)\mathrm{d}\tau\\
&\qquad\cdot\cos\left[2\pi f_{\mathrm{c}}\left(t_1-t_2\right)\right].
\end{aligned}$$

By making the substitution $\tau'=t_1-mT_{\mathrm{p}}-\tau$, and inserting from Equation 6.55, the expression can further be written as

$$\begin{aligned}
&R^{\mathrm{e}}_{\tilde{s},1,1}(t_1,t_2)\\
&=\frac{1+\sigma_A^2}{4T_{\mathrm{GRI}}}\\
&\cdot\sum_{m=0}^{7}\int_{2T_{\mathrm{GRI}}}\sum_{n=-\infty}^{\infty}e\left(\tau'-2nT_{\mathrm{GRI}}\right)e\left(\tau'+\overbrace{t_2-t_1}^{\alpha}-2nT_{\mathrm{GRI}}\right)\mathrm{d}\tau'\\
&\qquad\cdot\cos\left[2\pi f_{\mathrm{c}}\left(t_1-t_2\right)\right].
\end{aligned}$$

It is readily seen that the integral in the above expression equals to the time-averaged autocorrelation function of the eLoran pulse envelope[12], $R^{\mathrm{t}}_e(\alpha)$, and the expression can thus be rewritten as

$$R^{\mathrm{e}}_{\tilde{s},1,1}(t_1,t_2)=\frac{2\left(1+\sigma_A^2\right)}{T_{\mathrm{GRI}}}R^{\mathrm{t}}_e(\alpha)\cos\left(2\pi f_{\mathrm{c}}\alpha\right)\equiv R^{\mathrm{e}}_{\tilde{s},1,1}(\alpha).$$

In the complementary case, i.e. when $m\neq k$ or $n\neq l$, $R^{\mathrm{e}}_{\tilde{s},1,1}(t_1,t_2)$ can be shown to be given by

$$\begin{aligned}
&R^{\mathrm{e}}_{\tilde{s},1,1}(t_1,t_2)\\
&=\left|(m\neq k)\vee(n\neq l)\right|\\
&=\frac{1}{4T_{\mathrm{GRI}}}\sum_{m=0}^{7}\sum_{k=0}^{7}C_mC_k\sum_{l=-\infty}^{\infty}R^{\mathrm{t}}_e\left(\alpha+(m-k)\,T_{\mathrm{p}}-2lT_{\mathrm{GRI}}\right)\cos\left(2\pi f_{\mathrm{c}}\alpha\right)\\
&\qquad-\frac{2}{T_{\mathrm{GRI}}}R^{\mathrm{t}}_e(\alpha)\cos\left(2\pi f_{\mathrm{c}}\alpha\right).
\end{aligned}$$

11 Note that $\int_{2T_{\mathrm{GRI}}}\cos\left[2\pi f_{\mathrm{c}}\left(t_1+t_2-2\tau\right)\right]\mathrm{d}\tau=0$.

12 For definition of the time-averaged autocorrelation function see Appendix A

Combining the two cases above, it follows that $R^{\mathrm{e}}_{\tilde{s},1,1}(t_1, t_2)$, or rather $R^{\mathrm{e}}_{\tilde{s},1,1}(\alpha)$, is given by the following expression:

$$R^{\mathrm{e}}_{\tilde{s},1,1}(\alpha) = \frac{\cos(2\pi f_{\mathrm{c}}\alpha)}{4T_{\mathrm{GRI}}} \left[\sum_{m=0}^{7} \sum_{k=0}^{7} C_m C_k \cdot \sum_{l=-\infty}^{\infty} R^{\mathrm{t}}_e\left(\alpha + (m-k)\,T_{\mathrm{p}} - 2lT_{\mathrm{GRI}}\right) + 8\sigma_A^2 R^{\mathrm{t}}_e(\alpha) \right].$$

The remaining terms, $R^{\mathrm{e}}_{\tilde{s},1,2}(\alpha)$ to $R^{\mathrm{e}}_{\tilde{s},2,2}(\alpha)$, can be arrived at by following the same process as above:

$$R^{\mathrm{e}}_{\tilde{s},1,2}(\alpha) = \frac{\cos(2\pi f_{\mathrm{c}}\alpha)}{4T_{\mathrm{GRI}}} \sum_{m=0}^{7} \sum_{k=0}^{7} C_m C_{k+8} \cdot \sum_{l=-\infty}^{\infty} R^{\mathrm{t}}_e\left(\alpha + (m-k)\,T_{\mathrm{p}} - (2l+1)\,T_{\mathrm{GRI}}\right),$$

$$R^{\mathrm{e}}_{\tilde{s},2,1}(\alpha) = \frac{\cos(2\pi f_{\mathrm{c}}\alpha)}{4T_{\mathrm{GRI}}} \sum_{m=0}^{7} \sum_{k=0}^{7} C_{m+8} C_k \cdot \sum_{l=-\infty}^{\infty} R^{\mathrm{t}}_e\left(\alpha + (m-k)\,T_{\mathrm{p}} - (2l-1)\,T_{\mathrm{GRI}}\right),$$

$$R^{\mathrm{e}}_{\tilde{s},2,2}(\alpha) = \frac{\cos(2\pi f_{\mathrm{c}}\alpha)}{4T_{\mathrm{GRI}}} \left[\sum_{m=0}^{7} \sum_{k=0}^{7} C_{m+8} C_{k+8} \cdot \sum_{l=-\infty}^{\infty} R^{\mathrm{t}}_e\left(\alpha + (m-k)\,T_{\mathrm{p}} - 2lT_{\mathrm{GRI}}\right) + 8\sigma_A^2 R^{\mathrm{t}}_e(\alpha) \right].$$

The autocorrelation function of the jittered signal is then obtained by summing the four terms derived above. At this point, it will be convenient to also express the sum over l in the above equations using the convolution operation (denoted below by the $\star$ symbol):

$$\begin{aligned} &R^{\mathrm{e}}_{\tilde{s}}(\alpha) \\ &= \frac{\cos(2\pi f_{\mathrm{c}}\alpha)}{4T_{\mathrm{GRI}}} \left\{ \sum_{m=0}^{7} \sum_{k=0}^{7} \left[\left(C_m C_k + C_{m+8} C_{k+8}\right) R^{\mathrm{t}}_e\left(\alpha + (m-k)\,T_{\mathrm{p}}\right) \right.\right. \\ &\left. + \left(C_m C_{k+8} + C_{m+8} C_k\right) R^{\mathrm{t}}_e\left(\alpha + (m-k)\,T_{\mathrm{p}} - T_{\mathrm{GRI}}\right) \right] \\ &\left.\left. \star \sum_{l=-\infty}^{\infty} \delta\left(\alpha - 2lT_{\mathrm{GRI}}\right) + 16\sigma_A^2 R^{\mathrm{t}}_e(\alpha) \right\}. \end{aligned}$$

The PSD of the jittered signal is obtained by taking the Fourier transform of the autocorrelation function:

$$D_{\tilde{s}}^{e}(f) = \mathcal{F}_{\alpha,f}\left\{R_{\tilde{s}}^{e}(\alpha)\right\} = \left(|S_e(f-f_c)|^2 + |S_e(f+f_c)|^2\right) \cdot \left\{\frac{1}{16T_{\mathrm{GRI}}^2}\sum_{m=0}^{7}\sum_{k=0}^{7}\left[\left(C_mC_k + C_{m+8}C_{k+8}\right)e^{j2\pi f(m-k)T_{\mathrm{P}}} + \left(C_mC_{k+8} + C_{m+8}C_k\right)e^{j2\pi f\left[(m-k)T_{\mathrm{P}} - T_{\mathrm{GRI}}\right]}\right] \cdot \sum_{n=-\infty}^{\infty}\delta\left(f - \frac{n}{2T_{\mathrm{GRI}}}\right) + \frac{2\sigma_A^2}{T_{\mathrm{GRI}}}\right\}. \quad (6.56)$$

The term $S_e(f)$ in the above equation denotes the Fourier transform of the eLoran pulse envelope as calculated in Chapter 2. The double summation turns out to be equal to the modulus squared of the spectrum of the phase code function $S_b(f)$, also defined in Chapter 2. The PSD of the jittered signal can thus be expressed compactly as

$$D_{\tilde{s}}^{e}(f) = \left(|S_e(f-f_c)|^2 + |S_e(f+f_c)|^2\right) \cdot \left(\frac{|S_b(f)|^2}{16T_{\mathrm{GRI}}^2} \cdot \sum_{n=-\infty}^{\infty}\delta\left(f - \frac{n}{2T_{\mathrm{GRI}}}\right) + \frac{2\sigma_A^2}{T_{\mathrm{GRI}}}\right). \quad (6.57)$$

Discussion of Results

It can be seen from Equation 6.57 above that the PSD of the jittered signal has a *discrete component* (line spectrum formed by the Dirac comb), and a *continuous component* whose magnitude depends on the power of the amplitude jitter, σ_A^2 (see also Figure 62). The discrete component is identical to the time-averaged PSD of the ideal eLoran RF waveform. The continuous part of the PSD represents noise added to the signal as a result of the pulse-to-pulse amplitude jitter.

As will be shown in the following section, CRI cancelling algorithms can suppress the discrete part of the spectrum, however, the continuous, noise-like, component remains and is the main performance limiting factor for this kind of algorithms.

The two components of the PSD are plotted in Figure 62. The figure assumes that the signal jitters by 5% (one sigma) in amplitude. It can be seen from the plot that, for this level of jitter, the continuous component is approximately 37 dB below the discrete component, which suggests that the maximum achievable interference suppression when using CRI cancelling is likely to be in the region of 30 dB to 40 dB.

6.2.8 *Mitigating CRI by Cancelling: Achievable Performance*

This section builds on the results of the previous section and derives expressions for the residual pseudorange measurement error after CRI cancelling. The section follows the same structure as the performance analyses presented in earlier sections of this chapter.

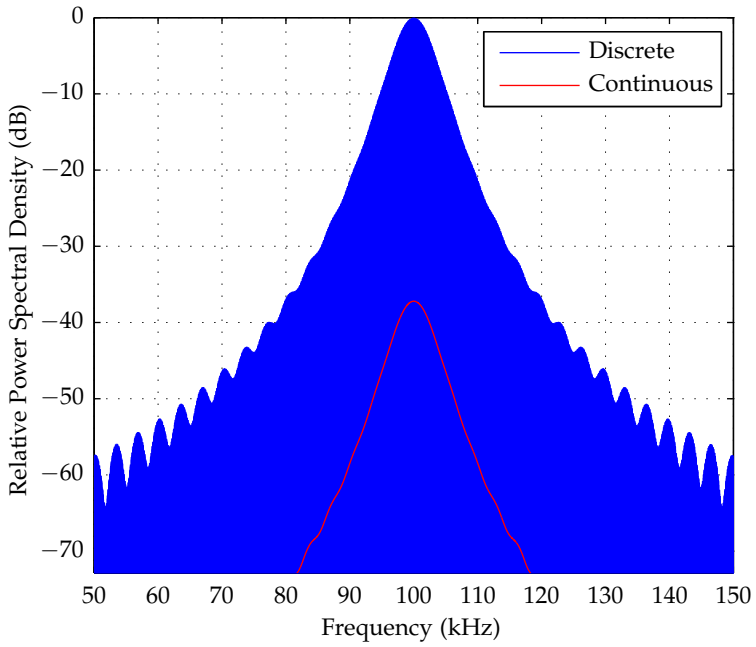

(a) Overall view

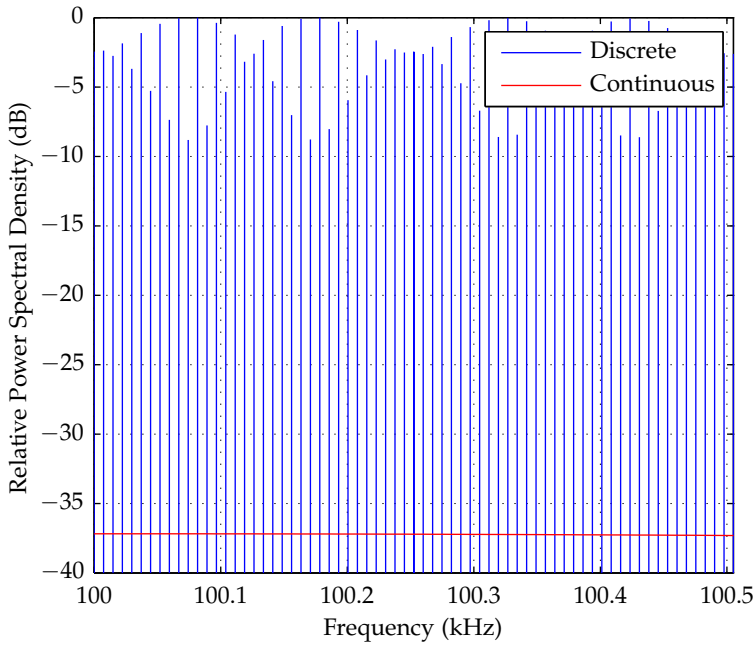

(b) Close-up

Figure 62: Power spectral density of a jittered eLoran RF signal (only positive frequencies are shown); signal: GRI 6731, secondary; amplitude jitter $\sigma_A = 0.05$.

Received Signal Model

In this analysis, the received signal will be modeled as a sum of two cross-rating eLoran waveforms, each defined by Equation 6.54 (Section 6.2.7):

$$\tilde{x}(t) = \underbrace{\tilde{s}(t; 0, \mathcal{C}_1, T_{\text{GRI},1}, 0)}_{\tilde{x}_1(t)} + \underbrace{\frac{1}{\sqrt{\text{SIR}}}\tilde{s}(t; \Delta\tau_2, \mathcal{C}_2, T_{\text{GRI},2}, \sigma_A)}_{\tilde{x}_2(t)}. \quad (6.58)$$

In the above equation, $\tilde{x}_1(t)$ represents the desired signal component and $\tilde{x}_2(t)$ is considered as interference ($T_{\text{GRI},1} \neq T_{\text{GRI},2}$); the interfering signal is subject to pulse-to-pulse amplitude jitter with standard deviation σ_A (expressed as a fraction of the mean signal amplitude). For simplicity, the desired signal will be modelled as deterministic (i.e. the standard deviation of the jitter will be set to zero in this case). This is a reasonable simplification as any amplitude jitter on the desired signal would be averaged out in the main comb filter and its effects on the results of this analysis would be negligible (note that the same cannot be assumed for the interference signal).

In line with the discussion in Section 6.2.3, the time offset $\Delta\tau_2$ will be treated as a random variable with a uniform distribution between 0 and $2T_{\text{GRI},2}$ (i.e. all possible values of the time offset are considered equally probable).

Signal Processing Model

For the purpose of this analysis, the signal processing model of Figure 48 will be modified in the same manner as in Section 6.2.3 (i.e. the frequency down-conversion block will be moved behind the comb and phase-decoding filters and the phase correction block). CRI cancelling will be modelled as shown in Figure 38 (Chapter 5).

Measurement Error Process

The only source of measurement error in the signal model is the cross-rating, amplitude-jittered, signal $\tilde{x}_2(t)$. As mentioned earlier, if $\Delta\tau_2$ is considered as a random variable uniformly distributed between 0 and $2T_{\text{GRI},2}$, then $\tilde{x}_2(t)$ becomes a WSS random process [141]. Consequently, also the measurement error process will be WSS, and can be characterised by ensemble-averaged statistics such as μ_ε and P_ε^e.

Response to the Desired Signal

Since the signal processing model used in this section contains an additional block to enable CRI cancelling, it is necessary to reconsider the receiver's response to the desired signal. Figure 63 depicts the additional signal processing block (see also Section 5.3.2 in Chapter 5).

As can be seen from the figure, the response of the CRI filter to the desired signal, $\tilde{x}_{1,x}(t)$, consists of two components:

$$\tilde{x}_{1,x}(t) = \tilde{x}_{1,b}(t) - \tilde{x}_{1,2}(t).$$

Here, $\tilde{x}_{1,b}(t)$ is the desired signal component at the output of the input bandpass filter, and $\tilde{x}_{1,2}(t)$ is a residual signal obtained by filtering the desired signal by the comb filter within the CRI filter. Since the part

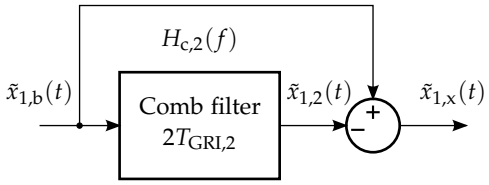

Figure 63: Response of the CRI filter to the desired signal component.

of the signal processing model up to the phase detector is linear, the receiver's response to the desired signal can be found by applying the superposition principle.

As shown in Section 6.2.1, the response to $\tilde{x}_{1,b}(t)$ is given by

$$x_{1,b,r}[u] = \left| e_b(\tau_p) \right|, \ \forall u \in \mathbb{Z}.$$

The response to the residual signal component $\tilde{x}_{1,2}(t)$ can be found using a frequency domain approach analogous to that used in Section 6.2.2. The Fourier series coefficient of the filtered residual signal can be written as follows:

$$\begin{aligned} c_{\tilde{x}_{1,2,r}}[n] = \frac{1}{4T_{GRI,1}} \left[S_e\left(\frac{n}{2T_{GRI,1}} - f_c\right) + S_e\left(\frac{n}{2T_{GRI,1}} + f_c\right) \right] \\ \cdot S_b\left(\frac{n}{2T_{GRI,1}}\right) \tilde{H}_b\left(\frac{n}{2T_{GRI,1}}\right) H_{c,2}\left(\frac{n}{2T_{GRI,1}}\right) H_{c,1}\left(\frac{n}{2T_{GRI,1}}\right) \\ \cdot H_p\left(\frac{n}{2T_{GRI,1}}\right) e^{-j\theta_b}, \ n \in \mathbb{N}, \end{aligned}$$

where $H_{c,2}(\cdot)$ is the frequency response of the comb filter within the CRI filter (averaging over $2T_{GRI,2}$), $H_{c,1}(\cdot)$ is the frequency response of the main comb filter (averaging over $2T_{GRI,1}$), and the remaining terms were defined earlier in Chapter 2 and Chapter 5.

Using the following identities

$$H_{c,1}\left(\frac{n}{2T_{GRI,1}}\right) = 1,$$

$$H_p\left(\frac{n}{2T_{GRI,1}}\right) = \frac{1}{16} S_b^*\left(\frac{n}{2T_{GRI,1}}\right) \underbrace{e^{-j2\pi \frac{n}{2T_{GRI,1}} 2T_{GRI,1}}}_{1}$$

the expression for the Fourier coefficients can be rewritten as

$$\begin{aligned} c_{\tilde{x}_{1,2,r}}[n] = \frac{e^{-j\theta_b}}{64T_{GRI,1}} \left[S_e\left(\frac{n}{2T_{GRI,1}} - f_c\right) + S_e\left(\frac{n}{2T_{GRI,1}} + f_c\right) \right] \\ \cdot \left| S_b\left(\frac{n}{2T_{GRI,1}}\right) \right|^2 \tilde{H}_b\left(\frac{n}{2T_{GRI,1}}\right) H_{c,2}\left(\frac{n}{2T_{GRI,1}}\right). \end{aligned}$$

The Fourier coefficients of the signal after frequency downconversion are then given by

$$c_{x_{1,2,\mathrm{r}}}[n] = \frac{\mathrm{e}^{-\mathrm{j}\theta_\mathrm{b}}}{32T_{GRI,1}} S_e\left(\frac{n}{2T_{GRI,1}}\right)\left|S_b\left(\frac{n}{2T_{GRI,1}}\right)\right|^2 \cdot H_\mathrm{b}\left(\frac{n}{2T_{GRI,1}}\right) H_{\mathrm{c},2}\left(\frac{n}{2T_{GRI,1}}\right),$$

where $H_\mathrm{b}(f) = \widetilde{H}_\mathrm{b}(f + f_c)$ is the frequency response of the equivalent low-pass filter representing the input bandpass filter.

After the downconversion, the signal is sampled at time instants defined by

$$t_u = uT_\mathrm{up} + \tau_\mathrm{p},\ u \in \mathbb{Z}, \tag{6.59}$$

where T_up is the measurement update interval (assumed to be an integer multiple of the PCI of the desired signal, $T_\mathrm{up} = N_\mathrm{up} \cdot 2T_{\mathrm{GRI},1}$, $N_\mathrm{up} \in \mathbb{N}$), and τ_p defines the position of the sampling point, as discussed earlier.

The sampled signal can be expressed using the Fourier series expansion of $x_{1,2,\mathrm{r}}(t)$ for $t = uT_\mathrm{up} + \tau_\mathrm{p}$:

$$\begin{aligned} x_{1,2,\mathrm{r}}[u] &= \sum_{n=-\infty}^{\infty} c_{x_{1,2,\mathrm{r}}}[n]\, \mathrm{e}^{\mathrm{j}n\frac{2\pi}{2T_{\mathrm{GRI},1}}\left(uT_\mathrm{up}+\tau_\mathrm{p}\right)} \\ &= \sum_{n=-\infty}^{\infty} c_{x_{1,2,\mathrm{r}}}[n]\, \mathrm{e}^{\mathrm{j}nu2\pi N_\mathrm{up}} \mathrm{e}^{\mathrm{j}n\frac{\pi}{T_{\mathrm{GRI},1}}\tau_\mathrm{p}} \\ &= \sum_{n=-\infty}^{\infty} c_{x_{1,2,\mathrm{r}}}[n]\, \mathrm{e}^{\mathrm{j}n\frac{\pi}{T_{\mathrm{GRI},1}}\tau_\mathrm{p}} \equiv x_{1,2,\mathrm{r}}. \end{aligned} \tag{6.60}$$

It can be seen from the above equation that the sampled signal, $x_{1,2,\mathrm{r}}[u]$, is constant in time. This is expected as the sampling period, T_up, is an integer multiple of the period of the continuous-time signal $x_{1,2,\mathrm{r}}(t)$. The residual signal, $x_{1,2,\mathrm{r}}[u]$, therefore adds a bias to the useful signal component at the phase detector.

The combined signal at the phase detector input can then be written as

$$\begin{aligned} x_{1,\mathrm{r}}[u] &= x_{1,\mathrm{b},\mathrm{r}}[u] - x_{1,2,\mathrm{r}}[u] \\ &= \left|e_\mathrm{b}(\tau_\mathrm{p})\right| - x_{1,2,\mathrm{r}}. \end{aligned}$$

Response to the Interfering Signal

By following the same reasoning as in Section 6.2.3, it can be shown that the I and Q components of the filtered (incl. CRI filtering; refer to Figure 63) and down-converted interference signal, $x_{2,\mathrm{r},\mathcal{I}}(t)$ and $x_{2,\mathrm{r},\mathcal{Q}}(t)$, resp. are WSS, uncorrelated, zero mean and their power is equal to the power of the filtered RF interference signal $\tilde{x}_{2,\mathrm{r}}(t)$ (see Equation 6.30 to Equation 6.32 above). Since the I and Q components are stationary, the ensemble averaged statistics of the sampled signals at the input to the phase detector, $x_{2,\mathrm{r},\mathcal{I}}[u]$, $x_{2,\mathrm{r},\mathcal{Q}}[u]$, are equal to those of the respective continous-time signals. Therefore, all that needs to be calculated is the power of the filtered RF interference, $P^\mathrm{e}_{\tilde{x}_{2,\mathrm{r}}}$. This can be accomplished using the signal's PSD as shown below.

The PSD of signal $\tilde{x}_{2,\mathrm{r}}(t)$ obtained from $\tilde{x}_2(t)$ by the input filtering (incl. CRI filtering) is given by

$$D^{\mathrm{e}}_{\tilde{x}_{2,\mathrm{r}}}(f) = \underbrace{\left|\tilde{H}_{\mathrm{b}}(f) H_{\mathrm{x}}(f) H_{\mathrm{c}}(f) H_{\mathrm{p}}(f)\right|^2}_{\left|\tilde{H}'_{\mathrm{f}}(f)\right|^2} D^{\mathrm{e}}_{\tilde{x}_2}(f), \tag{6.61}$$

where

$$D^{\mathrm{e}}_{\tilde{x}_2}(f) = \frac{D^{\mathrm{e}}_{\tilde{s}}(f)}{\mathrm{SIR}}$$

is the PSD of the interference signal at the receiver input (see Equation 6.57 and Equation 6.58 above), and $\tilde{H}_{\mathrm{b}}(f)$, $H_{\mathrm{x}}(f)$, $H_{\mathrm{c}}(f)$, and $H_{\mathrm{p}}(f)$ were defined earlier in Chapter 5.

The power of $\tilde{x}_{2,\mathrm{r}}(t)$ is therefore given by

$$\begin{aligned} P^{\mathrm{e}}_{\tilde{x}_{2,\mathrm{r}}} &= \int_{-\infty}^{\infty} D^{\mathrm{e}}_{\tilde{x}_{2,\mathrm{r}}}(f)\,\mathrm{d}f \\ &= \frac{1}{\mathrm{SIR}} \int_{-\infty}^{\infty} \left|\tilde{H}'_{\mathrm{f}}(f)\right|^2 D^{\mathrm{e}}_{\tilde{s}}(f)\,\mathrm{d}f \\ &= \frac{4\sigma_A^2}{\mathrm{SIR}\cdot T_{\mathrm{GRI},2}} \int_0^{\infty} \left|\tilde{H}'_{\mathrm{f}}(f)\, S_e(f - f_c)\right|^2 \mathrm{d}f \\ &\quad + \underbrace{\sum_{n=0}^{\infty} \frac{\left|\tilde{H}'_{\mathrm{f}}\left(\frac{n}{2T_{GRI,2}}\right) S_e\left(\frac{n}{2T_{GRI,2}} - f_c\right) S_b\left(\frac{n}{2T_{GRI,2}}\right)\right|^2}{8\mathrm{SIR}\cdot T^2_{\mathrm{GRI},2}}}_{\approx 0}. \end{aligned} \tag{6.62}$$

The last term in the above equation is negligible as the magnitude response of the CRI filter has deep notches at frequencies given by $n/(2T_{GRI,2})$. The other term is due to the noise introduced by the amplitude jitter; the integral in this term will be solved numerically.

Measurement Error Statistics

Using the above results the composite signal at the phase detector can be expressed as

$$\begin{aligned} x[u] &= x_{1,\mathrm{r}}[u] + x_{2,\mathrm{r}}[u] \\ &= \left|e_{\mathrm{b}}(\tau_{\mathrm{p}})\right| - x_{1,2,\mathrm{r}} + x_{2,\mathrm{r}}[u], \end{aligned}$$

where $\left|e_{\mathrm{b}}(\tau_{\mathrm{p}})\right|$ is the magnitute of the desired pulse at the sampling point, $x_{1,2,\mathrm{r}}$ corresponds to the bias introduced by the CRI filter, and $x_{2,\mathrm{r}}[u] = x_{2,\mathrm{r},\mathcal{I}}[u] + \mathrm{j}x_{2,\mathrm{r},\mathcal{Q}}[u]$ is the receiver's response to the interfering signal.

Since the comb filter used in the CRI filtering does not introduce any carrier phase shift, the bias term is real. The in-phase and quadrature components of $x[u]$ are therefore given by

$$x_{\mathcal{I}}[u] \equiv \mathrm{Re}[x[u]] = \left|e_{\mathrm{b}}(\tau_{\mathrm{p}})\right| - x_{1,2,\mathrm{r}} + x_{2,\mathrm{r},\mathcal{I}}[u],$$

$$x_{\mathcal{Q}}[u] \equiv \mathrm{Im}[x[u]] = x_{2,\mathrm{r},\mathcal{Q}}[u].$$

Assuming that SIR > -30 or so (recall from the previous chapter that the residual noise present after CRI cancelling is at a level approximately 37 dB below the cross-rating signal), and also that[13]

$$|e_b(\tau_p)| \gg |x_{1,2,r}|,$$

the (instantaneous) carrier phase estimation error can be approximated as

$$\begin{aligned}\varepsilon[u] = \angle x[u] &\approx \frac{x_Q[u]}{x_I[u]} \\ &\approx \frac{x_{2,r,Q}[u]}{|e_b(\tau_p)| - x_{1,2,r}}.\end{aligned}$$

The basic statistics of the measurement error are then obtained as follows:

$$\mu_\varepsilon \approx \mathrm{E}\left[\frac{x_{2,r,Q}[u]}{|e_b(\tau_p)| - x_{1,2,r}}\right] = 0,$$

$$\begin{aligned}P_\varepsilon^e = \mathrm{var}[\varepsilon[u]] &= \mathrm{E}\left[|\varepsilon[u]|^2\right] \\ &\approx \mathrm{E}\left[\left|\frac{x_{2,r,Q}[u]}{|e_b(\tau_p)| - x_{1,2,r}}\right|^2\right] \\ &= \frac{P_{\tilde{x}_{2,r}}^e}{\left||e_b(\tau_p)| - x_{1,2,r}\right|^2}.\end{aligned}$$

where $P_{\tilde{x}_{2,r}}^e$ and $x_{1,2,r}$ are calculated using Equation 6.62 and Equation 6.60 above, respectively.

The residual pseudorange measuerment error can be computed from the phase measurement error using Equation 6.39 given in Section 6.2.3.

Discussion of Results

Figure 64 shows the residual measurement error after CRI cancelling as a function of the SIR and standard deviation of the pulse-to-pulse amplitude jitter, σ_A. As expected, the residual error increases with decreasing SIR and increasing amount of jitter. The effect becomes noticeable at approximately 0 dB SIR; weaker interference is effectively cancelled.

Figure 65 plots the measurement error as a function of the GRI of the interfering signal for SIR $= -17$ dB and a 5% amplitude jitter. The residual errors at this particular SIR and jitter conditions are comparable in magnitude to those predicted by the model of uncompensated CRI for SIR $= 10$ dB (see Section 6.2.3). In other words, the cancelling algorithm analysed in this section provides approximately 27 dB of interference suppression. This analytical result is in a very good agreement with experimental conclusions drawn by Pelgrum [30] who states that:

> 'In practice, cross-rate reduction by cancellation of 15 to 30 dB should be achievable, depending on local circumstances and the receiver implementation'.

13 This assumption may be violated for some combination of GRIs. However, such combinations should be eliminated during the GRI selection process, as will be discussed in Chapter 10.

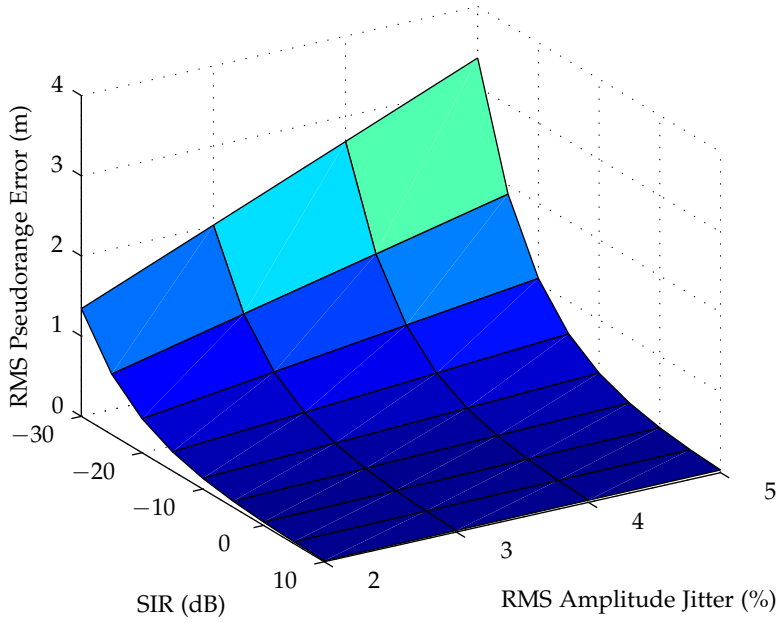

Figure 64: Residual pseudorange measurement error after CRI cancelling as a function of the SIR and standard deviation of the pulse-to-pulse amplitude jitter; desired signal: GRI 6731, secondary; interfering signal: 7499, master.

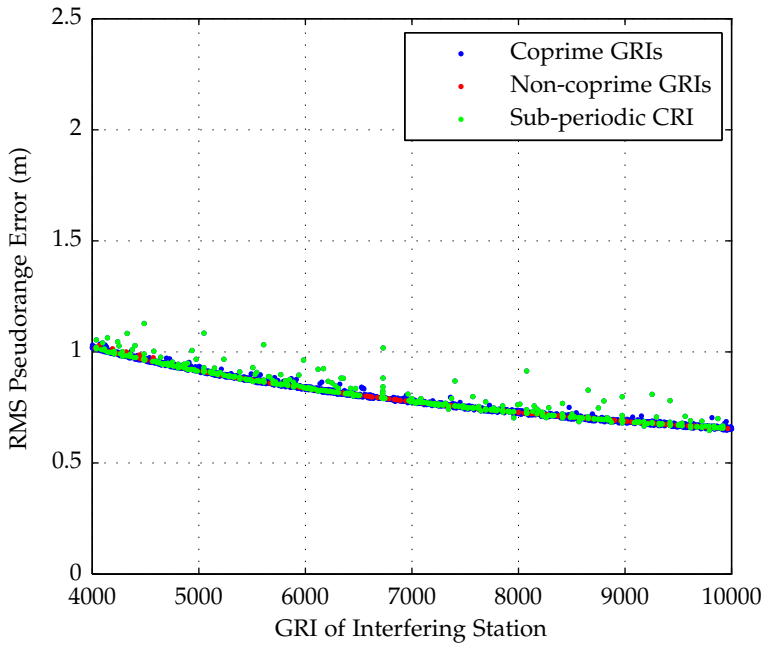

Figure 65: Residual pseudorange measurement error after CRI cancelling as a function of the interfering signal GRI; desired signal: GRI 6731, secondary; interfering signal: GRI as per horizontal axis, master; SIR $= -17$ dB.

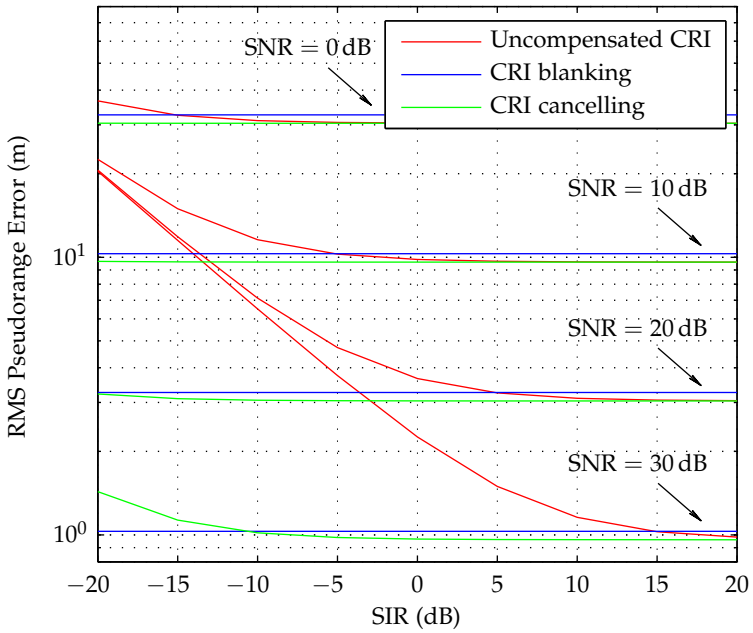

Figure 66: Pseudorange measurement error due to AWGN and CRI; desired signal: GRI 6731, secondary; interfering signal: GRI 7499, master; integration time $T_i \approx 5\,s$.

It is also worth noticing that there is considerably less variability in the measurement error between different GRIs than was the case with uncompensated CRI. This is because the residual error is mainly due to the continuous part of the interfering signal's PSD (see Figure 62), which is more homogeneously distributed across the Loran frequency band than the line spectrum of the eLoran signal (the discrete component of the PSD is suppressed by the cancelling algorithm).

The validity of this analytical model was also confirmed by a numerical simulation, as detailed in Chapter 8.

6.2.9 *Combination of CRI Mitigation Techniques*

The previous sections investigated the effects of RF noise and CRI on pseudorange measurements, and explored the efficiency of different CRI mitigation techniques. The question now arises as to which of the techniques is the best one for use in a practical receiver? As can be seen from Figure 66, the answer depends on the SIR and also, to an extent, on the SNR of the cross-rating signals.

Figure 66 shows the pseudorange error for an eLoran signal corrupted by AWGN and CRI from a single cross-rating station[14]. The figure compares three possible approaches to dealing with CRI: shown in red is the measurement error for a receiver that does not use any CRI mitigation algorithms; the blue trace shows the error for a receiver that uses CRI blanking; and the green one for a receiver that implements CRI cancelling. It can be seen from the figure that neither of these approaches is uniformly better than the others.

14 In accordance with findings of Chapter 8, the figure assumes a receiver implementation loss of $L_{impl} = 4.8$.

A receiver designer can choose to ignore the interfering signals. This approach seems acceptable when SIR exceeds 10 dB or so, as the CRI-induced errors will then be negligible compared to errors due to background noise and other factors. In low SNR conditions it would seem possible to choose an even lower SIR threshold.

In moderate SIR conditions, CRI cancelling outperforms CRI blanking. Note that, in this example, the difference between CRI cancelling and blanking is relatively small as there is only one interfering signal. If the number of interferers was higher, the difference in performance would be greater due to the additional blanking loss.

On the other hand, CRI blanking would seem to be preferable under low SIR conditions where the residual errors due to CRI cancelling may be significant. The designer also needs to consider whether the achievable performance improvement obtained through the use of CRI cancelling justifies the increased complexity of the receiver (note that the implementation of this algorithm gets considerably complex when the interfering signal is data-modulated).

In conclusion, the optimum CRI mitigation solution seems to be the combination of all three approaches mentioned above.

6.3 SUMMARY AND CONCLUSIONS

The first part of this chapter provided definitions of some essential terms, such as the SNR, SIR, and selected performance metrics. In the second part of this chapter a set of models were developed by the candidate to quantify the error in eLoran pseudorange measurements under a variety of conditions:

A model of the error due to RF noise (modelled here as AWGN) was presented in Section 6.2.1.

In Section 6.2.2, a model to quantify the measurement error in the presence of a single cross-rating signal was developed (the DFD model). The model assumes that all signal parameters remain constant over the observation period and that no CRI mitigation algorithms are used in the receiver (except for averaging). It is mainly suitable for analysing the complex interference patterns caused by uncompensated CRI.

A stochastic model was developed in Section 6.2.3 (referred to here as the SFD model) in which the signal time (and carrier phase) offset is treated as a random variable, and the measurement error is calculated as the average error over the range of all possible time offsets. The model was extended in Section 6.2.4 to include the effects of multiple interfering signals and sky wave borne CRI, and can be used in eLoran coverage and performance prediction to quantify the effects of uncompensated CRI.

Section 6.2.6 demonstrated how the effects of CRI blanking can be modelled using a simple probabilistic approach, and in Section 6.2.8, a model was developed to quantify the residual error after CRI cancelling.

In Section 6.2.9, the different ways of dealing with CRI in eLoran receivers were compared and the optimum approach to CRI mitigation was identified.

The analyses presented in this chapter have shown that the effects of CRI are a function of a great number of parameters, including:

- Signal-to-Interference Ratio;
- Signal-to-Noise Ratio;

- GRIs and phase codes of the cross-rating signals;
- CRI mitigation algorithms used in the receiver;
- Receiver integration time;
- The number of cross-rating GRIs and the number of stations within each GRI;
- Time offset between the cross-rating signals (i.e. the position within the coverage area).

It has been shown that uncompensated CRI can introduce substantial measurement errors, including a position-dependent bias in the pseudorange measurements. It has also been shown that state-of-the-art signal processing can significantly mitigate the effects of CRI, however, a combination of several CRI mitigation techniques is required to achieve optimum results.

7 POSITIONING ACCURACY

The aim of this chapter is to introduce the mathematical tools used to model the accuracy of eLoran positioning. The chapter builds on information given in Chapter 5, and together with Chapter 3 and Chapter 6, it lays the foundation for the eLoran coverage and performance model presented later in this thesis.

7.1 POSITIONING ACCURACY MEASURES

There are numerous ways of measuring the accuracy of positioning systems, and this can sometimes lead to confusion. The purpose of this section is to introduce the most commonly used accuracy measures, clarify terminology, and identify the most suitable measure for use in this study. Since eLoran does not provide height information, this section will focus only on 2D (horizontal) accuracy measures. It will be assumed throughout that the performance is measured at a fixed location (static performance) and that the underlying position error process is stationary.

7.1.1 *Repeatable vs. Absolute Horizontal Accuracy*

Horizontal accuracy measures are derived from the *horizontal position error*, which can be determined as the geodetic distance between the position fix, $\hat{\mathbf{p}}$, and a given reference point, $\mathbf{p}$. This reference point is taken to be either the average reported postion, or the precise geodetic location of the receiving antenna. The former is used in determining *repeatable accuracy* (also referred to as *precision*), i.e. the accuracy with which a user of a positioning system can return to a location whose coordinates were measured in the past using the same system; the latter gives the *absolute accuracy* with respect to the coordinates of a particular geodetic system.

7.1.2 *Average Measures vs. Order Statistics*

It is important to realise that some accuracy measures are defined as averages, and some as order statistics. An example of an average measure is the Distance Root-Mean-Square (DRMS):

$$a_{\text{DRMS}} = \sqrt{\mathrm{E}\left[\|\hat{\mathbf{p}} - \mathbf{p}\|^2\right]}.$$

Here $\|\hat{\mathbf{p}} - \mathbf{p}\|$ denotes the geodesic distance between the position estimate $\hat{\mathbf{p}}$ and the reference point $\mathbf{p}$.

In accuracy calculations it is common to use a local tangent plane coordinate system [130] centred at $\mathbf{p}$, with one axis, say x, oriented in the direction of increasing longitude (corresponding to the *relative easting* component of the position) and the other in the direction of

increasing latitude (*relative northing*). The DRMS accuracy can then be expressed simply as:

$$\begin{aligned} a_{\text{DRMS}} &= \sqrt{\mathrm{E}\left[x^2 + y^2\right]} \\ &= \sqrt{\mathrm{E}\left[x^2\right] + \mathrm{E}\left[y^2\right]} \\ &= \sqrt{\sigma_x^2 + \mathrm{E}^2\left[x\right] + \sigma_y^2 + \mathrm{E}^2\left[y\right]}, \end{aligned}$$

where σ_x^2 and σ_y^2 denote the variance of the relative easting and northing components, respectively, and the mean values, $\mathrm{E}\left[x\right]$ and $\mathrm{E}\left[y\right]$, are often assumed to be zero. Note also that position accuracy is often stated as a 2DRMS figure rather than DRMS, which is simply equal to

$$a_{\text{2DRMS}} = 2 \cdot a_{\text{DRMS}}.$$

An example of an order statistic would be the *Circular Error Probable* (CEP). This is defined as the radius of a circle, centred at the reference point $\mathbf{p}$, containing 50% of the position fixes. Probability levels other than 50% are often used. International maritime standards, such as IMO Resolution A.1046(27), define accuracy in terms of a position error not exceeded with a probability of 95%, which is also commonly referred to as *R95 accuracy*.

A convenience of the average position accuracy measures is that, unlike the order statistics, they can be determined without full knowledge of the probability distribution of the measurement errors. For this reason, average measures are often used in system coverage and performance modelling. However, system performance requirements are usually specified in terms of order statistics (see e.g. the IMO requirements mentioned above). It is therefore necessary to be able to convert between the two measure types. The relationship between the different measures is determined by the probability distribution of the error and, unfortunately, is not always a simple one.

7.1.3 *Probability Distribution of the Position Error*

In GNSS, the distribution of horizontal position fixes is often approximated by a bivariate Gaussian distribution with zero means, zero correlation between the two variables and equal variance in each direction (i.e. the distribution is assumed to be circular). This is a reasonable assumption, as the satellites are more or less uniformly distributed in the sky, they are at comparable distances from the user, and therefore the ranging errors for the individual satellites are of comparable magnitudes. Under the above assumptions, the distribution of the instantaneous horizontal position error is given by the Rayleigh distribution. The relationship between an average measure of accuracy, say DRMS, and any given percentile error can then be found using the Rayleigh CDF. Specifically, the 95% error bound would be predicted to be

$$a_{\text{R95,circ}} \approx 1.731 \cdot a_{\text{DRMS}}.$$

Unfortunately, the above expression may be a poor approximation for eLoran. Due to the transmitting stations being land-based, eLoran signal strengths for the stations used in the position solution can vary

by orders of magnitude. Also, transmitter geometry may often be far from optimal (for a more detailed discussion of the factors affecting the eLoran position accuracy see the following section). For these reasons, the distribution of the position fixes is usually elliptical rather than circular and the above approximation fails. For example, an error circle with a radius of a_{2DRMS} contains 95.4% to 98.2% of the position fixes, depending on the eccentricity of the distribution [1].

One way of specifying accuracy when dealing with elliptical distributions is to use *error ellipses* instead of error circles. The semi-major and semi-minor axes of the error ellipse, denoted σ_{ma} and σ_{mi}, respectively, can be calculated as the square root of the eignevalues of the covariance matrix of the relative easting and northing coordinates:

$$\text{var}\left[\hat{\mathbf{p}}_{xy}\right] = \begin{bmatrix} \sigma_x^2 & \sigma_{xy} \\ \sigma_{xy} & \sigma_y^2 \end{bmatrix},$$

$$\sigma_{\text{ma}}^2 = \frac{1}{2}\left[\sigma_x^2 + \sigma_y^2 + \sqrt{\left(\sigma_x^2 - \sigma_y^2\right)^2 + 4\sigma_{xy}^2}\right],$$

$$\sigma_{\text{mi}}^2 = \frac{1}{2}\left[\sigma_x^2 + \sigma_y^2 - \sqrt{\left(\sigma_x^2 - \sigma_y^2\right)^2 + 4\sigma_{xy}^2}\right].$$

The position accuracy is then usually specified by stating the standard deviation along the semi-major axis, σ_{ma}, together with the eccentricity of the error ellipse

$$c = \frac{\sigma_{\text{mi}}}{\sigma_{\text{ma}}}.$$

The above description gives some insight into the distribution of the position fixes in the horizontal plane, but it does not allow direct comparison with the maritime performance requirements, which are considered in terms of the R95 accuracy. Finding the 95% error circle radius for an elliptical distribution is a non-trivial task. However, approximations can be found in the literature relating the parameters of the error distribution to error cirle radii for different probability levels. For example, Harre [150] proposed the following approximation for the 95% error:

$$a_{\text{R95,Harre}} \approx \left(1.960787 + 0.004121 \cdot c + 0.114151 \cdot c^2 + 0.371707 \cdot c^3\right) \cdot \sigma_{\text{ma}}, \tag{7.1}$$

where σ_{ma} and c have been defined above. The Harre approximation will be used throughout this thesis in modelling the accuracy of eLoran position.

7.2 POSITION ERROR ANALYSIS

This section takes a closer look at the four key factors that determine the positioning accuracy of eLoran. These are:

1. Accuracy of pseudorange measurements;

1 These figures assume that the relative northing and easting errors are zero-mean Gaussian-distributed, see [64].

2. Accuracy of the pseudorange-to-range conversion;
3. Geometry of the transmitter stations in use;
4. Position estimation algorithm used in the receiver.

The fours factors are discussed in turn below.

7.2.1 *Accuracy of Pseudorange Measurements*

The accuracy of the pseudorange measurements is a function of many variables. These can be broadly divided into three categories:

- Signal design parameters, such as the GRIs, phase codes, etc. (see Chapter 2);
- Channel characteristics, including signal attenuation or the amount of noise and interference (Chapter 3);
- Receiver design and configuration - use of interference mitigation algorithms, receiver integration time, etc. (Chapter 4 and Chapter 5).

Models to estimate the measurement error that take all of the key factors mentioned above into account were presented in Chapter 6.

7.2.2 *Accuracy of the Pseudorange-to-Range Conversion*

As explained in previous chapters, when solving for position, eLoran receivers apply correction factors (PF, SF and ASF) to the raw timing measurements in order to account for spatial and temporal variations in the signal propagation velocity and for the effects of irregular terain. It is assumed throughout this work that the receiver has perfect knowledge of the correction factors at the point of reception. This is a reasonable assumption when the receiver is equipped with up-to-date ASF maps and operates within the range of an eLoran differential reference station. It is the responsibility of eLoran maritime application service providers to make sure that accurate ASF maps and real-time differential corrections are available to mariners in critical areas such as harbours and harbour approaches. Applying the appropriate correction factors provides the full eLoran accuracy which approaches the repeatable accuracy of the system.

It should be noted, however, that the positioning performance can be degraded as a result of spatial decorrelation of differential corrections and aging of ASF maps. These effects are being investigated by the GLA and, unfortunately, cannot be precisely quantified at the time of writing.

7.2.3 *Stations' Geometry*

The transmitter-receiver geometry is a crucial factor in obtaining an accurate position fix. The impact of the station's geometry on the positioning accuracy is usually described by the Horizontal Dilution of Precision (HDOP) factor. The concept of HDOP is best understood by considering the eLoran LS position estimation algorithm.

As shown in Chapter 5, eLoran receivers find the position by iteratively refining an initial position and clock bias estimate, $\hat{\mathbf{q}} = \left[\hat{\lambda}, \hat{\varphi}, \hat{\rho}_b\right]^T$.

For a receiver that uses the LS position solution algorithm, the corrections applied at each iteration are given by Equation 5.22:

$$\Delta\mathbf{q} = \left(\mathbf{A}^{\mathrm{T}}\mathbf{A}\right)^{-1}\mathbf{A}^{\mathrm{T}}\Delta\boldsymbol{\rho}.$$

After the algorithm has converged, $\Delta\boldsymbol{\rho}$ can be considered as a vector of range measurement errors and $\Delta\mathbf{q}$ as the position (and clock bias) error due to these measurement errors. Equation 5.22 can therefore be used to determine the basic statistics of the position error.

Since the measurement errors are usually assumed to be zero-mean, $\mathrm{E}[\Delta\boldsymbol{\rho}] = \mathbf{o}_{N_{\mathrm{pr}}}$, the position\clock error can also be expected to have a zero mean, $\mathrm{E}[\Delta\mathbf{q}] = \mathbf{o}_3$. The variance matrix of the position error can be written from Equation 5.22 as[2]

$$\mathrm{var}[\Delta\mathbf{q}] = \left(\mathbf{A}^{\mathrm{T}}\mathbf{A}\right)^{-1}\mathbf{A}^{\mathrm{T}}\mathrm{var}[\Delta\boldsymbol{\rho}]\,\mathbf{A}\left(\mathbf{A}^{\mathrm{T}}\mathbf{A}\right)^{-1}. \tag{7.2}$$

Assuming that the pseudorange measurement errors are mutually uncorrelated and have equal variance, say σ_ρ^2, the measurement error variance matrix can be expressed in the form

$$\mathrm{var}[\Delta\boldsymbol{\rho}] = \sigma_\rho^2\mathbf{I}_3,$$

and upon substituting to Equation 7.2, the expression for the position error variance matrix reduces to

$$\mathrm{var}[\Delta\mathbf{q}] \equiv \begin{pmatrix} \sigma_x^2 & \sigma_{xy} & \sigma_{xb} \\ \sigma_{xy} & \sigma_y^2 & \sigma_{yb} \\ \sigma_{xb} & \sigma_{yb} & \sigma_b^2 \end{pmatrix} = \sigma_\rho^2 \underbrace{\left(\mathbf{A}^{\mathrm{T}}\mathbf{A}\right)^{-1}}_{\mathbf{G}}. \tag{7.3}$$

This allows the position accuracy to be determined as a product of the measurement error, σ_ρ, and a dimensionless multiplier dependent only on the transmitter-receiver geometry. This multiplier is commonly referred to as HDOP:

$$a_{\mathrm{DRMS}} = \sqrt{\sigma_x^2 + \sigma_y^2} = \sigma_\rho \underbrace{\sqrt{G_{1,1} + G_{2,2}}}_{\mathrm{HDOP}}. \tag{7.4}$$

HDOP thus represents the amplification of the pseudorange standard error onto the position solution due to the stations' geometry.

A plot of HDOP values can help a network designer to identify geographical areas that will pose a repeatable accuracy problem, based solely on the location of the transmitting stations. Although it is based on a number of simplifing assumptions that may not be met in practice, HDOP proves to be a useful tool to optimally place transmitters.

As an example, Figure 67 plots the HDOP distribution over the British Isles based on the current configuration of the North-West European Loran stations, assuming that each station has a maximum range of 1200 km. The plot shows that the existing transmission network provides good geometry over most of Britain and the North Sea, however, increased HDOP values can be observed off the West and South Coast of Ireland. This suggests that there may be a need for a new station in Ireland, preferably located as far South-West as possible. The need

2 The following identity was used: $\mathrm{var}\{\mathbf{Bx}\} = \mathbf{B}\mathrm{var}\{\mathbf{x}\}\,\mathbf{B}^{\mathrm{T}}$, where $\mathbf{x}$ is a random $n \times 1$ vector and $\mathbf{B}$ is an $m \times n$ matrix.

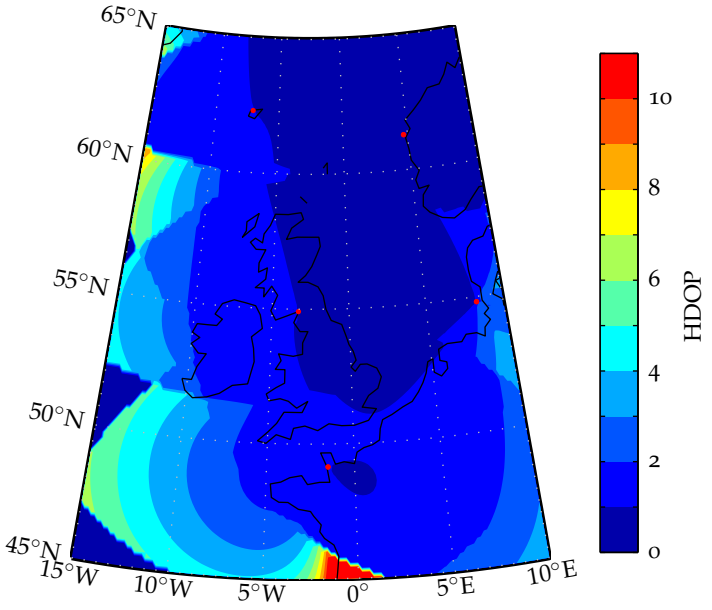

Figure 67: HDOP distribution over the British Isles for the North-West European Loran stations (shown by red dots); maximum range of a station assumed to be 1200 km.

for and possibility of such an extension will be further investigated in Chapter 9 and Chapter 11.

7.2.4 *Position Estimation Algorithm*

The choice of the position estimation algorithm can have a significant effect on the achievable positioning accuracy. Several alternatives to the traditional LS method were discussed in Chapter 5, and the decision was made to use the WLS algorithm as a model of eLoran positioning (see Equation 5.23). The following shows how to estimate the accuracy of the WLS solution.

As above, it is assumed that the measurement errors are zero mean and therefore the mean position error is also zero. Further, it will be assumed throughout that the measurement variance matrix, $\text{var}[\Delta\boldsymbol{\rho}]$, is diagonal with the elements on the main diagonal determined using the appropriate receiver performance models developed in Chapter 6.

The variance of the WLS solution is minimised when the weight matrix, $\mathbf{W}$, is equal to the inverse of the measurement variance matrix:

$$\mathbf{W} = (\text{var}[\Delta\boldsymbol{\rho}])^{-1}.$$

The variance matrix of the position error can then be obtained from Equation 5.23 as

$$\text{var}[\Delta\mathbf{q}] = \left(\mathbf{A}^{\mathrm{T}}\mathbf{W}\mathbf{A}\right)^{-1}, \tag{7.5}$$

and the DRMS accuracy, error ellipse parameters, and the 95% error radius can be determined from the variance matrix as shown earlier in this chapter.

7.3 SUMMARY AND CONCLUSIONS

The first part of this chapter explained the necessary definitions and introduced the Harre approximation for the conversion of error ellipse parameters to R95 accuracy. In the rest of the chapter the key factors that determine eLoran position accuracy were discussed and a method of estimating the DRMS and R95 accuracy based on the knowledge of the pseudorange measurement errors was described.

It was assumed that the receiver has perfect knowledge of the SF and ASF correction factors at the point of reception. This is a reasonable assumption when the receiver is equipped with up-to-date ASF maps and operates within the range of an eLoran differential reference station.

The techniques described in this chapter form the basis of the eLoran coverage and performance model presented in Chapter 9.

8 VALIDATION

This chapter aims to verify and validate the analytical receiver performance models developed in Chapter 6 and Chapter 7. The validation proceeds in three parts. First, the analytical predictions are compared with results obtained by computer simulations. These theoretical results are then validated by experimental data obtained by receiver performance testing conducted in a controlled radio environment. The results of the tests are also used to refine and calibrate the analytical models. Finally, eLoran data from a field trial is used to assess how accurately the models reflect reality.

The major part of this chapter is concerned with the validation of the pseudorange measurement error models of Chapter 6. Section 8.3.2 then presents the validation of the positioning accuracy model described in Chapter 7.

8.1 COMPUTER SIMULATIONS

In order to facilitate computer simulations of eLoran signal processing algorithms, the candidate created a set of Simulink® and MATLAB® tools. This section gives a brief description of the software tools developed and experiments conducted.

8.1.1 *eLoran Signal Processing Blockset for Simulink*

The MathWorks Simulink® environment is a powerful modelling tool widely used in the design and simulation of signal processing algorithms. It is based around a set of customisable function block libraries, and provides a graphical interface that enables the user to link the available function blocks to form larger systems.

For the purpose of this work, a Simulink® blockset was created which allows the generation of the eLoran RF signal waveforms according to the model presented in Chapter 3, and the execution of basic signal processing operations on the RF signal, as described in Chapter 5. The blocks in the eLoran Signal Processing Blockset (ESPB) are organised in three groups: the 'Sources' group which contains the eLoran signal generator and a generator of a band-limited White Gaussian Noise (WGN); the 'Channel' group which contains blocks to simulate some effects of the radio channel; and the 'Receiver' group which is subdivided into 'Signal Conditioning' and 'Baseband Signal Processing', and includes blocks such as the Standard Input Bandpass Filter, Comb Filter, Phase-decoding Filter, or the CRI Blanking and CRI Cancelling blocks. The blockset can be used to implement the receiver model developed in Chapter 5 and examine its response to both deterministic and random driving signals, thereby allowing the accuracy of the eLoran measurements to be evaluated.

A series of Simulink experiments were conducted with the aim to verify the analytical models of Chapter 6. Each experiment comprises a SimuLink model and a MATLAB script that performs the initialisation of the experiment, it starts the simulation and evaluates the results

after the simulation has been finished. A brief description of each experiment is given in Section 8.1.3.

8.1.2 *eLoran Toolbox for MATLAB*

The Simulink® ESPB models operate by processing RF signals sampled at 400 kHz. Consequently, processing a statistically significant sample set can be a time-consuming task. In order to speed up the simulations, simplified computational models were designed in MATLAB® which differ from the Simulink models in two ways.

Firstly, the MATLAB® models work with samples of the signal's complex envelope, rather than the RF waveforms, so that the need for frequency down-conversion is avoided. Secondly, the number of samples that are generated can be reduced as eLoran receivers effectively use, in the carrier phase estimation process, only one sample per pulse. This means that only 16 signal samples per PCI are required, as opposed to 32000 to 80000 samples (depending on the GRI) that need to be generated and processed with the ESPB. These simplifications considerably reduce the computation time, and the simulation results presented throughout this work were therefore obtained using the simplified MATLAB® models.

Each MATLAB® model was verified against its Simulink® counterpart by comparing results from a limited set of simulation runs.

8.1.3 *Simulation Scenarios*

A range of simulation scenarios were designed in order to verify the analytical results of Chapter 6. A description of each scenario is given below.

Performance in Additive White Gaussian Noise

This scenario was set up to verify the performance model derived in Section 6.2.1 (Chapter 6). The configuration of the experiment is shown in Figure 68. In this scenario, the wanted eLoran waveform is corrupted by band-limited AWGN and the noisy signal is then processed according to the signal processing model[1] of Figure 48 (Chapter 5) to obtain a vector of carrier phase measurements; from this data the basic statistics of the pseudorange measurement error are determined.

The experiment was repeated for a range of SNR values. In each run of the simulation 10^4 s worth of data was processed.

As shown in Section 6.2.1, the results of the simulations are in perfect agreement with analytical predictions based on Equation 6.12, thus proving the correctness of the analytical approach.

Performance in CRI

This scenario was set up to verify the performance models derived in Section 6.2.2 to Section 6.2.4 (Chapter 6). The configuration of the experiment is shown in Figure 69. In this scenario, the desired eLoran waveform is interfered by another eLoran waveform and the resulting

1 Note that, unlike the analogue prototype filter, the digital bandpass filter used in the Simulink model gives a zero phase shift at the carrier frequency. The Simulink models presented in this chapter therefore omit the phase correction block shown in the signal processing model of Figure 48.

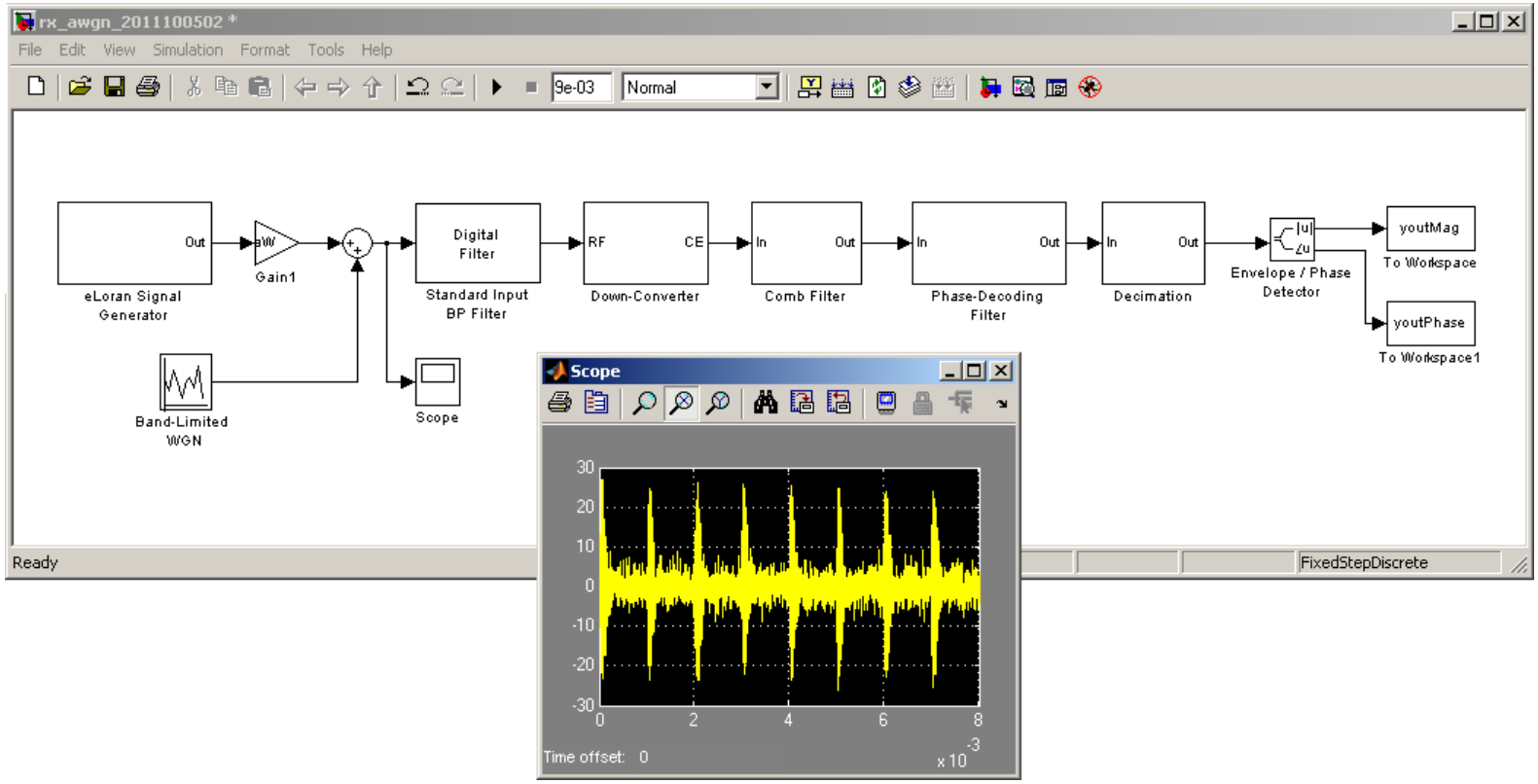

Figure 68: Simulink® model to evaluate eLoran receiver performance in AWGN.

signal is processed to obtain a vector of carrier phase measurements and the basic statistics of the ranging error.

A number of experiments were conducted using different values of the SIR and signal time offset, and different GRI combinations. In each run of the simulation approximately 2000 s worth of data (corresponding to two overlap intervals) was processed. In order to verify the stochastic models of Section 6.2.3 and Section 6.2.4, the simulation was repeated for time offsets between 0 and twice the greatest common divisor of the two interfering GRIs and the results from each run were averaged (recall that the interfering patterns are periodic in time offset with a period given by the greatest common divisor of the GRIs and that the models of Section 6.2.3 and Section 6.2.4 give the average error calculated over the whole range of possible time offset values). To verify the model of Section 6.2.4, additional signal sources were used to simulate multiple interferers and skywave borne CRI.

As shown in the respective sections of Chapter 6, the results of the simulations are in perfect agreement with the analytical predictions.

Mitigating CRI by Blanking

The scenario shown in Figure 70 was set up to verify the performance model presented in Section 6.2.6. Here, the wanted eLoran waveform is interfered with another eLoran waveform and band-limited AWGN and the statistics of the pseudorange measurement error are obtained by the same process as above. The receiver model differs from that used above in that it includes the CRI blanking block which works by setting its output to zero when a pulse group of the interfering signal arrives (see also Section 5.3.1, Chapter 5).

The experiment was repeated for an increasing number of interfering stations. In each run 10^4 s worth of data was processed.

The results of the simulations are again in perfect agreement with analytical predictions, as presented in Chapter 6.

Mitigating CRI by Cancelling

Figure 71 shows the simulation scenario used to verify the performance model presented in Section 6.2.8. In this scenario, the wanted eLoran waveform is interfered with another eLoran waveform and the basic statistics of the ranging error are obtained by the same process as above. The amplitude of the eLoran signals is jittered on a pulse-to-pulse basis according to the Gaussian distribution. The CRI blanking block in the receiver model has been replaced by the CRI cancelling block which works by subtracting from the received signal a replica of the interfering signal (see also Section 5.3.2, Chapter 5).

The experiment was repeated for different values of the SIR and standard deviation of the amplitude jitter. In each run 10^4 s worth of data was processed.

The results of the simulations and analytical predictions presented in Section 6.2.6 agree to within 1% of the values obtained by simulation.

8.2 RECEIVER TEST BENCH

One of the great difficulties encountered in this work was a lack of available information about eLoran receivers. Receiver manufacturers have not widely published the details of their eLoran receivers, and

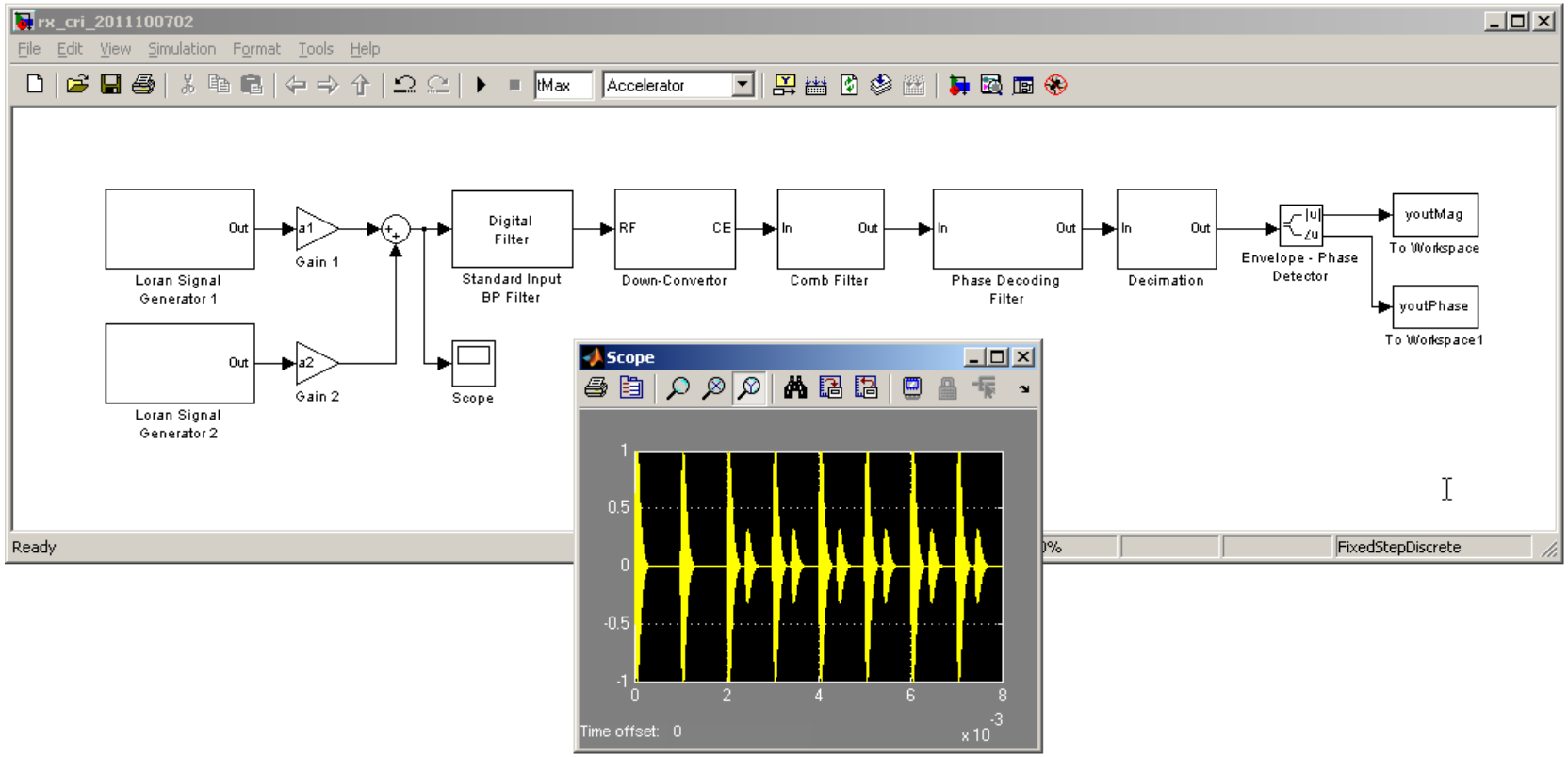

Figure 69: Simulink® model to evaluate receiver performance in CRI.

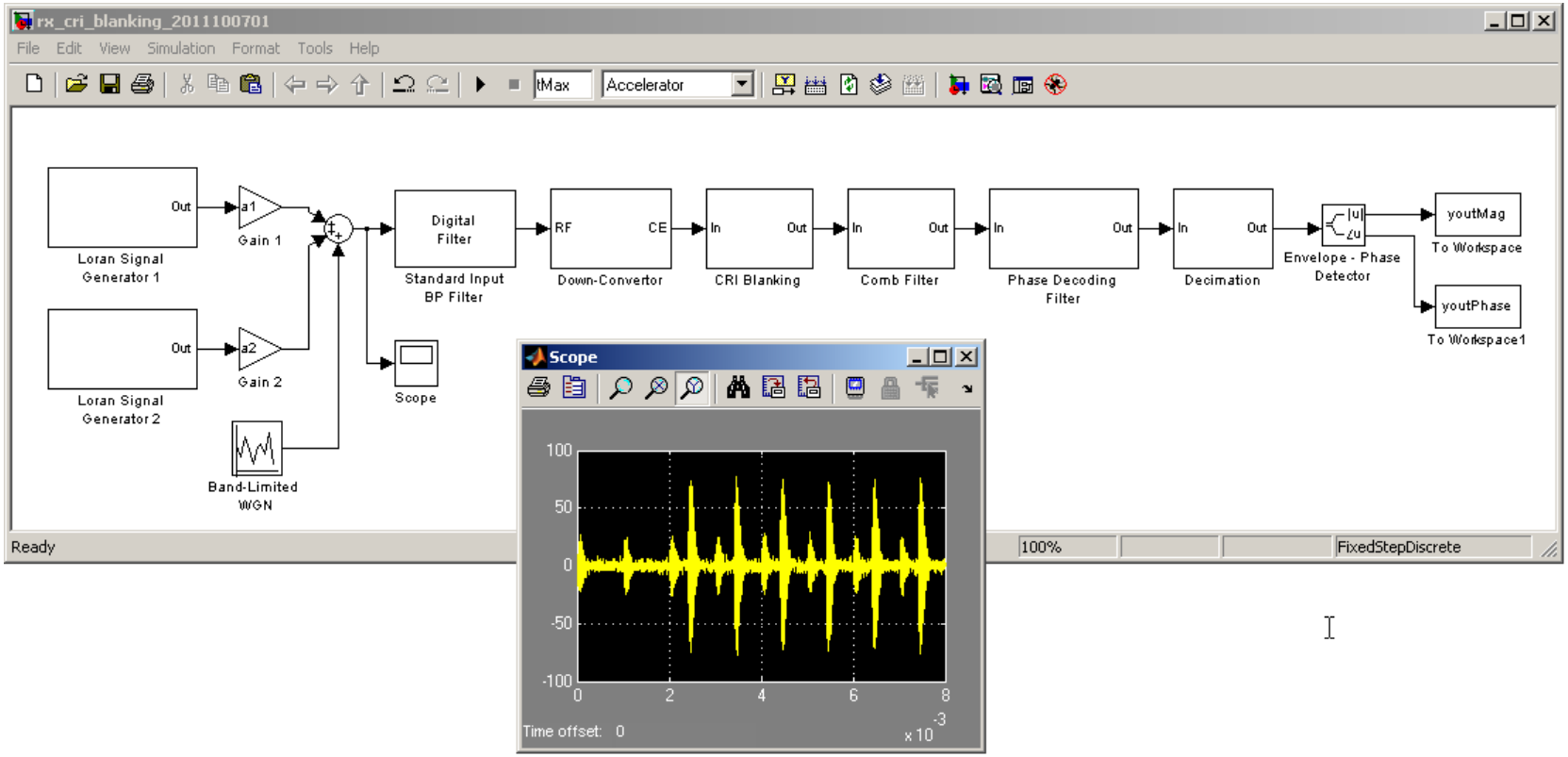

Figure 70: Simulink® model to evaluate the effects of CRI blanking.

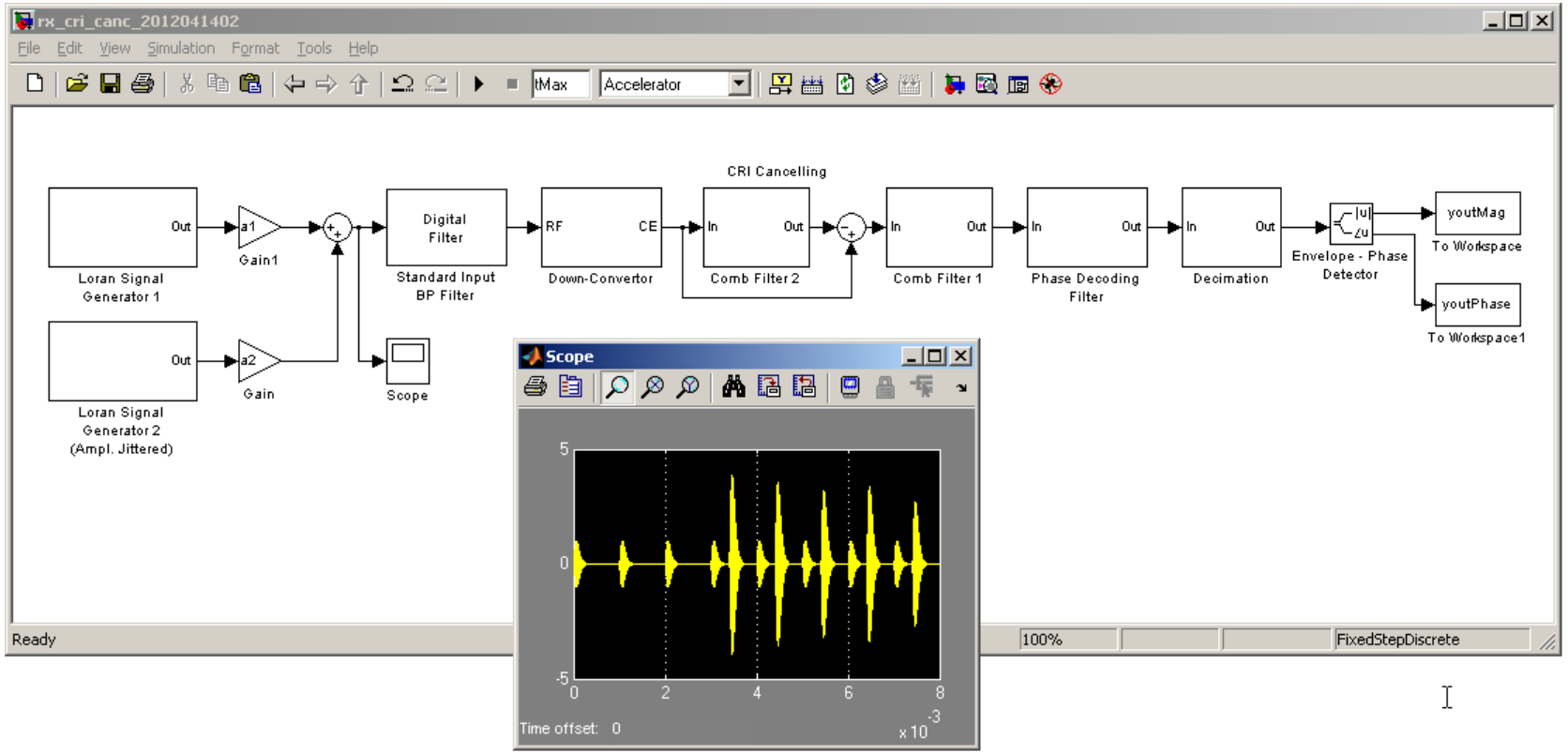

Figure 71: Simulink® model to evaluate the effectiveness of CRI cancelling (amplitude jitter in the interfering signal is exagerated).

eLoran receiver performance standards, which could provide a valuable guideline for these investigations, have not been completed at the time of writing[2].

In order to get a better understanding of the performance of commercially available receivers, the candidate developed an eLoran receiver test bench, which allows the performance to be studied under controlled noise and interference conditions. This section provides a brief overview of the hardware and software that make up the test bench, describes its current features and limitations, and presents some of the experiments conducted by the candidate in order to validate the performance models presented earlier in this work.

8.2.1 *Hardware*

Figure 72 depicts the main hardware components of the test bench system. The test bench consists of an eLoran signal simulator, a receiver coupler, a highly stable clock signal source, and a control\monitoring PC.

The simulator allows the generation of synthetic eLoran signals with user-defined parameters but can also be used for replaying of actual LF signals captured in the field. It consists of a PC workstation (PC1) equipped with a multi-channel Digital-to-Analogue Converter (DAC) board, communicating with the host system via a PCI bus. The board uses four 14-bit DACs which can operate at sampling frequencies of up to 105 MHz, thus providing four independent output channels, each with a maximum[3] bandwidth of around 52 MHz.

In the current set-up, a reference 10 MHz clock signal is supplied to the board from an external GPS-disciplined Rubidium clock. This signal is then internally divided to form the sampling frequency (either 2 MHz or 5 MHz have been used).

The simulator output is connected to an antenna input of a receiver under test through a receiver-specific coupler circuit[4]. The coupler serves several purposes: it transforms the unbalanced simulator signal into a balanced receiver input signal; it matches the output impedance of the simulator to the receiver input impedance; it also attenuates the simulator signals and galvanically isolates the simulator from the receiver, protecting the receiver from overload and damage.

Output data from the receiver under test, typically provided in the form of National Marine Electronics Association (NMEA) type messages, are logged using a separate computer (PC2). This data is then analysed to assess the receiver's ranging and positioning performance.

8.2.2 *Software*

Figure 73 illustrates the software architecture of the test bench system. At the heart of the system is the signal architect - a compiled MATLAB® application that allows the user to design the RF simulator signals. It takes user inputs from a configuration file and produces a custom eLoran scenario data file containing samples of the RF signal to be generated.

2 Marine eLoran receiver MPS are being developed within the RTCM - Special Committee 127 on eLoran Systems.
3 Note that this does not take into account throughput limitations in the host system.
4 Design courtesy of Reelektronika, b.v.

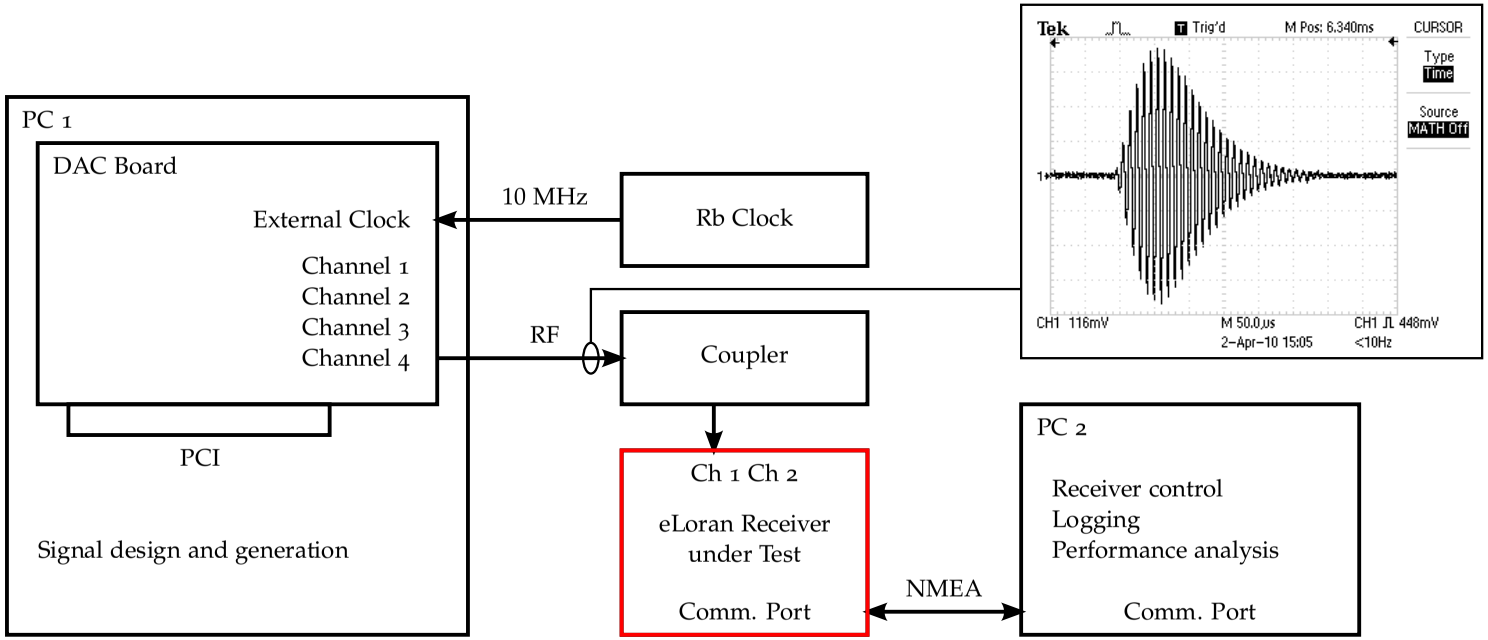

Figure 72: Schematic diagram of the eLoran receiver test bench set-up.

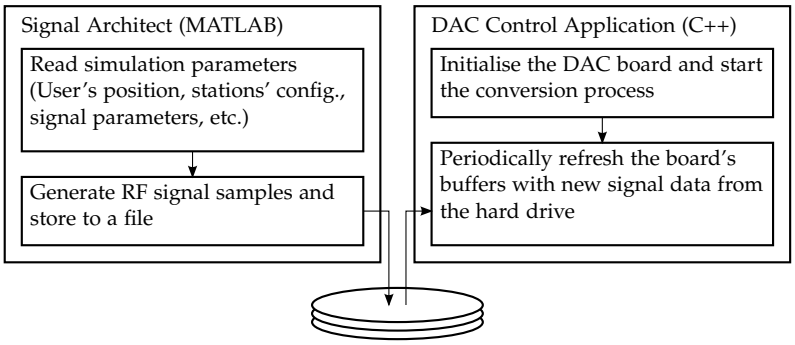

(a) Simulator software (PC1)

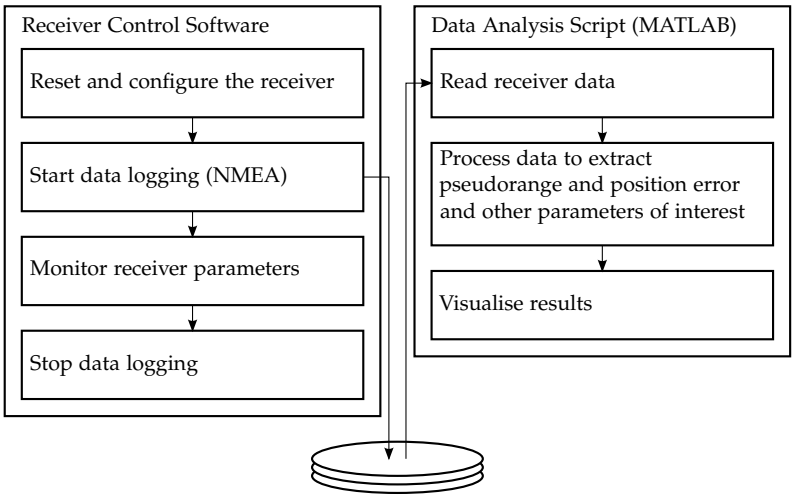

(b) Data analysis (PC2)

Figure 73: Simplified flowcharts of the simulator and data analysis software.

A simulation is started by executing a control application which reads signal samples from the data file created by the signal architect, and passes them to the DAC board for playback. This application is written in C++, which gives the necessary control over the time-critical tasks that need to be performed during the digital-to-analogue conversion process.

Since the waveform generation is fully software defined and decoupled from the time-critical digital-to-analogue conversion tasks, there are literally no limits as to the complexity of the waveforms that can be generated. For example, it is possible to simulate an arbitrary number of eLoran signals, use different noise and interference models, etc. Future extensions may include the simulation of motion and data modulation of the signals.

The analogue RF signal is fed into the receiver under test which processes it and produces an NMEA data stream containing signal timing and receiver positon estimates and other parameters of interest. In the current configuration, the NMEA data is logged using an application provided by the manufacturer of the receiver under test (Reelektronika LERXAnalyser). The same application is also used to configure the receiver and monitor its outputs in real time.

Data obtained during the receiver testing are analysed to produce receiver performance statistics using software developed in MATLAB®.

8.2.3 *Current Features and Limitations*

Currently, the receiver test bench allows the simulation of ground wave and sky wave eLoran signals and atmospheric noise. The effects of transmitter dual-rate blanking and pulse-to-pulse jitter can also be simulated. The signal parameters are either user-defined or calculated for a specified location from corresponding models referenced in Chapter 3. Atmospheric noise is simulated either as band-limited AWGN or as a mixture of Gaussian and impulsive noise, as specified in reference [134]. As mentioned above, there are no limitations to the number of transmitting stations or rates used in the simulation. The simulator therefore provides an excellent tool for studying the effects of CRI.

The simulator currently operates in only a single-channel (E-field) mode; however, tests performed on the simulator machine suggest that the chosen system architecture provides sufficient throughput for dual-channel operation, and therefore simulation of signals from an H-field antenna should also be possible.

Due to the software defined nature of the simulator, the system is very flexible and easily extendible with new functions via software updates.

8.2.4 *Simulator Calibration and Test of Proper Functioning*

Several tests were carried out in order to verify the proper functioning of the experimental test bench setup.

eLoran Waveform Accuracy

The first set of tests involved feeding pure synthetic eLoran signals of a single rate into a commercially available receiver (the Reelektronika LORADD with Plutargus v.1.0 firmware) and analysing the receiver outputs. The result of one of these tests is shown in Figure 74, which is a screenshot taken from the monitoring and control application supplied with the receiver (Reelektronika LERXAnalyser).

It can be seen from the figure that the standard deviation of the signal timing measurements is well below 1 ns (corresponding to a pseudorange error of less than 30 cm), and position errors are practically unmeasurable. The Batch Quality (B-Q) and Cycle Identification Quality (CI-Q) indicators for all signals are equal to 1, which indicates the best achievable signal quality. The ECDs are close to zero; some calibration of the simulator pulse ECD was necessary to achieve near-zero values as the receiver expects the incoming pulses to be distorted in a particular manner by the antenna and associated circuitry which is not part of the test bench setup. The reported SNRs were around 73 dB, which is in line with expectations based on the theoretical maximum achievable SQNR for a 14-bit DA converter[5].

These results confirm that the simulated eLoran waveforms are accurate, both in terms of timing and pulse shape, and can be used for receiver testing.

5 $\mathrm{SQNR}_{\max} = 6.02n + 1.7\ (\mathrm{dB})$, where n is the number of bits of the DA convertor.

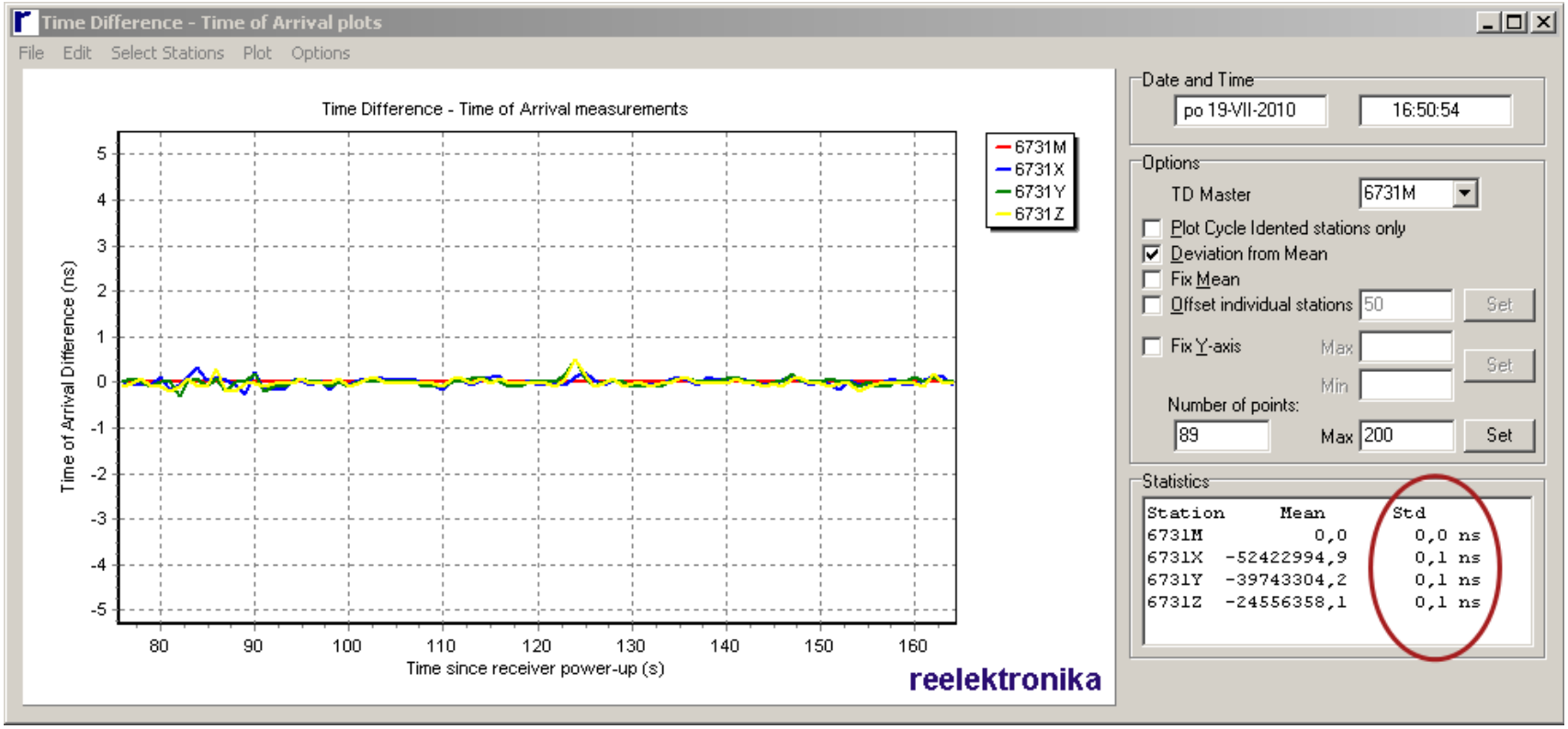

Figure 74: Receiving synthetic signals of the 6731 (Lessay) rate (Reelektronika LERXAnalyser software).

Noise Generator Calibration

A second set of tests were carried out to ensure the proper calibration of the simulator's noise generator. As explained in Chapter 3, the dominant source of noise in the LF band is the atmospheric noise. Due to the impulsive nature of the atmospheric noise associated with lightning discharges, the probability distribution of the noise process can be significantly non-Gaussian. Moreover, the statistical properties of the noise change over time. This begs the question as to how this type of noise should be simulated for the purpose of receiver testing?

At the time of this writing, eLoran receiver MPS and the methods of testing are still in development. However, it can be assumed that the eLoran test procedures will be analogous to those used for Loran-C. The existing Loran-C standards [131, 133, 132, 134, 135] allow two types of noise to be used for receiver testing:

1. Gaussian noise with a uniform power spectral density over the Loran band.
2. Simulated Atmospheric Noise, which is generated as a combination of a low-power, wideband Gaussian noise component, and an impulsive noise component consisting of short bursts of RF energy randomly distributed in time (for details of this model see document [134]).

In line with the discussion in Chapter 3, the author chose to use the Gaussian noise model. Where only the Gaussian noise is used, standards usually allow reducing the level of the noise generator to compensate for the differences between the atmospheric and Gaussian noise probability distributions (see standard [132]). The candidate decided not to compensate for the difference, as the actual atmospheric noise distribution can change significantly over time (see Chapter 3), and applying any correction factors would seem rather arbitrary. Consequently, receiver performance observed when using the signal simulator may be poorer than performance in actual atmospheric noise at the same SNR conditions.

When implementing the noise generator, it was important to ensure that the power of the simulated noise was set appropriately in order to produce the desired SNR readouts at the receiver. This was accomplished as follows:

In accordance with earlier assumptions, the noise in the received signal is modelled as band-limited AWGN. The simulator is a sampled system and the power of the band-limited noise will be uniformly distributed over the system's first Nyquist zone[6]. The single-sided power spectral density of the simulated noise can therefore be approximated (within the first Nyquist zone) by $N_{\text{sim}} = P_{w_{\text{sim}}} / (f_s/2)$, where $P_{w_{\text{sim}}}$ is the simulator noise power, and f_s is the sampling frequency used within the system. SNR is defined in this work as the ratio of the power of the eLoran signal, P_s, to the power of the noise obtained after filtering by the standard bandpass filter, P_{w_b} (for details of the SNR definitions used in this work see Chapter 6). The power of the filtered noise can be calculated as $P_{w_b} = B_{b,n} \cdot N_{\text{sim}} = B_{b,n} \cdot P_{w_{\text{sim}}} / (f_s/2)$, where $B_{b,n}$ is the

6 The interval of frequencies from 0 Hz to one-half of the sampling frequency.

noise bandwidth of the filter (see Chapter 5). The SNR can therefore be expressed as

$$\mathrm{SNR} = \frac{P_s}{P_{w_\mathrm{b}}} = \frac{P_s}{B_{\mathrm{b,n}} P_{w_\mathrm{sim}}} \cdot \frac{f_\mathrm{s}}{2},$$

from which, the desired simulator noise power can be calculated as

$$P_{w_\mathrm{sim}} = \frac{P_{w_\mathrm{b}}}{B_{\mathrm{b,n}}} \cdot \frac{f_\mathrm{s}}{2} = \frac{P_s}{B_{\mathrm{b,n}} \mathrm{SNR}} \cdot \frac{f_\mathrm{s}}{2}. \tag{8.1}$$

In the simulator, the atmospheric noise is therefore modelled by an uncorrelated, zero mean Gaussian process whose variance, P_{w_sim}, satisfies Equation 8.1.

In order to verify the correct SNR calibration a set of tests were conducted using the Reelektronika LORADD eLoran receiver. During the tests it was noted that the receiver reported SNR values approximately 3 dB lower than expected based on Equation 8.1 above; two possible explanations seem likely:

- The receiver uses a different SNR definition than that used in this work (see Chapter 6);
- The receiver uses a different sampling point position than assumed in this work (i.e. the receiver measures the carrier phase closer to the beginning of the pulse where the signal strength is lower).

For the sake of consistency, the current SNR definition as given in Chapter 6 is retained in the rest of this thesis (i.e. SNR values reported by the receiver during the tests described below are approximately 3 dB lower than the values used in measurement error prediction).

8.2.5 *Evaluating the Pseudorange Measurement Error*

Estimating the pseudorange measurement error from a receiver's output data is not entirely straightforward. Data output by eLoran receivers normally consist of signal TOA information rather than the pseudoranges. The timing data typically contain a slowly-varying error component which is due to the receiver's clock drift. This error component is common to all measurements made at a given time and will eventually cancel out in the position solution. Therefore it should not be included in the TOA\pseudorange error estimates. The clock error can be eliminated from the measurements in two ways.

One possibility is to pass the measured data through a high-pass filter that rejects the slowly-varying component of the error. Another possibility is to eliminate the error by forming Time Difference (TD) measurements for pairs of two or more signals. The TOA and pseudorange error for the individual signals can then be estimated as described below. The latter approach was used in this work.

Two Signals of the Same Strength and GRI

Consider TOA measurements $\hat{t}_{a,1}[u]$, $\hat{t}_{a,2}[u]$ performed on two eLoran signals at time u. Assuming that the receiver is stationary, the measuements can be modelled as

$$\hat{t}_{a,1}[u] = \tau_{ED,1} + \tau_{prop,1} + \tau_b[u] + \varepsilon_{t,1}[u]$$
$$\hat{t}_{a,2}[u] = \tau_{ED,2} + \tau_{prop,2} + \tau_b[u] + \varepsilon_{t,2}[u],$$

where $\tau_{ED,i}$ is the Emission Delay of the i-th station, $\tau_{prop,i}$ is the propagation delay, $\tau_b[u]$ is the clock bias (common to both signals, but changing slowly over time) and $\varepsilon_{t,i}[u]$ is the instantaneous TOA measurement error for each signal. By forming the time difference $\hat{t}_{d,21}[u] = \hat{t}_{a,2}[u] - \hat{t}_{a,1}[u]$, the clock bias is eliminated and one obtains

$$\hat{t}_{d,21}[u] = \underbrace{\tau_{ED,2} - \tau_{ED,1} + \tau_{prop,2} - \tau_{prop,1}}_{\text{constant}} + \underbrace{\varepsilon_{t,2}[u] - \varepsilon_{t,1}[u]}_{\text{TD meas. error}}.$$

Clearly, the average variance of the TD measurement, $\text{var}^a\left[\hat{t}_{d,21}[u]\right] \equiv \sigma^2_{TD,21}$, can be considered a sum of the variances of the TOA measurement errors of the individual signals used to form the TD[7], $\text{var}^a[\varepsilon_{t,1}[u]] \equiv \sigma^2_{t,1}$ and $\text{var}^a[\varepsilon_{t,2}[u]] \equiv \sigma^2_{t,2}$:

$$\sigma^2_{TD,21} = \sigma^2_{t,2} + \sigma^2_{t,1}.$$

If the two test signals are of the same strength and GRI, then it can be assumed that the average[8] measurement error for both the signals are the same and therefore equal to

$$\sigma^2_{t,1} = \sigma^2_{t,2} = \frac{\sigma^2_{TD,21}}{2}.$$

The General Case

In the general case, at least three test signals are needed to eliminate the clock error using this approach. Assume that the TD measurements are formed according to the following pattern: $2-1$, $3-1$, $2-3$. The corresponding TD variances are then:

$$\begin{aligned}\sigma^2_{TD,21} &= \sigma^2_{t,2} + \sigma^2_{t,1}\\ \sigma^2_{TD,31} &= \sigma^2_{t,3} + \sigma^2_{t,1}\\ \sigma^2_{TD,23} &= \sigma^2_{t,2} + \sigma^2_{t,3},\end{aligned}$$

and the timing error variances are therefore given by

$$\begin{aligned}\sigma^2_{t,1} &= \frac{\sigma^2_{TD,21} + \sigma^2_{TD,31} - \sigma^2_{TD,23}}{2}\\ \sigma^2_{t,2} &= \sigma^2_{TD,21} - \sigma^2_{t,1}\\ \sigma^2_{t,3} &= \sigma^2_{TD,31} - \sigma^2_{t,1}.\end{aligned}$$

The equivalent pseudorange error for the m-th signal is then estimated simply as $\sigma^2_{r,m} = c^2\sigma^2_{t,m}$, $m = 1, 2, 3$.

7 It is assumed that the errors on the individual signals are uncorrelated.
8 If the errors are due to CRI it may be necessary to average over all possible time alignments between the interfering pulse trains for this assumption to hold.

8.2.6 *Results of Receiver Testing*

In order to provide experimental backing for the theoretical results presented earlier in this work a series of experiments were conducted using the test bench and a commercially available eLoran receiver (the Reelektronika LORADD with Plutargus v.1.0 firmware). The test scenarios and results are summarised below.

Performance in WGN and Estimation of the Implementation Loss

The first scenario involved evaluating the receiver's response to a synthetic eLoran signal (GRI 6731) corrupted by band-limited AWGN. The receiver integration time was 5 seconds, which corresponds to $N_p = 594$ pulse samples per pseudorange measurement.

The experiment was repeated for a range of SNR values[9]. In each run, 30 minutes worth of data was processed (the amount of data processed in the test bench experiments was less than in the computer simulations described earlier, as the test bench experiments have to be conducted in real-time).

Figure 75 shows the results of the experiments along with theoretical predictions based on Equation 6.12 (Chapter 6), reproduced below. In line with expectations, the pseudorange errors observed in the experiments are slightly higher than the theoretical predictions. The difference can be calibrated out using the implementation loss factor, L_{impl}, which, for the particular receiver under test, turns out to be approximately 4.8.

It can also be seen from the measurements that the characteristics flattens at high SNRs. This is presumably a result of the receiver's internal noise (e.g. quantisation, phase, or thermal noise). The effect can be modelled by an additive constant, $\sigma^2_{\text{impl,r}}$, which, for the receiver under test, equals approximately $(0.45)^2$.

$$\sigma_r^2 \approx L_{\text{impl}} \frac{337.4^2}{N_p \cdot \text{SNR}_{\tau_p}} + \sigma^2_{\text{impl,r}}, \tag{8.2}$$

However, since this effect is only noticeable at very high SNRs unlikely to be encountered in practice, it can safely be neglected. In the rest of this work, the effects of AWGN will therefore be modelled using Equation 8.2 with $L_{\text{impl}} = 4.8$ and $\sigma^2_{\text{impl,r}} = 0$.

Performance in CRI

In order to assess the effects of CRI on the measurement error in a state-of-the-art eLoran receiver, a series of test bench experiments were conducted in which an eLoran signal was corrupted by band-limited AWGN and interfered with signals of a different GRI. The experiments were conducted for SIR values ranging from -10 dB to 40 dB.

As an example, Figure 76 plots the ranging error versus SIR for a GRI 6731 signal interfered with signals of GRI 7001. The SNR of the wanted signal was set to 30 dB. It can be seen from the plot that for high enough SIR values, the errors are largely determined by the additive noise and can be modelled as described earlier (see the

9 SNR is defined throughout this document as discussed in Chapter 6; it should be noted that SNRs reported by commercially available receivers may vary depending on the SNR definition and signal processing implementd in the receiver.

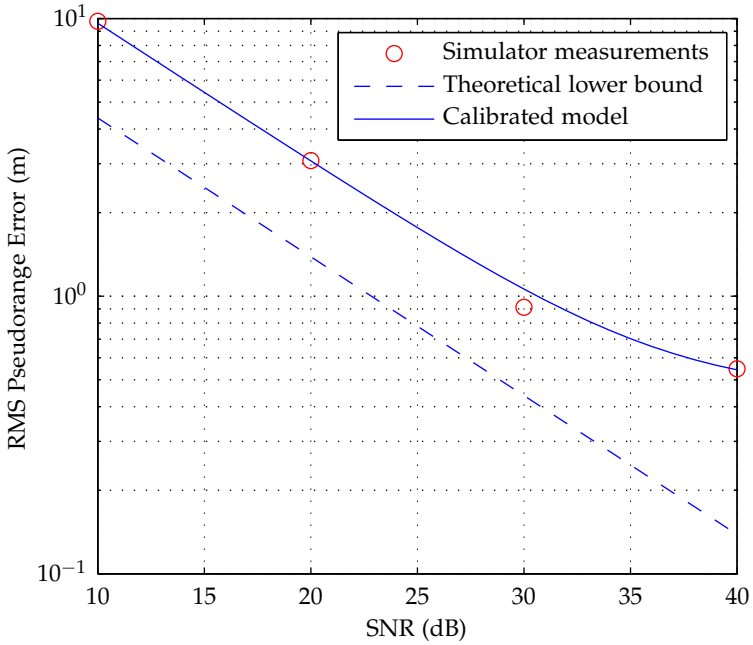

Figure 75: Pseudorange measurement error due to AWGN as a function of SNR; red: test bench results; dashed line: theoretical lower bound assuming $L_{\text{impl}} = \sigma^2_{\text{impl,r}} = 0$; solid line: calibrated analytical model assuming implementation loss $L_{\text{impl}} = 4.8$; $\sigma^2_{\text{impl,r}} = (0.45)^2$; integration time $T_{\text{i}} \approx 5\,\text{s}$.

dashed line in Figure 76 and Equation 8.2 above). As as SIR reduces, the measurement error gradually increases. In this region (i.e. at SIR above approximately 10 dB), the ranging error follows remarkably accurately the theoretical model for uncompensated CRI derived in Section 6.2.3 (Chapter 6).When the SIR drops below 10 dB a sudden transition occurs, and for a lower SIR the error levels off at a value consistent with theoretical predictions of the model for CRI blanking (Section 6.2.6).

The characteristics shown in Figure 76 therefore suggest that the receiver under test treats the CRI in one of the two following ways depending on the relative strength of the interference:

- When SIR $>$ 10 dB, the receiver does not use any CRI mitigation algorithms apart from the standard phase-decoding and comb-filtering operations, which provides sufficient suppression of the interference in the mentioned range of SIRs;
- When SIR $<$ 10 dB, the receiver uses CRI blanking to mitigate the interference.

Such behaviour would be in line with theoretical expectations based on the discussions in Chapter 6.

It is not clear from the experiments conducted, whether the receiver under test uses CRI cancelling. Receivers that use this technique would likely achieve better performance in the region above 10 dB SIR. Modelling the receiver performance in the way described above should, therefore, provide a conservative upper bound on the measurement error.

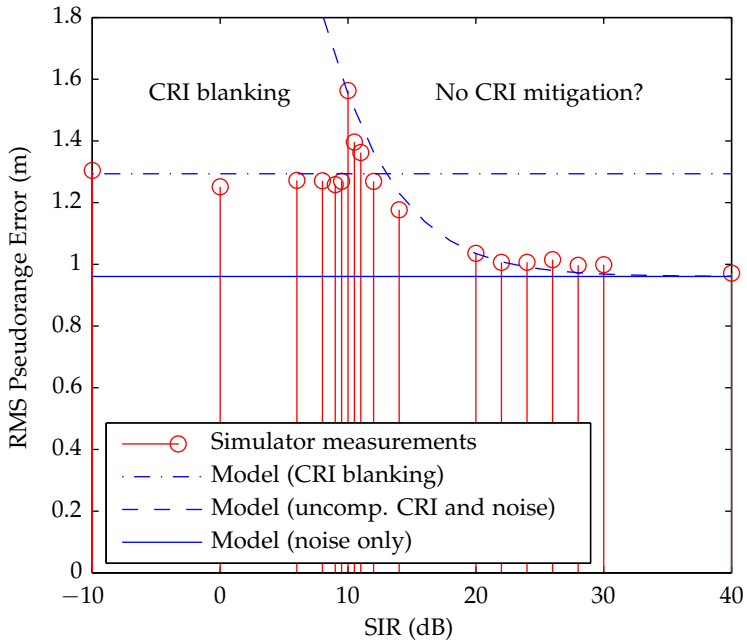

Figure 76: Pseudorange measurement error in the presence of CRI and AWGN as a function of SIR (test bench results vs. theoretical performance); desired signal: GRI 6731; interfering signal: GRI 7001; integration time $T_i \approx 5\,\text{s}$.

8.2.7 *Developing the Pseudorange Error Model*

Based on the results of the test bench experiments presented above, it is proposed that the following refined model for eLoran ranging performance is used throughout the rest of this work:

- The measurement error due to RF noise shall be modelled using Equation 8.2 above, with $L_{\text{impl}} = 4.8$, $\sigma^2_{\text{impl,r}} = 0$ and $N_p = (1 - L_b) \cdot N_{\text{p,nom}}$, where L_b is the blanking loss calculated using the technique referenced in the bullet point below, and $N_{\text{p,nom}}$ is the nominal number of eLoran pulses received within the integration interval.
- It is assumed that cross-rating signals for which $\text{SIR} \leq 10\,\text{dB}$ and whose $\text{SNR} > 0\,\text{dB}$ are suppressed by CRI blanking[10]. The effects of CRI blanking on the measurement error shall be modelled using the techniques developed in Section 6.2.5 and Section 6.2.6 of Chapter 6.
- The measurement error due to cross-rating signals for which $10\,\text{dB} < \text{SIR} \leq 20\,\text{dB}$ shall be modelled using the techniques developed in Section 6.2.3 and Section 6.2.4 of Chapter 6 (uncompensated CRI).
- Cross-rating signals for which $\text{SIR} > 20\,\text{dB}$ can be neglected (see Section 6.2.9 of Chapter 6).

10 Based on observations, it is assumed that signals with SNR lower than approximately 0 dB are not detectable by state-of-the-art eLoran receivers and therefore CRI mitigation algorithms cannot be applied to such signals.

Figure 77: Location of the measurement site used in the field trial with respect to the transmitter locations; white lines identify stations included in the position solution.

– Error contributions due to the different error sources shall be combined in the Root-Sum-Square (RSS) sense.

8.3 FIELD MEASUREMENTS

This section describes a field experiment conducted to ensure that the results obtained by simulator testing and analytical modelling reflect reality. The field experiment was carried out at the Trinity House depot in Harwich, United Kingdom (51.944768° N , 1.284446° E). The location of the measurement site with respect to the relevant transmitter locations is shown in Figure 77.

The measurement setup consisted of the Reelektronika LORADD receiver (the identical unit was used as during the simulator experiments), an associated E-field antenna, and a data collecting computer. The equipment was installed inside the GLA' Mobile Measurement Unit located on TH premises in Harwich.

The system was set to record signal TOA data, SNR, position and other parameters of interest over a period of approximately one hour.

8.3.1 *Pseudorange Measurement Error*

The loggings were first processed to obtain average SNR values and estimates of the pseudorange measurement error for each received signal. The key results of this processing are summarised in Table 10, along with the separation of each transmitter from the measurement site.

Further, a comparison was made with data obtained from a test bench experiment and with analytical predictions. The laboratory test replicated the radio conditions observed during the field trial (i.e. the simulation included the same number of signals as were observed in

STATION ID	STATION SEPARATION (km)	MEAN SNR (dB)	PSEUDORANGE STD. DEV. (m)
6731M (Lessay)	368	24	2.5
6731X (Soustons)	934	10	13.8
6731Y (Anthorn)	449	17	5.6
6731Z (Sylt)	565	16	6.3
7499M (Sylt)	565	16	7.0
7499X (Lessay)	368	24	4.7
7499Y (Værlandet)	1062	5	32.8

Table 10: Summary of field measurement data.

the field, and the signals' parameters were set such that SNRs reported by the receiver were equal to the average SNRs measured during the field experiment). The analytical models used in the comparison were those referenced in Section 8.2.7 above; a comparison was also made with a model presented by Lo et. al in reference [139], which was used in the LORIPP\LORAPP coverage and performance model (see Chapter 9). The results are shown graphically in Figure 78. The following conclusions can be drawn from the comparison:

Firstly, the analytical predictions of the revised pseudorange error model (Section 8.2.7) and the test bench results match closely the results of the field measurements. The experiment, therefore, validates both the test bench methodology and the pseudorange error model developed in this thesis.

Secondly, it can be seen from Figure 78 that residual CRI is a significant contributor to the measurement error in eLoran, particularly for weak signals (compare the 'noise and CRI' and 'noise only' models). It is also clear from the comparison that residual CRI has not been adequately modelled in existing coverage and performance models (see the 'Lo et al.' model).

8.3.2 *Positioning Accuracy*

The receiver loggings were further processed to estimate the positioning error. The key results of this processing are summarised in Figure 79 and Table 11.

Figure 79 gives the position scatter plots (relative to the mean position) together with an indication of the repeatable accuracy (R95). The upper plot shows data from the field trial at the Trinity House Harwich depot. The bottom one is the result of the test bench experiment that replicated the radio conditions seen during the field trial.

As can be seen from the plots, the accuracy figures seen in both experiments are practically identical and the overall shape and orientation of the scatter plots also compare very well. These results confirm that

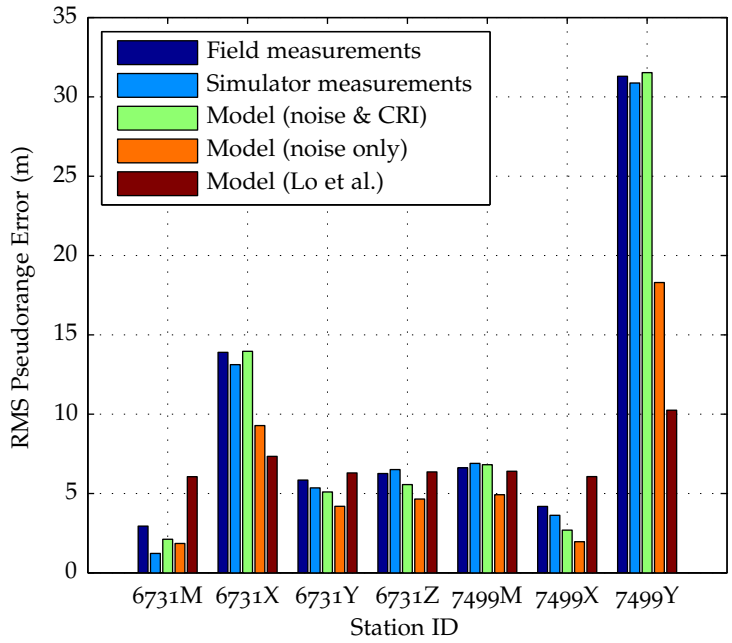

Figure 78: Pseudorange error: comparison of field measurement data with test bench and theoretical results and an earlier model presented by Lo et al. [139].

the test bench system produces an accurate representation of the real world radio environment.

Table 11 further shows the parameters of the error ellipses for the two data sets and compares the experimental figures with predictions obtained using the receiver performance models developed in this thesis. The theoretical predictions take into account signals of all four GRIs of the North-West European system. Signal SNRs were set equal to the mean SNR values given in Table 10 above (for signals that were not received during the field trial, predicted SNR values were used based on models described in Chapter 3).

It can be seen from Table 11 that the analytical model accurately predicts the eccentricity of the position error ellipse but it slightly underestimates the magnitude of the error. Upon inspection of the receiver loggings in the Reelektronika LERXAnalyser tool it was noticed that the receiver under test weights the measurements used in the position solution by what seems to be the square of the SNR of the respective signals, instead of using the inverse of the measurement covariance matrix (see Chapter 7). This seems to result in sub-optimal performance and may explain the slight difference between the predicted and actual positioning accuracy.

The difference between the theoretical predictions and measurement will be calibrated out by applying a multiplicative constant to Equation 7.1 (Chapter 7):

$$a'_{\mathrm{R95,Harre}} = c_{\mathrm{impl}} \cdot a_{\mathrm{R95,Harre}}, \tag{8.3}$$

PARAMETER	FIELD MEAS.	SIMULATOR MEAS.	PREDICTION
Semi-major axis (m)	5.45	5.20	4.62
Eccentricity	0.48	0.45	0.49
Accuracy, R95 (m)	10.84	10.86	9.40

Table 11: Positioning scatter plot parameters: comparison of field measurement and test bench data with theoretical predictions.

where, for the particular receiver model used in this work, the value of the constant will be assumed to be given by (see Table 11)

$$c_{\text{impl}} = \frac{10.84}{9.40} \approx 1.153.$$

8.4 SUMMARY AND CONCLUSIONS

In this chapter, the analytical performance models developed in Chapter 6 and Chapter 7 have been verified through computer simulations and receiver test bench experiments. Further, the validity of the results obtained by the laboratory testing was confirmed by field trial results.

Following the experiments, the pseudorange error model of Chapter 6 has been refined and calibrated to ensure that it accurately describes the performance of the eLoran receiver under test. The revised pseudorange error model assumes that the receiver mitigates CRI by SIR-sensitive blanking and is summarised in Section 8.2.7 above.

The position accuracy model described in Chapter 7 has also been calibrated to match the performance of the receiver under test. The calibrated model is described by Equation 8.3 above.

The experiments described in this chapter have shown that residual CRI is a significant contributor to the measurement error in eLoran, which should be taken into account when evaluating the system's performance. A system-wide evaluation of the effects of CRI will be presented in the following chapter.

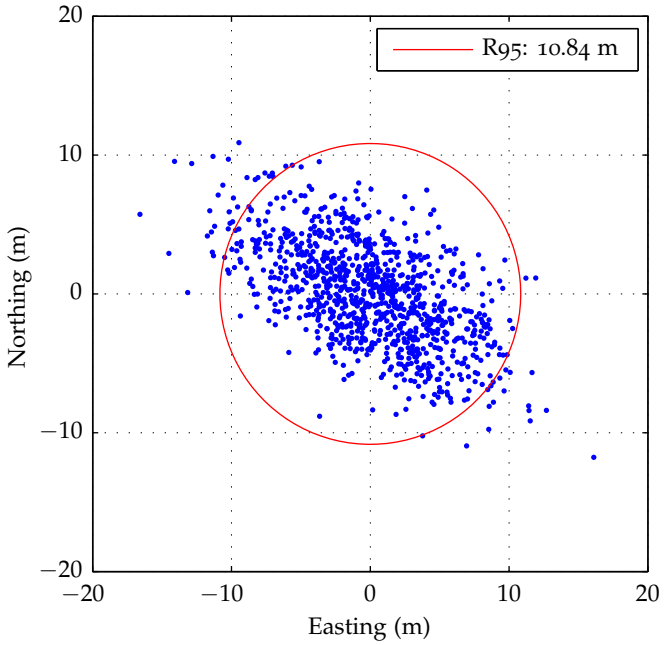

(a) Field measurements

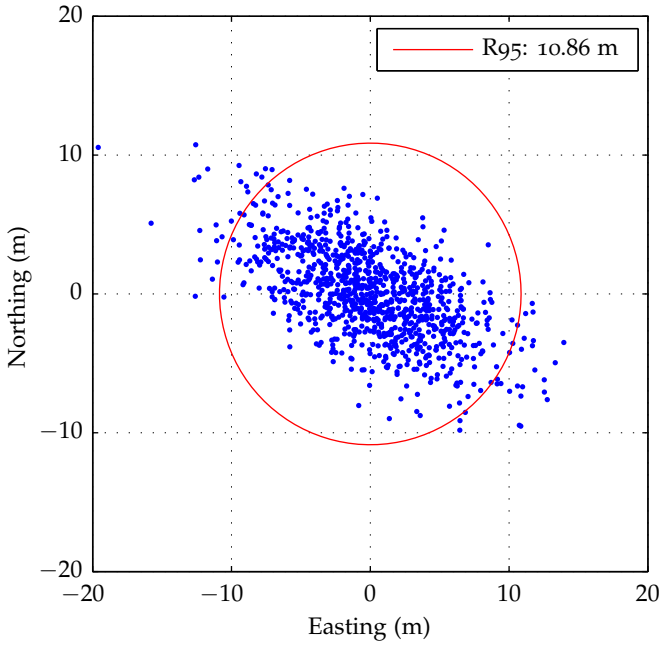

(b) Simulator measurements

Figure 79: Position scatter plots w.r.t. to the mean position: comparison of field measurement and simulator measurement data.

9 COVERAGE AND PERFORMANCE MODEL

This chapter brings together the models and findings of previous chapters to assess the impact of CRI on the coverage and performance of eLoran.

The performance of positioning systems is commonly measured using the four key metrics of accuracy, availability, continuity and integrity, as defined in Chapter 1, with the performance requirements for different application sectors being set by relevant international bodies such as the IMO and ICAO. This work focuses on the use of eLoran in the maritime transportation sector. A previous study [6] prepared for the U.S. Department of Transportation has shown that eLoran is capable of meeting the maritime performance requirements for HEA operations, and determined that the most demanding challenge towards the realisation of maritime eLoran is that of meeting the HEA accuracy requirement. For this reason, the focus of this work has been placed on the accuracy performance of eLoran.

In general, the coverage of a positioning system is the result of the four performance factors mentioned above. It is the geographic area where all of the performance requirements are met at the same time. Since this work deals only with the accuracy performance, the coverage is understood here as the geographic area where the HEA accuracy requirement of 10 m (R95) is met [151].

This chapter starts with a brief overview of existing Loran coverage and performance models and a description of a coverage prediction tool developed by the GLA. It then goes on to describe the key improvements to the traditional modelling techniques proposed by the candidate. These are mainly concerned with including the effects of CRI. The updated model is then used to assess the impact of CRI throughout the existing North-West European transmission network. Finally, the new model is validated against receiver data collected from GLA' vessels. The chapter therefore provides a tool to answer the first research question: 'What is the effect on accuracy performance within a coverage region when a new eLoran station is installed, given the increase in CRI and a modern eLoran receiver's ability to cope with such interference through blanking or cancelling of interfering pulses?'

9.1 OVERVIEW OF EXISTING MODELS

Loran coverage prediction has been performed for many years. This section gives an overview of Loran coverage and performance models described in the open literature. Four models are discussed here, namely: the USCG Loran-C accuracy model ; a model developed by the University of Wales, Bangor, to meet the needs of the North-West European Loran System (NELS) [87]; the Loran Integrity Performance Panel (LORIPP)\Loran Accuracy Performance Panel (LORAPP) model developed as part of the U.S. Loran-C Evaluation Programme [6]; and finally the GLA' eLoran coverage and performance model .

9.1.1 *The USCG Loran-C Accuracy Model*

The USCG operated Loran chains around the world and developed their own coverage prediction technique. This was limited to two criteria, namely station range and geometrical fix accuracy. For station range, the SNR of each transmitter station was checked to see if it was greater than -10 dB. Parameters that fed into the SNR calculation were ground wave signal strength and atmospheric noise field strength. Only the hyperbolic[1], single-chain, positioning mode was modelled.

9.1.2 *The Bangor Model*

In the early 1990's, Loran-C was to be extended in Europe under the NELS. Coverage prediction was therefore needed. In Europe, coverage prediction required more rigour than in the United States, as the radio environment in Europe was considerably much more noisy. The USCG method was deemed inadequate.

The University of Wales, Bangor took on the task of reviewing and improving the USCG techniques. They incorporated into their model sky wave interference, ECD evaluation, and CWI. They also studied novel receiver operating modes, such as cross-chain and master-independent navigation. The aim was to implement the various coverage limiting criteria as modules in a software suite, each generating arrays of data, which is then stored on the computer's hard drive. The coverage was to be synthesised by combining data from each criterion's array.

In 2004, the coverage prediction software was to be updated so that it was ready for the GLA' installation of a new station in Rugby. It was planned that the software would also be used for future European Loran efforts. However, the Radionavigation Research Group at the University of Wales, Bangor closed in 2005. At that time there was work being carried out in the U.S. to move towards eLoran but there was no one available to do the work on eLoran in Europe. The GLA needed to continue the development of the coverage software and decided to fund a PhD student to update the coverage software and bring it up to eLoran standards. The operation of the GLA' model is described in Section 9.1.4 below.

9.1.3 *The LORIPP\LORAPP Coverage Prediction Model*

A comprehensive Loran coverage prediction model was developed by the LORIPP and LORAPP as part of the U.S. Loran Evaluation Programme [6]. In addition to accuracy modelling, the LORIPP\LORAPP tool also allowed the availability and continuity contours to be determined, given a target integrity level.

The accuracy module of the software was based on the use of similar techniques as the USCG and Bangor models described above. Several key eLoran updates were implemented, such as the use of all-in-view receivers capable of simultaneously processing signals from different chains and the use of ASF maps and differential corrections to mitigate measurement biases (however, spatial de-correlation of the corrections was not modelled).

1 Hyperbolic positioning is based on measuring the time difference of arrival between signals from a master and two or more secondary stations, rather than on time of arrival measurements (see, for example, [64]).

The LORIPP\LORAPP tool was later evolved by the radionavigation team at Stanford University to include the effects of novel atmospheric noise processing techniques, cycle determination and station selection algorithms and models of ASF variation [73], [139]. However, neither CRI nor CWI were adequately modelled by the tool.

9.1.4 *The GLA' eLoran Coverage and Performance Model*

As mentioned before, the development of the GLA' coverage and performance model was motivated by the need to inform the GLA' eLoran programme. The model builds on the techniques and models developed at the University of Wales, Bangor, which have been modified to take into account the major eLoran updates. Models implemented at Stanford University in their coverage prediction tool (see above) were also studied and have been incorporated in the GLA' model. This includes availability, continuity and integrity calculations. The following describes the operation and key features of the model in more detail, focusing on the accuracy component.

The GLA' model is implemented in the MATLAB® environment. The first step in modelling the coverage is to set up a region over which coverage is required and decide which eLoran stations to include in the analysis. The coverage region is divided into grids consisting of rectangular elements of equal sizes, typically 0.1° in latitude by 0.1° in longitude. At each point in the grid the individual coverage limiting factors are modelled and the resulting data arrays are stored. When required, for coverage computation, these are then loaded into memory. By doing this, the tool ensures that all the computationally intensive work is done in advance and once only.

The level of accuracy is dependent on the variance of the pseudorange measurements. The main driver of pseudorange variance is the SNR of the received signal. The lower the SNR, the higher the pseudorange variance and therefore the poorer the positioning accuracy, as discussed in detail in the preceding chapters. The calculation of SNR requires knowledge of the signal strength of the Loran signal, and the level of external noise at the same location. In the current implementation of the GLA' coverage prediction software, ground wave field strength arrays are calculated using the Millington's method, as described earlier in Chapter 3. The dominant noise source in the Loran frequency band is atmospheric noise. Atmospheric noise is computed based on the model presented in ITU-R Recommendation P.372-9 [72]. The noise computation will be discussed in more detail in the following section.

In addition to ground wave, the effect of sky wave propagation also needs to be taken into account, since the sky wave limits the maximum usable range of a station and can also be a potent source of CRI. Sky wave field strength and sky wave delay arrays are computed based on ITU-R Recommendation 1147-2 [68].

When all the data arrays are available, algorithms within the software then test each grid point to see whether the eLoran signals meet certain acceptance criteria. For example, a signal of a particular station is used in the accuracy analysis only if its SNR is higher than 0 dB and the sky wave field strength to ground wave field strength ratio and sky wave delay are within the limits prescribed by the draft eLoran receiver MPS [123]. With the reduced set of signals at each grid point, pseudor-

ange measurement error and positioning accuracy are calculated and accuracy plots are generated.

9.2 DEVELOPING THE GLA' MODEL

As part of this PhD project, several imporant updates to the GLA' software have been made with the main aim of including the effects of CRI, improving the accuracy of the model and increasing the computational speed of the software. This section describes the key improvements made by the candidate.

9.2.1 *Modelling the Effects of CRI*

One of the key contributions of this work is that it has made it possible to accurately model the effects of CRI within the coverage area of an eLoran system. This has been achieved by including in the GLA' eLoran coverage prediction tool the pseudorange error model described in Section 8.2.7 of Chapter 8. Example plots showing the impact of CRI on the measurement error are included in the Section 9.3 below. To the best of the candidate's knowledge, this is the first time that such plots can be generated.

9.2.2 *Daytime vs. Night-time Performance*

Another modification to the GLA' model was motivated by the time-varying nature of the sky wave propagation and atmospheric noise.

The sky wave is one of the key factors in assessing the impact of CRI, as it may represent a major portion of the CRI energy arriving at the receiver, especially at greater distances from the cross-rating station. As discussed in detail in Chapter 3, sky wave levels vary considerably during the day, with daytime values being approximately 30 dB lower than the values observed at night.

The atmospheric noise is a major component of the external noise arriving at the receiver antenna and is one of the key drivers of the pseudorange measurement error in eLoran. As explained earlier, it is caused by lightning discharges that propagate over vast distances as sky waves. It can therefore be expected that conditions that are favourable for sky wave propagation also result in higher atmospheric noise levels. Indeed, such correlation was confirmed by an analysis of the ITU-R data in Recommendation [72] conducted by Poppe [70].

A question thus arises as to how the time-variable nature of the two mentioned factors should be taken into account in coverage prediction. The GLA' model used the annual median night-time sky wave field strengths in generating its predictions, i.e. the daytime vs. night-time variation was not taken into account. The time variability of the atmospheric noise level was not adequately reflected either. The traditional approach to atmospheric noise modelling in Loran is to use, as the representative value, the annual atmospheric noise field strength not exceeded 95% of the time. The candidate argues that this approach is too simplistic and somewhat arbitrary. It is not clear why the 95th percentile, and not for example the median, noise was chosen. Choosing such a high percentile value results in pessimistic predictions.

It should also be noted that the pseudorange error, as modelled in this thesis, is a non-linear function of SNR and SIR (recall SIR-sensitive CRI blanking). Representing the atmospheric noise and sky wave field strengths by only a single value therefore may not provide accurate pseudorange error predictions.

Taking into account the discussion above, the candidate would like to propose a new approach to modelling the time-varying factors in coverage prediction. The approach is best explained by considering the impact of these factors on the pseudorange measurement error.

The pseudorange error model developed in this work can be stated in the following general form:

$$\sigma_\rho^2(t) = C_1 + C_2(t)\underbrace{\frac{P_{\tilde{w}_b}(t)}{A_1^2}}_{\propto 1/\mathrm{SNR}} + C_3(t)\underbrace{\frac{A_2^2(t)}{A_1^2}}_{1/\mathrm{SIR}} + \ldots,$$

where the constant C_1 represents the effect of implementation imperfections at the transmitter and receiver, the second term on the right hand side of the equation is due to the external noise (a combination of the atmospheric and vessel's topside noise), and the third (and possibly higher) term(s) model the impact of CRI (see Section 8.2.7, Chapter 8). The coefficient C_2 is a function of several parameters, including the number of pulses used in the phase estimation process; A_1 is the amplitude of the desired eLoran signal; $P_{\tilde{w}_b} = P_e$ denotes the power of the external noise at the receiver; C_3 depends on the parameters of the desired and cross-rating eLoran signals, and on the CRI mitigation algorithms used; finally, A_2 is the amplitude of the cross-rating signal (only a single interferer is considered here for simplicity; extension to a greater number of interferers is straightforward).

Some of the quantities in the above equation may change significantly over time as a result of changing propagation conditions, and are therefore modelled as time-dependent variables (note the argument t in the above equation). The external noise power P_e is dominated by the power of the atmospheric noise and is modelled here as a cyclostationary random process with a probability distribution given by ITU-R Recommendation P.372-9 [72] and Recommendation M.1467 [75] which provides advice on modelling the vessel's topside noise (see also Chapter 3). The remaining parameters, such as the desired signal level, are modelled as deterministic constants with values determined using models referenced earlier.

From the above discussion it should be clear that the pseudorange measurement error, denoted $\sigma_\rho^2(t)$, also needs to be modelled as a cyclostationary random process. However, for the purpose of coverage and performance prediction a single representative value of σ_ρ^2 is required. The approach taken in this work is to use the average value (i.e. both time- and ensemble- averaged) of the process $\sigma_\rho^2(t)$ to characterise the error:

$$\mathrm{AvE}\left[\sigma_\rho^2(t)\right] \equiv \overline{\sigma_\rho^2} = \frac{1}{T}\int_T \int_{-\infty}^{\infty} \left[C_1 + C_2(t)\frac{w}{A_1^2} + C_3(t)\frac{A_2^2(t)}{A_1^2} + \ldots\right] \cdot f_{P_e}(w,t)\,\mathrm{d}w\mathrm{d}t,$$

where T is the period of cyclo-stationarity (assumed to be 1 year) and $f_{P_e}(w,t)$ is the time-variant Probability Density Function (PDF) of the external noise power, whose parameters can be obtained from the relevant ITU-R Recommendations referenced above.

For further discussion it will be convenient to split the integral into two parts - one taken over the values of time t that correspond to daytime sky wave propagation conditions (denoted by a d subscript), and one representing night-time conditions (denoted by the letter n). The coefficients C_2 and C_3 as well as the amplitude of the cross-rating signal, A_2, are unlikely to change significantly during either of these time intervals and will be assumed to be constant on each interval (the day/night-time values of the coefficients will again be denoted by the respective subscripts):

$$\overline{\sigma_\rho^2} = \frac{1}{T}\int_{\mathrm{d}}\int_{-\infty}^{\infty}\left(C_1 + C_{2,\mathrm{d}}\frac{w}{A_1^2} + C_{3,\mathrm{d}}\frac{A_{2,\mathrm{d}}^2}{A_1^2}\right)\cdot f_{P_e}(w,t)\,\mathrm{d}w\mathrm{d}t + \frac{1}{T}\int_{\mathrm{n}}\int_{-\infty}^{\infty}\left(C_1 + C_{2,\mathrm{n}}\frac{w}{A_1^2} + C_3\frac{A_{2,\mathrm{n}}^2}{A_1^2}\right)\cdot f_{P_e}(w,t)\,\mathrm{d}w\mathrm{d}t.$$

The equation can now be rewritten as

$$\begin{aligned}\overline{\sigma_\rho^2} = &\frac{1}{T}\left[\frac{C_{2,\mathrm{d}}}{A_1^2}\int_{\mathrm{d}}\int_{-\infty}^{\infty} w\cdot f_{P_e}(w,t)\,\mathrm{d}w\mathrm{d}t + \left(C_1 + C_{3,\mathrm{d}}\frac{A_{2,\mathrm{d}}^2}{A_1^2}\right)\int_{\mathrm{d}}\int_{-\infty}^{\infty} f_{P_e}(w,t)\,\mathrm{d}w\mathrm{d}t\right] + \\ &\frac{1}{T}\left[\frac{C_{2,\mathrm{n}}}{A_1^2}\int_{\mathrm{n}}\int_{-\infty}^{\infty} w\cdot f_{P_e}(w,t)\,\mathrm{d}w\mathrm{d}t + \left(C_1 + C_{3,\mathrm{n}}\frac{A_{2,\mathrm{n}}^2}{A_1^2}\right)\int_{\mathrm{n}}\int_{-\infty}^{\infty} f_{P_e}(w,t)\,\mathrm{d}w\mathrm{d}t\right].\end{aligned} \tag{9.1}$$

As mentioned above, the parameters of the PDF $f_{P_e}(w,t)$ can be obtained from data published in ITU-R Recommendations [72] and [75]. The Recommendation [72] specifies the parameters in 24 season-time blocks, i.e. the time-variant PDF is approximated by a collection of 24 time-invariant PDFs, $f_{P_{e,b}}(w)$, one for each block b. The integrals over time in the above equation can therefore be broken up into 24 parts, each evaluated over an interval of length $T_{b,\mathrm{d}}$ or $T_{b,\mathrm{n}}$, where the former is the amount of time in season-time block b when daytime sky wave propagation conditions are experienced, and the latter is the amount of time in a block corresponding to night-time conditions. Noting further that

$$\int_{-\infty}^{\infty} w\cdot f_{P_{e,b}}(w)\,\mathrm{d}w = \mathrm{E}\left[P_{e,b}\right],$$

and

$$\int_{-\infty}^{\infty} f_{P_{e,b}}(w)\,\mathrm{d}w = 1,$$

Equation 9.1 can be rewritten as

$$\overline{\sigma_\rho^2} = \frac{1}{T}\left[\frac{C_{2,\mathrm{d}}}{A_1^2}\sum_b T_{b,\mathrm{d}}\mathrm{E}\left[P_{\mathrm{e},b}\right] + \left(C_1 + C_{3,\mathrm{d}}\frac{A_{2,\mathrm{d}}^2}{A_1^2}\right)\underbrace{\sum_b T_{b,\mathrm{d}}}_{T_\mathrm{d}}\right] + \frac{1}{T}\left[\frac{C_{2,\mathrm{n}}}{A_1^2}\sum_b T_{b,\mathrm{n}}\mathrm{E}\left[P_{\mathrm{e},b}\right] + \left(C_1 + C_{3,\mathrm{n}}\frac{A_{2,\mathrm{n}}^2}{A_1^2}\right)\underbrace{\sum_b T_{b,\mathrm{n}}}_{T_\mathrm{n}}\right],$$

and further simplified as

$$\begin{aligned}\overline{\sigma_\rho^2} = &\frac{T_\mathrm{d}}{T}\underbrace{\left[C_1 + \frac{C_{2,\mathrm{d}}}{A_1^2}\sum_b \frac{T_{b,\mathrm{d}}}{T_\mathrm{d}}\mathrm{E}\left[P_{\mathrm{e},b}\right] + C_{3,\mathrm{d}}\frac{A_{2,\mathrm{d}}^2}{A_1^2}\right]}_{\text{day-time pseudorange error}} \\ &+ \frac{T_\mathrm{n}}{T}\underbrace{\left[C_1 + \frac{C_{2,\mathrm{n}}}{A_1^2}\sum_b \frac{T_{b,\mathrm{n}}}{T_\mathrm{n}}\mathrm{E}\left[P_{\mathrm{e},b}\right] + C_{3,\mathrm{n}}\frac{A_{2,\mathrm{n}}^2}{A_1^2}\right]}_{\text{night-time pseudorange error}}.\end{aligned} \tag{9.2}$$

The ratios $\frac{T_{b,\mathrm{d}}}{T_\mathrm{d}}$ and $\frac{T_{b,\mathrm{n}}}{T_\mathrm{n}}$, $b = 1, 2, \ldots, 24$, represent the proportion of day/night-time, respectively, taken up by each of the 24 season-time blocks specified in ITU-R P.372-9 [72], and the ratios $\frac{T_\mathrm{d}}{T}$ and $\frac{T_\mathrm{n}}{T}$ are the fraction of time classified as day/night-time, respectively. Values of these ratios applicable to the North-West European region can be calculated from data provided by Poppe [70] in her work on Marine Beacon DGPS coverage prediction, and are shown in Table 12 and below:

$$\frac{T_\mathrm{d}}{T} \approx 0.395,$$

$$\frac{T_\mathrm{n}}{T} \approx 0.605.$$

The sums

$$\sum_b \frac{T_{b,\mathrm{d}}}{T_\mathrm{d}}\mathrm{E}\left[P_{\mathrm{e},b}\right] \equiv \overline{P_\mathrm{d}},$$

and

$$\sum_b \frac{T_{b,\mathrm{n}}}{T_\mathrm{n}}\mathrm{E}\left[P_{\mathrm{e},b}\right] \equiv \overline{P_\mathrm{n}},$$

represent the *average daytime* and *average night-time external noise power*, respectively, to be used in SNR calculations. The calculation of the average noise is discussed further in the following section.

9.2.3 *Noise Averaging*

In order to be able to calculate the average daytime and night-time noise power in Equation 9.2 above, the mean external noise power for

SEASON	TIME	BLOCK IND.	DAYTIME	NIGHT-TIM
	0000 – 0400	1	0	0.105
	0400 – 0800	2	0.012	0.087
Winter	0800 – 1200	3	0.063	0.008
	1200 – 1600	4	0.069	0
	1600 – 2000	5	0.023	0.071
	2000 – 2400	6	0	0.105
	0000 – 0400	7	0.006	0.097
	0400 – 0800	8	0.063	0.008
Spring	0800 – 1200	9	0.069	0
	1200 – 1600	10	0.069	0
	1600 – 2000	11	0.063	0.008
	2000 – 2400	12	0.017	0.079
	0000 – 0400	13	0.012	0.087
	0400 – 0800	14	0.069	0
Summer	0800 – 1200	15	0.069	0
	1200 – 1600	16	0.069	0
	1600 – 2000	17	0.069	0
	2000 – 2400	18	0.034	0.053
	0000 – 0400	19	0	0.105
	0400 – 0800	20	0.029	0.061
Autumn	0800 – 1200	21	0.069	0
	1200 – 1600	22	0.069	0
	1600 – 2000	23	0.052	0.026
	2000 – 2400	24	0.006	0.097

Table 12: Proportion of day/night-time, $T_{b,\mathrm{d}}/T_{\mathrm{d}}$ and $T_{b,\mathrm{n}}/T_{\mathrm{n}}$, respectively, taken up by each ITU season-time block, b (after Poppe [70]).

each ITU season-time block, $\mathrm{E}\left[P_{\mathrm{e},b}\right]$, needs to be determined. This can be accomplished as follows: The noise equivalent RMS field strength corresponding to the external noise power available at the output of an electrically short monopole antenna during season-time block b (expressed in dBμV/m) is given by [72]:

$$E_{\mathrm{e},b} = F_{\mathrm{e},b} + 20\log f_{\mathrm{MHz}} + 10\log B - 95.5, \tag{9.3}$$

where $F_{\mathrm{e},b}$ is the external noise figure for block b (for definition of the noise figure and the remaining terms in the above equation see Section 3.3.1 in Chapter 3). Assuming, as before and without loss of generality, an antenna factor of $1\,\mathrm{m}^{-1}$, then the power of the received signal for a given season-time block, b, can be calculated as

$$P_{\mathrm{e},b} = 10^{E_{\mathrm{e},b}/10},$$

and the mean noise power for that season-time block can be expressed by substituting from Equation 9.3 into Equation 9.4 below:

$$\mathrm{E}\left[P_{\mathrm{e},b}\right] = \mathrm{E}\left[10^{E_{\mathrm{e},b}/10}\right] = \underbrace{10^{(20\log f_{\mathrm{MHz}}+10\log B-95.5)/10}}_{Bf_{\mathrm{MHz}}^2\cdot 10^{-9.55}}\mathrm{E}\left[10^{F_{\mathrm{e},b}/10}\right]. \tag{9.4}$$

The external noise figure $F_{\mathrm{e},b}$ in the above equation is assumed to follow a double-sided normal distribution with a different standard deviation below and above the median. The median, $F_{\mathrm{e,m},b}$, lower decile, $D_{\mathrm{l},b}$, and upper decile, $D_{\mathrm{u},b}$, of the distribution for each ITU season-time block can be obtained from ITU-R Recommendations [72, 75], as discussed in Chapter 3. The mean external noise figure can then be expressed as

$$\begin{aligned}\mathrm{E}\left[10^{F_{\mathrm{e},b}/10}\right] &= \int_{-\infty}^{\infty} 10^{\frac{w}{10}}\cdot f_{F_{\mathrm{e},b}}(w)\,\mathrm{d}w \\ &= \int_{-\infty}^{F_{\mathrm{e,m},b}} 10^{\frac{w}{10}}\cdot\mathcal{N}\left(w;F_{\mathrm{e,m},b},\sigma_{\mathrm{l},b}^2\right)\cdot\mathrm{d}w \\ &+ \int_{F_{\mathrm{e,m},b}}^{\infty} 10^{\frac{w}{10}}\cdot\mathcal{N}\left(w;F_{\mathrm{e,m},b},\sigma_{\mathrm{u},b}^2\right)\cdot\mathrm{d}w,\end{aligned}$$

where $\sigma_{\mathrm{l},b} \approx D_{\mathrm{l},b}/1.282$, $\sigma_{\mathrm{u},b} \approx D_{\mathrm{u},b}/1.282$, and $\mathcal{N}\left(w;\mu,\sigma^2\right)$ denotes the PDF of the normal distribution (see Appendix A).

The integrals in the above equation can be solved by the method of substitution and evaluate to

$$\begin{aligned}&\mathrm{E}\left[10^{F_{\mathrm{a},b}/10}\right] = \\ &\qquad \mathrm{e}^{\alpha F_{\mathrm{e,m},b}+\frac{1}{2}\alpha^2\sigma_{\mathrm{l},b}^2}\cdot\Phi\left(-\alpha\sigma_{\mathrm{l},b}\right) + \mathrm{e}^{\alpha F_{\mathrm{e,m},b}+\frac{1}{2}\alpha^2\sigma_{\mathrm{u},b}^2}\cdot\Phi\left(\alpha\sigma_{\mathrm{u},b}\right),\end{aligned}$$

where $\alpha = \frac{\ln(10)}{10}$, and $\Phi(\centerdot)$ is the Cumulative Distribution Function (CDF) of the standard normal distribution (see Appendix A). The mean noise power for a particular season-time block is then obtained by substitution for $\mathrm{E}\left[10^{F_{\mathrm{e},b}/10}\right]$ in Equation 9.4.

Figure 80 and Figure 81 show the distrubtion of the predicted average daytime and night-time noise over North-West Europe. It can be seen from the figures that there is approximately a 3 dB to 4 dB difference

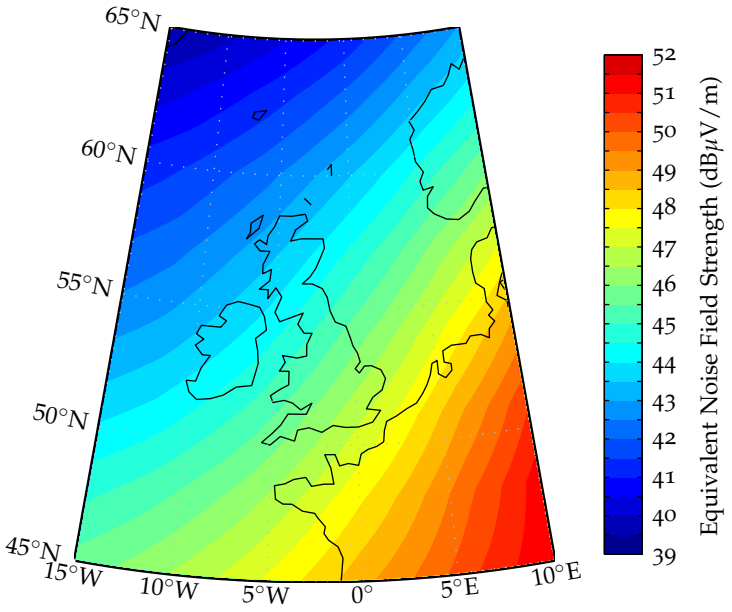

Figure 80: Equivalent average daytime noise field strength.

between the day/night-time noise levels experienced over the British Isles.

Regarding the day-time and night-time amplitudes of the cross-rating signal, $A_{2,d}$ and $A_{2,n}$, in Equation 9.2 above, the following approach is proposed: If the interference terms in Equation 9.2 represent a signal arriving via sky wave, then the night-time amplitude $A_{2,n}$ should be derived from the annual median night-time field strength obtained from ITU-R Recommendation P.1147 [68], and the daytime amplitude $A_{2,d}$ should be set to a value 30 dB lower, in accordance with the same ITU-R Recommendation. If the amplitudes represent interference arriving via ground wave, then both parameters should be set to the same value determined from the predicted ground wave field strength of the interferer.

All the necessary information for the calculation of the average external noise and average pseudorange error (Equation 9.2) is now available. Example plots of the noise and pseudorange error are shown in Section 9.3 below.

9.2.4 *Accuracy Calculations*

The next modification to the GLA's model involved the implementation of the Harre approximation for estimating the R95 position error described in Chapter 7. The new approach results in slightly higher error estimates than the traditional one which assumes a circular position error distribution.

Further, the position error model was calibrated to match the performance of a commercially available eLoran receiver, as described in Chapter 8.

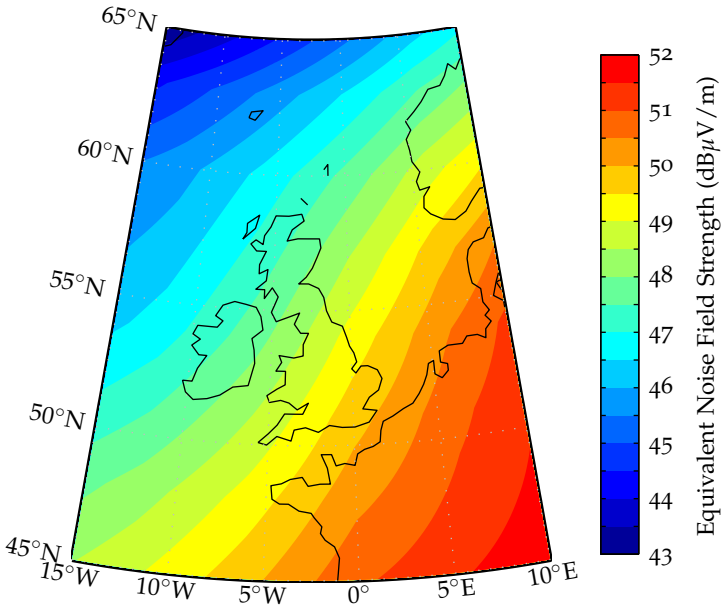

Figure 81: Equivalent average night-time noise field strength.

9.2.5 *Other Modifications*

In addition to the improvements described above, several software modifications to the GLA coverage prediction tool have been made, such as revision of loop-based code to use matrix operations (a process referred to in the MATLAB® documentation as 'vectorisation') in order to speed up the calculation of ground wave, sky wave, and external noise arrays, and to ensure that the code is in line with the corresponding ITU-R Recommendations.

9.3 EXAMPLE OUTPUTS

This section demonstrates the capability of the updated coverage and performance tool to model the effects of CRI and daytime vs. night-time radio conditions. The coverage plots presented here are based on the existing network of Loran stations in North-West Europe and assume that any propagation related measurement biases are eliminated through the use of ASF maps and real-time differential corrections, or an equivalent technique.

9.3.1 *The Importance of Receiver CRI Mitigation*

The models developed in this work have made it possible to quantify the impact of CRI on the pseudorange and positioning error for receivers using different CRI mitigation techniques, operating under different radio conditions. As an example, Figure 82 compares the pseudorange measurement error for a linear receiver that does not implement any CRI mitigation algorithms (except for the inherent averaging; see the SFD model derived in Chapter 6) and a typical eLoran receiver that mitigates CRI by SIR sensitive blanking (see Section 8.2.7

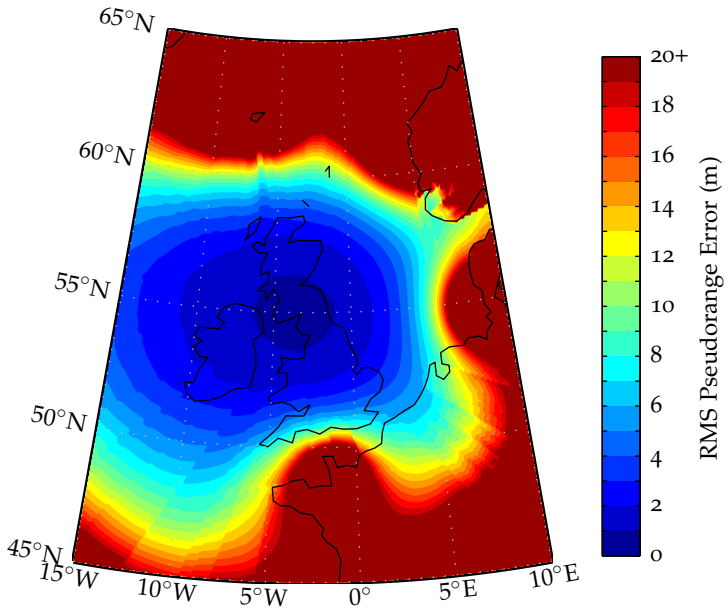

(a) Linear receiver without CRI mitigation; integration time $T_i \approx 5\,s$.

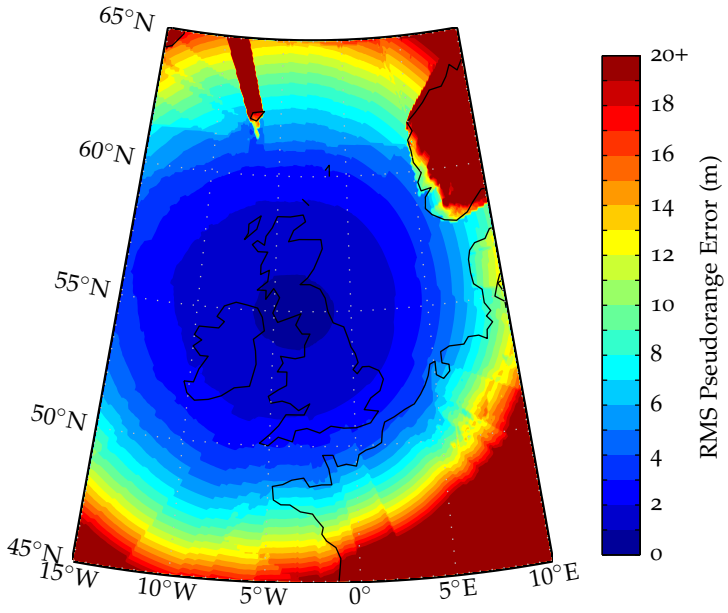

(b) Receiver with SIR sensitive CRI blanking; integration time $T_i \approx 5\,s$.

Figure 82: Average daytime pseudorange measurement error for the 6731Y Anthorn station.

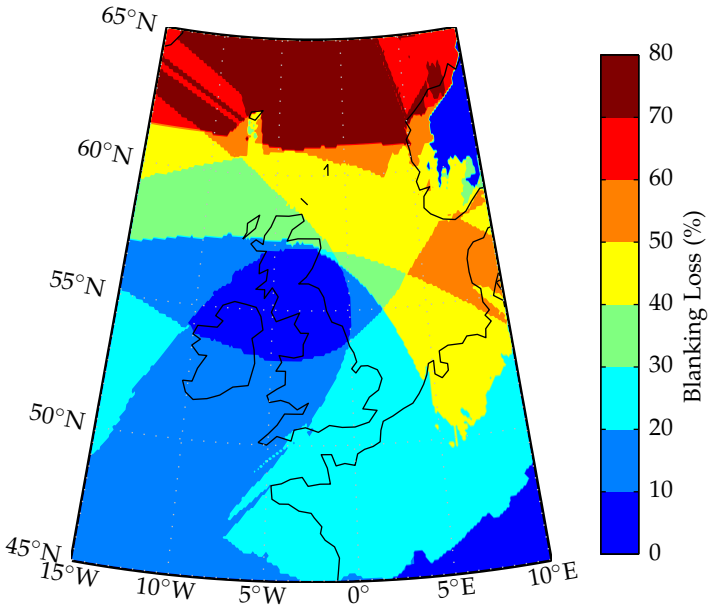

Figure 83: Blanking loss (daytime) for the 6731Y Anthorn station assuming a receiver that implements SIR sensitive CRI blanking.

in Chapter 8). The plots give predicted average RMS error for the 6731Y signal transmitted from Anthorn, Cumbria, experienced under daytime radio conditions. The error was calculated according to the first part of Equation 9.2 derived in Section 9.2.2.

The upper plot in Figure 82 clearly shows the adverse effects of uncompensated CRI experienced throughout the coverage area, in particular in areas surrounding the neighbouring stations that operate on different GRIs. The bottom plot assumes that all cross-rating signals in view that produce SIR less than 10 dB are blanked. As can be seen by comparison between the two plots, the CRI blanking greatly improves the receiver's performance, although it results in a substantial proportion of the received pulses being discarded. This is illustrated in Figure 83. The average blanking loss for the 6731Y station, over the geographic area shown in the figure, is 32% (corresponding to an SNR debit of approximately 1.7 dB), however, in parts of the area with a greater number of cross-rating stations in view over 70% of the pulses have to be blanked.

In order to further illustrate the importance of receiver CRI mitigation, Figure 84 shows predicted positioning accuracy assuming that no CRI mitigation algorithms are used. This plot should be compared to Figure 85 to Figure 87 below, which show the achievable accuracy for a blanking receiver. It is clear from the figures that effective CRI mitigation is vital to meeting the stringent HEA accuracy requirement.

9.3.2 *Daytime eLoran Accuracy Plots*

Figure 85 shows predicted positioning accuracy under the daytime radio conditions for a typical state-of-the-art eLoran receiver. As mentioned before, the daytime plots in this thesis are based on the use

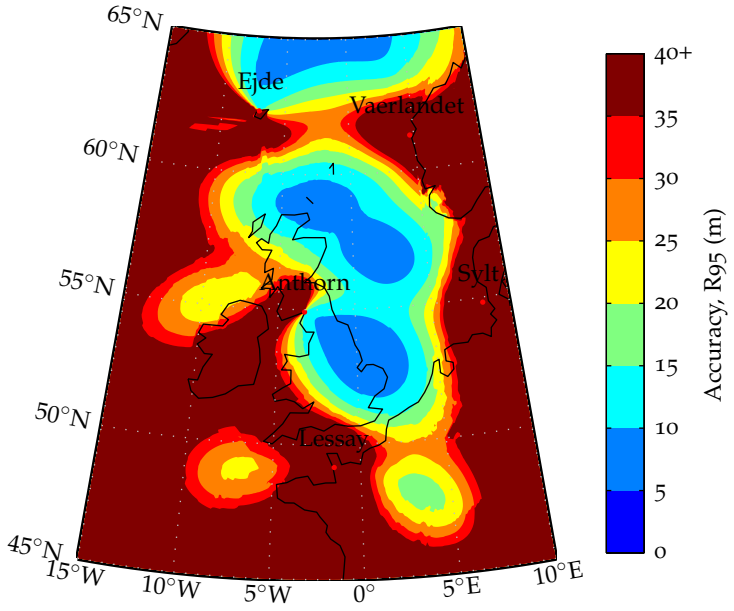

Figure 84: Daytime positioning accuracy without receiver CRI mitigation.

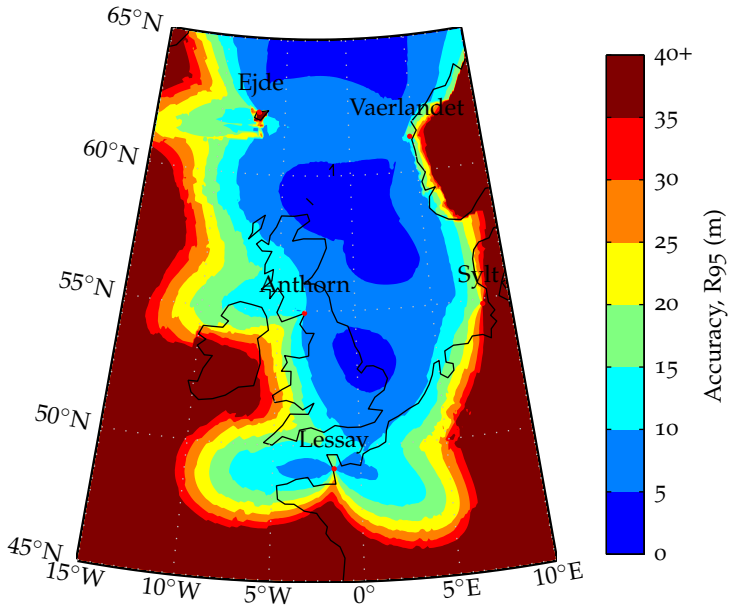

Figure 85: Daytime positioning accuracy with a CRI blanking receiver.

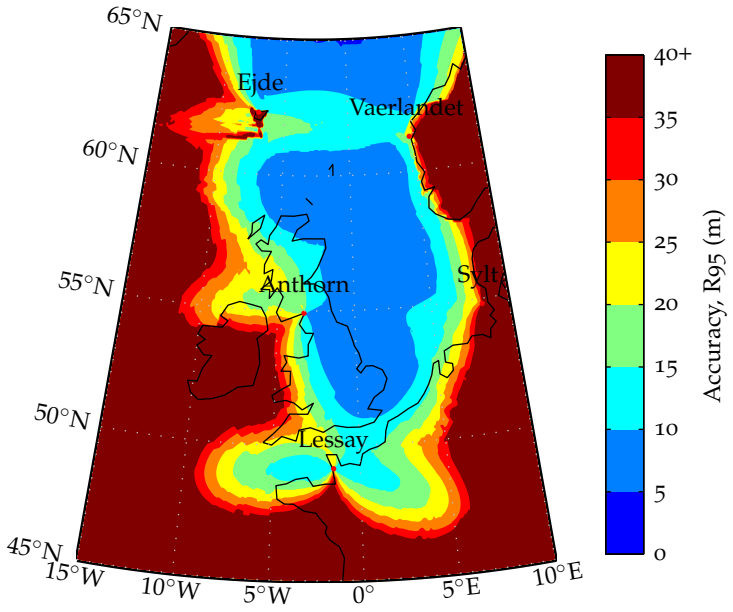

Figure 86: Night-time positioning accuracy with a CRI blanking receiver.

of the first part of Equation 9.2 for the pseudorange error derived in Section 9.2.2. The impact of CRI is modelled here as described in Section 8.2.7 of Chapter 8, i.e. it is assumed that the receiver mitigates CRI by SIR-sensitive blanking. The assumptions and models used in generating the daytime plots are summarised in Table 13.

By comparison of Figure 85 with Figure 84 it can be seen that modern eLoran signal processing considerably improves the positioning performance and results in much improved coverage, making eLoran available to mariners in more ports and harbours.

9.3.3 *Night-time eLoran Accuracy Plots*

Figure 86 shows predicted eLoran accuracy under night-time radio conditions. The night-time plots are based on the use of the second part of Equation 9.2 in Section 9.2.2. The assumptions and models used in generating the night-time plots are summarised in Table 14.

As discussed earlier, the night-time conditions are characterised by higher sky wave as well as atmospheric noise levels, resulting in increased levels of CRI, greater pseudorange errors and consequently poorer accuracy and coverage. This effect is clearly seen by comparing Figure 86 and Figure 85.

9.3.4 *Averaged Performance and Coverage*

The average positioning accuracy plot is generated by taking the weighted average of the daytime and night-time accuracy arrays, weighted by the ratios $\frac{T_d}{T}$ and $\frac{T_n}{T}$, respectively, defined in Section 9.2.2. The result of averaging the accuracy arrays is plotted in Figure 87.

PARAMETER	MODEL \ ASSUMPTIONS
Ground wave	
Field strength	Millington; ITU-R P.368-9
Ground conductivity	ITU-R P.832-2
Sky wave	
Field strength (day)	30 dB below night-time median; ITU-R P.1147-2
Delay	Morris [71]
Height of ionosphere (day)	70 km
Atmospheric noise	
Source of data	ITU-R P.372-9
Computation method	Safar (Thesis Section 9.2.3, day)
Vessel's topside noise	
Noise figure	$F_t = 103$ dB; ITU-R M.1467-1
CWI	Considered too insignificant to model (see Section 3.4.1)
CRI	
Computation model	Safar (Thesis Section 8.2.7)
Interferers	All North-West European stations
Receiver	
Bandpass filter	8-th order Butterworth; 86 kHz to 114 kHz passband
Min. SNR	0 dB
Sky wave limits	Marine eLoran receiver MPS [123]
Integration time	$T_i \approx 5$ s
Sampling point offset	$\tau_p = 62.25\,\mu$s (4.1 dB below peak)
Implementation loss	$L_{impl} = 6.8$ dB
Accuracy calculations	
Metric	R95
Computation method	Harre [150]

Table 13: Summary of assumptions and models used in evaluating the daytime coverage and performance.

PARAMETER	MODEL \ ASSUMPTIONS
Sky wave	
Field strength (day)	Night-time median; ITU-R P.1147-2
Height of ionosphere (night)	90 km
Atmospheric noise	
Source of data	ITU-R P.372-9
Computation method	Safar (Thesis Section 9.2.3, night)

Table 14: Summary of assumptions and models used in evaluating the night-time coverage and performance (only differences from the daytime model are shown).

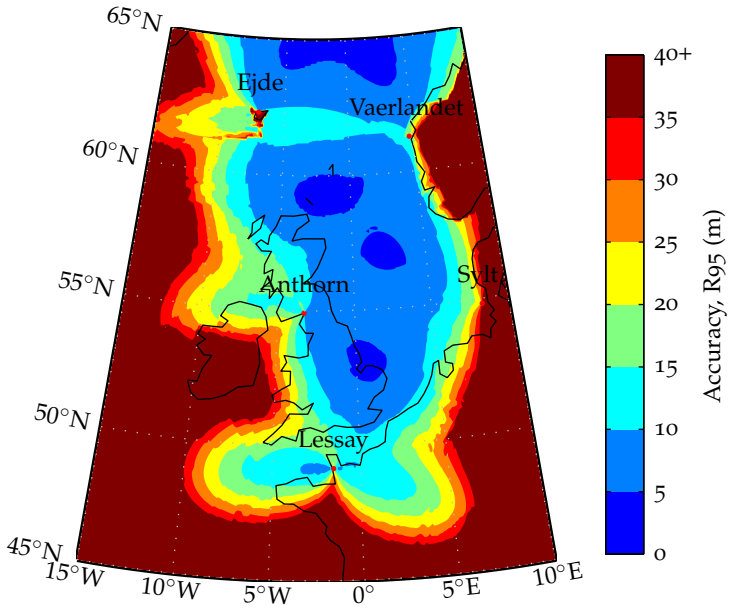

Figure 87: Average positioning accuracy with a CRI blanking receiver.

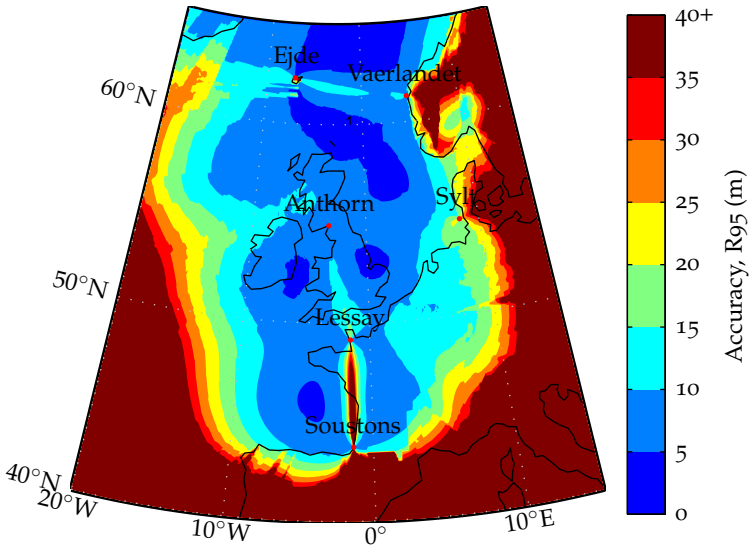

Figure 88: Average positioning accuracy for an eLoran receiver equipped with a synchronised atomic clock.

9.3.5 *The Need for Improved Coverage*

The accuracy plots presented above suggest that 10 m level accuracy, required for the maritime HEA operations, is achievable along the whole East Coast of Britain and over most of the North Sea (assuming that CRI is appropriately compensated and any propagation related measurement biases are eliminated). However, the level of performance achievable on the West Coast of Britain and over Ireland does not appear to be sufficient to support the HEA requirements.

Achieving full eLoran coverage of the British Isles and Ireland would seem to require the addition of one (or more) transmitters in Ireland, and this possibility will be investigated further in Chapter 11.

Another option may be to use eLoran receivers equipped with synchronised atomic clocks. This would make it possible to calculate position using eLoran signals from only two (spatially separated) stations and possibly remove the need for additional transmitters. At present, this option would add a considerable burden to the cost of user equipment, however, with the advent of chip-scale atomic clocks, this solution may become economically viable in the not too distant future. The predicted average accuracy for a receiver equipped with a synchronised clock is shown in Figure 88. This plot was achieved by leaving out the unity column vector in the geometry matrix representing the effect of the receiver clock bias (see Equation 5.20, Chapter 5) and reducing the minimum number of transmitters required to obtain a position fix to two.

STATION ID	STATION SEPARATION (km)	MEASURED SNR (dB)	PREDICTED SNR (dB)
6731M (Lessay)	368	24	28
6731X (Soustons)	934	10	11
6731Y (Anthorn)	449	17	25
6731Z (Sylt)	565	16	22
7499M (Sylt)	565	16	22
7499X (Lessay)	368	24	28
7499Y (Værlandet)	1062	5	9

Table 15: Comparison of measured and predicted SNR data for Harwich, UK.

9.4 VALIDATION OF THE NEW COVERAGE MODEL

In an attempt to validate the updated coverage and performance model, a comparison with data from a field trial conducted at the Trinity House (TH) Harwich depot and data collected from TH vessels was performed.

The measurement location and setup used during the field trial was described in Chapter 8. Table 15 compares the mean SNR values for the stations being received during the experiment with predictions from the coverage and performance model. It can be seen from the table that there is a 1 dB to 8 dB difference between the measurements and predictions, with the measured SNRs being lower than those predicted by approximately 5 dB on average. The variation can be attributed to the limited accuracy of the ground conductivity data used in the ground wave field strength prediction. The fact that the measured SNRs are lower than predictions is not too surprising either, given that the measurements were taken in an urban location likely to experience increased levels of man-made noise[2]. As a result, the positioning accuracy observed during the field trial is worse than the predicted value, as shown in Table 16. In cases such as this when the receiver location is known to experience increased levels of external noise, the model can be calibrated by, for example, adjusting the level of the topside noise F_t (see Section 3.3.3, Chapter 3).

In order to verify that the discrepancy in measured vs. modelled SNR is due to local noise sources on the shore rather than a deficiency in the model, position data were also collected from an eLoran receiver installed on board Trinity House Vessel (THV) Patricia. Figure 89 shows a scatter plot for a data set recorded while the Patricia was moored in the Harwich harbour area, approximately 300 m off the shore. The accuracy achieved at this location is in almost perfect agreement with the model, as can be seen from Table 16.

2 Some noise may also have been introduced by the data logging laptop and other equipment in the GLA' Mobile Measurement Unit

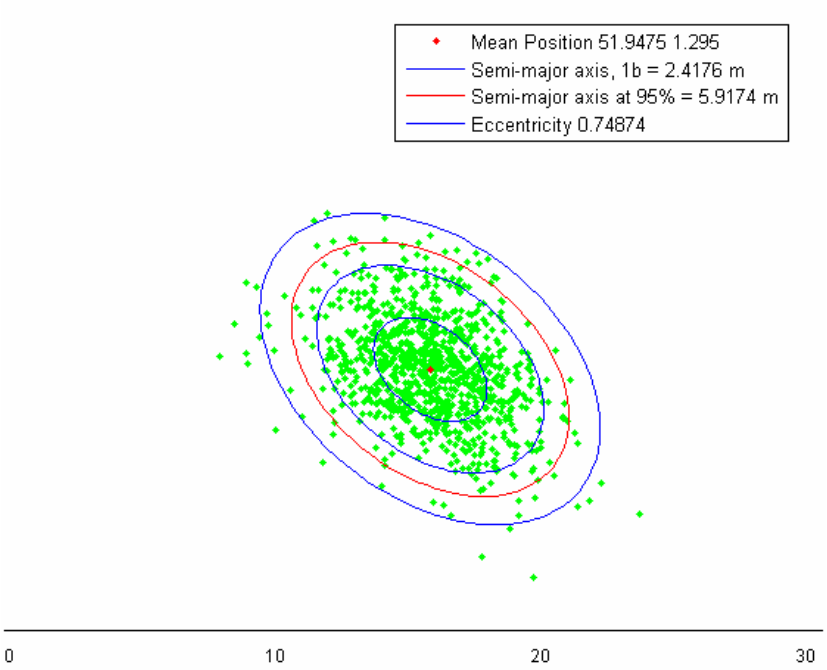

Figure 89: eLoran scatter plot for data recorded on board THV Patricia while moored in the Harwich harbour area; elliptical error shown corresponds to R95 error of 5.28 m (picture courtesy of the GLA).

LOCATION	MEASURED ACCURACY (m)	PREDICTED ACCURACY (m)
TH depot, Harwich	10.84	5.19
THV Patricia, Harwich Harbour	5.28	5.19

Table 16: Comparison of measured and predicted positioning accuracy for the Harwich area during daytime radio conditions; values shown give repeatable accuracy, R95.

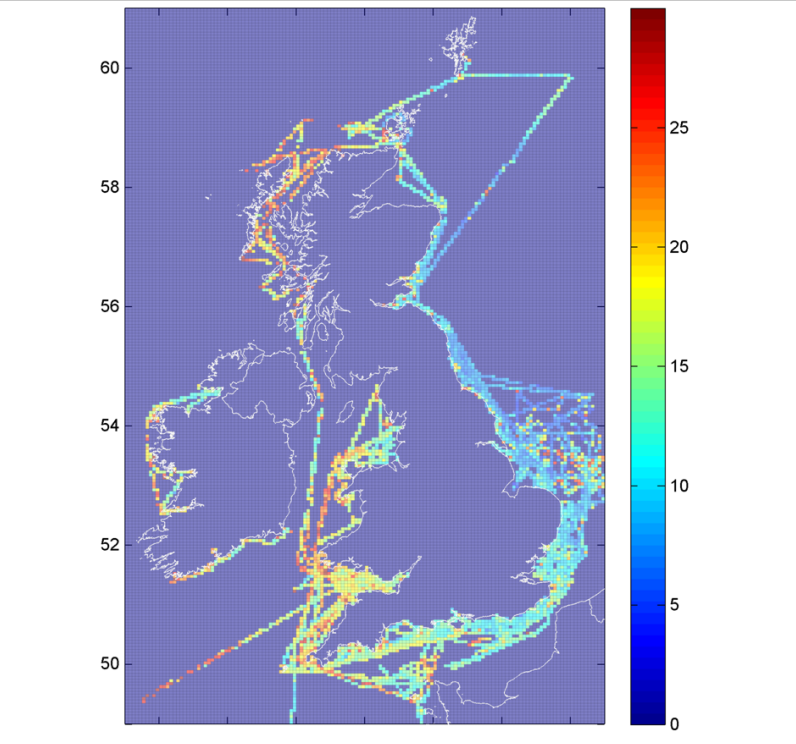

Figure 90: Positioning accuracy data collected from GLA' vessels; accuracy given in meters, R95 (picture courtesy of the GLA).

Courtesy of the GLA it was also possible to verify the general behaviour of the accuracy performance seen in Figure 87 by comparison with accuracy data collected from eLoran receivers aboard other GLA' vessels (Figure 90). The plot in Figure 90 shows data obtained by an analysis of GPS-calibrated Loran position fixes (both daytime and nighttime data is included). In this positioning mode the eLoran receiver continuously produces its own ASF estimates (based on GPS data) in order to eliminate the propagation related measurement biases typical of Loran. The resulting positioning accuracy is close to the repeatable accuracy of the system (this technique effectively immitates the use of eLoran ASF maps and real-time differential corrections by utlilising the GPS measurements). The available data is sparse, however, it is showing the same pattern of results: excellent accuracy on the East Coast of Britain, poor on the Irish Coast and in the Irish Sea.

The predicted average accuracy along the East Coast is in the 5 m to 10 m region. This is in good agreement with the measured accuracy which is approximately 10 m in this part of the coverage area. The predicted accuracy on the South West Coast is in the range of 20 m to 30 m, which again is in good agreement with the measurements.

Interestingly, the measured accuracy over some parts of Ireland appears to be better than the predictions. On consultation with the GLA it was determined that this is most likely due to the receivers using, in the position solution, stations that are beyond the sky wave limit set by the receiver MPS. It should be noted that under adverse sky wave propagation conditions these signals may not be usable for positioning in this region.

9.5 SUMMARY AND CONCLUSIONS

After a review of existing Loran coverage prediction models, this chapter proposed several key improvements to the traditional modelling techniques which enable the assessment of the impact of CRI on the accuracy performance and coverage of eLoran systems and result in greater prediction accuracy. These improvements have been implemented in a coverage prediction tool developed based on previous work by the GLA, and are summarised below:

1. The pseudorange error model developed in earlier chapters of this thesis has been included in the coverage prediction tool (see Section 9.2.1).

2. Separate daytime vs. night-time sky wave and external noise arrays have been generated to facilitate the coverage and performance assessment under day/night-time radio conditions (Section 9.2.2). It was deemed necessary to conduct separate day/night-time coverage analyses (rather than using annual daily averages) in order to appropriately account for the non-linear nature of receiver CRI mitigation.

3. The calculation of external noise arrays has been modified in order to appropriately take into account the probability distribution and time-varying nature of the atmospheric noise (Section 9.2.3). These new external noise arrrays replace the traditional atmospheric noise arrays, typically based on the 95-th percentile noise levels, as the traditional approach was deemed rather simplistic and resulted in pessimistic performance predictions.

4. A man-made external noise component was included in the model to account for sources of noise local to the receiver (Section 9.2.2 and Section 9.2.3).

5. The Harre approximation for estimating the R95 position error from the position error covariance matrix has been implemented (Section 9.2.4). This modification provides more accurate estimates of the R95 error than the tradional approach in areas where the distribution of position fixes deviates from circular.

The assumptions and models used in the updated coverage and performance model have been summarised in Table 13 and Table 14 in Section 9.3.

The updated model has been used to investigate the effects of CRI within a system formed by the existing North-West European stations. It has been shown that effective receiver CRI mitigation is vital to meeting the stringent HEA accuracy requirement. The results also suggest that there is a need for one or more eLoran transmitters in Ireland, and this will be investigated further in a case study presented in Chapter 11.

Finally, the new model has been validated by comparison with accuracy data collected from GLA' vessels.

10 GRI SELECTION

In contrast to the previous chapters, which were largely written from a signal processing point of view, the present chapter addresses the issue of CRI from a signal design perspective. Specifically, the chapter will focus on mitigating the effects of CRI through the careful selection of the Group Repetition Intervals (GRIs). Historically, the use of GRIs was coordinated by International Association of Marine Aids to Navigation and Lighthouse Authorities (IALA), with each Loran service provider proposing GRIs for their chains, following their methods and procedures. At the time of writing, there is no established GRI selection procedure for eLoran.

This chapter starts with an overview of the main factors that affect the GRI selection. It goes on to review GRI selection methods used in establishing Loran-C chains, and proposes a new GRI selection procedure for eLoran. This part of the thesis therefore provides the answer to the second research question: 'What is the best method for selecting a GRI for a new station installation given modern eLoran technology, including receiver signal processing techniques?'.

10.1 FACTORS AFFECTING GRI SELECTION

There are two key factors that affect GRI selection. Firstly, CWI can be caused by transmitters broadcasting close to the Loran frequency band. The significance of this problem, in particular for European chains, has been underlined many times before [77, 78, 85, 86, 29]. Secondly, CRI occurs due to overlapping Loran signals, as discussed in detail in previous chapters. Besides these two factors, there are also some other constraints, which will be explored later in the text.

10.1.1 *Continuous Wave Interference*

The issue of CWI was highlighted in Chapter 3, which also contains a literature review on CWI modelling and mitigation. This section focuses on the aspects of CWI that are particularly relevant to the GRI selection.

The Link between CWI and GRI Selection

The connection between CWI and the GRI selection is best understood by considering the frequency spectrum of the Loran signal in relation to the frequency response of the receiver. As explained in Chapter 2, the Loran spectrum consists of spectral lines $1/(2T_{\mathrm{GRI}})$ apart. This is shown schematically in Figure 91. In the first approximation, each CWI interferer can be regarded as a single spectral line (depicted in red). On reception, the interference is weighted by the receiver's magnitude response, as also indicated in Figure 91 (see the receiver model developed in Chapter 5). If the interference lines fall between the Loran spectral lines then they are less harmful than if they coincide (note that in the upper plot of Figure 91 the interference will be suppressed by at least

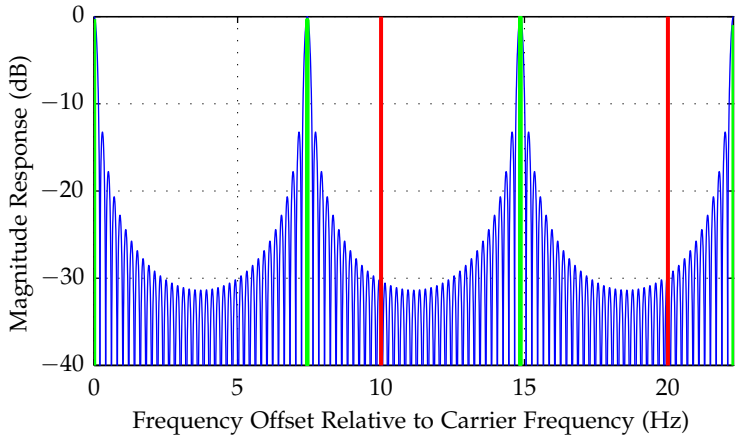

(a) GRI 6731

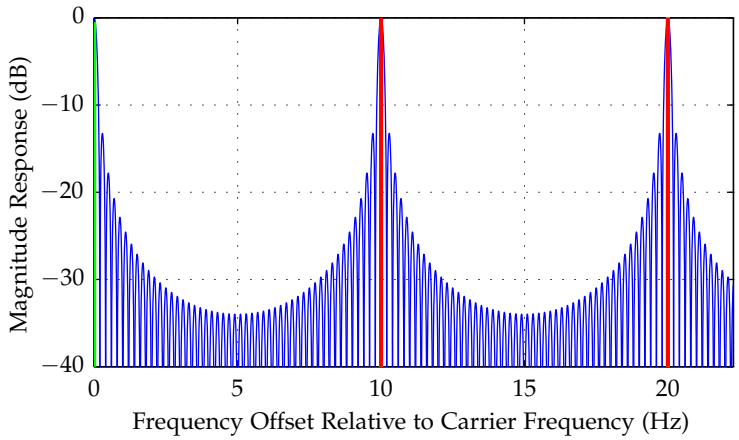

(b) GRI 5000

Figure 91: Close up of a comb-filter magnitude response (blue) and eLoran spectrum (green) for two different GRI values; red lines represent CWI.

30 dB, whereas in the bottom plot the interference passess through the comb filter unattenuated). Further, as a consequence of the receiver signal processing, an area of sensitivity to interference around each spectral line is introduced. It can now be clearly seen that with a given set of interferers some GRIs are more susceptible to CWI than others.

Classification of CWI

The Loran literature distinguishes between three types of CWI, based on the relation between the frequency of the interference, the GRI of the Loran signal, and the receiver integration time [38, 30]:

1. The interference is termed *synchronous* when the frequency of the continuous wave, f_i, coincides with one of the Loran spectral lines:

$$f_i = \frac{n}{2T_{\text{GRI}}}, \quad n \in \mathbb{N}.$$

Synchronous interference is considered the most insidious form of CWI. Since it is aligned with one of the Loran spectral lines,

it cannot be suppressed by comb-filtering. It introduces a bias in the carrier phase (and consequently ranging and position) measurements. It can also introduce a bias in the signal time offset measurements which may lead to incorrect phase ambiguity resolution.

2. *Near-synchronous* interference occurs when the frequency of the continuous wave lies within one of the main lobes of the receiver's comb filter characteristics (see Figure 91), i.e. when

$$\left| f_i - \frac{n}{2T_{\text{GRI}}} \right| < \frac{1}{T_{\text{i}}} \quad n \in \mathbb{N},$$

where T_{i} is the length of the receiver's integration interval. This type of interference manifests itself as an oscillating measurement error.

3. The term *asynchronous* interference is used when the frequency f_i falls outside the main lobes of the comb filter characteristics. Asynchronous interference is substantially attenuated by the comb filter but may significantly increase the measurement noise when the signal-to-interference ratio is low.

It should be noted that, in practice, CWI rarely consists of only one spectral line, and hence the distinction between the different interference types may not be as clear-cut as the above definitions suggest. Nevertheless, this classification is introduced here, as it lies at the heart of GRI selection techniques used in the past.

International Frequency Allocations

As discussed earlier, the receiver's magnitude response has peaks at frequencies

$$f_n = \frac{n}{2T_{\text{GRI}}}, \quad n \in \mathbb{N},$$

coinciding with the spectral lines of the GRI of interest. For a GRI that is an integer multiple of 100 μs (most GRIs world-wide), the above expression can be re-written as

$$f_n = \frac{n}{2 \cdot 10^{-4} \cdot k} = 5 \cdot 10^3 \frac{n}{k}, \quad k \in \{400, 401, \ldots 999\}, n \in \mathbb{N},$$

from which it follows that GRIs that are integer multiples of 100 μs are sensitive to synchronous CWI at frequencies being integer multiples of 5 kHz (and $k-1$ other frequencies in between the 5 kHz lines). Similarly, GRIs being multiples of 200 μs and 500 μs are sensitive to interference at multiples of 2.5 kHz and 1 kHz, respectively. Since there are many stations world-wide broadcasting on such frequencies[1], GRIs that are multiples of 200 μs or 500 μs are particularly susceptible to CWI and are usually eliminated in the GRI selection process. Loran-C chains in North-West Europe were designered with GRIs that are integer multiples of 10 μs and therefore have spectral lines at multiples of 50 kHz. This makes them significantly less prone to synchronous CWI.

1 Note that frequency channels in the LF band are typically allocated on 50 Hz increments.

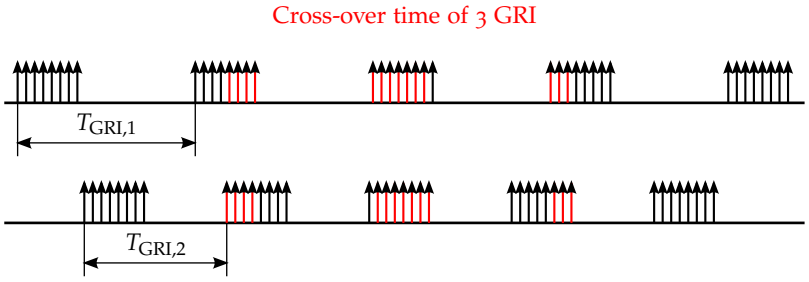

Figure 92: Schematic illustration of Cross-Rate Interference.

10.1.2 *Cross-Rate Interference*

The effects of CRI on eLoran performance were studied in detail in Chapter 6 where it was shown that the CRI-induced error is a complex function of the GRIs of the cross-rating signals, with some combinations of GRIs performing considerably worse than others. Due to the nature of the eLoran signal, CRI can never be completely prevented, however rules can be applied to the GRI selection, which minimise its effect. Several GRI selection strategies used in the past will be presented later in this chapter. While these differ in detail, they all use a set of three basic characteristics to identify potentially harmful combinations of GRIs. These are detailed here below.

Cross-over Time

Figure 92 shows the effect of CRI between two eLoran pulse trains. The *cross-over time* is usually defined as the number of successive groups of pulses affected by the overlaps between two cross-rating signals, as indicated in the figure. The cross-over time expressed in terms of the number of periods of the interfering signal (GRI, 2) can be calculated using the following formula [25, 152]:

$$T_x = 1 + \left\lfloor \frac{T_1 + T_2}{\left| T_{GRI,2} - \text{round}\left(\frac{T_{GRI,2}}{T_{GRI,1}}\right) \cdot T_{GRI,1} \right|} \right\rfloor ,$$

where T_1, T_2 is the time it takes for each respective station to transmit a pulse group (assumed 11500 μs for a master station if it broadcasts the ninth pulse and 9500 μs otherwise), and $T_{GRI,1}$, $T_{GRI,2}$ are the GRIs of the two cross-rating signals (expressed in seconds).

The cross-over time for any two GRIs that may interfere should be negligible compared with the number of pulse groups processed over the receiver's integration time, otherwise a significant measurement error can occur as a result of the pulse overlaps [25].

Overlap Time

The *overlap time*, T_o, was defined in Chapter 6 for the purpose of blanking loss evaluation. It is essentially the common period of two (or more) cross-rating signals, and it determines the time it takes for the interference pattern formed by the overlapping pulse groups to repeat itself. In order to "whiten" the spectrum of the CRI-induced measurement error, it is desirable that the overlap time is as long as possible.

Sub-periodic CRI Patterns

Another aspect of CRI that needs to be considered in the GRI selection is *sub-periodicity* in the overlap patterns [25] (for an explanation of the term see Section 6.2.3, Chapter 6 which also demonstrates the impact of sub-periodic CRI on the pseudorange measurement error). Strong sub-periodic patterns can cause excessive measurement errors and may also negatively affect the signal acquisition process. GRI combinations that cause such interference therefore must be eliminated in the GRI selection process.

10.1.3 *Other GRI Constraints*

Besides continuous wave interference and cross-rate interference there are a number of other constraints on GRI selection that need to be taken into account.

Chain Configuration and Signal Specification Requirements

The USCG Loran-C and the draft eLoran LORIPP\LORAPP signal specifications require the GRIs to be in the range of 4000 to 9999 (10′s of µs). Further, the specifications set out restrictions on the spacing between consecutive transmissions from stations in the same chain as will be detailed later. In order to meet these requirements anywhere within the coverage area, the selected GRI has to be greater than some minimal permissible value, $T_{\text{GRI,min}}$, determined by the configuration of the geographical location of the transmitters. A procedure for calculating the minimum GRI is given in Section 10.2.2.

Transmitter Constraints

With dual-rated transmitters, improper choice of GRI can lead to a higher pulse rate than the maximum rate specified by the manufacturer. For Loran-C transmitters this limit was 300 pulses-per-second. For eLoran, with modern solid-state transmitters, this number may be higher; recent new transmitter technology promises pulse rates of at least 700 pulses/s.

Depending on the transmitter model, there may be limitations on the resolution of the signal Coding\Emission delays which can in turn have impact on the minimum GRI. The ED assignement is dealt with in Section 10.2.2.

Finally, depending on the transmitter synchronisation method, there may need to be space built-in to the GRI for the presence of signals from Loran simulators that are used at Loran transmitters to measure and maintain Loran transmission timing. This is briefly discussed in Section 10.2.3.

UTC Time of Coincidence

Loran time and frequency users may be interested in the relationship of the Loran signals to 1 Pulse Per Second (PPS) UTC. Loran rates are sub-synchronous with the 1 PPS signal, which means that the beginnings of Loran PCIs do not occur in the same relationship with every UTC second, but will coincide with the 1 PPS UTC at regular time instants, termed Times of Coincidence (TOC) [52]. Clearly, the length of time between two successive TOCs depends on the GRI chosen and can

be shown to be between 6 and 17 minutes if the GRIs are selected in 100 μs steps, and between 1 and 3 hours if they are assigned with 10 μs resolution. A higher frequency of TOC occurence can facilitate the synchronisation of Loran equipment.

Loran Data Channel Considerations

There are several implementations of the Loran Data Channel (see Section 4.2.5, Chapter 4). The Loran data is either modulated onto the same pulses that are used for navigation, or on additional pulses appended to each pulse group. It is easy to see then that the longer the GRI the lower the achievable data rate of the transmissions. The maximum allowable GRI therefore sets a limit to the achievable data rate.

10.2 OVERVIEW OF EXISTING GRI SELECTION METHODS

This section gives an overview of existing GRI selection methods used in the past to set up Loran-C chains. The selection of the best GRI is accomplished by considering the factors and constraints discussed in the previous section. This takes place in a series of processing stages, each of which discounts particular GRI values from a candidate list, until a list of the most suitable GRIs ordered in preference is obtained. The following sections detail the GRI selection methods developed and used by the USCG, Technical University Delft and DCN[2] Brest.

10.2.1 *USCG Method*

The GRI selection process used by the USCG [152] proceeds in five broad steps which can be described under the following headings.

GRI Preselection

The purpose of the first stage was to limit the number of GRIs that would be investigated by considering the chain configuration, existing GRIs, signal specification and transmitter constraints. The steps in this stage can be summarised as follows:

- Determine the minimum allowable GRI for the given chain configuration. Allowable rates were selected in the range 4000 to 9990 in 100 μs GRI increments. No specific procedure to calculate the minimum GRI is given in [152] but reference is made to a software tool. For further detail on minimum GRI calculations see Section 10.2.2 below.
- Determine which Loran stations will interfere with the proposed chain. The primary consideration was the estimated field strength from each station of the interfering chain, not the expected coverage area of the chain. It was considered more harmful at this stage to neglect a station that will interfere than to include one that turns out not to interfere.

2 DCN (Direction des Constructions Navales; now DCNS S.A.) is a naval defence company founded by Cardinal de Richelieu in 1631. It operates the Control Centre for the North-West European Loran chains.

- Use the minimum GRI and the list of stations that may interfere to obtain a list of GRIs that are relatively prime to all GRIs that may interfere with the proposed chain (in the context of the USCG method 'relatively prime' means that the GCD of the GRI identifiers is equal to 10).
- Eliminate all GRIs that would result in exceeding the maximum transmitter pulse rate (only applied if there were dual-rated transmitters in the proposed chain).
- Eliminate GRIs that are divisible by 500 μs. As discussed earlier, these GRIs have spectral lines every 1 kHz and are therefore more susceptible to synchronous interference.
- Eliminate all GRIs that are presently assigned.
- If transmitters were dual-rated as a result of the proposed chain, the procedure would eliminate all GRIs that would have a cross-over time greater than 10 GRI.

CRI Analysis

The CRI analysis determined the worst-case Figure of Merit (FOM) for each candidate GRI combination by using a computer time-domain simulation of the signal tracking algorithm. The FOM was based on the receiver's tracking loop error observed for the four combinations of wanted and interfering, master and secondary signals.

The procedure assumed a receiver tracking loop time constant of 25 GRI, simulating the response of an aviation receiver, and a time constant of 200 GRI to simulate a marine or monitor receiver. The resulting FOM was the Root Sum of Squares value of the estimated tracking errors for the four combinations of signals and two receiver time constant settings.

Selection of GRIs for Hardware Simulation

A limited number of GRIs would be selected for hardware simulation tests. The final ranking of the candidate GRIs was based on the FOM and two other factors:

A major factor in choosing a new rate was the minimisation of the cross-over time. The final list of GRIs would be annotated with the cross-over time of each proposed GRI with each station that would be dual-rated. Combinations with cross-over time of less than 4 GRI were highlighted.

Secondly, GRIs divisible by 200 μs would also be highlighted. These GRIs have spectral lines every 2.5 kHz and should be avoided in order to reduce the possibility of the proposed rate being susceptible to synchronous interference.

Hardware Simulations

A hardware simulation of the proposed GRIs would be carried out using a Loran signal simulator and a monitoring receiver. Single combinations of GRI pairs would be tested once with the tracked signal at the GRI that may interfere with the proposed chain and once with the tracked signal at the GRI of the proposed chain. The data from these tests included a plot of the tracking error and its basic statistics. These tests were used as a guide for detection of unexpected problems.

10.2.2 *TU Delft Method*

The Technical University Delft GRI selection method [77, 78, 24] was developed in the 1990's when the North-West European Loran-C chains were planned. In contrast to the USCG procedure described above, where the main driver of the GRI selection process was CRI, the TU Delft method gives a higher priority to CWI. This is because Europe was a particularly busy radio environment in the 1990's, and CWI posed a serious threat to Loran.

The method proceeds in four broad steps, as described below.

GRI Preselection

The procedure starts with the preselection stage, the purpose of which is the same as in the USCG method, however, there were some differences.

Because of the hostile radio environment in Europe, GRIs in the NELS were selected in increments of 10 μs, rather than 100 μs as in the rest of the world. This means that European GRIs have spectral lines every 50 kHz instead of every 5 kHz, which makes them considerably less susceptible to CWI (see the discussion in Section 10.1.1). To further minimise the possibility of synchronous CWI, GRIs that are integer multiples of 20 μs, 30 μs and 50 μs (having spectral lines at multiples of 25 kHz,16.667 kHz, and 10 kHz, respectively) were eliminated from the selection process.

The next phase of the preselection stage was to determine the minimum GRI for the given chain configuration. Report [77] published by the TU Delft team gives detailed instructions regarding the minimum GRI calculations. Since the same calculations also apply to eLoran, the instructions are reproduced here below.

In the following, the subscript $m \in \{1, 2, \ldots, N_{\text{st}}\}$ is used to distinguish between different stations within a chain. Index $m = 1$ (and $m = N_{\text{st}} + 1$) corresponds to the master station, $m = 2$ denotes the first secondary station, etc. Further, the minimum time differences between the reception of signals from the master station and the first secondary station in a chain (as prescribed by the signal specification) will be denoted $\Delta\tau_{1,\text{min}} = 10900\,\mu$s. The minimum time difference between two consecutive secondary transmissions is $\Delta\tau_{m,\text{min}} = 9900\,\mu$s, $m \in \{2, 3, \ldots N_{\text{st}} - 1\}$, and the minimum separation between the last secondary transmission and master transmission from the next GRI is $\Delta\tau_{N_{\text{st}},\text{min}} = 9900\,\mu$s.

In order to meet the above signal timing requirements anywhere within the coverage area, the GRI has to be selected greater than some minimal permissible value, $T_{\text{GRI,min}}$, determined by the configuration of the chain. The smallest time difference between the reception of transmissions from stations m and $m + 1$, denoted $\Delta\tau_m$, can be found at the location of station $m + 1$:

$$\Delta\tau_m = \Delta\tau_{\text{ED},m} - \frac{r_m}{v_{\text{prop}}},$$

where $\Delta\tau_{\text{ED},m}$ is the difference in ED of stations m and $m + 1$, r_m is the ellipsoidal distance between the two transmitting stations, and v_{prop} is a conservative estimate of the signal propagation velocity. The signal

specification requires that $\Delta\tau_m$ is greater or equal to $\Delta\tau_{m,\min}$, as defined above, from which it follows that

$$\Delta\tau_{\mathrm{ED},m} \geq \Delta\tau_{m,\min} + \frac{r_m}{v_{\mathrm{prop}}}.$$

The minimum GRI can therefore be calculated as

$$T_{\mathrm{GRI,min}} = \sum_{m=1}^{N_{\mathrm{st}}} \Delta\tau_{m,\min} + \frac{r_m}{v_{\mathrm{prop}}}.$$

CWI Analysis

In the next stage, the candidate GRIs were ranked according to their susceptibility to CWI. The TU Delft method accomplished this by estimating, for each GRI, the worst-case measurement error due to CWI throughout the intended coverage area.

This approach required that field strengths for all potential interferers in the area of interest were evaluated. Transmitter power, frequency and location data for the purpose of the field strength calculations were sourced from the ITU International Frequency List, although there had been concerns about the reliability of the data contained within it. Note that even at the time of this writing the latest edition of the list [97] still contains stations of the long decommissioned Decca Navigator system.

Interferers' field strengths can be calculated using the classical ITU ground wave and sky wave propagation methods described in Chapter 3 of this thesis. The method adopted by TU Delft provided conservative estimates of interference based on a composite field strength curve combining data for ground wave propagation over seawater with sky wave measurements.

In order to asses the effect of the interference on a receiver's performace, the receiver's sensitivity characteristic had to be taken into account. In the TU Delft report [77] such a characteristic was derived by investigating how the sampling and tracking algorithms influence the received signal in the frequency domain. The receiver sensitivity acts as a transfer function on interference and produces effective field strengths as seen by the receiver, which show predicted levels of interference experienced by a receiver tracking that particular GRI. The total interference levels for each investigated GRI were estimated by taking the root of sum of squares of the individual effective field strengths.

To accomplish the CWI analysis, the interference levels needed to be related to the Loran field strengths. A Loran coverage area was defined and, within this coverage area, SIR and tracking error estimates were calculated. The mean value of this tracking error estimate was then used as a measure to rank the GRIs with respect to CWI.

CRI Analysis

Once the process of CWI analysis was finished, a list of promising GRIs was compiled. The next step in the procedure was to compare these against the GRIs of existing chains and to identify combinations resulting in unacceptable CRI.

Two different methods of CRI analysis were developed by TU Delft. Initially, a software tool similar to that used by USCG was used to examine the candidate GRIs on CRI [77, 38]. The tool allowed the CRI-induced tracking error to be observed by simulating the received signals

and basic receiver signal processing algorithms. Later, an approach proposed by Nieuwland and Arriens [24, 25] was adopted. This method defines a set of parameters and mathematical rules that allow the system designer to identify and eliminate GRI combinations showing unacceptable CRI. The rules described by Nieuwland and Arriens can be summarised as follows (see Section 10.1.2 above for further explanation of the terms used):

- The new GRI should be as short as possible and mutually prime with other potentially interfering GRIs.
- The cross-over time with the interfering GRIs should be minimised.
- The GRIs should show no sub-periodic interference patterns over short time periods.

Eliminating those GRIs, which show unacceptable CRI results in a final list of surviving GRIs.

Emission\Coding Delay Assignment

The TU Delft method also dealt with the selection of Emission\Coding Delays for the new stations. The initial report [77] assumed that the delays can be set with an arbitrary resolution and proposed to divide the time available in a GRI (i.e. the difference between the proposed GRI and the minimum GRI) equally among the different stations.

Report [78] used a different approach. There it was assumed that the emission delays would be selected with an 0.1 ms resolution, and the individual values were found by summation of the appropriate delay differences $\Delta\tau_{ED,m}$, defined in Section 10.2.2, each rounded to the nearest higher integer multiple of 0.1 ms. If the difference between a $\Delta\tau_{ED,m}$ and its rounded value was less than an arbitrarily set threshold of 20% of the propagation delay, the next higher multiple of 0.1 ms was chosen. The impact on the minimum GRI of using 1 ms resolution for the delays was also examined in that report.

For more details on the TU Delft method see reference [44].

10.2.3 *DCN Brest Method*

DCN Brest, the company that operates the Control Centre for the North-West European chains, published their guidelines on GRI selection [84] in 1993. The method described by DCN built on the studies performed by TU Delft and introduced several additional selection criteria. These include:

- Free slots for future extensions to the system;
- Free slots for signal simulators; and
- TOC repetition period considerations.

The document suggests that up to two 9.9 ms free slots may be required in each chain to support the two-way Loran time transfer method used for station synchronisation.

DCN also carried out field experiments to verify the TU Delft CWI analysis method. Several candidate GRIs were tested on their susceptibility to CWI. The tests showed that a 2 dB to 3 dB improvement in

SNR could be achieved by selecting GRIs at the finer, 10 μs, resolution rather than in 100 μs steps (which is in line with theoretical expectations discussed in Section 10.1.1). However, there was no significant difference in SNR between different 10 μs GRIs, which suggests that the benefit of using the detailed TU Delft CWI analysis is marginal.

10.3 DEVELOPING A GRI SELECTION METHOD FOR ELORAN

The GRI selection method described in this section is being proposed based on the results of the candidate's own research. The selection of the best GRI proceeds in a similar manner to that of the existing methods, however several important eLoran updates are introduced.

10.3.1 *GRI Preselection and Emission Delay Assignment*

In the first stage of the proposed GRI selection procedure the minimum GRI is determined using the TU Delft method described in Section 10.2.2 above. One minor modification is required to reflect changes in the eLoran vs. Loran-C signal specification. Since all eLoran stations transmit only eight pulses in a group[3], the required minimum time difference between the transmission of two successive stations in a chain can be set to the same value for all stations, i.e. $\Delta\tau_{m,\min} = 9900\,\mu$s, $m \in \{1, 2, 3, \ldots N_{\text{st}}\}$.

It will further be assumed that all transmitters are fully upgraded to eLoran standards and that consequently:

- There is no need for free slots for signal simulators to support the two-way Loran station synchronisation method used in Loran-C;
- Maximum achievable pulse rate is not a limiting factor in the choice of GRI[4];

The first stage of the GRI selection procedure also involves the assignment of the EDs to the individual stations in the new chain. This can be accomplished using the method desribed in report [78] and Section 10.2.2 of this document. It will be assumed that EDs are rounded up to 0.1 ms using the algorithm also described in Section 10.2.2.

The maximum GRI is typically set to 9999, in line with the signal specification, although the possibility of using longer GRIs is also explored later in this thesis.

10.3.2 *CWI Analysis*

As discussed above, previous work on GRI selection carried out in Europe in the 1990's paid a great deal of attention to CWI. However, advances in receiver design [83, 89, 90, 30] and a decline in use of the LF spectrum [44] mean that CWI is much less of a threat today than it was in the 1990's [91, 92].

Besides, it is not certain whether the detailed CWI analysis developed by TU Delft can provide any measurable benefit. One of the weaknesses of the method is that it models each interfering signal as a single

3 Note that Loran-C master stations broadcast nine pulses in a group. The ninth pulse was added for identification and integrity purposes [14] but is no longer required in eLoran due to receiver automation and the introduction of the Loran Data Channel.

4 Modern eLoran transmitters can deliver at least 700 pulses/s [153].

spectral line. In reality, the signal spectra always occupy a wider range of frequencies (typically in the order of hundreds of Hz, and up to 6 kHz [97]). This means that the spectra often span across several eLoran spectral lines, and consequently the differences in effect of CWI between different GRIs are not expected to be as significant as the TU Delft studies suggest (this suspicion would seem to be consistent with the findings of the field experiments conducted by DCN [84]). There are also concerns about the reliability of the database of interferers, as the ITU's International Frequency List (IFL) [97] clearly includes some inactive stations (for example decommissioned Decca stations). It is therefore considered that it is not useful to proceed to the detailed CWI analysis. Instead, the following, simpler, approach is proposed which eliminates all GRIs that are likely to be susceptible to CWI.

First, GRIs should be selected on 10 μs increments. Both theory and measurements [84] clearly show the advantage of using 10 μs GRIs over 100 μs ones, which were typically used in the past.

Second, it is proposed that only prime-number GRIs are used (i.e. the repetition interval should be divisible only by 10 μs and itself). Such GRIs will have spectral lines at frequencies given by

$$f_n = \frac{n}{2T_{\mathrm{GRI}}} = \frac{n}{2 \cdot 10^{-5} \cdot k} = 50 \cdot 10^3 \frac{n}{k},$$

where $n \in \mathbb{N}$ and k (the GRI expressed in 10's of μs) is a prime number greater or equal to the minimum permissible GRI. Clearly, these GRIs will be sensitive to CWI at integer multiples of 50 kHz but such interference can easily be suppressed by the receiver's input bandpass filter (it is assumed that there is no interference at 100 kHz as the band from 90 kHz to 110 kHz is allocated to Loran). The GRIs will also be sensitive to interference at a number of frequencies interleaved between the 50 kHz spectral lines with a spacing of $5 \cdot 10^4 / k$ Hz. However, these frequencies are unlikely to coincide with existing frequency allocations due to k being a prime number. If k was not prime, the GRIs would be sensitive at submultiples of 50 kHz that are likely to be in use by other services. For example, if k is divisible by 2, then the GRI will be sensistive to synchronous CWI at integer multiples of 25 kHz; if it is divisible by 4, it will be sensitive to CWI at multiples of 12.5 kHz, etc. Choosing a prime-number GRI thus minimises the probability that the system will be susceptible to synchronous CWI.

10.3.3 *CRI Analysis*

The proposed method of CRI analysis follows-up on algorithms derived in [25] and findings of the candidate's own research presented in this thesis. The method proceeds as follows:

- Eliminate all GRIs that are presently assigned. A list of all existing Loran and Chayka chains can be found in Appendix C of this thesis.
- Identify Loran stations that are likely to interfere with the one(s) being proposed. The primary consideration is the estimated field strength from each station. An existing station is included on the list of potential interferers if:

  - The separation between the existing and proposed stations is less than the maximum usable range of an eLoran station (assumed 1200 km for the purpose of this calculation); or
  - The separation is greater than the maximum usable range and the proposed\existing station causes a SIR of less than 20 dB at the maximum usable range of the existing\proposed station.

- Eliminate candidate GRIs that are not relatively prime with respect to the potentially interfering GRIs (i.e. the greatest common divisor of the two GRIs expressed in tens of microseconds is greater than 1).
- Eliminate GRIs that show potentially harmful sub-periodic patterns using the Farey sequence method developed in Section 6.2.3, Chapter 6.
- Eliminate GRIs that would have a cross-over time greater than 10 repetition intervals. This requirement ensures that the cross-over situation will not last for longer than approximately 1 s (i.e. significantly less than a typical receiver integration time), and therefore the impact on the ranging performance will be minimal. Also, the Reed-Solomon code used in Eurofix data communications is capable of correcting up to 10 consecutive symbol errors and therefore should be able to cope with the burst errors caused by CRI. It is important that the cross-over time is considered both in terms of the proposed and existing GRIs (note, for example, that when GRI 4000 and GRI 8000 interfere, then the overlaps affect at most one pulse group at a time in GRI 4000 but can affect all pulse groups in GRI 8000).
- Identify stations that are likely to be used in the position solution within the area of interest. For the purpose of this algorithm, all stations that are within the maximum usable station range of any point in the area of interest are included.
- Rank the remaining candidate GRIs according to the maximum cross-over time with the GRIs likely to be used for positioning.

10.3.4 *Coverage and Performance Optimisation*

The aim of this step is to determine which GRI in the set of promissing GRIs generated in the preceding stages of the procedure will provide the best coverage and performance across the geographical area of interest. Before this optimisation can be performed, it is necessary to define the optimality criterion. There seem to be two natural options:

- To minimise average positioning error within a given coverage area; or
- To maximise coverage area for a given positioning accuracy target.

Once the optimality criterion is selected, the coverage and performance model developed in Chapter 9 of this thesis can be used to determine the best GRI for the new station(s). The search for the optimum GRI should be restricted to those values with the shortest maximum cross-over time as identified by the CRI analysis.

10.3.5 *Hardware Simulation*

If an eLoran signal simulator (such as that described in Chapter 8) is available, tests can be carried out with end user equipment to confirm that the introduction of the new station(s) will not cause any unexpected problems. These tests should be conducted under typical SNR conditions encountered within the coverage area and should be repeated for a range of SIR values. Ranging errors should be analysed for both the proposed and existing signals.

10.4 SUMMARY AND CONCLUSIONS

This chapter has discussed the factors that affect GRI selection and reviewed existing Loran-C GRI selection techniques. A new procedure for GRI selection has been proposed which follows up on the methods used in the past, and introduces a number of eLoran updates, such as the use of modern eLoran signal processing techniques and the all-in-view positioning mode. The proposed procedure consists of the following five steps:

1. GRI preselection and Emission Delay assignment;
2. CWI analysis;
3. CRI analysis;
4. Coverage and performance optimisation;
5. Hardware simulation.

The following chapter demonstrates the use of the procedure through a case study involving the addition of two eLoran stations to the North-West European system.

11 CASE STUDY: NEW STATIONS IN IRELAND

eLoran research and development in Europe is driven by the GLA. The GLA have produced a Business Case for eLoran, selecting it as the most cost-effective way of providing resilient PNT for the IMO's e-Navigation concept within their waters. The GLA plan to implement eLoran in their service area in two phases. The first phase, IOC, will see the establishment of port approach level eLoran in seven main port approaches on the East Coast of the UK. The second phase, FOC, should extend coverage to all major ports in the UK and Ireland, as well as to the English Channel.

As discussed earlier in Chapter 9, it is likely that the full GLA service-wide eLoran coverage will require the addition of one or more transmitters at the West of Ireland. The intended extension of the transmission network provides an excellent opportunity to demonstrate the GRI selection procedure developed in the previous chapter by solving a real-life problem as a case study.

11.1 TRANSMITTER LOCATIONS

The GLA have identified a number of candidate transmitter sites in Ireland, and assessed these sites for their suitability to accommodate low-powered (3 kW to 100 kW EMRP) and full-power (250 kW EMRP) eLoran transmitters [154]. The assessment has shown that the optimal solution would consist of a full-power station at Tullamore, augmented by a low-powered station in the far South-West of Ireland. A site near Mizen Head was suggested as a possible location of the low-powered (up to 10 kW EMRP) transmitter. Additional details of the sites under consideration, including the type of antenna available at each site and maximum radiated power are shown in Table 17.

11.2 CHAIN CONFIGURATION

There are two options for how the new eLoran stations can be setup. They can either be integrated in an existing chain, or put on a new GRI of their own. Both options will be explored in this chapter. Additionally,

SITE	LOCATION	ANTENNA TYPE	EMRP (kW)
Tullamore	53.2784° N, 7.3719° E	296 m lattice structure w. capacitive top loading	250
Mizen Head	51.4555° N, 9.8080° E	91 m lattice structure w. capacitive top loading	10

Table 17: Potential transmitter locations in Ireland along with assumed transmitter parameters.

the possibility of putting all eLoran stations in North-West Europe on a single GRI will be investigated.

11.2.1 *Tullamore and Mizen Head on an Existing GRI*

The North-West European Loran system consists of four chains: 6731 Lessay, 7001 Bo, 7499 Sylt, and 9007 Ejde (details of the existing chains can be found in Appendix C). The existing stations closest to Ireland are parts of the 6731 Lessay, 7499 Sylt and 9007 Ejde chains. The first part of this case study will assess the feasibility of including the new stations on one of the existing GRIs. When introducing new stations, the possibility of integrating them into an existing chain should always be considered, as it is likely to result in lower CRI levels than when a new GRI is created.

The candidate GRIs must be checked to determine if they can accommodate additional stations. This will be done as the first step of the GRI selection process detailed below. As part of this process, the optimum order of transmissions within the chain needs to be determined as described earlier in Chapter 10. The transmission order should be such that the shortest possible minimum GRI is achieved. Note that this may not always be possible without changing the ED of the existing stations. It is also clear that the new stations will have to be configured as secondary stations, unless the stations' designation within the chain is changed.

11.2.2 *Tullamore and Mizen Head on a New GRI*

Another possibility that will be investigated is to put the additional stations on a new GRI. The option of an Irish "mini-chain" would allow the use of a much shorter GRI, providing improved performance with respect to noise, but increasing also the amount of CRI within the system. The advantages and drawbacks of using shorter vs. longer GRIs will be carefully assessed through the use of the coverage and performance model described in Chapter 9.

In order to allow for a future extension, a free slot will be built into the new GRI to enable the addition of a third station anywhere in Ireland, on the West Coast of Britain or North-West Coast of France.

The choice of master vs. secondary station designation is arbitrary in this case; it will be assumed that Tullamore (the full power transmitter) becomes the master station, although the reader is reminded that the use of phase codes for station identification is no longer necessary in eLoran as the stations can be identified using the Loran Data Channel or based on the fixed relation of the transmission time to UTC.

11.2.3 *All North-West European Stations on One GRI*

The third option that will be explored is to move all eLoran stations in North-West Europe to a single GRI. This would have the obvious advantage of eliminating CRI otherwise generated within the system. However, it is expected that this would also require the use of a significantly longer GRI, resulting in poorer performance with respect to noise as well as reduced data rates. The nett effect of such re-configuration will be assessed through coverage and performance modelling.

STATIONS	DIFFERENCE IN ED $\Delta\tau_{ED,m}$ (μs)
Lessay ↔ Soustons	13000
Soustons ↔ Anthorn	14300
Anthorn ↔ Sylt	14800
Sylt ↔ Tullamore	13500
Tullamore ↔ Mizen Head	10900
Mizen Head ↔ Lessay	12200
Sum	78700

Table 18: Tullamore and Mizen Head on 6731 Lessay (EDs of the existing stations assumed unchanged).

It will be assumed that Lessay becomes the master station in the new chain (again, this choice is arbitrary).

11.3 GRI SELECTION

This section applies the GRI selection procedure developed in Section 10.3 of Chapter 10 to the chain configurations proposed above.

11.3.1 *Tullamore and Mizen Head on 6731 Lessay*

GRI Preselection and Emission Delay Assignment

The first step in GRI selection is to determine the minimum GRI that enables the signal spacing requirements to be met anywhere in the coverage area. The minimum GRI can be found using the algorithm described in Section 10.2.2 of Chapter 10. To illustrate this process, Table 18 gives the differences in ED for the successive station transmissions, assuming that the two new stations are placed after the transmission from Sylt. The ED differences in Table 18 are rounded to the nearest higher multiple of 0.1 ms.

As can be seen from the table, the minimum GRI for this transmitter configuration (assuming that the EDs of the existing stations remain unchanged and no free slots for signal simulators are required) would be 7870. The minimum GRI for the optimum transmission sequence (i.e. if the EDs of the existing stations are reassigned) is 7430. Clearly, there is not enough space in GRI 6731 for the two new stations.

This is also illustrated graphically in Figure 93 which shows the time left within GRI 6731 (assuming the current transmitter configuration) when an additional station is placed within the coverage area. The figure shows, for example, that if a new station was set up on the South-East Coast of England, there would be approximately 2.4 ms left within the GRI. It can also be seen from the figure that Ireland lies just outside the region that can support a new station on this GRI. So GRI 6731 is rejected and the procedure is halted here.

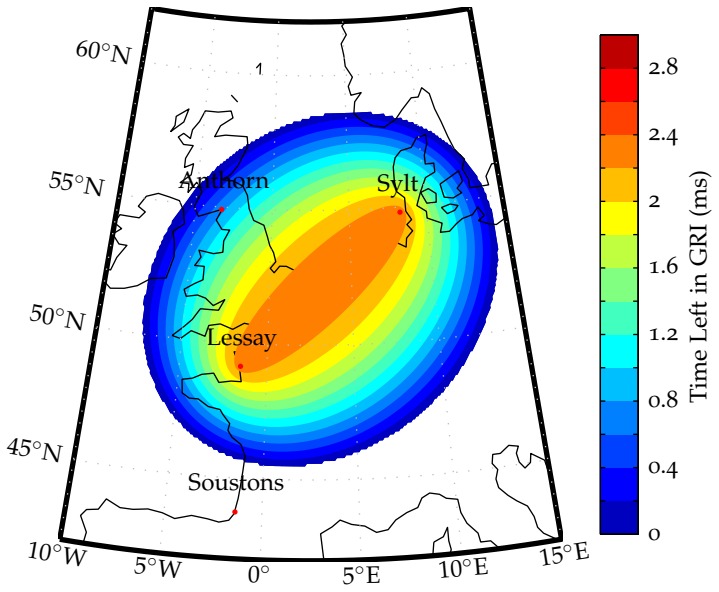

Figure 93: Time left in GRI 6731 after the addition of a fifth station.

11.3.2 *Tullamore and Mizen Head on 7499 Sylt*

GRI Preselection

Table 19 shows the timing relations between the transmissions within the 7499 Sylt chain, assuming that the two new stations are placed after the transmissions from Værlandet. Assuming also that the EDs of the existing stations remain unchanged and that there is no requirement for additional free slots for signal simulators[1], the minimum GRI turns out to be 6860. The minimum GRI for the optimum transmission sequence (Sylt - Lessay - Mizen - Tullamore - Værlandet) is 6370. So the new stations will fit within the existing chain and the procedure can continue.

CWI Analysis

7499 is a prime number and the GRI therefore passes the CWI check.

CRI Analysis

The first step of the proposed CRI analysis (see Section 10.3.3, Chapter 10) is to eliminate all candidate GRIs that are presently assigned. This is not applicable in this case, as the new stations are being put on an existing GRI.

The next step is to identify existing (e)Loran stations that are likely to interfere with the one(s) being proposed. The primary consideration is the estimated field strength from each station. In the case of GRI 7499 the algorithm described in Chapter 10 identifies 25 potentially

1 The present two-way Loran signal synchronisation method requires at least one free slot for signal simulators to be built into the GRIs. This is not necessary if the transmitters are fully upgraded to eLoran standards.

STATIONS	DIFFERENCE IN ED $\Delta\tau_{ED,m}$ (μs)
Sylt ↔ Lessay	14100
Lessay ↔ Værlandet	15400
Værlandet ↔ Tullamore	13900
Tullamore ↔ Mizen Head	10900
Mizen Head ↔ Sylt	14300
Sum	68600

Table 19: Tullamore and Mizen Head on 7499 Lessay (EDs of the existing stations assumed unchanged).

INTERFERING GRI	$T_{x,max}$	a	b	$\Delta\tau_{sub}$ (μs)
7430 China North Sea	28	-	-	-
7030 Saudi Arabia S	5	16	15	50
5543 Calcutta	1	17	23	60

Table 20: Cross-over time and sub-periodic CRI for GRI 7499 (the cross-over time has to be considered both in terms of the proposed and existing GRIs, therefore the maximum value of the two, $T_{x,max}$, is shown; a and b are the numerator and denominator, respectively, of the corresponding Farey point - see Section 6.2.3).

interfering GRIs[2], with stations as far as 11500 km being included in the analysis.

Candidate GRIs that are not mutually prime with the potentially interfering GRIs must be eliminated. Clearly, 7499 is mutually prime to all GRIs in the allowable range.

The last two steps of the CRI analysis consist of eliminating GRIs that show unacceptable sub-periodic CRI and cross-over time against any of the potentially interfering rates. Three potential problematic GRIs were flagged up at this stage of the process, as detailed in Table 20. None of the issues highlighted in the table is considered serious due to the large geographic separation between the newly introduced stations and the three chains in question.

Coverage and Performance Optimisation

Since an existing GRI is being used, there is no need for coverage optimisation, however, a comparison can be made against Figure 87, Chapter 9, which shows the accuracy coverage without the two additional stations. The predicted accuracy with the Tullamore and Mizen Head stations on GRI 7499 is shown in Figure 94. The accuracy plots presented in this chapter take into account signals from all North-West

2 This figure assumes that the U.S. Loran-C chains are active.

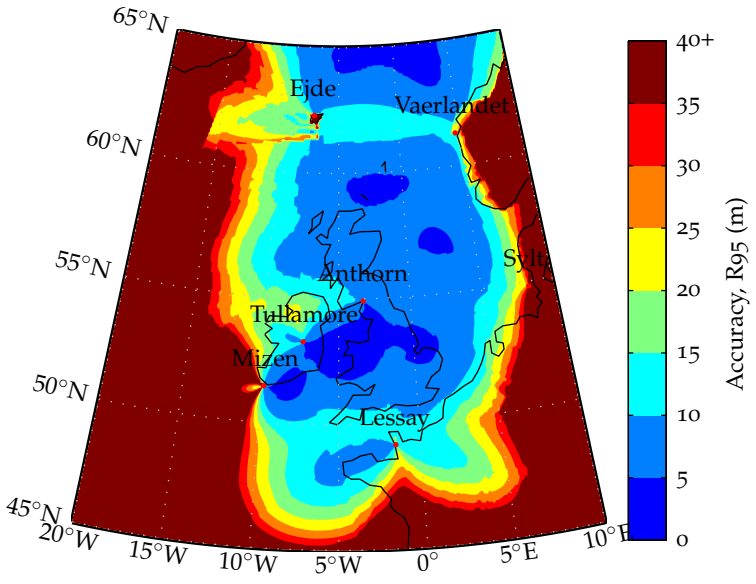

Figure 94: Average positioning accuracy with Tullamore and Mizen Head on GRI 7499.

European stations and the Chayka and Saudi Arabian chains, however, it is assumed that only the North-West European stations are used for positioning. The geographical area of interest used throughout this chapter extends from 45°N to 65°N and 20°W to 10°E. It has been determined by extensive simulation that the new stations have a negligible impact on coverage and performance outside this area.

The introduction of the two new stations results in a 31% increase in coverage area[3] (as measured within the area of interest). The average accuracy within the coverage area is predicted to be 6.68 m, vs. 6.65 m before the extension, with the drop most likely due to CRI.

Hardware Simulation

The last step of the proposed GRI selection procedure involves testing end user equipment on a signal simulator. A simulator suitable for such testing has been developed within this project (Chapter 8), however, the testing of new signals with comercially available receivers would require an intervention by the receiver manufacturer to update the eLoran station almanac. For this reason, this is left for future work.

11.3.3 *Tullamore and Mizen Head on 9007 Ejde*

GRI Preselection

Table 21 shows the timing relations between the transmissions within the 9007 Ejde chain, assuming that the two new stations are placed after the transmissions from Værlandet. Assuming also that the EDs of the existing stations remain unchanged and that there is no requirement for additional free slots for signal simulators, the minimum GRI turns

3 Defined here as the geographical area where the predicted R95 accuracy is 10 m or better.

STATIONS	DIFFERENCE IN ED $\Delta\tau_{ED,m}$ (μs)
Ejde ↔ Jan Mayen	14200
Jan Mayen ↔ Bø	13800
Bø ↔ Værlandet	13100
Værlandet ↔ Mizen Head	13900
Mizen Head ↔ Tullamore	10900
Tullamore ↔ Ejde	14100
Sum	80000

Table 21: Tullamore and Mizen Head on 9007 Lessay (EDs of the existing stations assumed unchanged).

out to be 8000 (note that this leaves a 10.07 ms free window in the GRI which may be sufficient time for a simulator slot in support of the legacy two-way Loran time transfer). The transmission sequence shown in Table 21 is also the optimum sequence.

Since the minimum GRI for the new transmitter configuration is less than the current GRI it seems possible to integrate the new stations on GRI 9007. This would in fact be in line with the original proposals from the University of Wales [87].

CWI Analysis

9007 is a prime number and therefore passes the CWI check.

CRI Analysis

The CRI analysis for GRI 9007 proceeds along the same lines as that of the previous section. As above, 25 potentially interfering GRIs can be identified, all of which are mutually prime with GRI 9007. Table 22 highlights four potential problematic GRIs that were identified by analysing the cross-over time and sub-periodic CRI patterns. The high cross-over time with the U.S. 8970 Great Lakes chain may be of concern if the U.S. stations are re-activated as the separation between the areas served by the two chains is only around 5000 km and the signals travel mostly over sea water. The other three highlighted issues are not expected to have any significant impact on the operation of the chains in question due to the long propagation distances involved, combined with a relatively low cross-over time (8830) and low transmitter power (5543).

Coverage and Performance Optimisation

Figure 95 shows the average positioning accuracy when Tullamore and Mizen Head are integrated into GRI 9007. Similarly to the previous case, the coverage area has increased by approximately 31% with respect to the coverage before the extension. The average accuracy within the coverage area is predicted to be 6.73 m, i.e. slightly worse than for the

INTERFERING GRI	$T_{x,max}$	a	b	$\Delta\tau_{sub}$ (μs)
8970 Great Lakes	52	-	-	-
8930 NW Pacific	25	-	-	-
8830 Saudi Arabia N	11	-	-	-
5543 Calcutta	1	8	13	30

Table 22: Cross-over time and sub-periodic CRI for GRI 9007 (the cross-over time has to be considered both in terms of the proposed and existing GRIs, therefore the maximum value of the two, $T_{x,max}$, is shown; a and b are the numerator and denominator, respectively, of the corresponding Farey point - see Section 6.2.3).

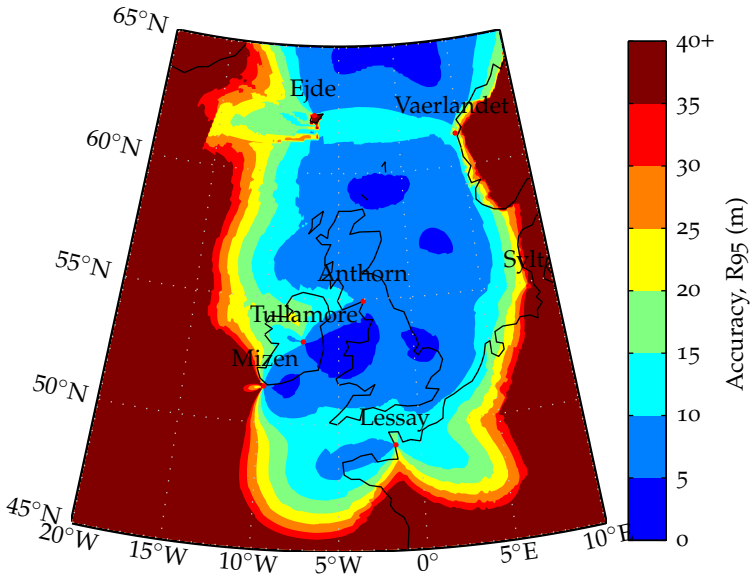

Figure 95: Average positioning accuracy with Tullamore and Mizen Head on GRI 9007.

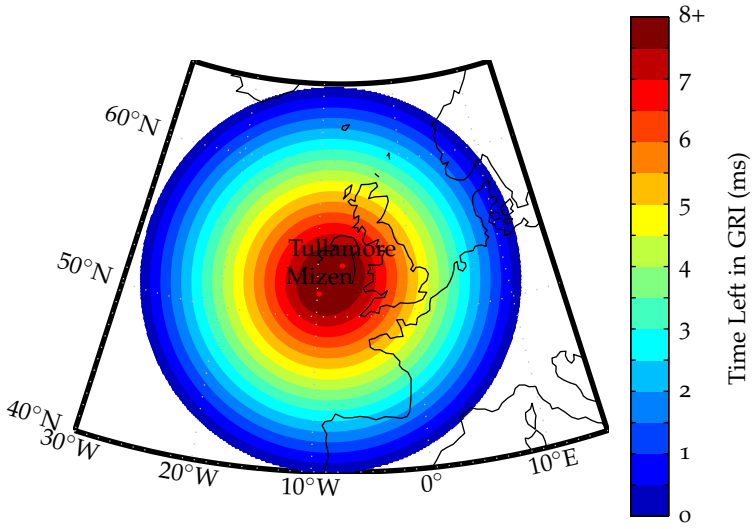

Figure 96: Time left within the Tullamore chain after the addition of a third station, if GRI 4000 is used.

GRI 7499 option. As expected, the GRI 9007 configuration provides a better performance to the north of Ireland (i.e. close to the other stations of the 9007 chain) but it performs worse than GRI 7499 in the southern part of the coverage area (where the GRI 7499 and 6731 signals dominate).

11.3.4 *Tullamore and Mizen Head on a New GRI*

The previous sections have shown that it is possible to integrate the two Irish stations on the existing GRI 9007 or GRI[4] 7499. In order to fully illustrate the proposed GRI selection method, the current section details the considerations required when setting up a new GRI.

GRI Preselection and Emission Delay Assignment

The first step in the GRI selection procedure is to determine the minimum permissible GRI by considering the chain configuration and requirements set by the signal specification. In this case, the chain consists of only two stations. The Minimum ED difference between Tullamore and Mizen Head, assuming that both the master and secondary stations transmit eight pulses in a group, is $\Delta\tau_{ED,1} = 10900$, which gives a minimum GRI of 2180. The minimum GRI will therefore be set to 4000, i.e. the minimum allowable GRI set by the signal specification. This will allow future extension with a third station, installed anywhere in the area shown in Figure 96.

The maximum GRI is set to 9999, in line with the signal specification.

4 GRI 7499 does not leave space for signal simulator slots.

CWI Analysis

As explained earlier, the effects of CWI are minimised by excluding all GRIs that are not prime. Eliminating all non-prime numbers in the range 4000 to 9999 leaves 679 candidate GRIs. These need to be further tested for their susceptibility to CRI.

CRI Analysis

The CRI analysis follows the same process as in the previous sections. Two scenarios will be considered in this section to reflect the U.S. shut down of the Loran-C chains.

The first step of the analysis is to eliminate all GRIs that are presently assigned (see Appendix C). If the U.S. stations are assumed to be active, 30 existing GRIs must be excluded, which results in 676 surviving candidate GRIs. Assuming the the U.S. are permanently de-activated, only 18 existing GRIs needs to be considered. The number of surviving GRIs is the same (note that most of the existing GRIs were already eliminated during the CWI analysis).

Next, the stations that are likely to interfere with the one being proposed have to be identified based on the estimated signal field strengths. With the U.S. stations active 26 potentially interfering GRIs can be identified. If the U.S. stations are assumed to be inactive 18 potential interferers are found. All 676 candidate GRIs are relatively prime with those identified in this step.

Eliminating candidate GRIs that show harmful sub-periodic CRI patterns or unacceptably long cross-over time leaves 12 surviving GRIs (U.S. stations active) vs. 26 survivors (U.S. stations not considered). The surviving GRIs are then ranked according to the maximum cross-over time with the GRIs that are likely to be used for positioning within the area of interest (in this case all North-West European stations and Chayka chains 4970, 8000 and 7990). The results for the best 12 GRIs are shown in Table 23 (U.S. stations active) and Table 24 (U.S. stations not considered), along with predicted coverage improvement and average accuracy (R95) achieved within the expected coverage area. As above, the coverage improvement is measured against Figure 87, Chapter 9.

Coverage and Performance Optimisation

The results shown in Table 23 (U.S. stations active) and Table 24 suggest that the best coverage and performance for the particular transmitter configuration under consideration would be achieved with the Tullamore and Mizen Head stations on GRI 8581 (see also Figure 97). Shorter GRIs give worse results due to the increased amount of CRI that is introduced into the system. Longer GRIs, on the other hand, provide less pulses to integrate over and therefore result in worse performance with respect to noise.

It can also be seen from the results that both the coverage improvement and positioning accuracy are slightly worse when the new stations operate on a new GRI than if they were integrated into an existing GRI. This is not surprising as the number of signals that will interfere with each other is always higher in the former case than in the latter. To illustrate this point, Figure 98 shows the predicted daytime blanking loss for Mizen Head on GRI 8581. Due to the low transmitter power and relatively high number of cross-rating signals present in the area,

CANDIDATE GRI	$T_{x,max}$	COVERAGE IMPROVEMENT (%)	AVERAGE ACCURACY (m)
6263	5	29	6.76
8581	5	30	6.76
6373	6	29	6.76
4657	7	28	6.78
4679	7	28	6.78
5261	7	29	6.77
9281	7	29	6.76
9283	7	29	6.76
9293	7	29	6.76
6481	8	29	6.76
7717	9	30	6.76
5171	10	29	6.77

Table 23: Candidate GRIs for the Irish chain assuming U.S. Loran stations are active.

CANDIDATE GRI	$T_{x,max}$	COVERAGE IMPROVEMENT (%)	AVERAGE ACCURACY (m)
5351	5	29	6.77
6263	5	29	6.76
8581	5	30	6.76
9403	5	29	6.76
9431	5	29	6.76
9497	5	29	6.76
6373	6	29	6.76
8627	6	29	6.76
9343	6	29	6.76
9613	6	29	6.76
9619	6	29	6.76
4657	7	28	6.78

Table 24: Candidate GRIs for the Irish chain assuming U.S. Loran stations are permanently deactivated.

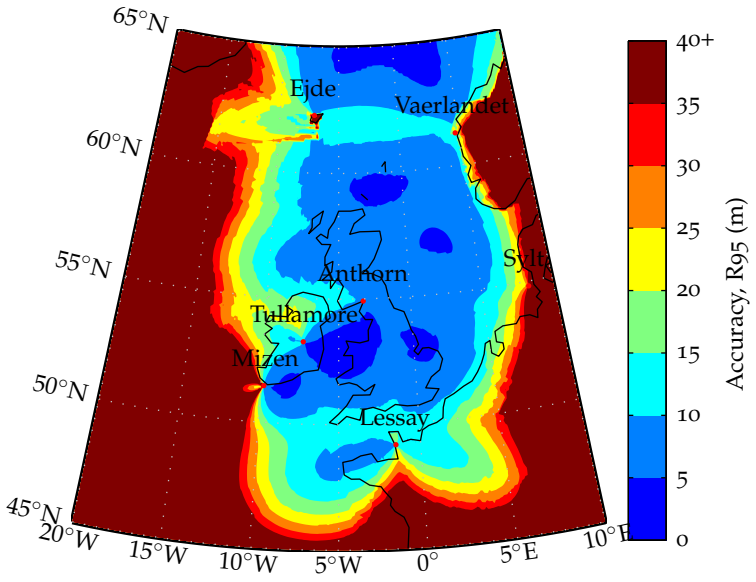

Figure 97: Average positioning accuracy with Tullamore and Mizen Head on GRI 8581.

the blanking loss can be seen to exceed 80% in the Irish Sea and over Britain. If the new stations are integrated into one of the existing GRIs, the blanking loss is reduced by approximately 10% .

11.3.5 *All North-West European Stations on One GRI*

It has been mentioned several times in this thesis that the cost of mitigating CRI is typically a substantial loss of useful signal pulses, and consequently a worse performance with respect to noise. This begs the question of whether any performance gains could be achieved through a complete redesign of the North-West European network, with CRI reduction being the top priority. This section takes the first step towards answering this question by modelling the coverage of the European system under the assumption that all stations are moved to one GRI.

GRI Selection

Fitting all stations in North-West Europe on one rate will obviously require the use of a non-standard GRI. The minimum GRI for the transmission order Lessay - Soustons - Mizen - Tullamore - Anthorn - Ejde - Jan Mayen - Berlevag - Bø - Værlandet is 13950, which is higher than the maximum permissible GRI prescribed by the signal specification. However, there is no fundamental reason why GRIs should be bounded from above and therefore the analysis will proceed with 13950 as the minimum GRI.

By following the same GRI selection procedure as in the preceding sections and assuming that the U.S. stations are not active, GRI 14251 is found to be the most suitable one for the new chain.

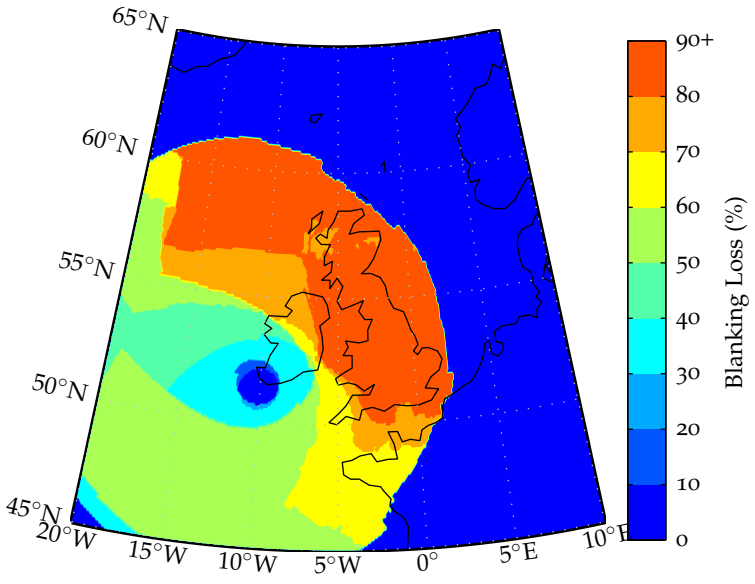

Figure 98: Blanking loss for the Mizen Head station on GRI 8581.

STATIONS' CONFIGURATION	COVERAGE IMPROVEMENT (%)	AVERAGE ACCURACY (m)
Tullamore and Mizen on 7499	31	6.68
Tullamore and Mizen on 9007	31	6.73
Tullamore and Mizen on 8581	30	6.76
All stations on 14251	23	7.24

Table 25: Summary of results.

Coverage and Performance Prediction

An accuracy plot for GRI 14251 is shown in Figure 99. The positive effects of moving all stations to one GRI can be seen, for example, on the North Coast of Ireland, where 10 m level accuracy now appears to be achievable. However, the net effect of using such a long GRI is clearly negative: the coverage improvement against the baseline configuration is only 23% and the average accuracy within the coverage area is 7.24 m (compare with figures achieved in the previous cases studied in this chapter). Also, the effective Eurofix data rate would drop to estimated 13.1 bit/s due to the long GRI.

11.4 SUMMARY AND CONCLUSIONS

This chapter has demonstrated the use of the eLoran GRI selection procedure developed in Chapter 10 through a case study involving the integration of two new transmitter stations, Tullamore and Mizen

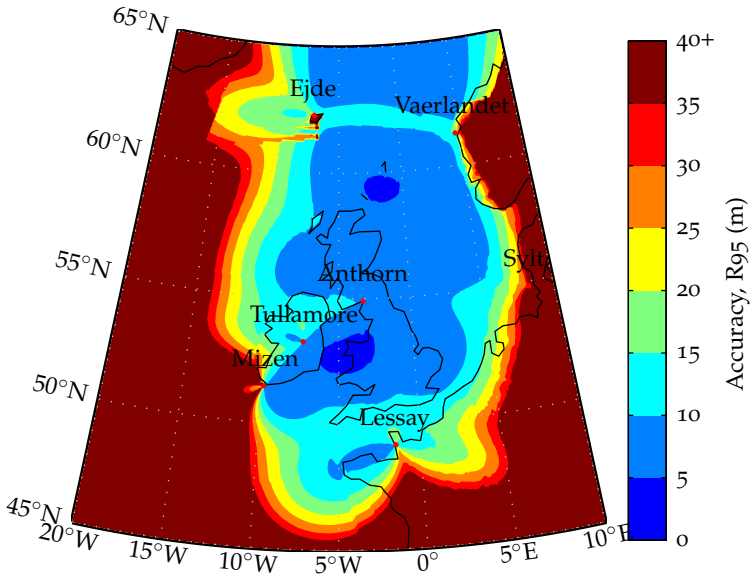

Figure 99: Average positioning accuracy for all North-West European stations on GRI 14251.

Head, Ireland, into the existing North-West European network. The objective of the case study was to investigate options for improving eLoran coverage on the West Coast of Britain and over Ireland while demonstrating the usefulness of the analysis techniques developed.

The key results are summarised in Table 25. The first part of the case study investigated the feasibility of including the new stations into one of the existing chains in North-West Europe. It has been determined that there is not enough space for the new stations in the 6731 Lessay GRI, however, it would be possible to integrate them into either the 7499 Sylt or 9007 Ejde chain (although the former does not leave any space for signal simulator slots to support the two-way Loran time transfer method currently in use in Europe; also, given the location of most of the stations in the 7499 Sylt chain to the east of the coverage area, it may be desirable to keep this GRI as an option for a possible future extension to the Baltic region). Both GRIs provide a similar level of coverage and performance, with GRI 7499 achieving slightly better accuracy results in the southern part of the coverage area and GRI 9007 performing better in the north.

The second part of the case study considered the option of putting the additional stations on a new GRI. A range of candidate GRIs have been identified (Table 23 and Table 24), with the optimum one determined to be 8581. As a consequence of the additional CRI introduced in the system, the coverage and performance is slightly worse when the new stations operate on the new GRI than if they were integrated into an existing chain. It therefore seems preferable to use one of the existing GRIs for the new stations.

Finally, the possibility of eliminating CRI within the North-West European system by moving all stations to a single GRI has been explored. Although this would seem to result in slight accuracy improvements in some parts of the coverage area, the net effect of such a change has been

found to be negative due to the long GRI required, and consequently a poor performance with respect to noise.

Unfortunately, none of the cases studied provides full 10 m accuracy coverage of Ireland. Further work should therefore investigate the possibility of using transmitter locations further west. Alternative transmission schemes could also be considered, such as that proposed by Helwig et al. [155], that would allow the elimination of CRI while keeping the signal duty cycle high enough to provide satisfactory performance. Lastly, the possibility of designing new signal waveforms could be explored, with the aim of increasing the average signal power available at the receiver while maintaining mutual interference at a minimum. The changes proposed above would, however, represent a significant departure from the current signal specification, the full implications of which would have to be carefully studied.

12 CONCLUSIONS

This thesis posed the following questions:

1. What is the effect on accuracy performance within a coverage region when a new eLoran station is installed, given the increase in CRI and a modern eLoran receiver's ability to cope with such interference through blanking or cancelling of interfering pulses?
2. What is the best method for selecting a GRI for a new station installation given modern eLoran technology, including receiver signal processing techniques?

Prior to this research it was not possible to accurately quantify the effects of CRI on the coverage and performance of eLoran systems, and GRI selection procedures were only available for the precursor of eLoran, Loran-C. In this work, analytical models of the pseudorange and positioning error due to CRI have been developed, validated and integrated into a coverage prediction tool. A review of existing GRI selection methods has also been carried out and a new procedure has been proposed, implementing several important eLoran updates.

Tools developed as part of this work have been used to assess the impact of CRI within the North-West European region and suggest optimal GRIs for two new stations in Ireland. This is the first time that the impact of CRI can be accurately modelled and optimal eLoran GRI selection can be performed.

12.1 REVIEW OF THESIS

Chapter 1 established the motivation for this research, which stems from concerns about the growing reliance of our society on GNSS and the lack of adequate backup solutions. The basics of the eLoran system, one of the potential backups to GNSS, were explained and the aims of this research were defined as outlined above. The chapter also presented a literature review on CRI and the GRI selection for Loran system design.

The problems studied in this work are closely related to the structure of the eLoran radio signal. In order to enable rigorous analysis of the problems in hand, it was necessary to develop a mathematical model of the received eLoran signal. This was achieved in Chapter 2, which dealt with the idealised transmitted signal and its characteristics, and Chapter 3, which described the effects of the LF radio channel on the signal. Time domain, spectral and correlation properties of the eLoran signal were studied, and the following channel effects and impairments were considered in developing the signal model: transmitter synchronisation error and pulse-to-pulse timing and amplitude stability; ground wave and sky wave propagation; signal re-radiation; external noise including atmospheric noise and vessel's topside noise; narrow-band interference (CWI); frequency offsets due to receiver movement and clock drift; and receiver's internal noise.

The resulting signal model consists of a superposition of waveforms from multiple eLoran stations, a white Gaussian noise process representing the external noise at the receiving antenna, and an ensemble of

harmonic signals to represent CWI. The validity of the model was demonstrated by comparison with captured real-world eLoran RF signals.

The next step towards answering the research questions was to develop a signal processing model of an eLoran receiver which would enable the assessment of the measurement error under noise and CRI conditions. Background information on eLoran receiver equipment and signal processing was provided in Chapter 4. In Chapter 5, an optimal receiver structure was proposed based on the principles of maximum likelihood estimation and the model of the received signal developed earlier. The following aspects of eLoran signal processing were considered in the development of the receiver model: the effects of the receiving antenna and input bandpass filter on the carrier phase and envelope of the eLoran pulses; channel sharing including modern CRI mitigation algorithms (CRI blanking and cancelling); sky wave rejection; carrier phase estimation; signal time of arrival calculation and pseudorange formation; and position estimation.

The signal processing model was used in Chapter 6, along with the results of Chapters 2 and 3, to determine bounds on the pseudorange measurement error under noise and interference conditions. Analytical models for the pseudorange error were derived that enable the effects of the following factors to be quantified: AWGN; uncompensated CRI due to single or multiple interferers including the effects of sky wave borne CRI; signal loss due to CRI blanking; and residual error after CRI cancelling. At the end of the chapter the different approaches to mitigating CRI were discussed and an optimal strategy for receiver CRI mitigation was suggested.

Chapter 7 was concerned with modelling the positioning performance of eLoran based on the pseudorange error estimates obtained using the models developed in Chapter 6. The techniques described in this chapter form the basis of the eLoran coverage and performance model presented in Chapter 9.

The analytical error models derived in this work were validated in Chapter 8 against computer simulations and results of receiver test bench and field experiments. The results of the tests were used to refine and calibrate the analytical models to ensure that they accurately describe the performance of a commercially available state-of-the-art eLoran receiver. This chapter also detailed the design of an eLoran signal simulator used in the receiver testing, which was developed as part of this project. The revised receiver performance model assumes that the receiver mitigates CRI by SIR-sensitive blanking, whereby all cross-rating signals that produce SIR less than 10 dB are blanked. Weaker interference is left uncompensated.

The experiments described in Chapter 8 showed that residual CRI is a significant contributor to the measurement error in eLoran, which should be taken into account when evaluating the system's performance. A methodology for a system-wide evaluation of the effects of CRI was then presented in Chapter 9. This chapter provided an overview of existing Loran coverage and performance models and described several major improvements to the traditional modelling techniques. These improvements were implemented in a coverage prediction tool developed on previous work by the GLA, and can be summarised under the following headings: integration of the pseudorange error models developed in Chapter 6 to take into account the effects of CRI; modelling of daytime vs. night-time radio conditions; improved atmospheric noise

model to appropriately take into account the non-stationary nature of the noise; modelling of noise sources local to the receiver (vessel's topside noise); and improved estimation of the R95 position error for elliptical distributions of position fixes. The updated model was used to assess the impact of CRI throughout the existing North-West European transmission network and was validated against receiver data collected from GLA' vessels. Chapter 9 therefore provides a tool to answer the first research question outlined above.

It was shown in Chapter 9 that effective receiver CRI mitigation is vital to meeting the stringent accuracy requirement for maritime HEA operations. The results also suggest that in order to provide full eLoran coverage throughout the GLA' service area, one or more new eLoran transmitters in Ireland are needed.

Chapter 10 focused on answering the second research question outlined above. A review of existing Loran-C GRI selection techniques was conducted and a new GRI selection procedure was proposed that takes into account the results of this research and all relevant eLoran updates. Chapter 11 then demonstrated the use of the procedure through a case study involving the addition of two new eLoran stations to the North-West European system to improve coverage off the West Coast of Britain and over Ireland.

The first part of the case study investigated the feasibility of including the new stations, Tullamore and Mizen Head, Ireland, into one of the existing chains in North-West Europe. It was determined that it would be possible to integrate the stations into either the 7499 Sylt or 9007 Ejde chain. The results suggest that both GRIs would provide a similar level of coverage and performance, with GRI 7499 achieving slightly better results in the southern part of the coverage area and GRI 9007 performing better in the north.

The second part of the case study considered the option of putting the additional stations on a new GRI. A range of candidate GRIs were identified, with the optimum one determined to be 8581. The predicted coverage and performance is slightly worse when the new stations operate on the new GRI than if they were integrated into an existing chain, and it therefore seems preferable to use one of the existing GRIs for the new stations.

Finally, the possibility of eliminating CRI within the North-West European system by moving all stations to a single GRI was explored, but was not considered viable due to the long GRI required.

None of the cases studied provided full 10 m accuracy coverage of Ireland. This is a consequence of poor receiver-transmitter geometry on the North-West of Ireland (even after the intended addition of the two stations) and relatively high levels of CRI within the system (first two cases) or low signal duty cycle (last case). Suggestions for further work in relation to this issue are given below.

12.2 CONTRIBUTION TO KNOWLEDGE

The candidate claims to have made the following contributions to knowledge:

- Presented a theoretical framework for the analysis of the eLoran navigation signal.

- Developed a signal processing model for an eLoran navigation receiver implementing state-of-the-art CRI mitigation algorithms.
- Derived analytical models of the pseudorange measurement error in an eLoran receiver due to the following factors: AWGN; uncompensated CRI from single or multiple interferers including the effects of sky wave borne CRI; signal loss due to CRI blanking; residual error after CRI cancelling.
- Analysed the pseudorange measurement error under CRI conditions and demonstrated the impact of non-coprime GRIs and sub-periodic CRI on the pseudorange error statistics.
- Established a relation between sub-periodic CRI and Farey sequences and designed a mathematically rigorous procedure for identifying pairs of GRIs that give rise to this kind of interference.
- Demonstrated analytically that the pseudorange measurement error due to uncompensated CRI does not average out with increasing integration time (a consequence of the current signal phase codes being unbalanced).
- Calculated the autocorrelation function and PSD of an amplitude-jittered eLoran signal to enable the analysis of residual measurement error after CRI cancelling.
- Presented a theoretical framework for eLoran accuracy modelling allowing the accurate estimation of the R95 position error from the covariance matrix of the position fix coordinates for elliptical distributions of the position fixes.
- Conducted numerical experiments to verify the analytical pseudorange and position error models derived in this work.
- Designed and implemented a hardware eLoran signal simulator and conducted tests with a state-of-the-art commercially available eLoran receiver to validate the analytical performance models derived in this thesis. This work was presented to the RTCM Special Committee 127 on eLoran systems and there are plans to use the simulator in the development of the MPS for marine eLoran receivers.
- Validated the analytical models and results obtained using the signal simulator through a field experiment involving the use of real off-air signals.
- Integrated the new performance models into a coverage prediction tool originally developed by the GLA.
- Reviewed the atmospheric noise and sky wave propagation models used in the GLA coverage prediction tool and modified the models so that the effects of daytime vs. night-time radio conditions, and the probability distribution and non-stationary nature of atmospheric noise is appropriately taken into account.
- Generated sample plots of the blanking loss distribution for selected stations in North-West Europe.

- Generated daytime, night-time and average accuracy coverage plots for the North-West European system that accurately represent the effects of CRI. To the best of the author's knowledge this is the first time such plots could be created.
- Generated an average accuracy plot for the North-West European system, assuming the receiver is equipped with synchronised atomic clock.
- Reviewed existing GRI selection methods for Loran-C and proposed a new GRI selection procedure for eLoran.
- Generated plots showing time left in an existing GRI after the addition of a new station into the existing chain.
- Identified candidate GRIs for two new eLoran stations in Ireland.
- Generated accuracy coverage plots for the North-West European system after the intended extension with two Irish stations and discussed the effects of different GRI configurations.

During this work, the candidate has presented aspects of this study at numerous international conferences [44, 40, 45, 46, 41, 42] and actively participated in the meetings of the European eLoran Forum and the RTCM Special Committee 127 on eLoran systems. He was awarded the Best Student Paper Award for his presentations at the 2008 and 2009 Conventions of the International Loran Association and his work was also positively received within RTCM, where he is currently leading work on receiver testing.

12.3 CONCLUSIONS

In summary, the following general conclusions can be drawn from this research:

- The effects of CRI are a function of a great number of parameters, including: Signal-to-Interference Ratio; Signal-to-Noise Ratio; GRIs and phase codes of the cross-rating signals; CRI mitigation algorithms used in the receiver; receiver integration time; the number of cross-rating GRIs and the number of stations within each GRI; and the time offset between the cross-rating signals (i.e. the position within the coverage area).
- Uncompensated CRI can introduce substantial measurement errors in linear receivers, including a position-dependent bias in the pseudorange measurements.
- State-of-the-art receiver signal processing can significantly mitigate the effects of CRI, however, a combination of several CRI mitigation techniques is required to achieve optimum results, and the residual impact on the measurement error generally cannot be considered negligible.
- The basic principles of GRI selection that applied to Loran-C apply equally to eLoran and can be used, when introducing a new eLoran station, to determine a set of candidate permissible GRIs. The differences in performance between the different candidate GRIs when receiver CRI mitigation is applied are subtle and no

general rule can be given for the selection of the best GRI. It is proposed that the best GRI for a particular station's configuration is found through coverage and performance modelling, taking into account CRI and modern receiver signal processing algorithms.

12.4 SUGGESTIONS FOR FUTURE WORK

Based on the findings of this research, several areas for follow-on work can be identified.

Firstly, given the impact of residual CRI on the positioning accuracy of eLoran, it would be desirable to also investigate the effect on the remaining system performance metrics - i.e. availability, continuity and integrity of the positioning service. This could be achieved by integrating the pseudorange error models developed by the candidate in the corresponding modules of the GLA' coverage prediction tool. Also the impact of CRI on the Eurofix message error rates may be worth investigating as CRI is expected to be a major source of error in Eurofix.

As far as GRI selection for new eLoran stations is concerned, the proposed method ensures (through the use of the measurement error models developed in this work) that the selected GRI achieves the best coverage and/or performance of all available GRIs. The author does not believe that any further improvements in coverage and performance can be achieved through the GRI selection alone, given the constraints of the current signal specification. However, it may be worth exploring the benefits of alternative transmission schemes, such as that proposed by Helwig et al. [155], that would allow the elimination of CRI within the system while keeping the signal duty cycle high enough to provide satisfactory performance with respect to noise.

Regarding eLoran coverage in Ireland, further work should investigate the possibility of using transmitter locations further west of the sites considered in Chapter 11.

Lastly, given that there does not seem to be a requirement for the backward compatibility with Loran-C any more, it may be worth opening some of the degrees of freedom in the signal design process and exploring the possibility of designing new signal waveforms, with the main aim of increasing the average signal power available at the receiver while maintaining mutual interference at a minimum.

Part III

APPENDIX

A MATHEMATICAL TOOLS AND IDENTITIES

This appendix gives definitions of the various mathematical functions and tools used throughout this thesis. It does not aim to explain the underlying concepts. For more information, the reader is referred to the literature cited throughout.

A.1 BASIC SIGNAL CHARACTERISTICS

The definitions given in this and the following section are in line with those used in reference [48].

A.1.1 *Continuous-Time Signals*

In the following, $s(t)$, $t \in \mathbb{R}$, is assumed to be a complex continuous-time signal.

Fourier Series (FS)

Assuming further that $s(t)$ is periodic in T_0, it can be expressed as Fourier series

$$s(t) = \sum_{n=-\infty}^{\infty} c_s[n] \exp\left(\mathrm{j}n\frac{2\pi}{T_0}t\right) \mathrm{d}t,$$

with coefficients given by

$$c_s[n] = \frac{1}{T_0}\int_{T_0} s(t) \exp\left(-\mathrm{j}n\frac{2\pi}{T_0}t\right) \mathrm{d}t,$$

where $\mathrm{j} = \sqrt{-1}$ is the imaginary unit.

The power spectrum of $s(t)$ is then given by

$$\left\{|c_s[n]|^2\right\}_{n=-\infty}^{\infty}.$$

The Fourier coefficients of the complex conjugate of $s(t)$, and its real and imaginary parts can be calculated as folows:

$$c_{s^*}[n] = \left\{\frac{1}{T_0}\int_{T_0} s(t) \exp\left[-\mathrm{j}(-n)\frac{2\pi}{T_0}t\right] \mathrm{d}t\right\}^* = c_s^*[-n],$$

$$c_{\mathrm{Re}[s]}[n] = \frac{1}{2T_0}\int_{T_0} [s(t) + s^*(t)] \exp\left(-\mathrm{j}n\frac{2\pi}{T_0}t\right) \mathrm{d}t = \frac{1}{2}\left(c_s[n] + c_s^*[-n]\right), \quad \text{(A.1)}$$

$$c_{\mathrm{Im}[s]}[n] = \frac{1}{2\mathrm{j}T_0}\int_{T_0}[s(t) - s^*(t)]\exp\left(-\mathrm{j}n\frac{2\pi}{T_0}t\right)\mathrm{d}t$$
$$= \frac{1}{2\mathrm{j}}\left(c_s[n] - c_s^*[-n]\right). \quad \text{(A.2)}$$

Fourier Transform (FT)

Throughout this work, S_s denotes the frequency spectrum (Fourier transform) of signal $s(t)$:

$$S_s(f) = \mathcal{F}_{t,f}\{s(t)\} = \int_{-\infty}^{\infty} s(t)\,\mathrm{e}^{-\mathrm{j}2\pi ft}\,\mathrm{d}t.$$

For clarity, the signal and fourier transform variables, respectively, may be shown in subscript. The expression for the inverse Fourier transform is as follows:

$$s(t) = \mathcal{F}_{f,t}^{-1}\{S_s(f)\} = \int_{-\infty}^{\infty} S_s(f)\,\mathrm{e}^{\mathrm{j}2\pi ft}\,\mathrm{d}f.$$

Theorem A.1. The Fourier transform of a periodic signal $s(t)$ can be expessed as

$$\mathcal{F}\{s(t)\} = \sum_{n=-\infty}^{\infty} c_s[n]\,\delta\left(f - \frac{n}{T_0}\right), \quad \text{(A.3)}$$

where T_0 is the period of $s(t)$ and $\{c_s[n]\}_{n=-\infty}^{\infty}$ are the complex coefficients of its Fourier series representation

$$c_s[n] = \frac{1}{T_0}\int_{T_0} s(t)\exp\left(-jn\frac{2\pi}{T_0}t\right)\mathrm{d}t.$$

Laplace Transform

The Laplace transform of signal $s(t)$ is calculated as

$$L_s(p) = \mathcal{L}\{s(t)\} = \int_0^{\infty} s(t)\,\mathrm{e}^{-pt}\,\mathrm{d}t,$$

where p is a complex variable. The inverse Laplace transform is given by

$$s(t) = \mathcal{L}^{-1}\{L_s(p)\} = \frac{1}{2\pi\mathrm{j}}\lim_{T\to\infty}\int_{c-\mathrm{j}T}^{c+\mathrm{j}T} L_s(p)\,\mathrm{e}^{pt}\,\mathrm{d}p,$$

where c is a real number so that the contour path of integration is in the region of convergence of $L_s(p)$.

Time-Averaged Characteristics

Signal energy

$$E_s = \int_{-\infty}^{\infty} |s(t)|^2\,\mathrm{d}t;$$

(Time-averaged) signal power

$$P_s^{\mathrm{t}} = \mathrm{Av}\left[|s(t)|^2\right],$$

where Av [.] is the time-averaging operator defined as

$$\mathrm{Av}\left[s\left(t\right)\right] = \mu_s^{\mathrm{t}} = \lim_{T\to\infty} \frac{1}{2T} \int_{-T}^{T} s\left(t\right) \mathrm{d}t;$$

(Time-averaged) signal variance

$$\mathrm{var}^{\mathrm{t}}[s\left(t\right)] = \mathrm{Av}\left[\left|s\left(t\right) - \mu_s^{\mathrm{t}}\right|^2\right] = P_s^{\mathrm{t}} - \left|\mu_s^{\mathrm{t}}\right|^2;$$

Root-Mean-Squared (RMS) value

$$\mathrm{rms}\left[s\left(t\right)\right] = \sqrt{\mathrm{Av}\left[\left|s\left(t\right)\right|^2\right]} = \sqrt{P_s^{\mathrm{t}}}$$

Mutual power

$$P_{s_1 s_2}^{\mathrm{t}} = \mathrm{Av}\left[s_1\left(t\right) s_2^*\left(t\right)\right];$$

The following identity holds for the power of the sum of M signals

$$\mathrm{Av}\left[\left|\sum_{m=1}^{M} s_m\left(t\right)\right|^2\right] = \sum_{m=1}^{M} \underbrace{\mathrm{Av}\left[\left|s_m\left(t\right)\right|^2\right]}_{P_{s_m}^{\mathrm{t}}} + \sum_{m=1}^{M} \sum_{\substack{n=1 \\ n\neq m}}^{M} \underbrace{\mathrm{Av}\left[s_m\left(t\right) s_n^*\left(t\right)\right]}_{P_{s_m s_n}^{\mathrm{t}}}. \quad \text{(A.4)}$$

For energy signals[1], the (time-averaged) energy autocorrelation function is defined as

$$R_s^{\mathrm{t}}(\alpha) = \int_{-\infty}^{\infty} s^*\left(t\right) s\left(t+\alpha\right) \mathrm{d}t;$$

The ESD is defined as

$$D_s^{\mathrm{t}}(f) = \left|\mathcal{F}\left\{s\left(t\right)\right\}\right|^2 = \left|S_s\left(f\right)\right|^2.$$

The following identity holds

$$D_s^{\mathrm{t}}(f) = \mathcal{F}_{\tau,f}\left\{R_s^{\mathrm{t}}(\tau)\right\}.$$

For power signals[2], the (time-averaged) power autocorrelation function is defined as[3]

$$R_s^{\mathrm{t}}(\alpha) = \mathrm{Av}\left[s^*\left(t\right) s\left(t+\alpha\right)\right];$$

The (time-averaged) PSD is defined as

$$D_s^{\mathrm{t}}(f) = \lim_{T\to\infty} \lim_{U\to\infty} \frac{1}{2U} \int_{-U}^{U} \frac{1}{2T} \left|S_{s_T}\left(u, f\right)\right|^2 \mathrm{d}u,$$

1 Signals with finite energy.
2 Signals with a non-zero, finite power.
3 Both the energy and the power autocorrelation functions are denoted by the same symbol; it should always be clear from the context which definition applies.

where

$$S_{s_T}(u,f) = \int_{u-T}^{u+T} s(t)\, \mathrm{e}^{-\mathrm{j}2\pi f t}\, \mathrm{d}t.$$

The following identity holds

$$D_s^{\mathrm{t}}(f) = \mathcal{F}_{\alpha,f}\left\{R_s^{\mathrm{t}}(\alpha)\right\}.$$

Ensemble-Averaged Characteristics

The ensemble-averaging operator (or statistical expectation) $\mathrm{E}[\centerdot]$ for a measureable function of a random variable X, $g(X)$, given that X has a PDF $f_X(x)$ is defined as follows

$$\mathrm{E}[g(X)] = \int_{-\infty}^{\infty} g(x)\, f_X(x)\, \mathrm{d}x.$$

For a random signal $s(t)$, the following ensemble-averaged characteristics can then be defined:

The expected value

$$\mu_s^{\mathrm{e}}(t) = \mathrm{E}[s(t)];$$

Variance

$$\mathrm{var}[s(t)] = \mathrm{E}\left[|s(t) - \mu_s^{\mathrm{e}}(t)|^2\right];$$

(Probabilistic) power (or mean-squared value)

$$P_s^{\mathrm{e}}(t) = \mathrm{E}\left[|s(t)|^2\right];$$

(Ensemble-averaged) autocorrelation function

$$R_s^{\mathrm{e}}(t+\tau, t) = \mathrm{E}[s^*(t)\, s(t+\tau)];$$

Instantaneous (ensemble-averaged) power spectral density

$$D_s^{\mathrm{e}}(f,t) = \mathcal{F}_{\tau,f}\left\{R_s^{\mathrm{e}}(t+\tau,t)\right\}.$$

Average Characteristics

The combination of the time- and the ensemble-averaging operators, $\mathrm{Av}[\mathrm{E}[(\centerdot)]]$, will be denoted $\mathrm{AvE}[(\centerdot)]$. The following average characteristics can then be defined:

Average expected value:

$$\mu_s^{\mathrm{a}} = \mathrm{AvE}[s(t)];$$

Average variance

$$\mathrm{var}^{\mathrm{a}}[s(t)] = \mathrm{AvE}\left[|s(t) - \mu_s^{\mathrm{a}}|^2\right];$$

Average power

$$\begin{aligned} P_s^{\mathrm{a}} = \mathrm{E}\left[P_s^t\right] &= \mathrm{AvE}\left[|s(t)|^2\right] \\ &= \mathrm{var}^{\mathrm{a}}[s(t)] + |\mu_s^{\mathrm{a}}|^2; \end{aligned}$$

Average autocorrelation function

$$R_s^{\mathrm{a}}(\tau) = \mathrm{AvE}\left[s^*(t)\, s(t+\tau)\right];$$

Average power spectral density

$$D_s^{\mathrm{a}}(f) = \mathcal{F}_{\tau,f}\left\{R_s^{\mathrm{a}}(\tau)\right\};$$

Average energy

$$E_s^{\mathrm{a}} = \mathrm{E}\left[\int_{-\infty}^{\infty} |s(t)|^2 \,\mathrm{d}t\right].$$

A.1.2 *Discrete-Time Signals*

In the following, $s[k]$, $k \in \mathbb{Z}$, is assumed to be a complex discrete-time signal.

Discrete Fourier Series (DFS)

$$c_s^{\mathrm{d}}[n] = \frac{1}{N_0} \sum_{k=k_0}^{k_0+N_0-1} s[k]\, \mathrm{e}^{-\mathrm{j}n\frac{2\pi}{N_0}k};$$

$$s[k] = \sum_{n=0}^{N_0-1} c_s^{\mathrm{d}}[n]\, \mathrm{e}^{\mathrm{j}n\frac{2\pi}{N_0}k}.$$

Time-Averaged Characteristics

The time-averaging operator for discrete-time signals is defined as[4]

$$\mathrm{Av}\left[s[k]\right] = \mu_s^{\mathrm{t}} = \lim_{N\to\infty} \frac{1}{2N+1} \sum_{k=-N}^{N} s[k].$$

The (time-averaged) signal variance and RMS value are defined using the operator in the same manner as for continuous-time signals.

For energy signals, the (discrete, time-averaged) energy autocorrelation function is defined as

$$R_s^{\mathrm{t}}[l] = \sum_k s[k]\, s^*[k-l].$$

A.2 BANDPASS SIGNALS AND SYSTEMS

This section defines some equivalent representations of bandpass signals and systems commonly used in RF signal analysis. A *bandpass signal* is defined here as a signal whose spectrum is non-negligible only in a band of frequencies of total extent B, say, centered about frequency $\pm f_{\mathrm{c}}$. Analogically, a *bandpass system* will be defined as an LTI system whose magnitude response is non-negligible only at frequencies within $B/2$ of $\pm f_{\mathrm{c}}$.

4 The time-averaging operator and characteristics for both continuous- and discrete- time signals are denoted by the same symbols; it should always be clear from the context which definition applies.

A.2.1 *Complex Envelope*

The complex envelope $s(t)$ of a real signal $\tilde{s}(t)$ can be calculated as follows:

$$s(t) = \left[2\tilde{s}(t)\,\mathrm{e}^{-\mathrm{j}2\pi f_0 t}\right]_{\mathrm{LP}}.$$

The complex envelope can be described in terms of its *inphase*, $s_{\mathcal{I}}(t) = \mathrm{Re}[s(t)]$, and *quadrature*, $s_{\mathcal{Q}}(t) = \mathrm{Im}[s(t)]$, components

$$s(t) = s_{\mathcal{I}}(t) + j s_{\mathcal{Q}}(t),$$

or equivalently by its *envelope*, $A(t) = |s(t)|$, and *phase*, $\phi(t) = \angle s(t)$:

$$s(t) = A(t) \cdot \exp(j\phi(t)).$$

The bandpass signal can be reconstructed from the complex envelope by the following operation:

$$\tilde{s}(t) = \mathrm{Re}\left[s(t)\,\mathrm{e}^{\mathrm{j}2\pi f_0 t}\right]. \tag{A.5}$$

The spectrum of the complex envelope $s(t)$ of a bandpass signal $\tilde{s}(t)$ can be obtained as

$$S_s(f) = 2\mathrm{u}(f + f_0)\, S_{\tilde{s}}(f + f_0),$$

where $f_0 > 0$ is a real constant.

Assuming $\tilde{s}(t)$ is a WSS process, the following identities for the PSD of the complex envelope and its components hold [156]:

$$D^{\mathrm{e}}_{\tilde{s}}(f) = 4D^{\mathrm{e}}_{\tilde{s}}(f + f_0)\,\mathrm{u}(f + f_0); \tag{A.6}$$

$$D^{\mathrm{e}}_{s_{\mathcal{I}}}(f) = D^{\mathrm{e}}_{s_{\mathcal{Q}}}(f) = D^{\mathrm{e}}_{\tilde{s}}(f + f_0)\,\mathrm{u}(f + f_0) + D^{\mathrm{e}}_{\tilde{s}}(f - f_0)\,\mathrm{u}(-f + f_0). \tag{A.7}$$

A.2.2 *Equivalent Lowpass System*

Let $\widetilde{H}(f)$ be the frequency response of a bandpass system and $S_{\tilde{x}}(f)$, $S_{\tilde{y}}(f)$ the spectrum of its input and output signals, respectively, so that

$$S_{\tilde{y}}(f) = \widetilde{H}(f)\, S_{\tilde{x}}(f).$$

The spectrum of the complex envelope of the output signal can then be written as

$$\begin{aligned} S_y(f) &= 2\mathrm{u}(f + f_0)\, S_{\tilde{y}}(f + f_0) \\ &= 2\mathrm{u}(f + f_0)\, \widetilde{H}(f + f_0)\, S_{\tilde{x}}(f + f_0) \\ &= \widetilde{H}(f + f_0)\, S_x(f); \end{aligned}$$

This equation can be rewritten as

$$S_y(f) = H(f)\, S_x(f), \tag{A.8}$$

where

$$H(f) = \widetilde{H}(f + f_0).$$

The system having such frequency response will be referred to as the *equivalent lowpass system*.

A.2.3 *Band-Limited White Noise*

White noise will be defined here as a strict-sense stationary random signal, $w(t)$, whose power spectral density is constant over the whole range of frequencies

$$D^{\mathrm{e}}_{w}(f) = \frac{N_0}{2},$$

say. Consequently, the signal is *zero-mean*[5]

$$\mathrm{E}[w(t)] = 0,$$

and its autocorrelation function is given by

$$R^{\mathrm{e}}_{w}(\tau) = \mathcal{F}^{-1}_{f,\tau}\{D^{\mathrm{e}}_{w}(f)\} = \frac{N_0}{2}\delta(\tau),$$

i.e. the noise values at arbitrarily close time-instants are uncorrelated.

White noise is a useful mathematical model, however, it clearly is an idealisation (note that such process would have to have infinite power; also, in any practical system only a limited bandwidth is available, which makes the existence of such process impossible in the physical world). In practical systems, the spectrum of the noise is always limited to a certain range of frequencies. *Band-limited white noise* will be defined here as a WSS stochastic process, $\widetilde{w}_{\mathrm{b}}(t)$, whose PSD is given by the following expression

$$D^{\mathrm{e}}_{\widetilde{w}_{\mathrm{b}}}(f) = \begin{cases} \frac{N_0}{2} & \text{for } |f - f_0| < \frac{B}{2} \text{ or } |f + f_0| < \frac{B}{2}, \\ 0 & \text{otherwise.} \end{cases}$$

Its basic statistical characteristics are as follows:

$$\mathrm{E}[\widetilde{w}_{\mathrm{b}}(t)] = 0,$$

$$R^{\mathrm{e}}_{\widetilde{w}_{\mathrm{b}}}(\tau) = \mathcal{F}^{-1}_{f,\tau}\left\{D^{\mathrm{e}}_{\widetilde{w}_{\mathrm{b}}}(f)\right\} = N_0 B \mathrm{sinc}(B\tau)\cos(2\pi f_0 \tau), \tag{A.9}$$

$$P^{\mathrm{e}}_{\widetilde{w}_{\mathrm{b}}} = \mathrm{var}[\widetilde{w}_{\mathrm{b}}(t)] = R^{\mathrm{e}}_{\widetilde{w}_{\mathrm{b}}}(0) = N_0 B.$$

5 Non-zero mean implies the presence of a Dirac delta in the PSD of a signal.

Complex Envelope of Band-Limited White Noise

For a given $f_0 > 0$ the band-limited white noise, $\widetilde{w}_\mathrm{b}(t)$, can also be expressed in terms of its complex envelope, $w_\mathrm{b}(t)$:

$$w_\mathrm{b}(t) = w_{\mathrm{b},\mathcal{I}}(t) + \mathrm{j} w_{\mathrm{b},\mathcal{Q}}(t),$$

$$\widetilde{w}_\mathrm{b}(t) = w_{\mathrm{b},\mathcal{I}}(t)\cos(2\pi f_0 t) - w_{\mathrm{b},\mathcal{Q}}(t)\sin(2\pi f_0 t),$$

where the latter follows from Equation A.5.

It can be shown (see e.g. [48]) that $w_{\mathrm{b},\mathcal{I}}(t)$, $w_{\mathrm{b},\mathcal{Q}}(t)$ are WSS signals and that

$$\mathrm{E}\left[w_{\mathrm{b},\mathcal{I}}(t)\, w_{\mathrm{b},\mathcal{Q}}(t+\tau)\right] = 0, \forall\tau.$$

Further, from Equation A.6 and Equation A.7 it follows that

$$D^\mathrm{e}_{w_\mathrm{b}}(f) = \begin{cases} 2N_0 & \text{for } |f| < \frac{B}{2}, \\ 0 & \text{otherwise,} \end{cases}$$

and

$$D^\mathrm{e}_{w_{\mathrm{b},\mathcal{I}}}(f) = D^\mathrm{e}_{w_{\mathrm{b},\mathcal{Q}}}(f) = \begin{cases} N_0 & \text{for } |f| < \frac{B}{2}, \\ 0 & \text{otherwise.} \end{cases}$$

The basic statistical characteristics of the complex envelope are then as follows:

$$\mathrm{E}\left[w_{\mathrm{b},\mathcal{I}}(t)\right] = \mathrm{E}\left[w_{\mathrm{b},\mathcal{Q}}(t)\right] = \mathrm{E}\left[w_\mathrm{b}(t)\right] = 0,$$

$$R^\mathrm{e}_{w_{\mathrm{b},\mathcal{I}}}(\tau) = R^\mathrm{e}_{w_{\mathrm{b},\mathcal{Q}}}(\tau) = \mathcal{F}^{-1}_{f,\tau}\left\{D^\mathrm{e}_{w_{\mathrm{b},\mathcal{I}}}(f)\right\} = N_0 B \mathrm{sinc}(B\tau); \quad \text{(A.10)}$$

$$P^\mathrm{e}_{w_{\mathrm{b},\mathcal{I}}} = P^\mathrm{e}_{w_{\mathrm{b},\mathcal{Q}}} = \mathrm{var}\left[w_{\mathrm{b},\mathcal{I}}(t)\right] = \mathrm{var}\left[w_{\mathrm{b},\mathcal{Q}}(t)\right] = N_0 B;$$

$$P^\mathrm{e}_{w_\mathrm{b}} = P^\mathrm{e}_{w_{\mathrm{b},\mathcal{I}}} + P^\mathrm{e}_{w_{\mathrm{b},\mathcal{Q}}} = 2N_0 B.$$

NOISE BANDWIDTH OF AN LTI SYSTEM In situations where a white noise process passes through an LTI system it is often sufficient to characterise the system by a single number, the *noise bandwidth*, defined as

$$B_\mathrm{n} = \frac{1}{2}\frac{1}{|H(f_0)|^2}\int_{-\infty}^{\infty} |H(f)|^2 df, \quad \text{(A.11)}$$

in which $|H(f_0)|^2$ is the system's gain at the passband center frequency f_0. Some authors also define the *double-sided noise bandwidth* $B_{\mathrm{n},2} = 2B_\mathrm{n}$.

Essentially, B_n is the bandwidth of a "brick wall" filter that, when driven by white noise, produces the same output power as the original system with frequency response $H(f)$ would produce.

Assuming that the white noise at the input of the system has a (double-sided) spectral density $N_0/2$, the power of the noise at the system's output is then calculated simply as

$$P_n = B_{\mathrm{n},2} \cdot \frac{N_0}{2} = B_{\mathrm{n}} \cdot N_0. \tag{A.12}$$

A.3 SELECTED NUMBER-THEORETI CONCEPTS

A.3.1 *Congruence Relation*

For a given positive integer p, two integers q and r are called *congruent modulo* p, written

$$q \equiv r \pmod{p}$$

if $(q - r)$ is divisible by p (or equivalently if q and r have the same remainder when divided by p).

A.3.2 *Farey Sequences*

Algorithm A.1 shows a MATLAB function to generate the numerators and denominators for the members of a Farey sequence of order n.

A.4 MISCELLANEOUS FUNCTION DEFINITIONS

The sinc function

$$\operatorname{sinc}(t) = \frac{\sin(\pi t)}{\pi t};$$

Four-quadrant arctan function

$$\operatorname{arctan2}(q, i) = \begin{cases} \arctan\left(\frac{q}{i}\right) & i > 0 \\ \pi + \arctan\left(\frac{q}{i}\right) & q \geq 0, i < 0 \\ -\pi + \arctan\left(\frac{q}{i}\right) & q < 0, i < 0 \\ \frac{\pi}{2} & q > 0, i = 0 \\ -\frac{\pi}{2} & q < 0, i = 0 \\ \text{undefined} & q = 0, i = 0 \end{cases}$$

PDF of the standard normal distribution

$$\mathcal{N}(x) = \frac{1}{\sqrt{2\pi}} \mathrm{e}^{-\frac{x^2}{2}};$$

PDF of the (general) normal distribution

$$\mathcal{N}\left(x; \mu, \sigma^2\right) = \frac{1}{\sigma\sqrt{2\pi}} \mathrm{e}^{-\frac{(x-\mu)^2}{2\sigma^2}};$$

CDF of the standard normal distribution

$$\Phi(x) = \frac{1}{\sqrt{2\pi}} \int_{-\infty}^{x} e^{-\frac{t^2}{2}} dt.$$

Algorithm A.1 Generating algorithm for a Farey sequence of order n.

```
function [a, b] = farey(n)
  a = 0;
  b = 1;
  c = 1;
  d = n;
  while (c(end) < n)
    k = floor((n+b(end))/d(end));
    a(end+1) = c(end);
    b(end+1) = d(end);
    c(end+1) = k*c(end) - a(end-1);
    d(end+1) = k*d(end) - b(end-1);
  end
```

B

THE STANDARD INPUT BANDPASS FILTER

B.0.1 *Filter Model*

Transfer Function

The *transfer function* of an LTI system is defined here as the ratio of the Laplace transform[1] of its output to the Laplace transform of its input.

The transfer function of a stable, causal, LTI system can be expressed as [48]

$$H_{\mathcal{L}}(p) = \frac{\sum_{i=0}^{N} b_i p^{N-i}}{\sum_{i=0}^{M} a_i p^{M-i}},$$

where p is a complex variable and a_i, b_i are assumed to be real constants. Finding the constants a_i, b_i so that the system implements a filter with given properties is a well-established process in the filter design theory. The constants a_i and b_i are then referred to as the *filter coefficients*, and the *order* of the filter is equal to the greater of M and N.

The coefficients of the standard eLoran input bandpass filter are given in Table 26.

Zero-Pole Gain Form

The transfer function can alternatively be expressed in the *zero-pole gain form*

$$H_{\mathcal{L}}(p) = K\frac{\prod_{i=1}^{N}(p - z_i)}{\prod_{i=1}^{M}(p - p_i)},$$

where z_i and p_i are the (generally) complex *zeros* and *poles* of the filter, and K is a real gain factor. This form of the transfer function becomes useful when calculating the *magnitude and phase response* of the filter. A well-known result [48] in the linear systems theory is that

1 See Appendix A.

i	a_i	b_i
0	1.000000000000000e+000	0
1	4.597251245337094e+005	0
2	1.653859219836248e+012	0
3	5.480338606948230e+017	0
4	9.815886629960719e+023	9.579693161374595e+020
5	2.121145362540722e+029	0
6	2.477562490235085e+035	0
7	2.665553213898303e+040	0
8	2.244151422009589e+046	0

Table 26: Transfer function coefficients of the standard front-end filter.

i	z_i	p_i
1	0	-3.802906376566507e+004 +7.077963427123667e+005i
2	0	-3.802906376566507e+004 -7.077963427123667e+005i
3	0	-8.569732144900445e+004 +6.513960219935830e+005i
4	0	-8.569732144900445e+004 -6.513960219935830e+005i
5	-	-7.684005507072748e+004 +5.840708362467017e+005i
6	-	-7.684005507072748e+004 -5.840708362467017e+005i
7	-	-2.929612198145763e+004 +5.452589661925297e+005i
8	-	-2.929612198145763e+004 -5.452589661925297e+005i

Table 27: Zeros and poles of the standard front-end filter; gain factor $k = 9.579693161374595e + 020$

the frequency response of a causal, stable LTI system, $H(f)$, can be obtained by substituting $p = \mathrm{j}2\pi f$ in the transfer function of the system, i.e. $H(f) = H_{\mathcal{L}}(\mathrm{j}2\pi f)$. Referring to the equation above, the magnitude response can thus be calculated as

$$|H(f)| = |K| \frac{\prod_{i=1}^{N} |\mathrm{j}2\pi f - z_i|}{\prod_{i=1}^{M} |\mathrm{j}2\pi f - p_i|},$$

and the phase response as

$$\angle H(f) = \angle K + \sum_{i=1}^{N} \angle(\mathrm{j}2\pi f - z_i) - \sum_{i=1}^{M} \angle(\mathrm{j}2\pi f - p_i).$$

Residue Form

By performing partial fraction expansion of the transfer function one obtains what is called the *residue form*. Provided that the degree of the polynomial in the numerator of the transfer function is less than that of the polynomial in the denominator and supposing that there are no multiple poles, the expansion takes the following form

$$H_{\mathcal{L}}(p) = \sum_{i=1}^{M} \frac{r_i}{p - p_i},$$

where p_i are the filter poles and r_i are (generally) complex constants called residues. Expanding the transfer function into the residue form proves useful when calculating the response of the system to a given waveform using the Laplace transform.

"Brick Wall" Approximation

When the input signal to the filter can be considered as a white noise process it is often sufficient to characterise the filter by its *noise bandwidth*, as described in Section A.2.3.

i	r_i
1	-4.680916656545348e+004 +1.687433074228402e+004i
2	-4.680916656545397e+004 -1.687433074228296e+004i
3	5.575386653013420e+004 -9.820837905542238e+004i
4	5.575386653012965e+004 +9.820837905541981e+004i
5	2.551482172972271e+004 +9.799159033860121e+004i
6	2.551482172972245e+004 -9.799159033859999e+004i
7	-3.445952169439862e+004 -1.678826213142560e+004i
8	-3.445952169439817e+004 +1.678826213142609e+004i

Table 28: Coefficients of the residue form of the transfer function of the standard front-end filter.

C

LIST OF LORAN STATIONS

This list was compiled by the author based on information obtained from open sources, however, it is often difficult to confirm the validity of the information, therefore it is assumed to be correct.

GRI	Station	Position	ED (μs)	PWR (kW)
4970				
	Inta	65.96658° N 60.30907° E	N.A.	700
	Isle of Pankratiev	76.12609° N 60.21532° E	N.A.	700
	Tumanny	69.05233° N 35.67064° E	N.A.	700
5543				
	Balasore	21.48556° N 86.92167° E	0.00	43
	Diamond Harbor	22.17167° N 88.20694° E	18510.68	11
	Patpur	20.44667° N 85.82972° E	36542.75	11
5930				
	Caribou	46.80760° N 67.92700° W	0.00	800
	Nantucket	41.25330° N 69.97740° W	13131.88	400
	Cape Race	46.77560° N 53.17430° W	28755.02	500
	FoxHarbour	52.37650° N 55.70770° W	41594.59	900
5960				
	Norilsk	69.36226° N 86.69638° E	0.00	700
	Taimylyr	72.58027° N 122.11113° E	1.00	700
	Isle of Pankratiev	76.12609° N 60.21532° E	2.00	700
	Inta	65.96658° N 60.30907° E	3.00	700

GRI	Station	Position	ED (μs)	PWR (kW)
5980				
	Petropavlovsk	53.12988° N 157.69525° E	0.00	700
	Attu	52.82890° N 173.18040° E	14467.56	400
	Alexandrovsk	51.07856° N 142.70138° E	31506.50	700
5990				
	Williams	51.96640° N 122.36710° W	0.00	400
	ShoalCove	55.43910° N 131.25530° W	13343.60	560
	George	47.06340° N 119.74420° W	28927.36	1400
	PortHardy	50.60830° N 127.35790° W	42268.63	350
6042				
	Dhrangadhra	23.00389° N 71.52750° E	0.00	11
	Veraval	20.95194° N 70.33694° E	13862.41	11
	Billamora	20.76111° N 73.03806° E	40977.61	11
6731				
	Lessay	49.14867° N 1.50473° W	0.00	250
	Soustons	43.73975° N 1.38044° W	13000.00	250
	Anthorn	54.91121° N 3.28728° W	27300.00	200
	Sylt	54.80833° N 8.29357° E	42100.00	250
6780				
	Hexian	23.96774° N 111.71953° E	0.00	1200
	Raoping	23.72387° N 116.89579° E	14464.69	1200
	Chongzuo	22.54318° N 107.22269° E	26925.76	1200

GRI	Station	Position	ED (μs)	PWR (kW)
7001				
	Bo	68.63506° N 14.46315° E	0.00	400
	JanMayen	70.91430° N 8.73237° W	14100.00	250
	Berlevag	70.84528° N 29.20444° E	29100.00	250
7030				
	Al Khamasin	20.46723° N 44.58136° E	0.00	1000
	Salwa	24.83379° N 50.57016° E	13620.00	1000
	Afif	23.81026° N 42.85505° E	27265.00	1000
	Ash Shaykh	28.15444° N 34.76126° E	41414.00	1000
	Al Muwassam	16.43223° N 42.80136° E	57554.00	1000
7270				
	ComfortCove	49.33150° N 54.86180° W	0.00	250
	CapeRace	46.77560° N 53.17430° W	12037.49	500
	FoxHarbour	52.37650° N 55.70770° W	26148.01	900
7430				
	Rongcheng	37.06438° N 122.32388° E	0.00	1200
	Xuancheng	31.06887° N 118.88601° E	13459.70	1200
	Helong	42.71988° N 129.10756° E	30852.32	1200
7499				
	Sylt	54.80833° N 8.29357° E	0.00	250
	Lessay	49.14867° N 1.50473° W	14100.00	250
	Vaerlandet	61.29707° N 4.69628° E	29500.00	250

GRI	Station	Position	ED (μs)	PWR (kW)
7950				
	Alexandrovsk	51.07856° N 142.70138° E	0.00	700
	Petropavlovsk	53.12988° N 157.69525° E	14506.50	700
	Ussurijsk	44.53325° N 131.63983° E	33678.00	700
	Okhotsk	59.41724° N 143.08970° E	64102.05	10
7960				
	Tok	63.32860° N 142.80870° W	0.00	560
	Kodiak	57.43900° N 152.36960° W	13804.45	400
	ShoalCove	55.43910° N 131.25530° W	29651.14	560
	PortClarence	65.24450° N 166.88670° W	47932.52	1000
7980				
	Malone	30.99410° N 85.16910° W	0.00	800
	Grangeville	30.72590° N 90.82860° W	12809.54	800
	Raymondville	26.53200° N 97.83320° W	27443.38	540
	Jupiter	27.03290° N 80.11470° W	45201.88	350
	CarolinaBeach	34.06280° N 77.91280° W	61542.72	600
7990				
	Sellia Marina	38.87242° N 16.71853° E	0.00	165
	Lampedusa	35.52248° N 12.52522° E	12755.98	325
	Kargabarun	40.97252° N 27.86724° E	32273.29	165
	Estartit	42.06018° N 3.20446° E	50999.71	165

GRI	Station	Position	ED (μs)	PWR (kW)
8000				
	Bryansk	53.13072° N 34.91244° E	0.00	450
	Petrozavodsk	61.75900° N 33.69456° E	13217.21	700
	Slonim	53.13200° N 25.39611° E	27125.00	450
	Simferopol	44.88894° N 33.87328° E	53070.25	550
	Syzran	53.28822° N 48.11483° E	67941.60	700
8290				
	Havre	48.74410° N 109.98160° W	0.00	400
	Baudette	48.61390° N 94.55500° W	14786.56	800
	Gillette	44.00310° N 105.62330° W	29084.44	540
	Williams	51.96640° N 122.36710° W	45171.62	400
8390				
	Xuancheng	31.06887° N 118.88601° E	0.00	1200
	Raoping	23.72387° N 116.89579° E	13795.52	1200
	Rongcheng	37.06438° N 122.32388° E	31459.70	1200
8830				
	Afif	23.81026° N 42.85505° E	0.00	1000
	Salwa	24.83379° N 50.57016° E	13645.00	1000
	Al Khamasin	20.46723° N 44.58136° E	27265.00	1000
	Ash Shaykh	28.15444° N 34.76126° E	42645.00	1000
	Al Muwassam	16.43223° N 42.80136° E	58790.00	1000

GRI	Station	Position	ED (μs)	PWR (kW)
8930				
	Niijima	34.40332° N 139.27208° E	0.00	1000
	Gaesashi	26.60695° N 128.14915° E	15580.86	1000
	Minamitorishima	24.28556° N 153.98161° E	36051.53	1100
	Tokachibuto	42.74367° N 143.71938° E	53349.53	600
	Pohang	36.18485° N 129.34096° E	73085.64	150
8970				
	Dana	39.85210° N 87.48660° W	0.00	400
	Malone	30.99410° N 85.16910° W	14355.11	800
	Seneca	42.71410° N 76.82590° W	31162.06	800
	Baudette	48.61390° N 94.55500° W	47753.74	800
	BoiseCity	36.50580° N 102.89990° W	63669.46	900
9007				
	Ejde	62.29995° N 7.07391° W	0.00	400
	JanMayen	70.91430° N 8.73237° W	14200.00	250
	Bo	68.63506° N 14.46315° E	28000.00	400
	Vaerlandet	61.29707° N 4.69628° E	41100.00	250

GRI	Station	Position	ED (μs)	PWR (kW)
9610				
	BoiseCity	36.50580° N 102.89990° W	0.00	900
	Gillette	44.00310° N 105.62330° W	13884.48	540
	Searchlight	35.32180° N 114.80470° W	28611.61	560
	LasCruces	32.07170° N 106.86790° W	42044.93	540
	Raymondville	26.53200° N 97.83320° W	56024.80	540
	Grangeville	30.72590° N 90.82860° W	69304.00	800
9930				
	Pohang	36.18485° N 129.34096° E	0.00	150
	Kwang Ju	35.03983° N 126.54092° E	11946.97	50
	Gaesashi	26.60695° N 128.14915° E	25565.52	1000
	Niijima	34.40332° N 139.27208° E	40085.64	1000
	Ussurijsk	44.53325° N 131.63983° E	54162.44	700
9940				
	Fallon	39.55190° N 118.83220° W	0.00	400
	George	47.06340° N 119.74420° W	13796.90	1400
	Middletown	38.78250° N 122.49550° W	28094.50	400
	Searchlight	35.32180° N 114.80470° W	41967.30	560

GRI	Station	Position	ED (μs)	PWR (kW)
9960				
	Seneca	42.71410° N 76.82590° W	0.00	800
	Caribou	46.80760° N 67.92700° W	13797.20	800
	Nantucket	41.25330° N 69.97740° W	26969.93	400
	CarolinaBeach	34.06280° N 77.91280° W	42221.65	600
	Dana	39.85210° N 87.48660° W	57162.06	400
9990				
	StPaul	57.15340° N 170.25170° W	0.00	400
	Attu	52.82890° N 173.18040° E	14875.25	400
	PortClarence	65.24450° N 166.88670° W	32068.95	1000
	Kodiak	57.43900° N 152.36960° W	46590.45	400

BIBLIOGRAPHY

[1] J. Clynch, "The Hunt for RFI - Unjamming a Coast Harbor," January 2003. (Cited on page 3.)

[2] A. Grant, P. Williams, N. Ward, and S. Basker, "GPS Jamming and the Impact on Maritime Navigation," *The Journal of Navigation*, vol. 62, pp. 173–187, 2009. (Cited on page 3.)

[3] M. Thomas, "Global Navigation Space Systems: reliance and vulnerabilities," tech. rep., The Royal Academy of Engineering, 2011. (Cited on page 3.)

[4] John A. Volpe National Transportation System Center, *Vulnerability Assessment of the Transportation Infrastructure Relying on the Global Positioning System*, 2001. (Cited on page 3.)

[5] International Loran Association, *Enhanced Loran (eLoran) Definition Document*, 2007. v. 1.0. (Cited on pages 3, 5, 6, 7, 17, 34, 46, and 96.)

[6] M. J. Narins, "Loran's Capability to Mitigate the Impact of a GPS Outage on GPS Position, Navigation, and Time Applications," tech. rep., Federal Aviation Administration, 2004. (Cited on pages 3, 5, 7, 17, 77, 211, and 212.)

[7] "STATEMENT FROM DHS PRESS SECRETARY LAURA KEEHHNER ON THE ADOPTION OF NATIONAL BACKUP SYSTEM TO GPS." US Department of Homeland Security, February 2008. (Cited on page 4.)

[8] B. Parkinson, J. Doherty, J. Darrah, A. Donahue, L. Hirsch, D. Jewell, D. W. Klepczynski, J. Levine, K. Lewis, E. Stear, P. Ward, and P. Rambow, "Independent Assessment Team (IAT) Summary of Initial Findings on eLoran," tech. rep., Institute for Defense Analyses, 2009. (Cited on page 4.)

[9] D. Jewell, "eLORAN and UrsaNav: Timing Is Everything." GPS World website, March 2012. (Cited on page 4.)

[10] D. A. Divis, "New Foundation Formed to Pursue eLoran as Backup for GPS." Inside GNSS website, November 2013. (Cited on page 4.)

[11] "U.S. Cong. Senate. 113th Congress, 2nd Session. An Act to Authorize Appropriations for the Coast Guard for Fiscal Years 2015 and 2016, and for Other Purposes," February 2014. (Cited on page 4.)

[12] P. Williams, C. Hargreaves, D. Last, and N. Ward, "eLoran in the UK: Leading the Way," in *Proceedings of the ION Pacific PNT Conference*, April 2013. (Cited on page 4.)

[13] "North Korea's GPS Jamming Prompts South Korea to Endorse Nationwide eLoran System." InsideGNSS website, April 2013. (Cited on page 4.)

[14] United States Coast Guard, *Specification of the Transmitted LORAN-C Signal*, 1994. COMDTINST M16562.4A. (Cited on pages 7, 17, 91, 119, 129, and 243.)

[15] W. F. Roland, "Loran-C Phase Code and Rate Manipulation for Reduced Cross Chain Interference," in *Proceedings of the 3rd Technical Symposium of the Wild Goose Association*, 1974. (Cited on pages 10 and 11.)

[16] D. A. Feldman, P. E. Pakos, and C. E. Potts, "On the Analysis and Minimization of Mutual Interference of Loran-C Chains," in *Proceedings of the 4th Technical Symposium of the Wild Goose Association*, 1975. (Cited on pages 10 and 11.)

[17] R. V. Gressang, I. G. G., and M. R. A., "A Case History of Reducing LORAN Chain Cross Rate Interference by Using a Balanced Phase Code," in *Proceedings of the 6th Annual Convention of the Wild Goose Association*, 1977. (Cited on page 10.)

[18] R. S. Engelbrecht and A. Weisshaar, "The Effect of Cross-Rate Interference on LORAN-C Performance," in *Proceedings of the 15th Annual Technical Symposium of the Wild Goose Association*, 1986. (Cited on page 11.)

[19] P. W. Schick, "Cross-Rate Interference Effects and Differential Loran Operation," in *Proceedings of the 25th Annual Technical Symposium, Wild Goose Association*, 1996. (Cited on page 11.)

[20] V. J. P. Etten, "Reduction of Interference to LORAN-C," in *Proceedings of the 8th Annual Convention of the Wild Goose Association*, 1979. (Cited on page 11.)

[21] R. Frank, "Polyphase complementary codes," vol. 26, no. 6, pp. 641–647, 1980. (Cited on page 11.)

[22] R. L. Frank, "The Origin and Evolution of LORAN Phase Coding," in *Proceedings of the 10th Annual Technical Symposium of the Wild Goose Association*, 1981. (Cited on page 11.)

[23] P. Swaszek, G. Johnson, R. Shalaev, and R. Hartnett, "Loran phase codes, revisited," in *Proc. IEEE/ION Position, Location and Navigation Symposium*, pp. 800–809, 2008. (Cited on page 11.)

[24] A. K. Nieuwland and H. J. L. Arriens, "Determining Cross-Rate Interference for the North-West European Loran-C Chains," tech. rep., TU Delft, 1993. (Cited on pages 11, 240, and 242.)

[25] A. K. Nieuwland, "GRI Ranking Based on Cross-Rate Interference in Loran-C," *The Journal of Navigation*, vol. 48, pp. 136 – 152, 1995. (Cited on pages 11, 236, 237, 242, and 244.)

[26] M. Zeltser and M. El-Arini, "The Impact of Cross-Rate Interference on LORAN-C Receivers," vol. AES-21, no. 1, pp. 36–46, 1985. (Cited on page 11.)

[27] A. Helwig, G. Offermans, and D. V. Willigen, "Implementation and Testing of Eurofix in Standard Loran-C Receiver Technology," in *Proceedings of the 25th Annual Technical Symposium, Wild Goose Association*, 1996. (Cited on page 11.)

[28] B. Peterson, K. Gross, and E. Bowen, "Loran Receiver Structure for Cross Rate Interference Cancellation," in *Proceedings of 22nd Annual Technical Symposium of the Wild Goose Association*, 1993. (Cited on pages 11 and 98.)

[29] W. Pelgrum, "Noise - From a Receiver Perspective," in *Proceedings of the 34th Annual Convention and Technical Symposium of the International Loran Association*, 2005. (Cited on pages 11, 97, and 233.)

[30] W. Pelgrum, *New Potential of Low-Frequency Radionavigation in the 21st Century*. PhD thesis, TU Delft, Delft, 2006. (Cited on pages 11, 12, 33, 34, 36, 39, 46, 49, 52, 55, 65, 67, 68, 89, 104, 109, 173, 234, and 243.)

[31] G. Johnson, M. Wiggins, P. F. Swaszek, L. Hartshorn, and R. Hartnett, "Possible Optimizations for the US Loran System," in *Proc. IEEE/ION Position, Location, And Navigation Symposium*, pp. 695–704, April 25–27, 2006. (Cited on page 11.)

[32] L. J. Beekhuis and A. H., "Eurofix and the effect of Cross Rate Interference," in *Proceedings of the 22nd Annual Technical Symposium, Wild Goose Association*, 1993. (Cited on page 11.)

[33] G. W. A. Offermans, D. V. Willigen, and E. Breeuwer, "EUROFIX: Have We Reached the Limit?," in *Proceedings of the 23rd Annual Technical Symposium, Wild Goose Association*, 1994. (Cited on page 11.)

[34] W. N. Dean, "Study of Loran-C Transmission of DGPS Data," in *Proceedings of the 23rd Annual Technical Symposium, Wild Goose Association*, 1994. (Cited on page 11.)

[35] G. Offermans, A. Helwig, and D. V. Willigen, "Eurofix transmission strategies for dual-rated Loran-C stations," in *Proceedings of the 27th Annual Technical Symposium, Wild Goose Association*, 1998. (Cited on page 11.)

[36] S. Lo and P. Enge, "Analysis of the Enhanced LORAN Data Channel," in *German Institute of Navigation Conference*, 2001. (Cited on page 11.)

[37] S. Lo, B. Peterson, and P. Enge, "Loran data modulation: A primer," *IEEE Aerospace and Electronic Systems Magazine*, vol. 22, no. 9, pp. 31–51, 2007. (Cited on pages 11 and 77.)

[38] M. Beckmann, *Carrier Wave Signals Interfering with Loran-C*. PhD thesis, TU Delft, 1992. (Cited on pages 12, 55, 234, and 241.)

[39] J. Safar, F. Vejrazka, and P. Williams, "Accuracy Performance of eLoran Receivers under Cross-Rate Interference Conditions," *Annual of Navigation*, vol. 19, pp. 133–148, 2012. (Cited on page 14.)

[40] J. Safar, P. Williams, S. Basker, and F. Vejrazka, "Cross-Rate Interference and Implications for Core eLoran Service Provision," in *Proceedings of the International Loran Association (ILA) 38th Annual Meeting*, (Portland, ME, U.S.), 2009. (Cited on pages 14, 16, and 267.)

[41] J. Safar, F. Vejrazka, and P. Williams, "Assessing the limits of eLoran positioning accuracy," in *Proceedings of the TransNav 2011 International Symposium on Marine Navigation and Safety of Sea Transportation* (A. Weintrit, ed.), (Gdynia, Poland), pp. 55–63, Gdynia Maritime University, CRC Press/Balkema, June 2011. ISBN: 978-0-415-69113-0. (Cited on pages 14, 16, and 267.)

[42] P. Williams, C. Hargreaves, J. Safar, C. K. Lebekwe, G. Shaw, and N. Ward, "Resilient PNT in e-Navigation," in *Proceedings of the Royal Institute of Navigation NAV10 Conference and Exhibition*, 2010. (Cited on pages 14, 16, and 267.)

[43] J. Safar, C. K. Lebekwe, and P. Williams, "Accuracy Performance of eLoran for Maritime Applications," *Annual of Navigation*, vol. 16, pp. 109–122, 2010. (Cited on page 14.)

[44] J. Safar, P. Williams, and S. Gug, "Group Repetition Interval Selection for eLoran," in *Proceedings of the Royal Institute of Navigation (RIN) NAV08/ International Loran Association (ILA) 37th Annual Meeting*, (London, UK), 2008. (Cited on pages 14, 16, 55, 59, 242, 243, and 267.)

[45] J. Safar, P. Williams, S. Basker, and F. Vejrazka, "Group Repetition Interval Selection and Core eLoran Service Capacity," in *Proceedings of the 13th IAIN World Congress*, (Stockholm), 2009. (Cited on pages 16 and 267.)

[46] J. Safar, C. K. Lebekwe, and P. Williams, "Accuracy Performance of eLoran for Maritime Applications," in *Proceedings of the NAVSUP 2010 conference*, (Gdynia, Poland), 2010. (Cited on pages 16 and 267.)

[47] "LORIPP/LORAPP Draft Specification of the eLoran System, Rev. 3.0," September 2008. RTCM Paper 196-2008-SC127-036. (Cited on pages 17, 18, 19, 20, 21, 27, 30, 31, 34, 155, and 162.)

[48] Z. Hrdina and F. Vejrazka, *Signaly a soustavy*. Czech Technical University, Prague. (Cited on pages 26, 126, 146, 271, 278, and 283.)

[49] C. Appel, "New Life for LORAN, Part 1," 2004. (Cited on page 33.)

[50] C. Appel, "New Life for LORAN, Part 2," 2004. (Cited on page 33.)

[51] T. Hardy, "Next Generation LF Transmitter Technology for (e)LORAN Systems," in *Proceedings of the Royal Institute of Navigation (RIN) NAV08/ International Loran Association (ILA) 37th Annual Meeting*, (London, UK), 2008. (Cited on pages 33 and 34.)

[52] W. F. Roland, "Loran-C Chain and UTC Synchronization," in *Proceedings of the 28th Annual Technical Symposium of the International Loran Association*, 1999. (Cited on pages 34 and 237.)

[53] T. Celano, "Time and Frequency Equipment Capstone," in *Proceedings of the International Loran Association (ILA) 33th Annual Meeting*, 2004. (Cited on page 34.)

[54] D. van Willigen, R. Kellenbach, C. Dekker, and W. van Buuren, "eDLoran - Next Generation of Differential Loran," 2014. (Cited on page 34.)

[55] International Telecommunication Union, *ITU-R Rec. 368-9, Ground-Wave Propagation Curves for Frequencies between 10 kHz and 30 MHz*, 2007. (Cited on pages 35, 36, and 58.)

[56] International Telecommunication Union, *ITU-R Rec. BS.561-2, Definitions of Radiation in LF, MF and HF Broadcasting Bands*, 1986. (Cited on page 35.)

[57] T. S. Rapport, *Wireless Communications: Principles and Practice*. 2002. (Cited on page 36.)

[58] International Telecommunication Union, *ITU-R P.832-2 World Atlas of Ground Conductivities*, January 1999. (Cited on page 36.)

[59] "MINIMUM PERFORMANCE STANDARDS FOR MARINE LORAN RECEIVING EQUIPMENT," Tech. Rep. RTCM Paper 211-2009-SC127-068, RTCM, 2009. Revision 1.4, Draft. (Cited on pages 38 and 39.)

[60] G. Johnson, P. Swaszek, R. Hartnett, R. Shalaev, and C. Oates, "BALOR model validity for the airport ASF mapping methodology," in *Proceedings of the Institute of Navigation National Technical Meeting*, 2006. (Cited on page 39.)

[61] P. Williams, "eLoran Tutorials: Propagation," October 2008. eLoran Tutorial Programme, Church House, Westminster, London. (Cited on page 39.)

[62] H. T. Sherman, "FINALLY - A PRACTICAL ECD ESTIMATING TECHNIQUE," in *Proceedings of 13th Annual Technical Symposium of the Wild Goose Association*, 1984. (Cited on page 40.)

[63] P. Williams and D. Last, "Modelling Loran-C envelope-to-cycle differences in mountainous terrain," in *Proceedings of the DGON European Radio Navigation Networks Symposium*, (Munich, Germany), 2003. (Cited on page 40.)

[64] B. Forssell, *Radionavigation Systems*. Artech House, 2008. (Cited on pages 41, 65, 76, 181, and 212.)

[65] "The Ionosphere," May 2014. (Cited on page 41.)

[66] International Telecommunication Union, *ITU-R P.684-6, Prediction of field stregth at frequencies below about 150 kHz*, 2012. (Cited on pages 41 and 42.)

[67] L. Barclay, *Propagation of Radiowaves*. The Institution of Engineering and Technology, London, UK, 2nd ed., 2003. (Cited on page 41.)

[68] International Telecommunication Union, *ITU-R P.1147-2, Prediction of Sky-wave Field Strength at Frequencies Between About 150 kHz and 1700 kHz*, 2003. (Cited on pages 41, 42, 43, 59, 213, and 220.)

[69] "Consultations with the General Lighthouse Authorities of the UK and Ireland," 2013. (Cited on page 42.)

[70] D. C. Poppe, *Coverage and Performance Prediction of DGPS Systems Employing Radiobeacon Transmissions*. PhD thesis, University of Wales, Bangor, 1995. (Cited on pages 43, 214, 217, and 218.)

[71] P. B. Morris, "Conditions Leading to Anomalously Early Skywave," in *Proceedings of 32nd Annual Convention and Technical Symposium*, 2003. (Cited on pages 43, 45, and 226.)

[72] International Telecommunication Union, *ITU-R P.372-9, Radio Noise*. (Cited on pages 47, 48, 49, 50, 51, 53, 59, 213, 214, 215, 216, 217, and 219.)

[73] C. Boyce, *Atmospheric Noise Mitigation for LORAN*. PhD thesis, Stanford University, 2007. (Cited on pages 49, 51, and 213.)

[74] D. van Willigen, *Hard Limiting And Sequential Detecting LORAN-C Sensor*. PhD thesis, TU Delft, 1985. (Cited on pages 49 and 67.)

[75] International Telecommunication Union, *ITU-R M.1467-1, Prediction of Sea Area A2 and NAVTEX Ranges and Protection of the A2 Global Maritime Distress and Safety System Distress Watch Channel*, 2006. (Cited on pages 52, 63, 215, 216, and 219.)

[76] International Telecommunication Union, *ITU-R M.589-3, Technical characteristics of methods of data transmission and interference protection for radionavigation services in the frequency bands between 70 and 130 kHz*, August 2001. (Cited on page 54.)

[77] H. J. L. Arriens and M. Beckmann, "Selecting Group Repetition Intervals for North-West European Loran-C Chains," tech. rep., Delft University of Technology, 1992. (Cited on pages 55, 233, 240, 241, and 242.)

[78] H. J. L. Arriens and A. K. Nieuwland, "Selecting Group Repetition Intervals for North-West European Loran-C Chains Addendum," tech. rep., Delft University of Technology, 1993. (Cited on pages 55, 233, 240, 242, and 243.)

[79] L. P. Remmerswaal and D. V. Willigen, "Interference and Loran-C: A European Problem," in *Proceedings of the 17th Annual Technical Symposium*, 1988. (Cited on page 55.)

[80] L. Remmerswaal and D. van Willigen, "Some aspects of interference on Loran-C," *IEE Proceedings F Radar and Signal Processing*, vol. 136, no. 3, pp. 109–117, 1989. (Cited on page 55.)

[81] H. J. L. Arriens and M. Beckmann, "Selecting Group Repetition Intervals for European Chains," in *Proceedings of the 18th Annual Technical Symposium, Wild Goose Association*, 1989. (Cited on page 55.)

[82] M. Beckmann, "Synchronous Interference to Loran-C and its Influence on Cycle Identification," in *Proceedings of the 19th Annual Technical Symposium*, 1990. (Cited on page 55.)

[83] M. Beckmann, "Interference Detection and Suppression Methods for Loran-C Receivers," in *Proceedings of the 19th Annual Technical Symposium, Wild Goose Association*, 1990. (Cited on pages 55 and 243.)

[84] F. Hubert, "GRIs Selection in the NELS," tech. rep., DGA DCN Brest, 1993. (Cited on pages 55, 242, and 244.)

[85] D. Last and Y. Bian, "Carrier wave interference and Loran-C receiver performance," *IEE Proceedings F Radar and Signal Processing*, vol. 140, no. 5, pp. 273–283, 1993. (Cited on pages 55 and 233.)

[86] D. Last and B. Yi, "Carrier-wave interference to Loran-C: a statistical evaluation," vol. 29, pp. 1260–1274, Oct. 1993. (Cited on pages 55, 59, and 233.)

[87] D. Last, "Coverage and performance predictions for the northwest european loran-c system," *SIMULATION*, vol. 60, pp. 318–326, 1993. (Cited on pages 55, 211, and 253.)

[88] "NELS Manual Annex F: NELS Specification of the Transmitted Loran-C Signal," tech. rep., NELS, 2003. (Cited on pages 55 and 91.)

[89] K. H. Strom and T. Eltoft, "Cancelation of Continuous Wave Interferences in Loran-C Receivers using an Adaptive Predictor," 1995. (Cited on pages 55 and 243.)

[90] A. A. Abbo, *Highly-Integrated Navigation Receiver Architecture*. PhD thesis, TU Delft, 1999. (Cited on pages 55 and 243.)

[91] "Consultations with Reelektronika b.v.," 2008. (Cited on pages 55, 65, 74, 88, and 243.)

[92] "Notes from a discussion between University of Wales, Bangor and Reelektronika b.v.," September 2004. (Cited on pages 55, 65, 68, and 243.)

[93] U. Rohde, *Communications Receivers, DSP, Software Radios, and Design*. McGraw-Hill, 3rd ed., 2004. (Cited on page 55.)

[94] E. H. Nordholt and D. van Willigen, "A New Approach to Active Antenna Design," *IEEE Transactions on Antennas and Propagation*, vol. 28, pp. 904–910, 1980. (Cited on pages 55 and 67.)

[95] J. R. Vig, "Quartz Crystal Resonators and Oscillators For Frequency Control and Timing Applications - A Tutorial," January 2007. (Cited on page 56.)

[96] "Consultations with Reelektronika b.v.," 2010. (Cited on pages 57, 65, and 70.)

[97] "ITU BR International Frequency Information Circular (Terrestrial Services)." DVD, July 2008. (Cited on pages 59, 241, and 244.)

[98] M. Füllekrug, "Wideband digital low-frequency radio receiver," *Measurement Science and Technology*, vol. 21, no. 1, pp. 1–9, 2009. (Cited on page 59.)

[99] M. Füllekrug, M. Parrot, M. Ash, I. Astin, P. Williams, and R. Talhi, "Transionospheric attenuation of 100 kHz radio waves inferred from satellite and ground based observations," *Geophysical Research Letters*, vol. 36, no. 6, pp. 1–5, 2009. (Cited on page 59.)

[100] International Telecommunication Union, *ITU-R P.372-8, Radio Noise*, 2003. (Cited on page 62.)

[101] R. V. Nee and H. J. Andersen, "Optimum Loran-C Signal Processing: First Experimental Results," in *Proceedings of the 22nd Annual Technical Symposium, Wild Goose Association*, 1993. (Cited on page 65.)

[102] D. van Nee, "An advanced LORAN-C receiver structure," *SIMULATION*, vol. 60, no. 5, pp. 335–340, 1993. (Cited on page 65.)

[103] R. V. Nee, *Multipath and Multi-Transmitter Interference in Spread-Spectrum Communication and Navigation Systems*. PhD thesis, TU Delft, 1995. (Cited on page 65.)

[104] B. Peterson, "LORAN C H-Field DDC Receiver," tech. rep., United States Coast Guard Academy Department of Engineering, 2001. (Cited on page 65.)

[105] G. Offermans and A. Helwig, *Integrated Navigation System Eurofix, Vision Concept, Design, Implementation & Test*. PhD thesis, TU Delft, 2003. ISBN 90-901-7418-4. (Cited on pages 65, 77, 78, and 97.)

[106] J. Safar, "CRI from a Receiver Perspective (Discussions with Reelektronika)." Unpublished, March 2009. (Cited on page 65.)

[107] "Consultations with CrossRate Technology, LLC," 2009. (Cited on page 65.)

[108] "Consultations with Plutargus," 2010. (Cited on pages 65 and 121.)

[109] "Consultations with UrsaNav Inc.," May 2014. (Cited on pages 65, 69, and 70.)

[110] B. W. Parkinson and J. J. Spilker, *Global Positioning System: Theory and Applications*, vol. Volume I. American Institute of Aeronautics and Astronautics, Inc., 1996. (Cited on pages 69 and 71.)

[111] O. Mancini, "Tutorial Precision Frequency Generation Utilizing OCXO and Rubidium Atomic Standards with Applications for Commercial, Space, Military, and Challenging Environments," March 2004. (Cited on page 70.)

[112] P. Closas, C. Fernandez-Prades, and J. A. Fernandez-Rubio, "Maximum Likelihood Estimation of Position in GNSS," *IEEE Signal Processing Letters*, vol. 14, pp. 359 – 361, 2007. (Cited on page 72.)

[113] P. Closas, C. Fernandez-Prades, D. Bernal, and J. A. Fernandez-Rubio, "Bayesian Direct Position Estimation," in *Proceedings of ION GNSS 21st International Technical Meeting of the Satellite Division*, 2008. (Cited on page 72.)

[114] P. Closas, *Bayesian Signal Processing Techniques for GNSS Receivers: from Multipath Mitigation to Positioning*. PhD thesis, Universitat Politecnica de Catalunya, Barcelona, 2009. (Cited on page 72.)

[115] D. A. Feldman, *An Atmospheric Noise Model with Application to Low Frequency Navigation Systems*. PhD thesis, Massachusetts Institute of Technology, 1972. (Cited on page 72.)

[116] S. M. Kay, *Fundamentals of Statistical SIgnal Processing*, vol. Volume II, Detection Theory. Prentice Hall PTR. (Cited on page 72.)

[117] W. N. Dean, "Clarinet Pilgrim System," in *Proceedings of the 2nd Annual Symposium of the Wild Goose Loran-C Association*, (Washington, D.C.), 1973. (Cited on page 77.)

[118] S. Lo, B. Peterson, P. Enge, and P. Swaszek, "Loran data modulation: extensions and examples," *IEEE Aerospace and Electronic Systems Magazine*, vol. 43, no. 2, pp. 628–644, 2007. (Cited on page 77.)

[119] B. B. Peterson, A. Helwig, and G. Offermans, "Improvements in Error Rate in Eurofix Communications Data Link via Cross Rate Canceling and Antenna Beam Steering," in *Proceedings of the 55th Annual Meeting of The Institute of Navigation*, 1999. (Cited on page 78.)

[120] S. M. Kay, *Fundamentals of Statistical Processing, Volume I: Estimation Theory*. Prentice Hall PTR, 1993. (Cited on pages 83, 84, 114, 115, and 129.)

[121] Z. Hrdina, *Statisticka radiotechnika*. Czech Technical University, Prague, 1996. ISBN 80-01-01489-4. (Cited on page 85.)

[122] H. Meyr, M. Moeneclaey, and S. A. Fechtel, *Digital Communication Receivers: Synchronization, Channel Estimation, and Signal Processing*. John Wiley & Sons, Inc., 1998. (Cited on page 88.)

[123] "MINIMUM PERFORMANCE STANDARDS FOR MARINE eLORAN RECEIVING EQUIPMENT," Tech. Rep. RTCM Paper 175-2011-SC127-094, RTCM, 2010. Revision 2.0, Draft. (Cited on pages 89, 106, 110, 112, 120, 213, and 226.)

[124] "Consultations with Prof. Durk van Willigen, Reelektronika b.v.," November 2010. (Cited on page 89.)

[125] Personal discussions with Dr. Arthur Helwig (Reelektronika b.v.). (Cited on page 99.)

[126] S. Lo, R. Wenzel, and P. Enge, "Analysis and Modeling of Skywave Behavior," in *Proceedings of the 38th Annual Convention and Technical Symposium of the International Loran Association*, 2009. (Cited on page 104.)

[127] A. Mohammed, F. L. Roux, and D. Last, "Eigen-decomposition techniques for skywave interference detection in loran-c receivers," in *Proceedings of the 32nd Annual Convention and Technical Symposium of the International Loran Association*, 2003. (Cited on page 109.)

[128] M. Abbas, H. Chemnitzer, and D. Last, "Full performance analysis of IFFT spectral-division technique for skywave identification in Loran-C," in *Proceedings of 31st Annual Convention and Technical Symposium, International Loran Association (ILA31)*, 2002. (Cited on page 109.)

[129] A. Mohammed, Y. Bian, and D. Last, "Rational Modelling Techniques for the Identification of Loran-C Skywaves," in *Proceedings of the 23rd Annual Technical Symposium, Wild Goose Association*, 1994. (Cited on page 109.)

[130] M. S. Grewal, L. R. Weill, and A. P. Andrews, *Global Positioning Systems, Inertial Navigation, and Integration*. John Wiley & Sons, Inc., 2001. (Cited on pages 115 and 179.)

[131] "MINIMUM PERFORMANCE STANDARDS (MPS) MARINE LORAN-C RECEIVING EQUIPMENT," 1977. (Cited on pages 119 and 199.)

[132] "Minimum operational performance standards for airborne area navigation equipment using loran-c inputs," 1986. (Cited on pages 120 and 199.)

[133] N. Beauregard, "Loran-C Receiver Test Procedures," Tech. Rep. DOT/FAA/CT-TN85/30, U.S. Federal Aviation Administration, 1985. (Cited on pages 120 and 199.)

[134] "Airborne area navigation equipment using loran c inputs." (Cited on pages 120, 197, and 199.)

[135] "Loran-C receivers for ships - Minimum performance standards - Methods of testing and required test results." (Cited on pages 120 and 199.)

[136] "Locus Inc. website." (Cited on pages 120 and 121.)

[137] J. V. Carroll, "Notes on the Computation and Use of Atmospheric Signal-to-Noise Ratio in Loran Receivers," in *Proceedings of the Twentieth Annual Technical Symposium, Wild Goose Association*, 1991. (Cited on page 121.)

[138] R. Erikson, "WHAT ARE WE MEASURING?," in *Proceedings of the Twentieth Annual Technical Symposium, Wild Goose Association*, 1991. (Cited on page 121.)

[139] S. Lo, B. Peterson, C. Boyce, and P. Enge, "Loran Coverage Availability Simulation Tool," in *Proceedings of the Royal Institute of Navigation (RIN) NAV08/ International Loran Association 37th Annual Meeting*, 2008. (Cited on pages 129, 206, 207, and 213.)

[140] T. H. Cormen, C. E. Leiserson, R. L. Rivest, and C. Stein, *Introduction to Algorithms*. The MIT Press, 3rd ed., 2009. (Cited on page 134.)

[141] A. Papoulis and S. U. Pillai, *Probability, Random Variables, and Stochastic Processes*. McGraw-Hill Higher Education, 2002. (Cited on pages 145, 147, and 169.)

[142] G. H. Hardy and E. M. Wright, *An Introduction to the Theory of Numbers*. Oxford University Press, 1975. (Cited on page 150.)

[143] R. M. Howard, *Principles of Random Signal Analysis and Low Noise Design*. John Wiley & Sons, Inc., 2002. (Cited on pages 152 and 153.)

[144] K. S. Miller and R. J. Schwarz, "On the interference of pulse trains," *Journal of Applied Physics*, vol. 24, pp. 1032–1036, Aug 1953. (Cited on page 156.)

[145] H. D. Friedman, "Coincidence of pulse trains," *Journal of Applied Physics*, vol. 25, pp. 1001–1005, Aug 1954. (Cited on pages 156 and 157.)

[146] S. Stein and D. Johansen, "A statistical description of coincidences among random pulse trains," *Proceedings of the IRE*, vol. 46, pp. 827–830, May 1958. (Cited on pages 159 and 161.)

[147] A. G. Self and B. G. Smith, "Intercept time and its prediction," *IEE Proceedings F Communications, Radar and Signal Processing*, vol. 132, pp. 215–220, July 1985. (Cited on pages 159 and 161.)

[148] M. G. Kendall and P. A. P. Moran, *Geometrical Probability*. Charles Griffin & Company Limited, London, 1963. (Cited on page 161.)

[149] G. G. Macfarlane, "On the Energy-Spectrum of An Almost Periodic Succession of Pulses," in *Proceedings of IRE*, 1949. (Cited on page 163.)

[150] I. Harre, "A Standardized Algorithm for the Determination of Position Errors by the Example of GPS with and without Selective Availability," *International Hydrographic Review*, vol. 2, June 2001. (Cited on pages 181 and 226.)

[151] *IMO Resolution A.1046(27), World Wide Radionavigation System*, December 2011. (Cited on page 211.)

[152] R. W. Nutting, *Loran-C Rate Selection Process*. United States Coast Guard, 1988. (Cited on pages 236 and 238.)

[153] C. Stout, G. Offermans, A. Helwig, C. Schue, B. Walker, T. Hardy, and K. Zwicker, "Low Frequency (LF) Solutions for Alternative Positioning, Navigation, Timing and Data (APNT&D)," in *Proceedings of the European Navigation Conference*, November 2011. (Cited on page 243.)

[154] P. Williams, "Options for an eLoran Transmitter in Ireland," tech. rep., The General Lighthouse Authorities of the UK and Ireland, 2012. (Cited on page 247.)

[155] A. Helwig, G. Offermans, C. Stout, C. Schue, B. Walker, T. Hardy, S. Martin, and K. Zwicker, "Low Frequency (LF) Solutions for Alternative Positioning, Navigation, Timing and Data (APNT&D) and Associated Receiver Technology," in *Proceedings of the Royal Institute of Navigation NAV10 Conference, Church House, London*, November 2010. (Cited on pages 261 and 268.)

[156] J. Sykora, *Teorie digitalni komunikace*. Czech Technical University, Prague, 2003. (Cited on page 276.)

COLOPHON

This thesis was typeset with LaTeX 2ε using Hermann Zapf's *Palatino* and *Euler* type faces (Type 1 PostScript fonts *URW Palladio L* and *FPL* were used). The listings are typeset in *Bera Mono*, originally developed by Bitstream, Inc. as "Bitstream Vera". (Type 1 PostScript fonts were made available by Malte Rosenau and Ulrich Dirr.)

The typographic style was inspired by Bringhurst's genius as presented in *The Elements of Typographic Style*. It is available for LaTeX via CTAN as "`classicthesis`".

Final Version as of 21st August 2014 at 15:43.